DEUTSCHES ELEKTRONEN-SYNCHROTRON DESY

DESY 81-044
July 1981

REVIEW OF e^+e^- EXPERIMENTS WITH PLUTO FROM 3 TO 31 GeV

by

L. Criegee and G. Knies

NOTKESTRASSE 85 · 2 HAMBURG 52

To be sure that your preprints are promptly included in the HIGH ENERGY PHYSICS INDEX , send them to the following address (if possible by air mail) :

DESY
Bibliothek
Notkestrasse 85
2 Hamburg 52
Germany

DESY 81-044
July 1981

Review of e^+e^- Experiments with PLUTO from 3 to 31 GeV

by

Lutz Criegee
and
Gerhard Knies

DESY

Abstract

The contributions of the PLUTO experiment to e^+e^- physics at collision energies in the range of 3 - 31 GeV are reviewed. The review briefly sketches the storage rings DORIS and PETRA at DESY, and describes the most important features of the PLUTO detector, of data processing, and of the analysis methods. It covers the physics results in the fields of electroweak interactions, of the heavy lepton τ and the search for still heavier leptons, of hadron production with evidence for quark and gluon jets, as well as multiparton effects, of Υ decays and their relation to QCD, and concludes with first results in high-energy photon-photon interactions.

Table of content

1. Introduction

2. The storage rings DORIS and PETRA

References

Figure captions

3. The PLUTO detector

3.1 The magnet

3.2 Track chambers

3.3 Shower counters

3.4 Muon detection

3.5 Luminosity monitor

3.6 The forward spectrometers

3.7 The trigger
3.7.1 The wire logic
3.7.2 Neutral energy trigger
3.7.3 The RAM master logic

3.8 Data analysis procedures
3.8.1 Data flow
3.8.2 Track analysis
3.8.3 Event selection
3.8.4 The total hadronic cross section

3.9 Acceptance calculations
3.9.1 Phase space event simulation
3.9.2 Jets
3.9.3 Two-photon interactions
3.9.4 QED reactions
3.9.5 Heavy leptons
3.9.6 Detector response and analysis chain
3.9.7 Radiative corrections

References

Figure captions

4. QED Tests
Upper limits on cutoff parameters and electroweak effects

4.1 Introduction

4.2 Radiative corrections and QED modifications

4.3 The data

4.4 QED cutoff parameters

4.5 Electroweak effects
4.5.1 Limits on v^2, a^2 and M_Z
4.5.2 Limits on the Salam-Weinberg angle θ_W
4.5.3 Models with 2 neutral gauge bosons

4.6 Summary and conclusion

Appendix 4A: Formulae for QED modificaitons

4A.1 Cut-off parameterization

4A.2 Electroweak cross sections

Appendix 4B: Data analysis in QED reactions

4B.1 $e^+e^- \to e^+e^-$

4B.2 $e^+e^- \to \gamma\gamma$

4B.3 $ee \to \mu\mu$

4B.4 $ee \to \tau\tau$

References

Figure captions

5. The heavy lepton τ

5.1 Introduction

5.2 Evidence for heavy lepton production
5.2.1 Search for heavy lepton events
5.2.2 μe events from charm?
5.2.3 Results on heavy lepton parameters

5.3 The hadronic decay modes of the τ
5.3.1 The decay $\tau \to \nu\pi^0$
The decay $\tau \to \nu\rho^0\pi$

5.4 Some limits on τ parameters
5.4.1 Limit on the lifetime
5.4.2 Limit on the τ neutrino mass
5.4.3 Limit on the τ charge radius

5.5 Search for leptons heavier than the τ

5.6 Summary on heavy leptons

References

Figure captions

6. Hadron production in the continuum

6.1 The total hadronic cross section

6.2 Charm effects
6.2.1 Inclusive K^0 production
6.2.2 Inclusive J/ψ production

6.3 Jets
6.3.1 Jet analysis
6.3.2 Two-jet topologies
6.3.3 Evidence for hard gluons

6.4 Multiparton effects
6.4.1 Energy-energy correlations
6.4.2 Multiplicity distributions
6.4.3 Transverse momenta

References

Figure captions

7. The Υ and J/ψ resonances

7.1 Υ discovery and open questions

7.2 The Υ search at DORIS

7.3 Parameters of the Υ resonance
7.3.1 Mass and width of the Υ
7.3.2 Production cross section, electronic width and constituent charge

7.4 Decay modes of the Υ, and the total width
7.4.1 The leptonic branching ratio
7.4.2 The fraction of direct hadronic decays
7.4.3 The total width of the Υ
7.4.4 Γ_{dir} and the running strong coupling constant
7.4.5 The C-parity forbidden decay $\Upsilon \to \gamma\gamma$

7.5 Topological properties of direct Υ decays - Search for 3 gluon decay
7.5.1 The direct decay sample
7.5.2 Event shape in momentum space
7.5.3 Jet formation: thrust and triplicity analysis

7.6 Inclusive single particle properties
7.6.1 Multiplicity of charged tracks
7.6.2 Momentum distributions
7.6.3 Inclusive K^0_S production

7.7 Summary and conclusions for Υ (9.46)

7.8 J/ψ and ψ' resonances
7.8.1 Topological decay properties
7.8.2 The decay rate $J/\psi \to \gamma f$
7.8.3 f polarization

References

Figure captions

8. Photon - photon interactions

8.1 Kinematics
8.2 Selection of $\gamma\gamma$ events
8.3 Production of lepton and hadron pairs
8.4 The total hadronic $\gamma\gamma$ cross section
8.5 High $p_\perp$ jets

Appendix: Electron-electron and photon-photon cross section

References

Figure captions

Acknowledgements

1. Introduction

With the discovery of the J/ψ particle in 1974 e^+e^- storage rings became the focal point of interest in particle physics. Within a few years a series of exciting results concerning the constituents of matter and the forces between them was produced.

A beautiful confirmation of the weak isodoublet nature of quarks was provided by the study of open charm state decays, suggesting a close parallelism between quarks and leptons. The discovery of the τ lepton and the determination of its sequential character was the first evidence for a third generation of lepton isodoublets and gave rise to speculations on a third quark isodoublet. Detailed measurements of the ϒ resonances unambigously confirmed their nature as quark-antiquark bound states of a new quark flavour, with charge -1/3, fitting as the "bottom" partner into the expected third quark doublet.

ϒ decays also confirmed fundamental properties of gluons as expected for QCD quanta. The spectroscopy of quarkonia, i.e. of the $c\bar{c}$ and $b\bar{b}$ bound states, disclosed beautiful positronium like level schemes and yielded data for precise tests of predictions based on the QCD picture of the forces between quarks. The observation of clear 2-jet events was an impressive manifestation of the production of confined quarks as the underlying process of hadron production. The observation of clear 3-jet events at PETRA energies, confirmed expectations for hard bremsstrahlung of colour field quanta and furnished the most striking confirmation of a basic QCD process. In addition there is a growing amount of data on hadron production and jet properties which provide a challenge for a thorough understanding of the fragmentation process in terms of QCD.

The energy dependence of cross sections for lepton pair production and hadron production, in the energy range of $10 < s < 1000$ GeV^2 has verified the pointlike nature of the electric charge of partons and leptons down to the same limits, indicating their equally fundamental role as constituents of matters. Tests of validity of QED have been extended significantly up to four-momentum transfers of over 1000 GeV^2, and first tests of weak interactions at large q^2, in lepton-pair and hadron production are becoming feasible. Finally, a new type of reaction, hadron production in photon-photon collisions is opening a very promising field of physics.

The PLUTO detector started its first test run in late 1974, just in time to confirm the newly discovered J/ψ and ψ' resonances. It continued data taking in the years 1976 and 1978/79, at the storage rings DORIS and PETRA. With these data the PLUTO collaboration [+] could achieve significant contributions to the e^+e^- physics over the CMS energy range from 3 to 32 GeV. The history of the PLUTO experiment as reported in this paper thus appears suitable to illustrate, in a coherent fashion, the exciting progress in this fruitful field of particle physics. At the same time with the PLUTO experiment, other experiments at DORIS, SPEAR and PETRA have produced important results in the same field of physics, in a sometimes hard but also fruitful competition. Wherever appropriate we give reference to related results, without trying to be comprehensive.

This report will first briefly introduce the storage rings DORIS I, DORIS II, and PETRA (Sect.2), and describe the PLUTO detector including data taking and analysis procedures (Sect. 3). It will then expand on the physics results obtained in the fields of QED (Sect. 4), of heavy lepton τ (Sect. 5), of hadron production in the continuum (Sect. 6) and of $c\bar{c}$ and $b\bar{b}$ resonances (Sect. 7), and conclude with interesting first results on photon-photon interactions (Sect. 8).

[+] The PLUTO collaboration started with 15 members (see Sect. 7.8), and grew up to about 65 members in 1980. Until 1980 the following physicists have been working in the PLUTO collaboration:

Ch. Berger, H. Genzel, R. Grigull, W. Lackas and F. Raupach
I. Phys. Institut der RWTH Aachen [1], Germany,

A. Klovning, E. Lillestöl and E. Lillethun[2]
University of Bergen [3], Norway,

H. Ackermann, G. Alexander[4], G. Bella[4], J. Bürger, J. Burmester[2],
L. Criegee, H.C. Dehne, R. Devenish[5], A. Eskreys[6], G. Flügge[7],
J.D. Fox[2], G. Franke, W. Gabriel[2], Ch. Gerke, E. Hackmack[2],
P. Harms[2], G. Horlitz[2], Th. Kahl[8], G. Knies, W. Krechlock[2],
E. Lehmann[2], H. Mehrgard[2], H.D. Mertiens[2], U. Michelsen, K.H. Pape,
H.D. Reich, M. Scarr[9], R. Schmitz[2], T.N. Ranga Swamy[2], B. Stella[10],
R.L. Thompson[2], U. Timm, W. Wagner, H.Wahl[12], S. Wolff[2],
P. Waloschek, G.G. Winter and W. Zimmermann
Deutsches Elektronen Synchrotron DESY, Hamburg, Germany,

Footnote continued:

O. Achterberg, V. Blobel, L. Boesten, H. Daumann[2], A.F. Garfinkel[13],
V. Hepp[14], H. Jensing[2], H. Kapitza, B. Koppitz, B. Lewendel,
E.Lohrmann[2], W. Lührsen, R. Maschuw[7], R. van Staa[2],
H. Spitzer and G. Wetjen[2]
II. Institut für Experimentalphysik der Universität Hamburg [1], Germany,

C.Y. Chang, R.G. Glasser, R.G. Kellogg, K.H. Lau[7], R.O. Polvado,
B. Sechi-Zorn, J.A. Skard, A. Skuja, G. Welch and G.T. Zorn,
University of Maryland [15], USA

A. Bäcker, F. Barreiro, S. Brandt, K. Derikum, A. Diekmann[2],
C. Grupen, H.J. Meyer, B. Neumann, M. Rost and G. Zech
Gesamthochschule Siegen [1], Germany,

T. Azemoon[16], H.J. Daum, H. Meyer, O. Meyer,
M. Rössler[2], D. Schmidt and K. Wacker[17]
Gesamthochschule Wuppertal [1], Germany

1 Supported by the BMFT, Federal Republic of Germany
2 Former member of the PLUTO Collaboration
3 Partially supported by the Norwegian Council for Science and Humanities
4 On leave from Tel Aviv University, Israel
5 Now at Oxford University, UK
6 Now at Institute of Nucl. Physics, Krakow, Poland
7 Now at University of Karlsruhe, Germany
8 Now at MPI für Physik und Astrophysik, München, Germany
9 On leave from University of Glasgow, UK
10 On leave from University of Rome, Italy; partially supported by INFN
11 Now at Humboldt University, Arcata, CA, USA
12 Now at CERN, Geneva, Switzerland
13 Now at Purdue University, Lafayette, IN, USA
14 Now at Heidelberg University, Germany
15 Partially supported by Dept. of Energy, USA
16 Now at University College, London, UK
17 Now at Harvard University, Cambridge, MA, USA

2. The storage rings DORIS and PETRA

The e^+e^- storage ring DORIS (double orbit intersecting storage ring) was designed during the years 1966-1967 with the emphasis on exploring QED and hadronic physics in the 2 - 3 GeV c.m. energy range [201]. Since at these energies the luminosity is limited by the beam-beam interaction, the storage ring was built such as to store and collide a large number of electron (and positron) bunches. Fig. 2.1 shows the layout of the injection system and the storage ring. Electrons are first accelerated in the linear accelerator to 450 MeV, then in the synchrotron to the desired energy, and finally injected into one of the DORIS rings. The positrons are produced by electrons striking a converter in the middle of the linear accelerator, then focussed and accelerated in the second half and in the synchrotron as indicated, and are then stored in the second ring which is placed partly above and partly below the electron ring. Table 2.I lists some important parameters.

Both rings have vertical bends such as to intersect in two interaction regions at a crossing angle of 12 mrad (beam-beam). The bunch cross section at the intersections is small. Typical values are 1 mm (rms) horizontally, 0.1 mm vertically and 1 cm along the beam. The time structure of the beam-beam interactions is quasi - continuous, namely one short (<0.2 nsc) flash every 2 nsec. It is imposed by the 500 MHz acceleration which is needed to compensate for the power lost by synchrotron radiation. Peak luminosities of typically 0.5×10^{30} cm^{-2} sec at 3 GeV and 4×10^{30} cm^{-2} sec^{-1} at 5 GeV c.m. energy have been achieved.

The stored currents and therefore the luminosity are limited by interactions between successive bunches, and at high energies also by the available r.f. power. Here the luminosity can be increased by concentrating the same current onto fewer bunches. At 5 GeV DORIS was therefore operated with 120 instead of 480 circulating bunches.

In order to reach the T region, DORIS had to be converted into a single-ring machine [202]. For this purpose the upper two half rings (Fig. 2.1) were 'connected' by dipole magnets producing a vertical bend on both sides of the interaction regions. All available r.f. and magnet power was concentrated into this new single ring. The time schedule and the success of this changeover were impressive: In summer 1977, shortly after the discovery of the T at FNAL [203],

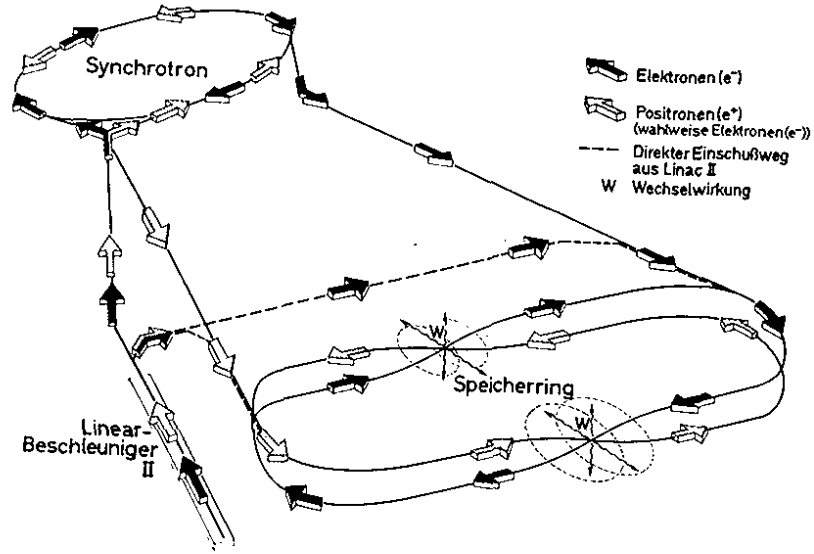

13397

Fig.2.1 Layout of the DORIS storage rings (2 ring operation), and of the injection system (DESY and LINAC II).

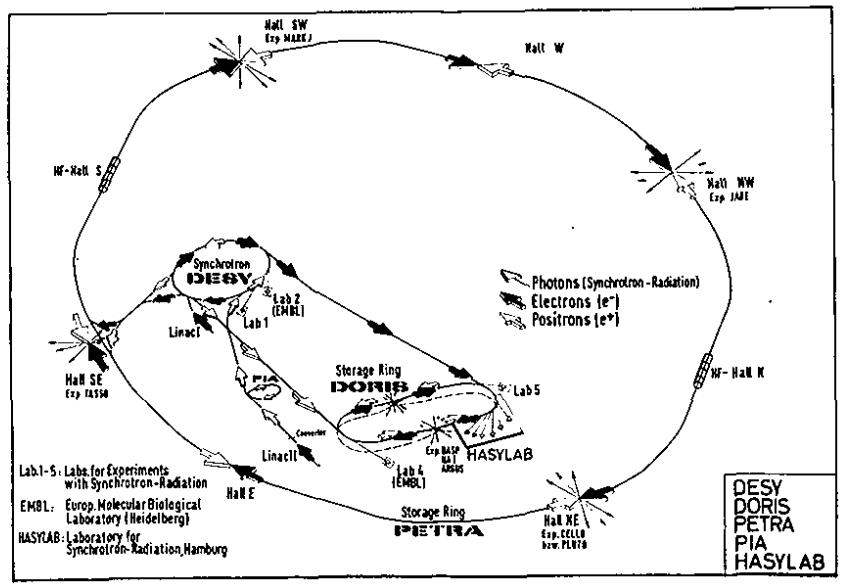

Fig.2.2 Layout of the PETRA storage ring, and of the injection system.

3222

a proposal was forwarded by the PLUTO and the machine group. Already in November the new system produced luminosity at 7.7 GeV. In early 1978, more r.f. cavities - borrowed from PETRA, which was nearing completion - were installed. The magnet control was extended such as to account for different saturation properties of various magnet elements. In early April the machine delivered the first luminosity at energies above 9.2 GeV for the search for the ϒ resonances (see Sect. 7).

The storage ring PETRA (positron-electron-tandem-ring-accelerator) was built during the years 1976-1978, with the aim of covering the energy region up to about 40 GeV [204]. The layout is shown in Fig. 2.2. (See also table 2.1) The injection energy is usually 7 GeV, except for operations below 14 GeV c.m. energies. Electrons are directly injected from the synchrotron, while positrons, because of their weaker current, have to be accumulated before. During the first year of operation the positrons were stored in DORIS at 2 GeV, then reinjected into the synchrotron and accelerated up to the PETRA injection energy. Since this application more or less paralysed DORIS' operation in the ϒ range, a small (450 MeV) intermediate storage ring PIA (positron-intensity-accumulator) was built and completed in 1979 [205]. It accumulates $\sim 10^{10}$ positrons at a time and compresses them into one short bunch, which is then accelerated in the synchrotron and added onto one of the circulating PETRA bunches [+].

Luminosity runs for the experiments (PLUTO, MARK J and TASSO first, then JADE, and later CELLO) started in November 1978. The maximum c.m. energy was first 17 GeV, and raised to 31.6 GeV in Juli 1979, and to 36.6 GeV in 1980. The energy can still be raised by increasing the r.f. power and number of cavities. Although quite expensive, such a program is well justified by the chance of finding and investigating the toponium family [206], and also by larger electroweak effects (Sect. 4). As the next step, an increase to 41 GeV is planned for 1982.

[+] Note that due to the synchrotron radiation the oscillations of the stored particles are damped, so that Liouville's theorem does not apply, and new particles can be stacked into the same phase volume.

Table 2.I: Storage ring parameters

	DORIS I	DORIS II	PETRA	
Circumference	288	288	2304	m
max. beam energy	4.2	5.1	19	GeV
typical beam current	200	20	15	mA
typical peak luminosity	2×10^{30} $(E_{CM}/3.4\ GeV)^2$	1×10^{30} $(E_{CM}/3.5\ GeV)^2$	5×10^{30} $(E_{CM}/6.6\ GeV)^2$	$cm^{-2}sec^{-1}$ MeV
width of c.m. energy	480 (120)	1	2	per charge
number of bunches	1	1	2	
typical bunch height (σ)	0.1	0.1	0.06	mm
width (σ)	0.8	0.8	0.7	mm
length (σ)	10	10	10	mm
typical beam lifetime	6	3	6	h
length of interaction region (with mini-β)	5	5	15 (9)	m

References

[201] Vorschlag zum Bau eines 3 GeV Elektron-Positron-Doppelspeicherrings für DESY, Hamburg 1967

[202] The DORIS Storage Ring Group, W. Bothe et al., DESY 79/08 (1979), and references quoted therein

[203] S.W. Herb et al., Phys.Rev.Lett. 39 (1977) 252

[204] PETRA, updated version of the PETRA proposal, DESY 1976

[205] A.Febel and G.Hemmie, IEEE Transactions NS 26 (1979) 3244

[206] S.L.Glashow, Phys.Rev.Lett. 45 (1980) 1914

Figure captions

Fig. 2.1 Layout of the DORIS storage rings (2 ring operation), and of the injection system (DESY and LINAC II).

Fig. 2.2 Layout of the PETRA storage ring, and of the injection system.

3. The PLUTO detector

PLUTO was designed as a magnetic detector in which charged particles could be analysed over a large fraction of the full solid angle. Fig. 3.1 shows a sketch of the 1976 setup.

The magnet produces a roughly uniform field of 20 kΓ (see 3.1), oriented parallel to the beams. The field volume is filled with cylindrical track chambers (see 3.2). The iron return yoke serves as an absorber to distinguish muons from hadrons. Fig. 3.2 gives a side view of the extended detector as used in the PETRA experiments. The track detector has now been completely surrounded by shower counters. The forward and backward small-angle regions, 1^{o}-15^{o}, have been covered by spectrometers for detecting electrons degraded in $\gamma\gamma$ scattering. The iron yoke has been backed up by an additional absorber to allow muon-hadron separation at higher momenta.

3.1 The magnet

A superconducting coil of copper-stabilized Nb-Ti wires, operated at 4.5^{o}K, produces the magnetic field. Fig. 3.3 shows a picture of the magnet, with the cryostat containing the coil. The useable magnetic volume is given by the diameter of the cryostat, 1.4 m., and by the distance of the pole faces, 1.05 m. The field strength was 20 kGauss during the 1976 run period, and 16.5 kGauss after the pole faces had been carved out to accommodate the endcap shower counters. The non-uniformity of the axial field component is less than 10% over most of the volume, as shown in Fig. 3.4 It is small enough to be neglected in the first step of the track analysis,

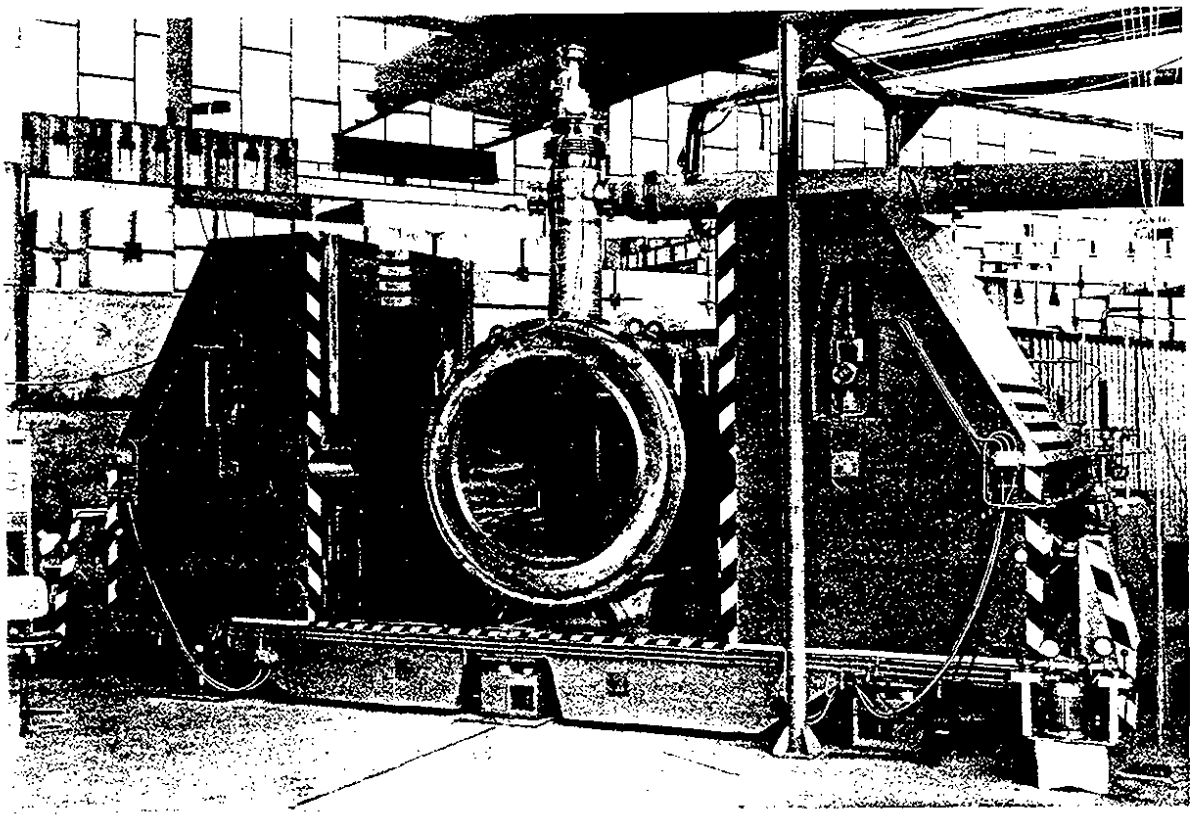

Fig. 3.3 Magnet with cryostat of superconductive coil and separated iron yokes

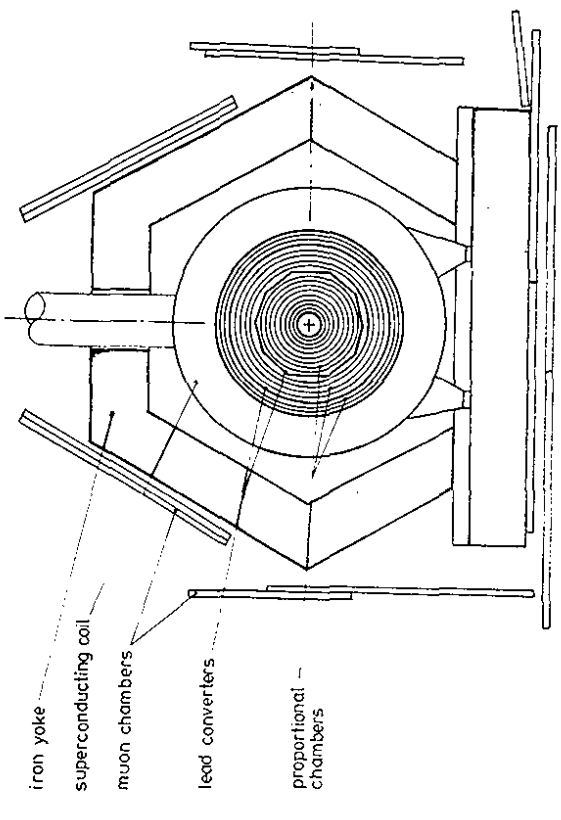

Fig. 3.1 PLUTO (1976) viewed along the beam

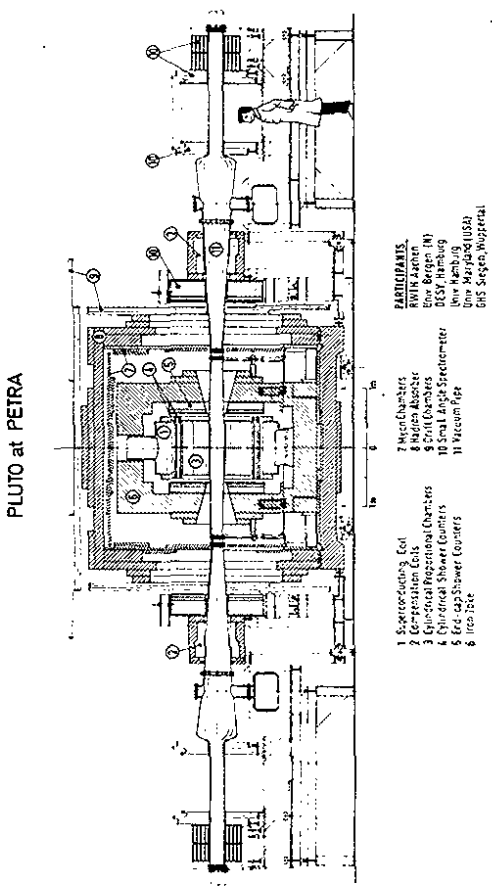

Fig. 3.2 PLUTO (1979), side view

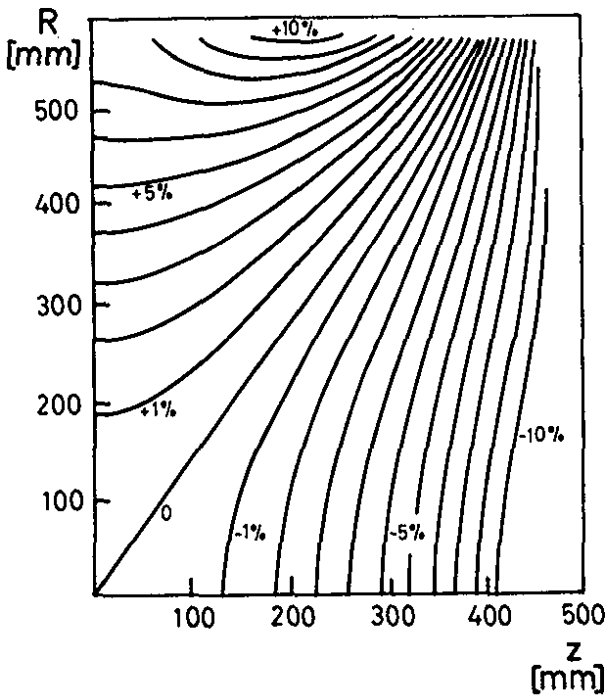

Fig. 3.4 Lines of constant magnetic field B_z, labelled by relative deviation from center field

thus saving considerable amounts of computer time, and is then only applied to the refined analysis of selected events (3.8). The influence of the axial field on the storage ring, an undesired coupling of horizontal and vertical beam oscillations, is compensated by a pair of superconducting coils with opposite field. All coils together require a cryogenic power of 150 W, and a total power of about 250 kW, to be compared to 2 MW for a normally conducting version.

3.2 Track chambers

The tracking system was designed to give a good topological resolution of multitrack events, both perpendicular (x,y) and parallel (z) to the beam, and a good momentum resolution for kinematical analysis. It had also to allow for a complex trigger, to meet the anticipated background. Proportional chambers with wires parallel to the beam offered, at the time, the easiest solution. The cathodes are built of fibreglass, coated with 35 µm of copper. The coating is segmented into stripes which are tilted $\pm 45^0$ to the wires (a few layers also at 90^0, see [301]). For every discharge a wire signal plus two pulses influenced on the stripes are read out, thus giving a 1-constrained point in space. The layout produces a high density of space coordinates along a track, at the price of multiple scattering affecting the resolution for low momentum particles.The momentum resolution for pions which are constrained to the beam line (σ_R = 2 mm) is shown in Fig.3.5 . At high momenta the resolution is given by $\sigma_p/p = 3\ \% \cdot p\ (GeV)$. The resolution is about constant over 60% of the solid angle, but deteriorates rapidly towards the forward and backward direction. The lower line gives the momentum resolution for elastic two-prongs like $\mu^+\mu^-$.

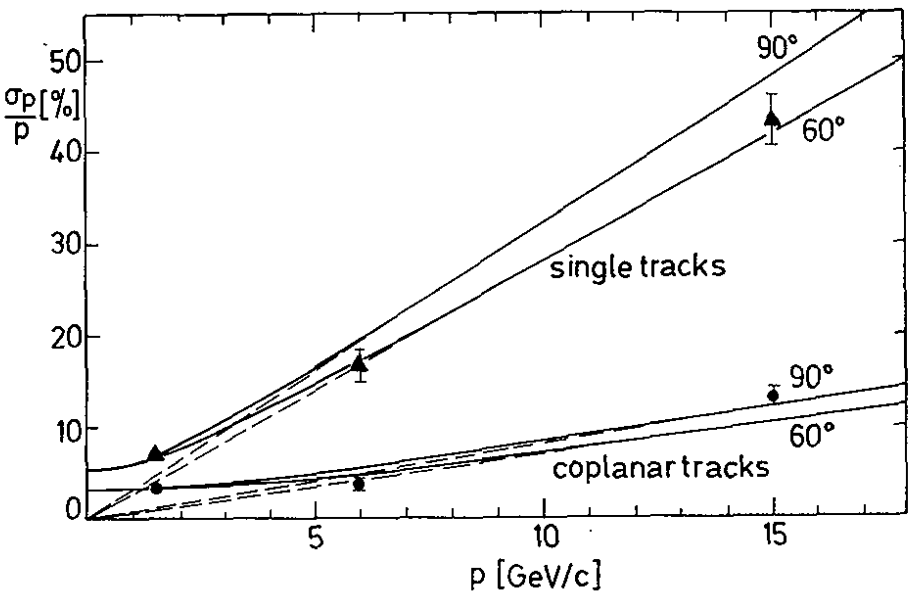

Fig. 3.5 Relative momentum resolution as a function of momentum. Upper curves: single particles at 60^0 and 90^0 (to beam axis), plus measurements from $\mu^+\mu^-$ (triangles, averaged over angles. The 1.5 GeV/c points have been scaled from 20 to 16.5 k Gauss.). Lower curves and points: same for two-particle fit. Dashed lines would result from coordinate errors only, with no multiple scattering

3.3 Shower counters

In the first version of the PLUTO detector photon detection was accomplished by two lead rings of 0.4 and 2.0 radiation lengths, inserted in between the track chambers (Fig. 3.1). They were useful for enhancing the trigger efficiency for low-multiplicity events, for the detection and direction measurement of photons, and for π - e - separation. As an example the separation of τ - decays from $\mu\mu\gamma$ events is shown in Fig. 3.6: τ candidates having one identified μ and one converted photon are plotted vs. the square of the missing mass. The entry is shaded if the photon direction is consistent with the missing momentum. These identified $\mu\mu\gamma$ events thus check the efficiency of the missing mass cut used for the separation. Electrons are recognized for $|\cos\Theta| < 0.55$ from the shower patterns they produce behind the lead plates. The detection probability depends on the level of the π-e misidentification tolerated. For a clean method with a $(1.2 \pm 0.2)\%$ probability of taking a hadron as an electron, the detection efficiency was determined as 30% for electron momenta of 440 MeV/c and 65% above 1 GeV/c.

As the importance of measuring the neutral energy became more and more apparent, PLUTO was modified in 1977 such that almost the complete solid angle (96 %) was covered with lead-scintillator shower counters. The two outmost cylindrical wire chambers were replaced by the barrel counter, sketched in Fig. 3.7. It consists of 60 modules of lead-scintillator sandwiches arranged in two layers with a total thickness of 8.6 radiation lengths. This thickness is marginal for sampling the showers of $\gtrsim$ 10 GeV photons and electrons, but does give a fair measure of the neutral energy of hadronic events which is predominantly emitted via low energy ($x_\gamma < 0.2$)

DESY 26094

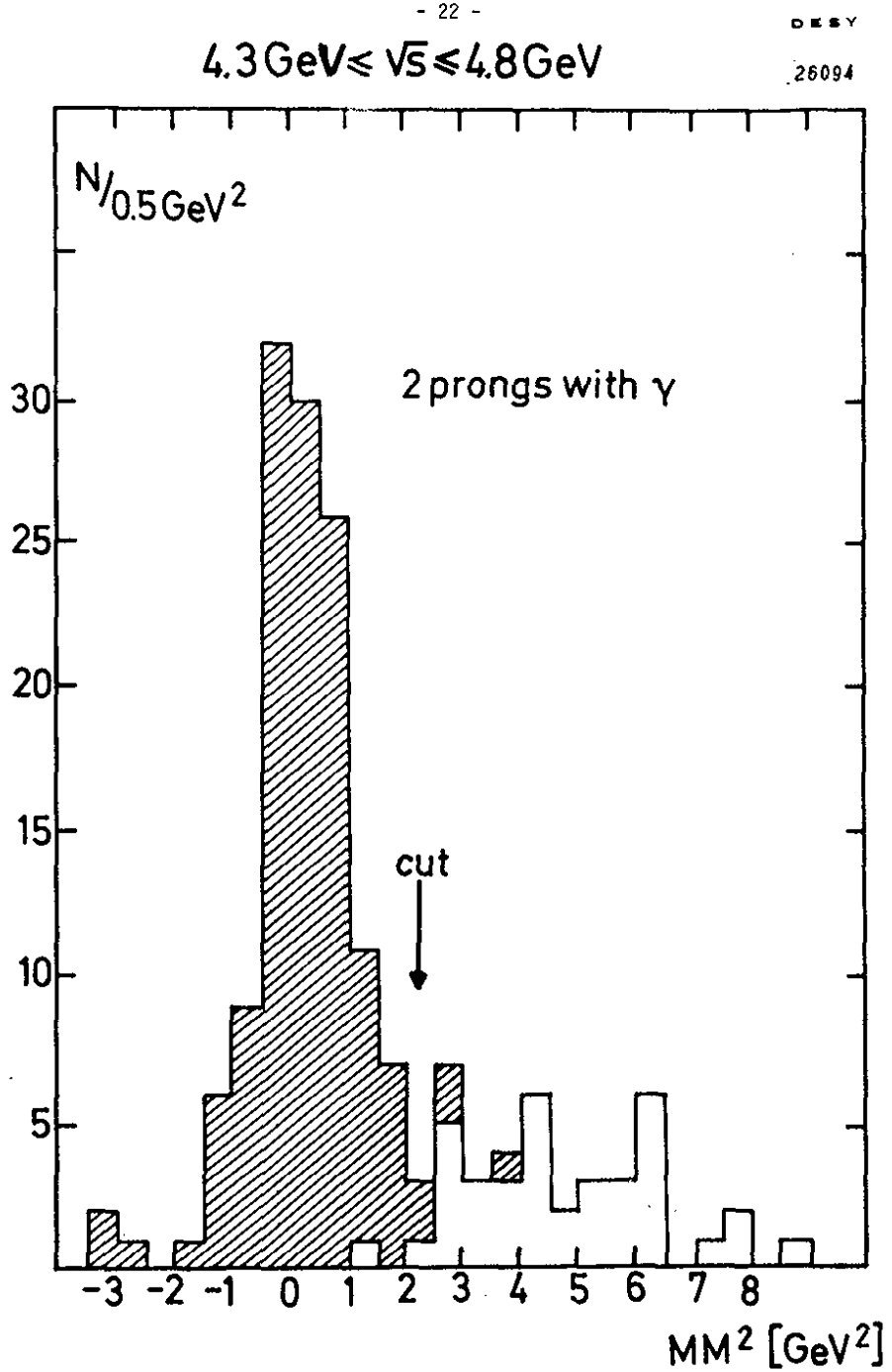

Fig. 3.6 Separation of $\tau\bar{\tau}$ from $\mu\bar{\mu}\gamma$ events through photon detection (see text)

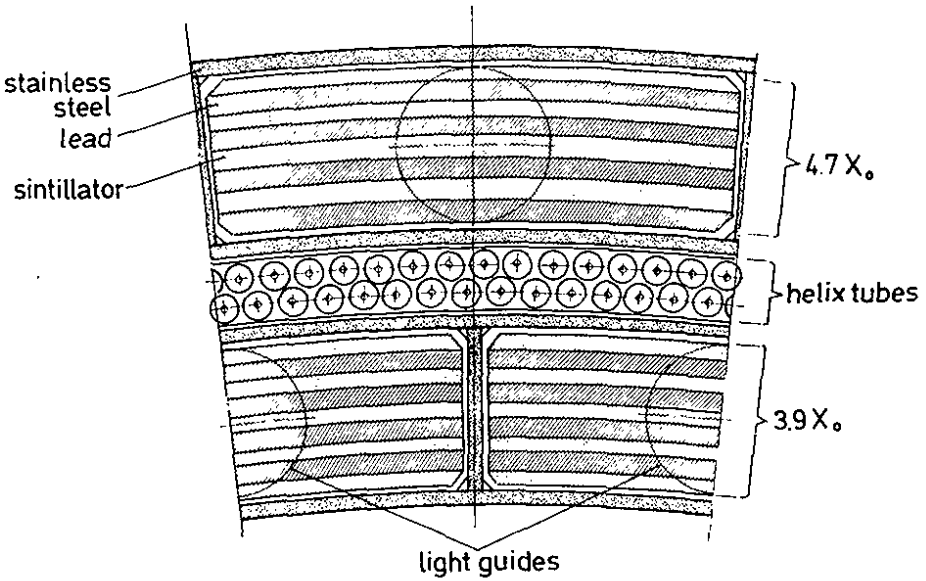

Fig. 3.7 Cross section through barrel shower counter with lead-scintillator sandwiches and helix tubes

photons. The resolution is also strongly limited by photon statistics, because the given geometry did not allow optimum light collection. For electrons the resolution is $\sigma_E/E = 35\ \% / \sqrt{E}$ (E in GeV).

Spatial resolution within the barrel counters is achieved by a double layer of helix-tubes [302]. They provide an angular resolution of $\sigma_\phi = 1.3^0$ and $\sigma_\Theta = 1.4^0$ for isolated showers.

The end faces of the tracking volume are covered each by 30 pie-shaped lead-scintillator sandwiches of 10.3 radiation lengths. The energy resolution is $\sigma_E/E = 19\ \% / \sqrt{E}$. One layer of multiwire proportional chambers is inserted in the sandwich, providing a measurement of the polar angle with a resolution $\sigma_\Theta = 1^0$ [303].

3.4 Muon detection

e^+e^- annihilation is a very efficient reaction for the pair production of hadrons and leptons with new quantum numbers. Conservation of these quantum numbers (see Section 6.2) leads to stable particles which can only decay through weak interactions. Since part of the weak decays leads to leptons, muon and electron detection are particularly powerful tools for detecting the production of new quantum numbers.

The separation of muons from hadrons requires a thick hadron absorber and a short flight path before, in order to suppress the decay-in-flight of pions and kaons. The average flight path in PLUTO is about 60 cm. The coil and flux return yoke provide an absorber with an average thickness equivalent to 70 cm of iron. The momentum cutoff varies between 0.9 and 1.4 GeV/c. Outside of the absorber 49 % of the solid angle is covered with proportional tube chambers. Particles are identified as

muons if they hit the expected position within $\pm$ 15 cm. The probability that hadrons of 1-1.5 GeV/c were identified as muons (punch through) was determined from multihadron events collected at the J/ψ resonance as (2.8 $\pm$ 0.7) %.

For the higher momentum muons expected at PETRA the iron yoke was complemented by an extra hadron absorber such as to obtain a uniform, position-independent thickness of 100 cm iron (equivalent), corresponding to a muon energy of 1.4 GeV. The outside is covered with two layers of drift chambers, allowing a two-coordinate measurement over 80 % of the full solid angle. The punch-through probability for hadrons has been calculated from published data [304, 305] as $2.4\ ^{+1}_{-0.4}$% per event at 30 GeV.

3.5 Luminosity monitor

The luminosity L measures the product of $e^\pm$ flux and $e^\mp$ 'target' density and gives the reaction rate from a cross section σ as

$$\frac{dN}{dt} = L \cdot \sigma$$

Since no methods are available to measure the beam density profile directly, the luminosity is determined from Bhabha scattering as a gauge reaction. The cross section is known to agree with the QED prediction up to momentum transfers of 10^3 GeV^2 and c.m. energies up to 30 GeV [306], if the lowest order diagram and a calculable [307-309] 2-10 % radiative correction are taken into account.

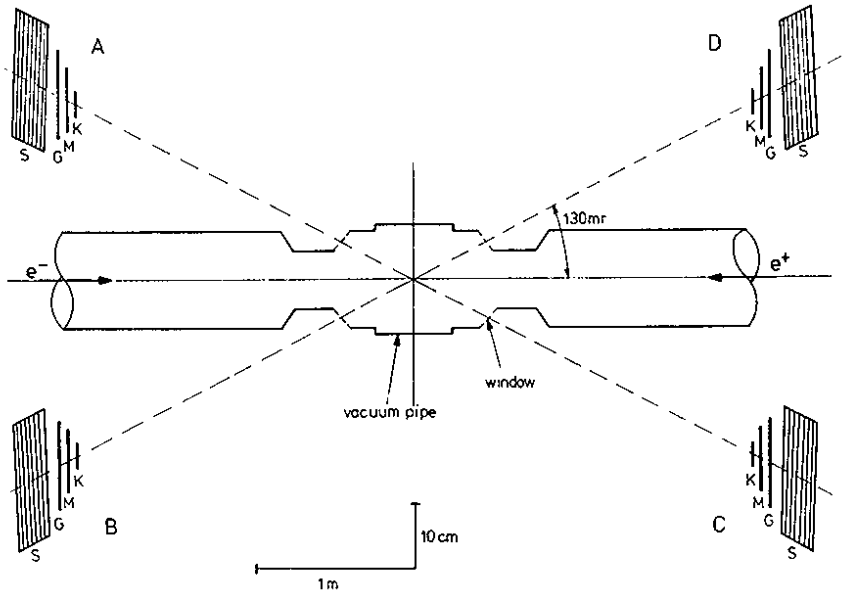

Fig. 3.8 Luminosity monitor as used at DORIS, with small (K), medium (M) and large (G) scintillation counters, and shower counters (S) (Top view)

Bhabha scattering at small angles gives high rates suitable for instantaneous monitoring. It was measured at DORIS with a system of four telescopes, which will be described in this section, and at PETRA with the forward spectrometers (3.6) of PLUTO. After the barrel and endcap shower counters (3.4) had been installed, Bhabha scattering was also measured in the central detector. Although the latter rate was too small for instantaneous monitoring, it still exceeded those of the hadronic events by more than a factor of 20, thus providing a statistically significant normalization.

The small angle monitoring system used at DORIS is sketched in Fig. 3.8. The four telescopes are positioned horizontally at 130 mrad with respect to the beam, and vertically at the crossing angle (12 mrad in 1976, 0^0 later). Each consists of three scintillation counters of increasing size, backed by a lead-scintillator shower counter. A Bhabha count is defined as a coincidence between one medium and the opposite large szintillator, together with the corresponding shower counters. Because of the Θ^{-4}-dependence of the cross section the individual rates of the four telescopes are extremely sensitive to small displacements of the interaction point. However, the sum of the rates (which contains the medium-medium coincidences twice) varies less than 1 % if the interaction point moves by 5 cm along or 2cm perpendicular to the beam direction. The systematic error of the luminosity measurements, arising mainly from the knowledge of the geometry and the rejection of electron showers scattered into the acceptance, is estimated to be less than 5 %. This estimate was verified by a comparison with the wide-angle Bhabha scattering measured at 7.7 and 9.4 GeV.

3.6 The forward spectrometers

Whereas the cross section for e^+e^- annihilation falls with the 2nd power of the energy, the hadron production via two photons

$$e^+e^- \rightarrow e^+e^- + X$$

is expected to rise logarithmically. At PETRA energies the two-photon cross section is sufficiently large to be studied both in its own right and as a non-negligible 'background' to be separated from the annihilation.

The $\gamma\gamma$ reactions can be 'tagged' by measuring one or two of the final state electrons. For this purpose the PLUTO detector was equipped with two spectrometers each in the forward and backward direction. The so-called small-angle tagger (SAT) covers an angular range from 23 to 70 mrad, while the large-angle tagger (LAT) extends from 70 to 260 mrad and smoothly joins the range subtended by the end cap shower counter [310].

The setup is shown in Fig. 3.9. Each of the SAT's consists of 96 blocks of lead glass, 12.5 radiation length thick. The energy resolution has been determined in a test beam, as well with Bhabha events at PETRA. Both give consistently

$$\sigma_E/E = 8.5\ \% / \sqrt{E}\ \ (\mathrm{GeV}).$$

Charged particles are tracked by 4 planes of proportional wire chambers in front of each SAT.

The LAT consists of 18 lead-scintillator sandwiches, 14.5 radiation length thick. The energy resolution is 11 % / $\sqrt{E}$, also checked with Bhabha events. Charged particle and shower localization is achieved by 4 layers of proportional tube chambers, 2 in front and two inside the shower counter.

The LAT and in particular the SAT are also used for monitoring the lumi-

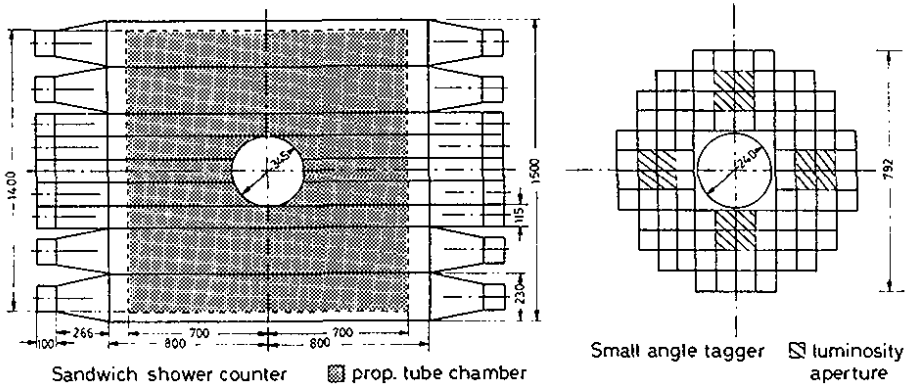

Fig. 3.9 Cross section of forward spectrometer with small angle (SAT) and large angle tagger (LAT). The acceptance for the luminosity measurements is defined by the 4 x 4 'center' blocks of the SAT (hatched), in coincidence with any one of the opposite ones. (Dimensions in mm).

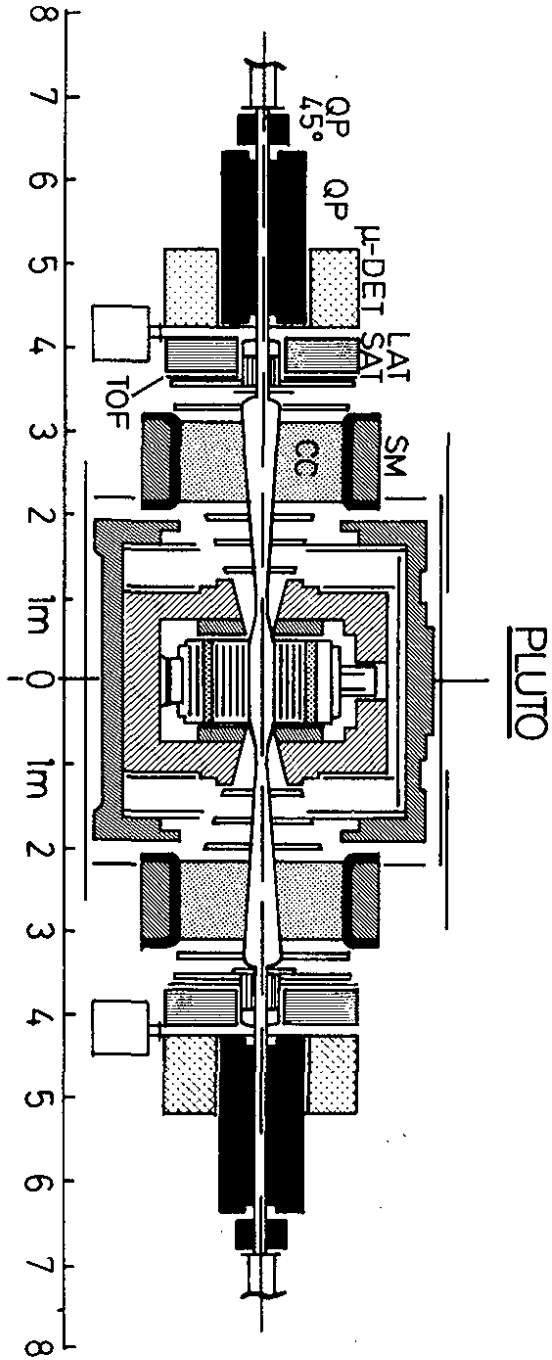

Fig. 3.10 PLUTO 1981 with upgraded forward spectrometers, consisting of analysing magnet (SM), drift chambers, Čerenkov counter (CC), small angle tagger (SAT) and enlarged large angle tagger (LAT). The long quadrupoles (QP) are part of the 'mini-β' focussing system, while the short ones (QP 45°) compensate the field of the central and the forward magnets.

nosity. The total luminosity integrated over the 12 - 32 GeV runs has been cross-checked against the one obtained from Bhabha events observed in the endcap shower counters. The ratio of the two, 1.026 ± 0.012, indicates that the systematic error of the luminosity measurements is smaller than 3% [311]. For the data taking of 1981 the forward spectrometers were upgraded as to allow a momentum measurement and particle identification (Fig. 3.10).

3.7 The trigger

The rate of e^+e^-annihilation which is obtained from the available luminosities and the small cross sections is low, of the order of a few events per hour. The trigger should therefore be soft enough to accept a large fraction of these events, and also to respond to known (and unknown) channels with a weak signature, like $e^+e^- \to \tau^+\tau^- \to \pi e\, \nu\nu\nu$. At the same time it has to prevent excessive background rates from beam-gas interactions, lost beam particles, cosmic rays and synchrotron radiation. The trigger conditions should be easily changeable and adaptable to varying background conditions, which sometimes depend critically on the energy and operating conditions of the storage ring.

To meet these conditions, a pattern logic was built in 1973 [312, 301] (see 3.7.1) which was capable of recognizing and counting charged tracks in the proportional wire chambers, and to trigger on a preset number of tracks. With the installation of the shower counters the trigger could respond to neutral energy, too (3.7.2). More complex decisions involving the neutral energy were enforced through the anticipated high background at PETRA (partly due to the open small-angle regions which had been heavily shielded before).

In order to keep this complex trigger flexible enough, a programmable master logic was developed which could be changed from a computer terminal whithout any other hardware being touched ('RAM' logic, 3.7.3).

3.7.1 The wire logic

The proportional wire logic consists of two stages, (i) a pretrigger which has to make a firstdecision within 300 nsec, and (ii) the so-called sequential logic which performs a more sophisticated, but slower search for track patterns within 40 μs.

The pretrigger (i) uses 10 cylindrical chambers grouped into 5 pairs, called 'rings'. The minimal pattern recognized is one wire signal in each chamber of the same ring, spaced by less than 9^{o} in azimuth. The typical pretrigger, used most of the time, requires two such minimal patterns, either in one inner and one outer ring, or in two non-adjacent octants of the same ring. The condition is equivalent to one longer or two shorter tracks with momenta above 180 MeV/c. At the higher PETRA energies the pretrigger requirement had to be raised to two inner rings showing two minimal patterns each, spaced as above.

The sequential logic (ii) was designed to detect more complicated wire patterns. For this purpose, the wire signals of 10 chambers are mapped onto 10 'circular' 120-bit shift registers. A pattern unit is attached to one azimuthal sector, and the whole event is rotated one full turn in 120 steps. During the rotation, the pattern unit recognizes tracks in several different combinations of chambers, and counts them. In addition, the number of coplanar track pairs is counted. The standard trigger used at DORIS demanded two tracks with $|\cos\Theta| < 0.87$, and $p \cdot \sin\Theta \geq 240$ MeV/c. The acceptance for hadronic events was enhanced by also triggering on ≥3 track elements observed behind the lead plates. Typical values determined by a Monte-Carlo simulation were 87 % (92 %, 99 %) for $\pi^+\pi^-2\pi^0$ ($2\pi^+\pi^-$, $2\pi^+2\pi^-\pi^0$) events at 5 GeV.

The track trigger at PETRA responded to ≥ 2 tracks with $|\cos\theta| < 0.64$ which were spaced by more than 94^{o} in azimuth. The condition was relieved depending on the detected neutral energy. The sequential logic usually produced less than 5% dead time.

3.7.2 Neutral energy trigger

With the installation of the active shower counters a number of very useful trigger conditions was added, as well for electromagnetic as hadronic processes. The 'low' signal of barrel or end cap which responded to minimum ionizing particles served as a pretrigger and was used to gate all ADC's. Analog sums of the barrel (resp. end cap) counters provided a 'medium' (800 MeV) and 'high' (1.5, resp. 3 GeV) signal, plus special QED (e^+e^-, $\gamma\gamma$) triggers requiring 2x0.6 GeV (resp. 2x1.2) deposited in opposite sides. The experiment was triggered on the 'high' and QED signals. The RAM master logic (3.7.3) also allowed triggers requiring medium or low shower signals with low multiplicity track signatures. With increasing beam energy of PETRA, the 'medium' and QED threshold were raised to 3, 6 and 2x2.5 GeV respectively. The forward spectrometer provided 'low' and 'high' signals for each of the two SAT and LAT shower counters, corresponding to 1.5 and 4 GeV of neutral energy [303].

3.7.3 The RAM master logic

The need for a flexible and well documented master trigger demanded computer-controlled switching of the conditions. The most general solution is a computer memory, which associates with every possible combination of input signals one 1-bit cell, loaded with '1' for accepting or '0' for rejecting the event. Fast memory chips which make such a scheme appli-

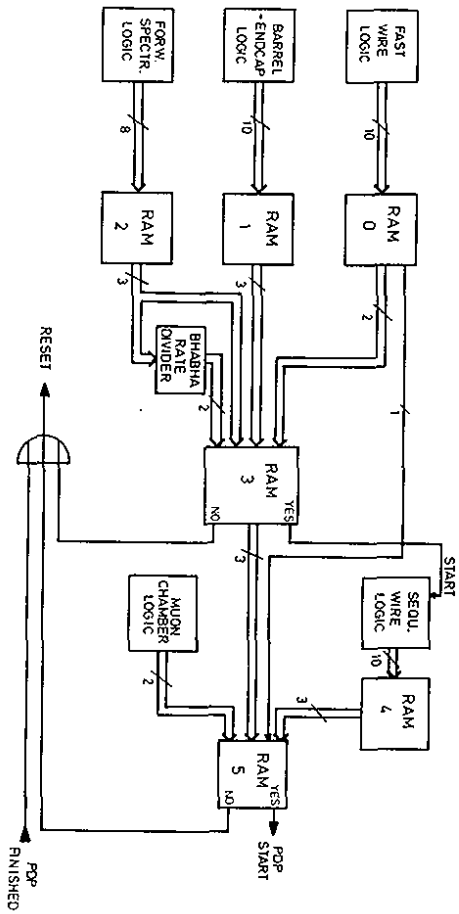

Fig. 3.11 Block diagram of RAM master trigger as explained in text. The undesiredly high rate of Bhabha events is divided by a factor of typically 8. If however a Bhabha signal is accompagnied by a signal of the central detector, the event is kept as a $\gamma\gamma$ candidate.

cable for a fast trigger have become available in recent years. For reasons of economy the trigger has been cascaded as shown in Fig.3.11 [313]. The basic unit is a random access memory ('RAM') of 1024 four-bit cells, each one addressed by one particular combination of ten input signals, and responding in less than 50 nsec. Three of the output bits are interpreted as a 'level' describing the significance of the input (0 = nothing, 7 = maximum). The fourth bit is used for a permanent parity check. RAM0, RAM1, and RAM2 act as encoders, that is assign a level of significance to the signal of the respective subdetector. RAM3 assigns a level to the combined information. For level zero a reset is issued in time to make the detector ready for the next bunch crossing. Otherwise, the sequential logic is started, its output assessed through RAM4, and the complete information used for the final yes-no decision of RAM5.

The RAM contents that control the trigger, about 14000 significant bits, are prepared at a terminal of the DESY central computer in a symbolic language, and decoded and loaded by the experimental computer (PDP11). Both the symbolic coding and the actual loading (reread) are stored for on- and offline checks and documentation. In addition, the input and output status of all RAMs is recorded together with every event, so that every trigger decision can be reproduced afterwards. Apart from some rare cases of faulty RAM loading procedures which were immediately recognized by an on-line check, no failures of the operation were observed.

3.8 Data analysis procedures

3.8.1 Data flow

Once an event has been accepted by the trigger, all information is transferred via an on-line 'PDP' (11/45), a fast link, and an intermediate disk storage of the 'IBM' (370/168) to magnetic tape. While the PDP mainly organizes the data collection and transfer, the IBM online program does extensive checking and bookkeeping. Sometimes the PDP was also used to reject cosmic rays and obvious beam-gas events. The real data analysis and reduction starts from the tapes and proceeds through a prefilter, the track finding, and a main event filter, leading to a condensed general event tape. From here the procedure branches into a preselection of QED, of $\gamma\gamma$, and of hadronic annihilation events, each yielding a special event tape. These event tapes contain, in addition to track and shower parameters, all the original data like wire signals, ADC and TDC contents. It is thus possible to apply improved calibrations and analysis procedures just to the condensed event tapes, without having to start from the much larger original tape volumes.

3.8.2 Track analysis

The prefilter first eliminates part of cosmic and beam-gas events by simple criteria, thus saving computer time. The main track routine searches for patterns of wire coordinates compatible with a circle in the $r-\phi$ plane, and determines the track parameters and their covariance matrices. In order not to loose tracks from decaying kaons and converted photons, the interaction point is not used in the search and the fits. The 'z'-routine then searches for cathode signals which are compatible with a helix, and determines the complete track parameters. Events which have at least one track ($\geq$2 tracks for $E_{cm} < 5.2$ GeV) from the vicinity of the nominal interaction point are copied to a general event tape.

3.8.3 Event selection

The e^+e^- interaction point is determined, as a function of time, from Bhabha events. This then allows a narrower selection of tracks originating from the interaction point. In order to be selected as a hadron candidate, an event must have at least two such tracks. QED events are suppressed by demanding for 2-prongs an azimuthal difference $|\Delta\phi_{12}| < 150^0$, and for 3-prongs at least two of the differences $|\Delta\phi_{ij}| < 150^0$ [+]. The hadron candidates are copied to the 'hadron' tape. A refined version is produced later which is based on an improved track fit accounting for field non-uniformities, energy loss and coordinate correlations from multiple scattering.

Special event selections are made for the study of QED (Sect. 4), heavy leptons (Sect. 5), and $\gamma\gamma$ processes (Sect. 8).

3.8.4 The total hadronic cross section

Starting from the hadron tapes (3.8.3), the final cuts for the annihilation cross section are optimized and applied. They are aimed at a further suppression of beam-gas and QED background. Their details depend on the version of the detector and the storage ring. Beam-gas background was reduced at DORIS by omitting $\leq$ 4 prongs with net positive charge, and counting the charge conjugate events twice. After the shower counters had been installed, and PLUTO worked as a calorimeter, beam-gas background was almost completely eliminated by a cut in the total energy (typically $0.5 \cdot E_{cm}$ [++]). After these cuts, the event sample still contains contaminations from higher order QED processes, in particular from $e^+e^- \to e^+e^-\gamma$. In the first version of PLUTO, such events were visually recognized by the showers they produce behind the lead

---

[+] For $\leq$5 GeV. For part of the high energy data the cuts were relaxed to $<165^0$.

[++] The influence of the energy and other cuts has been systematically investigated in [615].

plates, and accounted for by a global subtraction of 1 ± 0.1 nb. After the installation of the shower counters the QED background could be eliminated event by event.

The remaining beam-gas and cosmic background, amounting to 29% in data without shower counters and to $\leq$ 3% in data with shower counters (and the one bunch machine operation), was determined from the vertex distribution along the beam (Fig. 3.12), and was statistically subtracted.

3.9 Acceptance calculations

The acceptance of the detector depends in a complicated way on angular and energy cuts and other inefficiencies introduced by the trigger, various detector parts and by the analysis. A reliable calculation of the acceptance therefore requires a complete Monte Carlo simulation of the process, including event generation, detector response, and analysis. Unfortunately, the first step is a priori unknown, in particular the total production of hadrons. The simulation has to start from models of the production, and proceed by adjusting the parameters of the models such that the results agree with all relevant features of the data. The model dependence leaves an uncertainty of order 5% in the total hadronic cross section. Radiative corrections [314, 307-309] were partly accounted for by including radiative processes in the simulation, and partly applied directly to 'uncorrected' cross sections.

3.9.1 Phase space event simulation

The phase space model was mainly applied to the data below 5 GeV, and as a test model for deciding how far the decay features of the T could be explained without assuming specific dynamical structures.

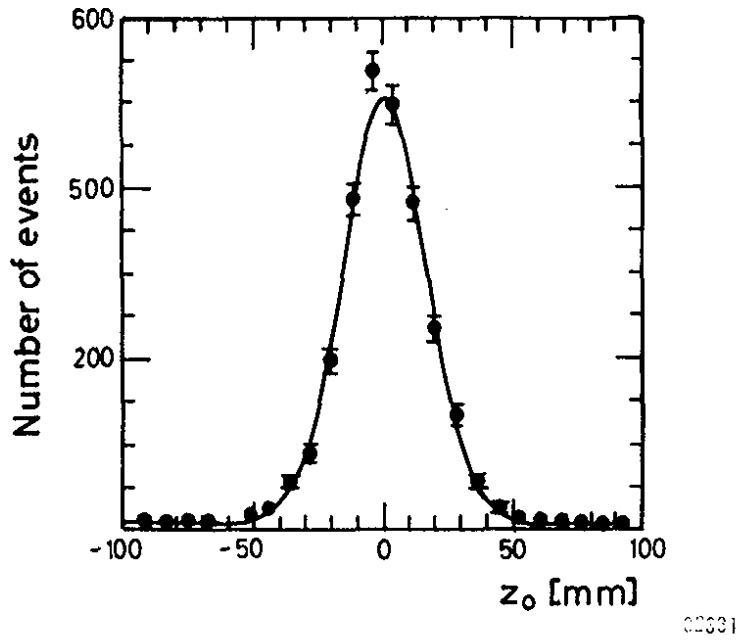

Fig. 3.12 Vertex distribution of candidates for hadronic events along the beam. (E_{CM} = 9.4 GeV; see also Figs. 8.2, 8.3)

Pions and kaons are generated in a 5 : 1 ratio, consistent with the measurements of the K_S^0 production (see 6.2.1). The influence of this ratio on the acceptance is very small (< 1%). The charged and neutral multiplicity are generated according to a Poisson distribution, each with a mean of 4 at 4.5 GeV, as a first approximation. For a fine adjustment the generated events are processed through the full detection simulation and analysis chain (see below), resulting in a spectrum of degraded classes for each initial charged multiplicity ((++--) → (++--), (++-), (+--), (++), (+-), (--)). The initial distribution is then adjusted such as to give the best fit of the degraded classes to the data.
The fraction of charged/total energy is adjusted similarly such as to agree with the observed fraction.

3.9.2 Jets

Two-jet production at low energies, < 5 GeV, is simulated by introducing limited $\langle p_\perp \rangle$ via different weighting of phase-space events.

At higher energies, a genuine two-jet structure is produced according to the quark fragmentation model of Field and Feynman [315]: The original quark creates a $q\bar{q}$ pair out of the vacuum, and then combines with the $\bar{q}$ to a meson. The remaining quark retains the fraction η of the original energy and parallel momentum $(E + p_\parallel)$, with a distribution $f(\eta) = 1 - a + a\eta^2$ $(a = 0.77)$. It creates a new pair, and so forth, until all of the original $(E + p_\parallel)$ is used up. The vector/pseudoscalar ratio 1/1, the strange/nonstrange ratio 1/4, and the mean transverse momentum of the generated quarks ($\sigma_q = 247$ MeV/c) are taken as suggested by the authors +.

+ Recent investigations of jet topologies [611,6909] and of inclusive K_S^0 spectra [6908] have led to slightly different values, namely σ_q = 290 ± 20 MeV/c and a strange / nonstrange ratio of 1 / 9.

Instable particles decay according to their known properties. For the application at PETRA energies, heavy quarks are added to the original light ones, with a partition function $f(\eta) = 1$, and also the decays of heavy quarks according to Ref. [316].

Events with hard gluon emission are created according to Refs. [317, 318]. The gluon is treated as a pair of quarks which then fragment independently.

A special generator for three-gluon events was constructed for evaluating the decay of the Υ. The matrix element of the positronium decay into three photons is used to generate the initial gluon state. Each gluon is assumed to fragment like a quark. The total fragmentation is described by a function which includes constant $\langle p_\perp \rangle$, constant density in rapidity and a logarithmically rising multiplicity. The parameters are adjusted such that the events approach all two-jet features in the limit of one gluon approaching zero energy.

3.9.3 Two-photon interactions

The generator for hadron production in photon-photon interactions was built, in close analogy to hadron-hadron interactions (VDM), as a multipion phase space with limited $p_\perp$. The mean multiplicity was taken from e^+e^- annihilation data, parameterized as $\langle n_{ch} \rangle = \max(3.0, 2.0 + 0.7 \ln W^2)$, the charged to neutral ratio as 2:1. The $p_\perp$ generator was adjusted to the data. The observed $p_\perp$ distribution (Fig. 3.13) was well reproduced by generating 75% of the events according to $\exp - 5.0\ p_T^2$, and 25% acc. to $\exp - p_T^2$ [319]. The distribution of the photon-photon invariant masses was generated according to the photon flux factors described in Sect. 8.1.

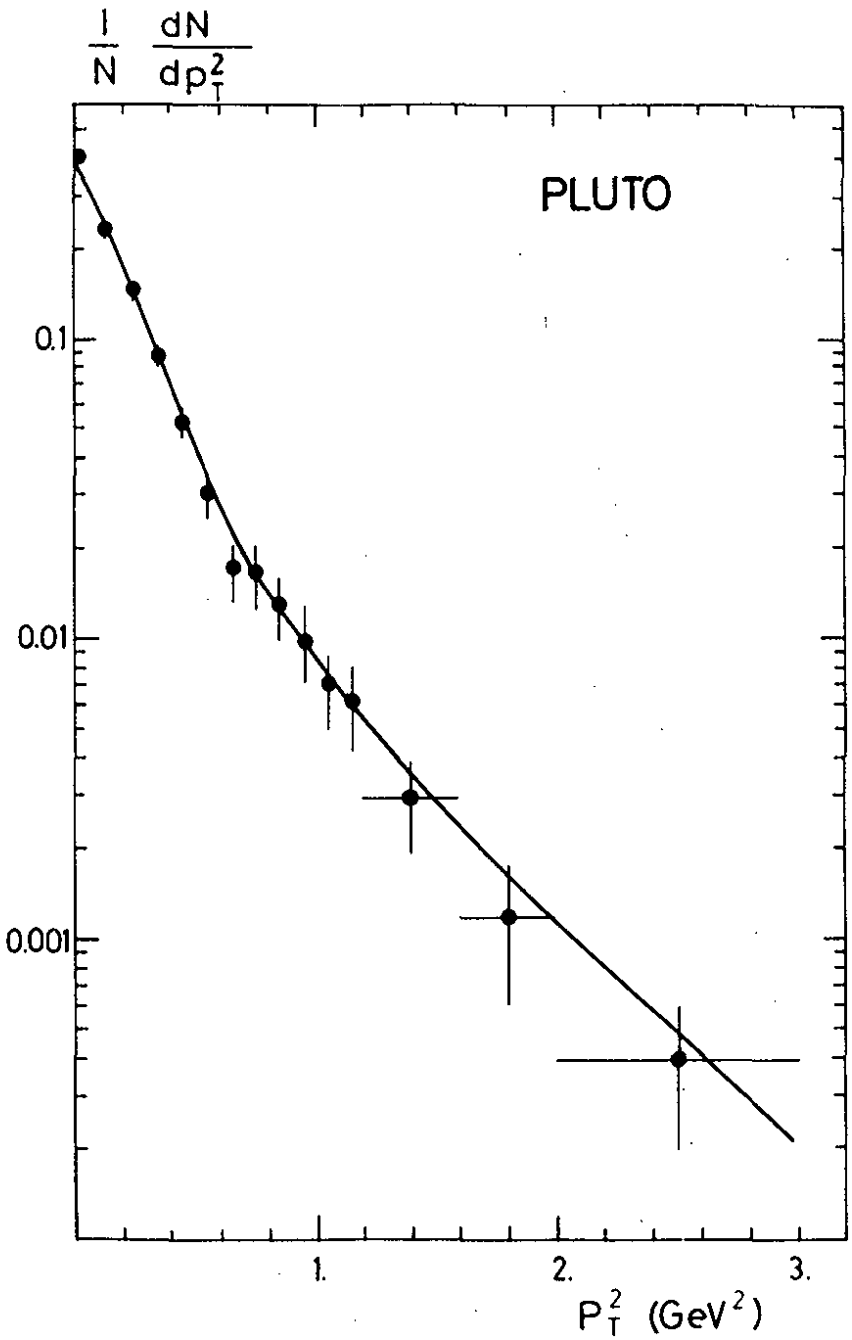

Fig. 3.13 Distribution of transverse particle momenta as observed and simulated (full curve) in photon-photon interactions

3.9.4 QED reactions

Monte Carlo simulations of the reactions $e^+e^- \to e^+e^-$ $(+\gamma)$, $\mu^+\mu^-$ $(+\gamma)$ and $\gamma\gamma$ $(+\gamma)$ were performed firstly to determine the small fraction of events in which the detector response produced a wrong signature, and secondly to check the contribution of radiative events ('$+\gamma$' acc. to [307 - 309]) which were accepted within the given (acoplanarity) cuts. The latter contributions were always found to be consistent with the ones calculated from the matrix elements for an ideal detection.

The reactions $e^+e^- \to e^+e^-e^+e^-$, $e^+e^-\mu^+\mu^-$ which produce the majority of the twoprongs in $\gamma\gamma$ reaction were simulated with a program written by J. Vermaeseren [320, 321].

3.9.5 Heavy leptons

The reaction $e^+e^- \to \tau^+\tau^-$ was generated assuming zero neutrino mass and a (V-A) decay matrix element, with the known branching ratios [322] and an estimate for $\tau \to \nu 4\pi$. Spin correlations between the τ^+ and τ^- were ignored.

In addition, hypothetical heavier leptons were simulated [323] with the same universal weak current producing an equal number of $e\nu$, $\mu\nu$, $\tau\nu$, $u\bar{d}$ $c\bar{s}$ pairs, with the quarks fragmenting into standard hadron jets [315].

3.9.6 Detector response and analysis chain

The generated particles are all traced through the detectors. Multiple Coulomb-scattering and energy loss are included in the simulation, also particle decays, and the evolution of electron-photon showers. For every charged particle passing a track chamber, the number of wire and cathode signals is generated such as to agree with the observed distributions and efficiencies. The complete track chamber information,

including the trigger response, and the shower information is passed through all stages of the analysis program that processes the real data. In this way the analysis procedure and the effect of various selection criteria can be studied in great detail. The Monte Carlo simulation also allows a detailed check of kinematical fit procedures.

3.9.7 Radiative corrections

Photon emission in the initial state causes the e^+e^- annihilation to be measured at a lower than the nominal c.m. energy. It amounts to a folding of the true cross section and will lead to an increase or decrease of the observed rate, depending on whether the cross section at the degraded energies is lower than at the nominal energy (for instance on top of a resonance) or higher (above resonances and in the continuum).

The basic formulae expressing this folding, together with small vertex corrections were taken from Refs. [314, 324] for the J/ψ, ψ' and the continuum, and from Ref. [325] for fitting the T resonance and the nearby continuum cross section. The true non-resonant cross section, and the integral over the true resonant cross section are obtained as fit parameters.

The initial state radiation generally leads to an observed cross section with smoothed structures. Unfolding this effect will enhance the observed structures and exaggerate statistical fluctuations. For unfolding the 'wiggly' cross section between 4 and 4.5 GeV, an iterative correction procedure was used which tends to avoid such exaggerations [301]. In fact,

the additional fine structure produced by the correction is less than ± 5%. For the analysis of the data taken at PETRA the effects of the initial state radiation were already included in the Monte Carlo acceptance calculation and automatically corrected for.

Radiative corrections to the small-angle monitor are calculated according to Ref. [307]. They depend only weakly on the energy, and amount to typically 5% (2%) for the monitors used at DORIS (PETRA).

References

[301] A.Bäcker, thesis, DESY F33-77/03 (1977)
[302] O.Achterberg et al., Nucl.Instrum. 156 (1978) 287
[303] B.Koppitz, thesis, PLUTO 80/05 (1980)
[304] F.A.Harris et al., Nucl.Instrum. 103 (1972) 345
[305] T.A.Gabriel and B.L.Bishop, Nucl.Instrum. 155 (1978) 81
[306] PLUTO Collaboration, Ch.Berger et al., Z.Phys. C4 (1980) 269
[307] F.A.Berends, K.J.F.Gaemers and R.Gastmans, Nucl.Phys. B68 (1974) 541
[308] F.A.Berends and G.J.Komen, Phys.Lett. 63B (1976) 432
[309] F.A.Berends and R.Kleiss, DESY 80/66 (1980)
[310] PLUTO Collaboration, Ch.Berger et al., Phys.Lett. 89B (1979) 120; F.Raupach, thesis, Aachen report, PITHA 81/05 (1981) W.Lackas, thesis, Aachen report, PITHA 81/17 (1981)
[311] W.Lührsen, thesis, PLUTO 81/ (1981)
[312] E.Iarocci and P.Waloschek, DESY 72/12 (1972) H.Mehrgardt et al., Proc.Intern.Conf.on Instr. for high energy physics, p. 287 (1973)
[313] K.H.Pape, PLUTO-80/02 (1980)
[314] G.Bonneau and F.Martin, Nucl.Phys. B27 (1971) 381
[315] R.D.Field and R.P.Feynman, Nucl.Phys. B136 (1978) 1
[316] A.Ali, J.G.Körner, G.Kramer, J.Willrodt, Z.Phys. C1 (1979) 203
[317] P.Hoyer, P.Osland, H.G.Sander, T.F.Walsh and P.M.Zerwas, Nucl.Phys. B161 (1979) 349
[318] A.Ali, E.Pietarinen, G.Kramer, J.Willrodt, Phys.Lett. 93B (1980) 155
[319] PLUTO Collaboration, Ch.Berger et al., Phys.Lett. 99B (1981) 287
[320] J.Vermaeseren, private communication
[321] R.Bhattacharga, J.Smith and G.Grammer, Phys.Rev. D15 (1977) 3267
[322] Particle data group, C.Bricman et al., Phys.Lett. 75B (1978) 1; Rev.Mod.Phys. 52 (1980) No.2
[323] O.Meyer, thesis, PLUTO 81/01 (1981)
[324] J.D.Jackson and D.L.Scharre, Nucl.Instrum.Methods 178 (1975) 3
[325] M.Greco, G.Pancheri and Y.Srivastava, Nucl.Phys. B101 (1975) 234
[326] Vorschlag zum Bau eines 3 GeV Elektron-Positron-Doppelspeicherrings für DESY, Kap. III, Hamburg (1967)

Figure Captions

Fig. 3.1 PLUTO (1976) viewed along the beam

Fig. 3.2 PLUTO (1979), side view

Fig. 3.3 Magnet with cryostat of superconductive coil and separated iron yokes

Fig. 3.4 Lines of constant magnetic field B_z, labelled by relative deviation from center field

Fig. 3.5 Relative momentum resolution as a function of momentum. Upper curves: single particles at 60^0 and 90^0 (to beam axis), plus measurements from $\mu^+\mu^-$ (triangles, averaged over angles. The 1.5 GeV/c points have been scaled from 20 to 16.5 k Gauss.). Lower curves and points: same for two-particle fit. Dashed lines would result from coordinate errors only, with no multiple scattering

Fig. 3.6 Separation of $\tau\bar{\tau}$ from $\mu\bar{\mu}\gamma$ events through photon detection (see text)

Fig. 3.7 Cross section through barrel shower counter with lead-scintillator sandwiches and helix tubes

Fig. 3.8 Luminosity monitor as used at DORIS, with small (K), medium (M) and large (G) scintillation counters, and shower counters (S) (Top view)

Fig. 3.9 Cross section of forward spectrometer with small angle (SAT) and large angle tagger (LAT). The acceptance for the luminosity measurements is defined by the 4 x 4 'center' blocks of the SAT (hatched), in coincidence with any one of the opposite ones. (Dimensions in mm)

Fig. 3.10 PLUTO 1981 with upgraded forward spectrometers, consisting of analysing magnet (SM), drift chambers, Čerenkov counter (CC), small angle tagger (SAT) and enlarged large angle tagger (LAT). The long quadrupoles (QP) are part of the 'mini-β' focussing system, while the short ones (QP 45^0) compensate the field of the central and the forward magnets

Fig. 3.11 Block diagram of RAM master trigger as explained in the text. The rate divider reduces the high rate of Bhabha events by a preset factor (typically 8). If however a Bhabha trigger is accompagnied by a signal of RAM 0 or RAM 1 (central detector), the event is kept as a $\gamma\gamma$ candidate

Fig. 3.12 Vertex distribution of candidates for hadronic events along the beam. (E_{CM} = 9.4 GeV; see also Figs. 8.2, 8.3)

Fig. 3.13 Distribution of transverse particle momenta as observed and simulated (full curve) in photon-photon interactions

4. QED Tests
Upper limits on cutoff parameters and electroweak effects

4.1 Introduction

Quantum electrodynamics (QED) is known to describe a vast amount of electromagnetic phenomena to a high precision. It has evolved from an understanding of macroscopic electromagnetic phenomena, in terms of charges and electromagnetic fields, leading to Maxwell's equations. Field quantization together with the Dirac equation for fermions then yielded QED which allows for predictions of the interaction of photons with particles having pointlike charges, also at microscopic distances - or large momentum transfers - including the creation of particle-antiparticle pairs. Since the early days of QED it has therefore been of great interest [401] to find out whether below some very short distances - or beyond some very large momentum transfers - nature is different from the picture QED is based on. The high energies of PETRA allowed for a further step in testing the validity of QED, namely up to momentum transfers of ~1000 GeV^2, or down to distances of $<10^{-15}$ cm.

Deviations from pure QED are expected

(i) from the hadronic vacuum polarization [402],

(ii) from weal neutral current interactions [403],

(iii) as a *general breakdown at large space like* ($q^2 < 0$) *or time like* ($q^2 = s > 0$) momentum transfers, or short distances, e.g. as a consequence of a non pointlike nature of the charges involved or from excited heavy states of the leptons [404].

In e^+e^- *storage ring experiments such deviations from QED can be looked for in* the following reactions:

$$e^+e^- \rightarrow e^+e^- \qquad (4.1)$$

$$\mu^+\mu^- \qquad (4.2)$$

$$\tau^+\tau^- \qquad (4.3)$$

$$\gamma^+\gamma^- \qquad (4.4)$$

and in final states containing additional photons or lepton pairs. The hadronic vacuum polarization has been most clearly observed, and measured quantitatively as a sizeable effect in reactions (4.1) and (4.2) at the energies of the ρ, ω, ϕ, J/ψ and Υ resonances [405], and will not be pursued further here. As a 'trivial' modification of QED it is included in the radiative corrections (see below). No other deviations from pure QED have been observed so far in these reactions [+] [401]. But since deviations due to (ii) and (iii) are expected to grow like s or even faster, experiments at PETRA are 10 times more sensitive than the best previous tests [408]. In processes with time like photon propagators, interference with the weak neutral current grows proportional to s and produces deviations from pure QED cross sections of up to a few percent at $s \approx 1000\ GeV^2$. These effects show up in the reactions (4.1-4.3). Effects from other modifications (iii), parameterized by so called QED cutoff parameters Λ, can also be studied in reactions (4.1 - 4.3), and in addition in reaction (4.4). This latter reaction has no first order weak interaction contribution.

In the following subsection we describe the nomenclature of writing QED cross sections, and of incorporating modifications. Then we present the corresponding experimental results. Their implications for the QED cutoff parameters, and for electroweak effects are discussed in sections 4.4, and 4.5, respectively. In appendix 4A we give a compilation of formulae used to describe these deviations. Finally, in appendix 4B we include an account of the data analysis of the four QED reactions.

4.2 Radiative corrections and QED modifications

For a comparison of QED predictions with the data of reactions 4.1 - 4.4, the theoretical predictions are usually given in terms of first order QED cross sections, σ_1^{QED} (see diagrams in Figs. 4.1 and 4.2) and, to account for effects from higher order QED diagrams and from hadronic vacuum polarization (Figs. 4.3 and 4.4), by the so called radiative corrections δ_{RAD}:

[+] Electroweak interference effects have been measured with high precision in polarized electron nucleon scattering at SLAC at low momentum transfers [406] and in optical rotation of linearly polarized laser light at Novosibirsk [407].

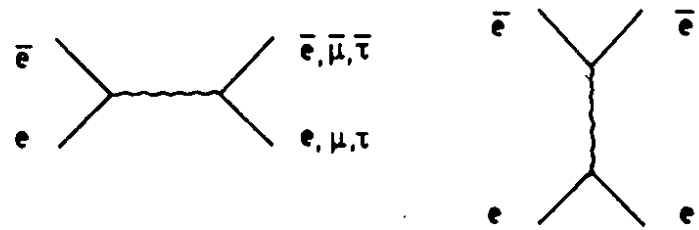

Fig. 4.1 First order QED diagrams for $e^+e^- \to l^+l^-$

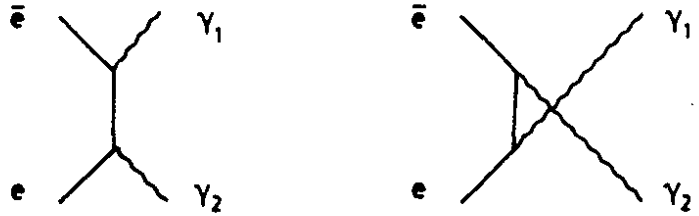

Fig. 4.2 First order QED diagrams for $e^+e^- \to \gamma\gamma$

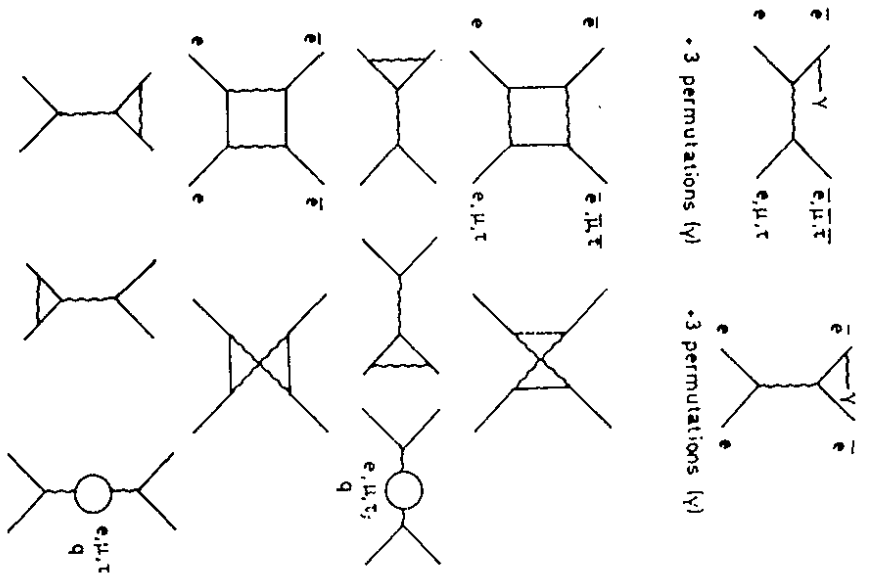

Fig. 4.3 Diagrams contributing to radiative corrections of order α^3, for $e^+e^- \to l^+l^-$

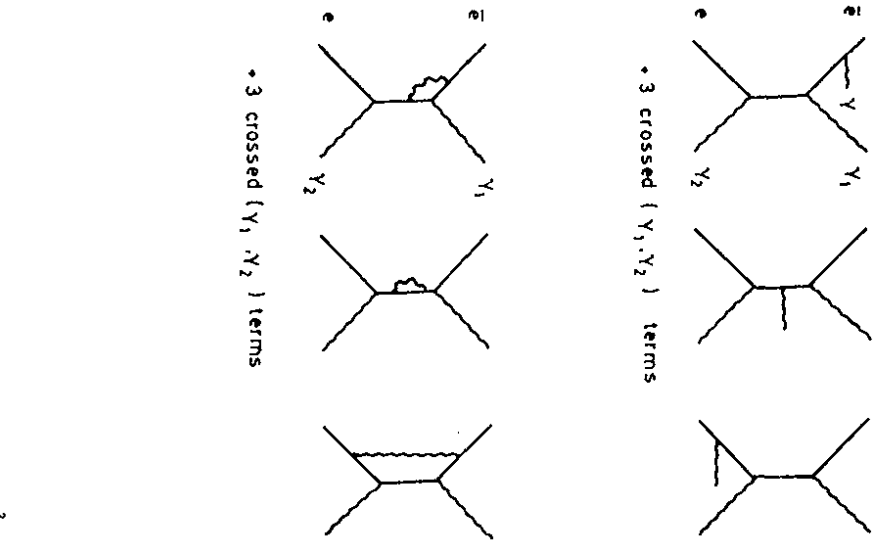

Fig. 4.4 Diagrams contributing to radiative corrections of order α^3, for $e^+e^- \to \gamma\gamma$

$$\sigma^{QED} = \sigma_1^{QED} (1 + \delta_{RAD}) \qquad (4.5)$$

On the r.h.s. σ_1^{QED} is a purely theoretical quantity whereas the radiative corrections depend on the detector resolution and on acceptance cuts for events in reactions 4.1 - 4.4. Therefore one usually corrects (using QED) the experimental cross section σ^{EXP}, which is already corrected for acceptance, with δ_{RAD} such that it can be compared directly to σ_1^{QED} (if $\delta_{RAD} << 1$):

$$\sigma^{CORR} = \sigma^{EXP} (1 - \delta_{RAD}) \qquad (4.6)$$

The radiative and the hadronic vacuum polarization corrections δ_{RAD} have been calculated up to order α^3 by Refs. [409, 410] (see diagrams in Figs. 4.3 and 4.4). Since the deviations we are looking for are of similar size as the calculated radiative corrections it is important to check the radiative corrections independently. This is possible in radiative Bhabha scatters with hard photons (i.e. $e^+e^- \to e^+e^-\gamma$) which are partly accepted by the criteria for the Bhabha sample. Because of the - unobserved or unresolved - photon the final state e^+ and e^- particles are in general no longer coplanar with the beams. In Fig. 4.5 we show the predicted acoplanarity angle distribution. It has a large angle tail from hard photon radiation, mainly in the initial state, and agrees very well with the observed acoplanarity distribution. The width of the peak at small angles reflects the angular resolution.

The QED predictions also depend on beam polarization. All cross section predictions given here are assuming no beam polarization. A transverse beam polarization which is expected for e^+e^- storage rings [424] does not affect the analysis described here since we have a uniform acceptance in the azimuthal angle. No longitudinal polarization is expected since there are no horizontal fields strong enough to rotate a possible transverse polarization.

The first order predictions of modified versions of QED can be written in terms of first order pure QED predictions as

$$\sigma_1^{MOD} \equiv \sigma_1^{QED} (1 + \delta_\Lambda + \delta_W) \qquad (4.7)$$

with δ_Λ for general large q^2 QED breakdown effects and δ_W for electroweak interference effects.

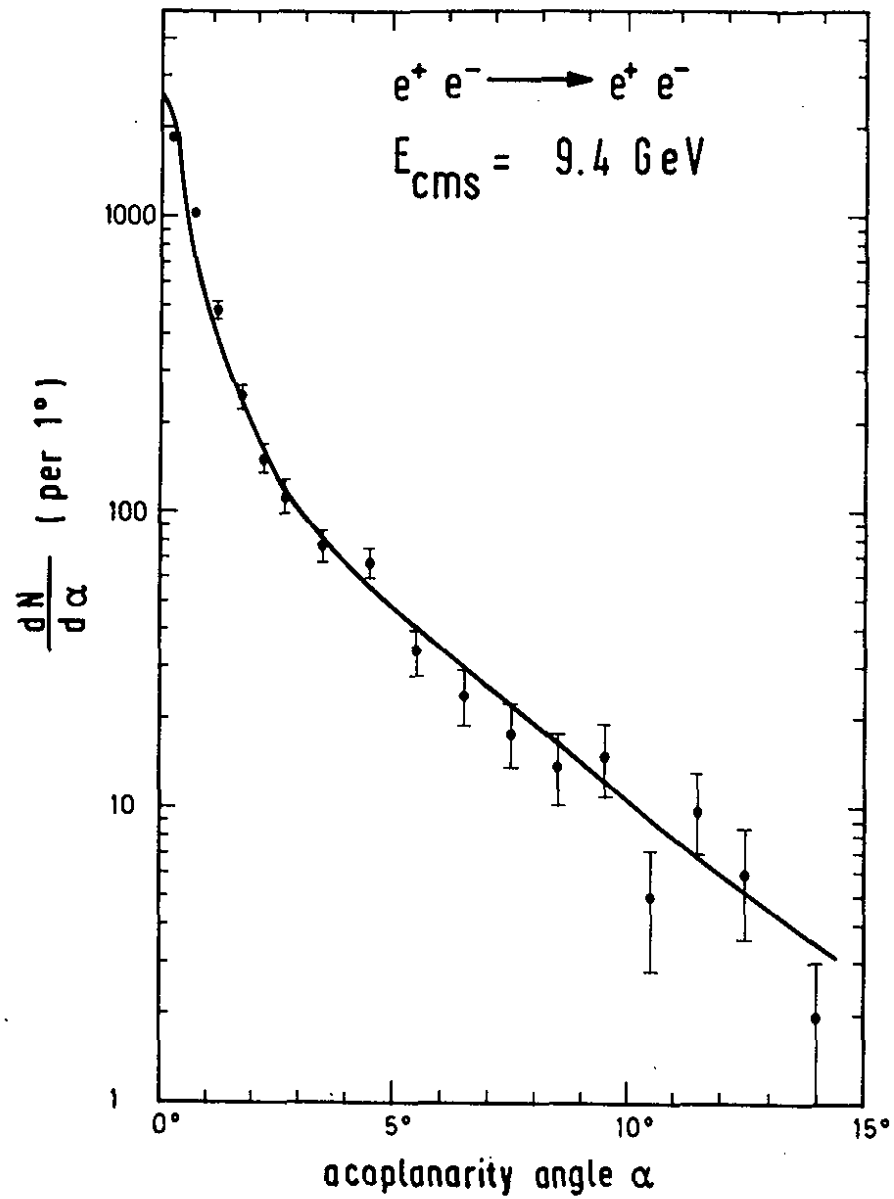

Fig. 4.5 Distribution of the acoplanarity angle α from the Bhabha event sample, at W = 9.4 GeV

If we assume that radiative corrections for σ_1^{MOD} are similar to those for σ_1^{QED} we can determine δ_Λ and δ_W from the data through

$$\sigma^{CORR} = \sigma_1^{QED} (1 + \delta_\Lambda + \delta_W) \qquad (4.8)$$

Since later we find $\sigma^{CORR} = \sigma_1^{QED}$ within the accuracy of the data, we determine limits on possible modifications, by setting $\delta_W = 0$ for limits on δ_Λ, and vice versa.

Explicite expressions for δ_Λ and δ_W can be given in specific models, and limits on δ_Λ and δ_W can then be translated into limits on parameters of these models. In appendix 4A we summarize expressions for these QED modifications.

The electroweak deviations δ_W are calculated by adding Z^0 exchange diagrams to the one photon exchange diagrams in Fig. 4.1. The electroweak effects then depend on 3 free parameters: v^2, a^2 and M_Z, which are related to the electroweak ('Salam-Weinberg') mixing angle θ_W in the GSW theory [403]. The total cross section modifications depend mainly on the vector current coupling v^2, while the μ pair charge asymmetry [411] depends mainly on the axial current coupling a^2. The mass M_Z affects the energy dependence of electroweak effects.

The deviations δ_Λ from breakdowns of QED at large momentum transfers are expressed as modifications of lepton-photon vertex functions or propagators [404]. In the first order amplitudes for ee → ee, μμ and ττ the two lepton-photon-lepton vertices and the photon propagator are multiplied by momentum transfer dependent factors $V(q^2)$ (for the vertex) and $D(q^2)$ (for the propagator). They can be combined into one overall form factor F for the scattering amplitude:

$$V_T^2(s) \cdot D_T(s) = F_T(s) \quad \text{for the time like amplitude} \qquad (4.9a)$$

$$V_S^2(q^2) \cdot D_S(q^2) = F_S(q^2) \quad \text{for the space like amplitude} \qquad (4.9b)$$

The modifications can be different at space like and at time like momentum transfers, and also different for the e, μ and τ leptons. Since no deviations from QED are observed in any of the four reactions (4.1 - 4.4) we assume (i) electromagnetic lepton universality, i.e. the same vertex function for different leptons, and (ii) the same form factor parameterizations for time like and space

like momentum transfers, and (iii) we consider only the lowest possible orders in q^2 for the form factors.

For the lepton pair channels (reactions 4.1 - 4.3) we use the form factor parameterization

$$F(q^2) = 1 \pm \frac{q^2}{\Lambda_\pm^2} \qquad (4.10)$$

which can be considered the first order approximation in q^2/Λ^2 for the formfactor $F = \Lambda_\pm^2 / (\Lambda_\pm^2 \mp q^2)$ proposed in the literature [404]. Two cutoff parameters, Λ_+ and Λ_-, are introduced to allow for $F \geq 1$ and $F \leq 1$. $\Lambda = \infty$ restores pure QED. Λ_+ can be related in the static limit to the charge radius of leptons. If e and γ are pointlike particles, but μ or τ leptons were independently extended we would measure their charge radius in reactions 4.2 and 4.3 as [401]

$$\langle r^2 \rangle = \frac{6\hbar^2c^2}{\Lambda_+^2} = \frac{3\hbar^2c^2}{s} = \left(\frac{\sigma_1^{CORR}}{\sigma_1^{QED}} - 1\right) \qquad (4.11)$$

Finite values of Λ_- can arise from a heavy neutral particle interfering with the photon in reactions (4.1 - 4.3).

In the γ pair channel (reaction 4.4) the QED break downs as discussed for the lepton pair channels cannot produce deviations proportional to Q^2 because of cancellations due to current conservation [404e, 404g, 412]. In this case, the so called "sea gull" graph [404g, i], gives rise to a q^4/Λ^4 term in the form factor:

$$F(q^2) = 1 \pm q^4/\Lambda_\pm^4 \qquad (4.12)$$

A slightly different cross section modification for $ee \to \gamma\gamma$ arises from the exchange of a virtual excited (heavy) electron [404h].

To illustrate the effect of the modifications, we show in Figs. (4.6 c-f) how the modified QED predictions for reactions (4.1 - 4.3), depend on different values of the cutoff parameters $\Lambda_\pm$, and of the Salam-Weinberg angle θ_W. In Bhabha scattering the cross sections at small angles (mainly space like contributions, small $|q^2|$) are almost unaffected. Only the large angle part is sensitive. Both modifications have much stronger effects (by a factor ~3) in

lepton pair production, than in Bhabha scattering, since there all contributions come from the time like diagram with a high value of $q^2 = s$. The forward/backward (or: charge) asymmetry A in the lepton pair production reactions 4.2 and 4.3:

$$A = \frac{\sigma(\cos\theta > 0) - \sigma(\cos\theta < 0)}{\sigma(\cos\theta > 0) + \sigma(\cos\theta < 0)} \qquad (4.13)$$

is still rather small at $s \approx 1000$ GeV^2 (~-6%) if $M_Z \geq 90$ GeV, and requires a high statistics measurement.

In photon pair production (4.4) the high q^2 QED modifications affect the size and the shape of differential cross sections. Since deviations here are proportional to q^4/Λ^4 the expected cross section modifications are much smaller than in lepton pair production, at comparable values of Λ.

4.3 The data

Reactions (4.1 - 4.4) have been measured with PLUTO [413] and also in other PETRA experiments [414]. In Table 4.1 we summarize the event numbers observed in the PLUTO experiment, and the acceptance cuts in the four channels. Further details on the data analysis are given in appendix 4B.

Table 4.1 Acceptance cuts and event numbers in the QED reactions

Reaction $e^+e^- \to$	# of events	Production angle $\lvert\cos\theta\rvert <$	Acollinearity angle $\alpha <$
e^+e^-	5700	0.8	15^0
$\mu^+\mu^-$	228	0.75	10^0
$\tau^+\tau^-$	139	– [1]	–
$\gamma\gamma$	1020	0.75	20^0

[1] In 2 prongs $|\cos\theta| < 0.6$ for each track, and in 4 prongs $|\cos\theta| < 0.75$ for each track.

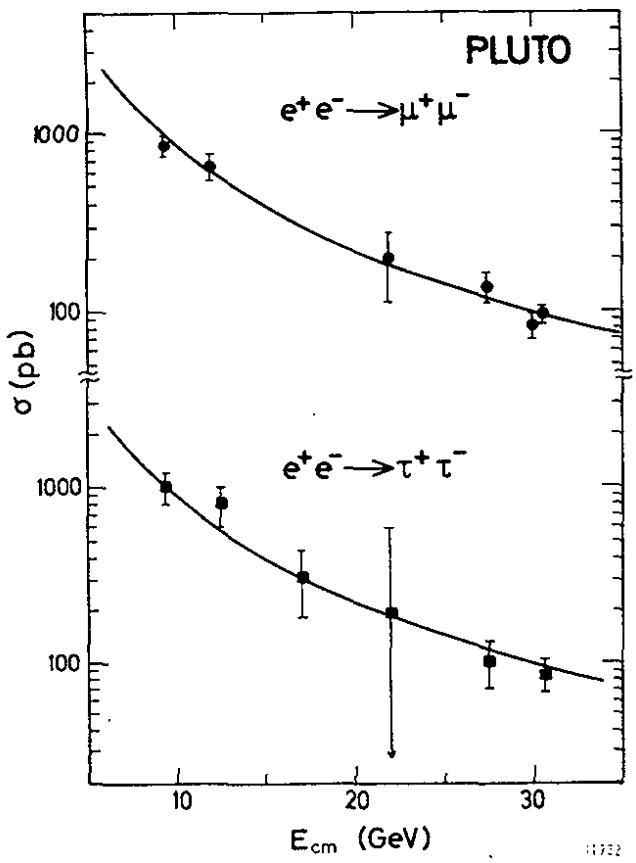

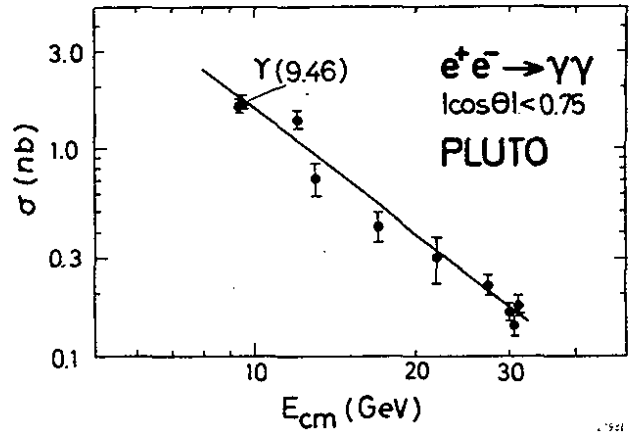

Fig. 4.7 Total cross section σ^{CORR} for the reactions (a) $e^+e^- \to \mu^+\mu^-$ and $\tau^+\tau^-$, and (b) for $e^+e^- \to \gamma\gamma$ at $|\cos\theta| < 0.75$ as function of energy, after corrections for acceptance and radiative processes (see eq. 4.6). Curves are first order QED cross sections

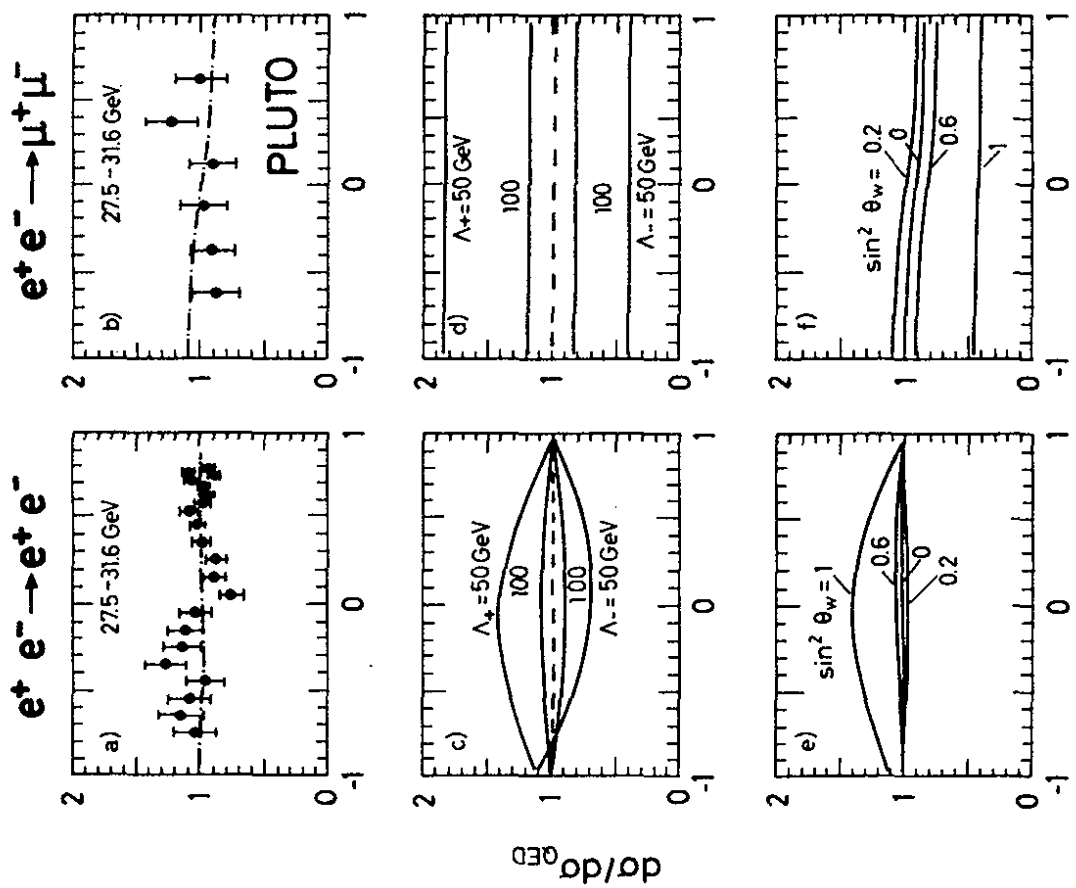

Fig. 4.6 Differential cross section $d\sigma^{CORR}/d\sigma_1^{QED}$ for (a) $e^+e^- \to e^+e^-$ and (b) $e^+e^- \to \mu^+\mu^-$; $d\sigma_1^{MOD}/d\sigma_1^{QED}$ for QED modifications by form factors (c,d) and by electroweak interference (e,f)

The luminosities needed for calculating cross sections are determined from Bhabha scattering at small forward angles ($0.7 < \cos\theta < 0.8$) where $|q^2|$ is much smaller than s ($|q^2| \approx 0.1s$). Therefore the effect of any QED modification on luminosity determination is negligible as compared to its effect on the lepton pair production cross section at $q^2 = s$, as can be seen in Fig. (4.6 c-f).

The total cross sections for μ, τ and γ pair production are shown in Figs.4.7a, b and c, as a function of s. They show the expected 1/s dependence and agree with the QED cross section. In Figs. 4.6 (a and b) we show the ratio $d\sigma^{CORR}/d\sigma_1^{QED}$ versus $\cos\theta$ for ee and $\mu\mu$, averaged over data of $27.5 < W < 31.6$ GeV. At all data points this ratio is consistent with 1. The ratio is trivially equal to 1 for forward Bhabha scattering ($0.7 < \cos\theta < 0.8$) which has been used to determine the luminosity [+]. The μ pair asymmetry, derived from Fig. 4.6b (for $|\cos\theta| < 0.75$, $s = 911$ GeV^2) is

$$A = 7\% \pm 8\% \text{ (stat.)} \pm 2\% \text{ (syst.)} \qquad (4.14)$$

compared to -5.8% expected in the standard electroweak model [403] for $\sin^2\theta_W = 0.23$. Finally the differential cross section for $ee \to \gamma\gamma$ is shown in Fig. 4.8. In the latter figure the data is not corrected for δ_{RAD} and resolution. These effects are included here in the theoretical curves.

In no one of the distributions is any evidence for a deviation from pure QED observed. This null result - together with the errors - will be expressed in the two following sections in terms of limits on parameters describing possible deviations.

[+] Actually we used the electroweak cross section σ^{EW} for Bhabha scattering with $\sin^2\theta_W = 0.23$ (see app. 4A) instead of σ^{QED} to determine the luminosity. The difference is <1% at these angles.

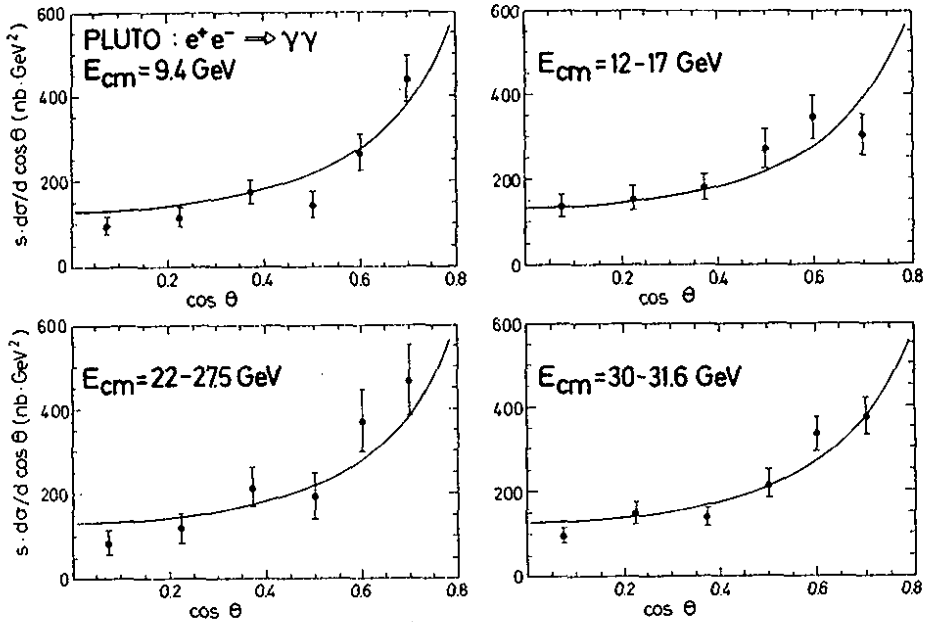

Fig. 4.8 Differential cross section $sd\sigma/d\cos\theta$ for $e^+e^- \to \gamma\gamma$, at 4 energies, not corrected for radiative effects and angular resolution. The curves are the corresponding QED prediction, with radiative corrections up to order α^3

4.4 QED cutoff parameters

From the data shown in the previous section we can infer limits on the cutoff parameters Λ in the form factors (eqs. 4.10 and 4.12). The limits given in table 4.2 have been determined separately from each of the reactions (4.1 - 4.4) with the assumptions discussed in section 4.2.

Table 4.2 Lower limits (95% c.l.) on QED cutoff parameters Λ, in GeV, as determined in the reactions 4.1 - 4.4. Cases $\gamma\gamma$ (a) and $\gamma\gamma$ (b) are explained in the text.

	ee	$\mu\mu$	$\tau\tau$	$\gamma\gamma$(a)	$\gamma\gamma$(b)
Λ_+	234	107	79	46	46
Λ_-	80	101	63	36	--

More detailed cutoff parameters Λ can be introduced in the lepton pair channels by dropping the assumption of electromagnetic lepton universality and by allowing for independent space like and time like cutoff parameters, Λ_S and Λ_T, in eq. 4.10. Results along these lines are given in ref. [413a].

The limits on Λ (table 4.2) from the $\gamma\gamma$ channel are weaker since the form factor here depends on $(1/\Lambda)^4$ rather than $(1/\Lambda)^2$. In column $\gamma\gamma$(a) Λ is the QED cutoff parameter of the form factor (4.12) which multiplies the first order amplitudes for reactions (4.4). In column $\gamma\gamma$(b) the parameter Λ_+ is related to the mass of an exchanged (hypothetic) excited electron. Here the limit for Λ_+ can be interpreted as a lower mass limit for the excited electron, if it has an electromagnetic coupling with the same strength as the electron [404h]. There is no physics motivation for a corresponding Λ_- parameter.

4.5 Electroweak effects

Assuming that there are no other modifications of QED ($\delta_\Lambda = 0$) we can use the combined data in Fig.4.6a,b from reactions (4.1 - 4.2) to place limits on the

electroweak parameters [+]. First we evaluate for a single neutral boson model the limits on the vector and the axial current couplings, v^2 and a^2, and on M_Z as independent quantities. Then we link these parameters through the Salam-Weinberg angle θ_W and determine an upper limit on $\sin^2\theta_W$. Finally we infer limits on boson masses for models with 2 neutral gauge bosons. For definitions and formulae we refer to appendix 4A.

4.5.1 Limits on v^2, a^2 and M_Z

As a first step we set $M_Z = \infty$ which gives the weakest constraints on v^2 and a^2 in a fit to our data:

$$v^2 = -0.09 \pm 0.60 \pm 0.29 \qquad (4.15a)$$

$$a^2 = -0.77 \pm 0.96 \pm 0.09 \qquad (4.15b)$$

These numbers are consistent with $v^2 = a^2 = 0$, i.e. with the absence of any weak interaction effects, but also with the standard electroweak model [403]:

$$a^2 = 1, \quad v^2 = 0.0064 \text{ for } \sin^2\theta_W = 0.23.$$

The results on v^2 and a^2 (4.15) are correlated (see App. 4A, eqs. (4A.5) and (4A.6)). Fig. 4.9 shows the 95% c.l. contour from the ee and $\mu\mu$ data in the a^2, v^2 plane, both for $M_Z = \infty$, and for $M_Z = 80$, 60, 40 GeV. In combination with the 2 (ambiguous) results for a^2 and v^2 from elastic νe scattering data [415] we can exclude Z^0 masses < 40 GeV. Furthermore, our data slightly favour the νe solution with small v^2 and dominating a^2.

The lower limits for Λ_- (table 4.2) cannot be trivially converted into a limit on M_Z. Although the electroweak and the cutoff parameterization have (first order) poles at $s = M_Z^2$ and $s = \Lambda_-^2$, respectively, their functional dependences on s/M_Z^2 and s/Λ_-^2, respectively, are different.

[+] Reaction (4.3) - which in principle carries also the information provided by reaction (4.2) - is not used in this analysis since (i) the detection efficiency is only ~20%, and (ii) the production angle of τ pairs is not measured.

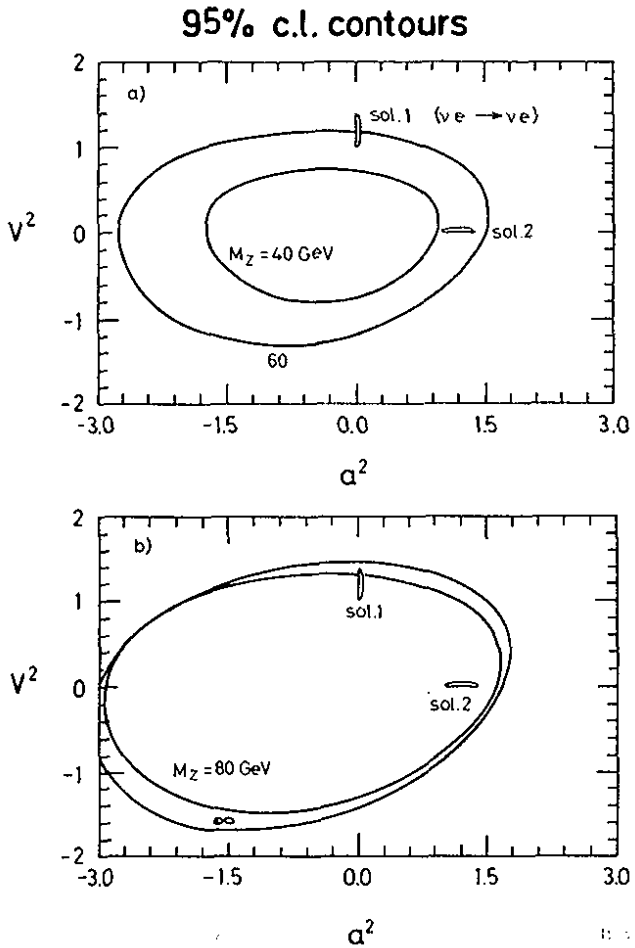

Fig. 4.9 95% c.l. contour plots from fits of v^2 and a^2 to the data of fig. 4.7a,b
(a) assuming Z^0 masses of 40 and 60 GeV
(b) assuming Z^0 masses of 80 and ∞ GeV.
Also shown are the two solutions for v^2 and a^2 as derived from elastic neutrino electron scattering [415]

4.5.2 Limits on the Salam-Weinberg angle θ_W

In the standard electroweak model [403] $\sin^2\theta_W$ is the only parameter, and we have the relations

$$a^2 = 1, \quad v^2 = (1-4\sin^2\theta_W)^2 \qquad (4.16a, b)$$

$$M_Z^2 = \left(\frac{37.4\ \text{GeV}}{\sin\theta_W \cos\theta_W}\right)^2 \qquad (4.16c)$$

With these constraints a fit to our data yields

$$\sin^2\theta_W = 0.22 \pm 0.22 \qquad (4.17a)$$

or $$\sin^2\theta_W < 0.52 \quad \text{at 95\% c.l.} \qquad (4.17b)$$

The result is consistent with the world average of $\sin^2\theta_W = 0.228 \pm 0.010$ [416], obtained from $\gamma - Z_0$ interference at much lower momentum transfers.

4.5.3 Models with 2 neutral gauge bosons

There are extensions of the standard model by a further symmetry group G to $SU_L(2)\times U(1)\times G$ in such a way that the predictions of the $SU_L(2)\times U(1)$ model are reproduced for neutrino cross sections [415] and for polarized electron nucleon scattering [406] at low momentum transfers. In such extensions [417, 418] two neutral bosons occur with masses $M_1 \leq M_Z \leq M_2$, and the parameter v^2 is changed to

$$v^2 = (1 - 4\sin^2\theta_W)^2 + 16\,C\,, \quad C \geq 0 \qquad (4.18a)$$

where C is related to the gauge boson masses and couplings by

$$C = \gamma \cdot (M_1^2 - M_Z^2)(M_Z^2 - M_2^2) / (M_1 M_2)^2 \qquad (4.18b)$$

γ has the value $\cos^4\theta_W$ in $G = \tilde{U}(1)$ (de Groot and Schildknecht [417]) and $\sin^4\theta_W$ in G = SU(2) (Barger et al. [418]).

Using $\sin^2\theta_W = 0.23$ the limit on v^2 is then essentially a limit on C. The PLUTO data yield

$$C < 0.06 \qquad (95\%\ \text{c.l.}) \qquad (4.19)$$

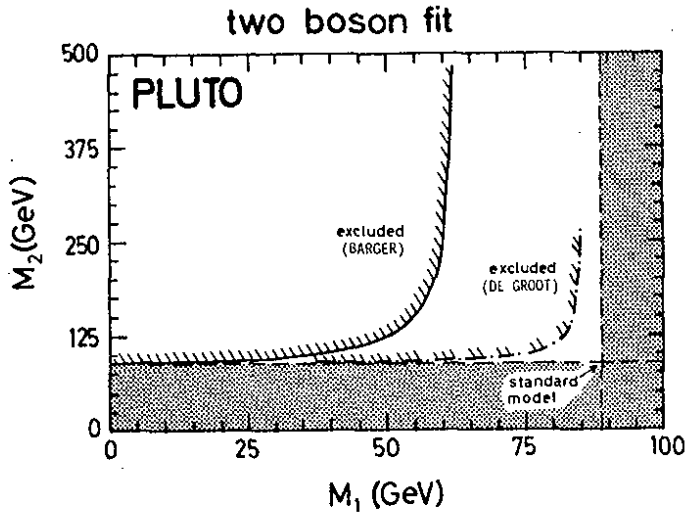

Fig. 4.10 95% c.l. limits on the masses in the two neutral vector boson models of refs. 417 (de Groot and Schildknecht) and 418 (Berger et al.). The dotted area is excluded by the models ($M_1 < M_Z < M_2$)

This imposes correlated bounds on M_1 and M_2 as shown in Fig. 4.10. We find that for the stronger coupling model ($\gamma = \cos^4\theta_W$, [417]) the mass of one of the two vector bosons can deviate from the Z_0 mass by at most 16%.

4.6 Summary and conclusion

In summary the PLUTO experiment has found

(i) that QED is confirmed up to $s = 1000$ GeV^2 and $q^2 = -850$ GeV^2. The cutoff parameters correspond to distances of $1/\Lambda_+ \approx 2.10^{-16}$ cm down to which the validity of QED has been probed. This is an improvement by a factor 3 as compared to pre-PETRA experiments;

(ii) no significant weak interaction effects at energies of $W \sim 30$ GeV, with an integrated luminosity of 2900 nb^{-1};

(iii) non-trivial limits on the strength of weak interactions in purely leptonic reactions.

Similar conclusions have been drawn from the JADE, MARK J, and TASSO experiments [414a,b,c].

Appendix 4A Formulae for QED modifications

4 A.1 Cut-off parameterization

The modified Bhabha cross section, with $q^2 = -s \sin^2\frac{\theta}{2}$, and $q'^2 = -s \cos^2\frac{\theta}{2}$, reads

$$\frac{d\sigma}{d\Omega} = \frac{\alpha^2}{2s}\left\{\frac{q'^4+s^2}{q^4}|F_S(q^2)|^2 + \frac{2q'^4}{q^2 s}\mathrm{Re}(F_S F_T^*) + \frac{q'^4+q^4}{s^2}|F_T(s)|^2\right\} \qquad (4A.1a)$$

$$= \frac{d\sigma_{QED}}{d\Omega}(1+\delta_\Lambda(s,\theta)) \qquad (4A.1b)$$

$$\text{with } \delta_{\Lambda_\pm}(s,\theta) = \frac{3s}{\Lambda_\pm^2}\frac{1-\cos^2\theta}{3+\cos^2\theta} + O(s^2/\Lambda^4)$$

For Λ = 100 GeV, $\sqrt{s}$ = 31 GeV: $\delta_\Lambda \sim 10\%$ at 90^0 and zero at 0^0.
The $\mu^+\mu^-$ and $\tau^+\tau^-$ cross sections which have contributions from time-like photons only, for $\sqrt{s} >> m_\tau, m_\mu$ read:

$$\frac{d\sigma}{d\Omega} = \frac{\alpha^2}{4s}(1+\cos^2\theta)\,|F_T(s)|^2 \qquad (4A.2a)$$

$$= \frac{d\sigma_{QED}}{d\Omega}(1+\delta_\Lambda(s)) \qquad (4A.2b)$$

$$\text{with } \delta_{\Lambda_\pm}(s) = \pm\frac{2s}{\Lambda_\pm^2} + O(s^2/\Lambda^4)$$

In this case δ_Λ is independent of θ; for Λ = 100 GeV, $\sqrt{s}$ = 31 GeV: $\delta_\Lambda \sim 20\%$.

For $ee \to \gamma\gamma$ two different modifications have been considered in the literature

(a) Propagator and vertex modifications:
Here it can be shown [404e, 404g, 415] that all contributions of the order (q^2/Λ^2) cancel and that the amplitude modification can be parameterized by form factors:

$$F(q^4) = 1 \pm \frac{q^4}{\Lambda_\pm^4} \qquad (4A.3)$$

Hence:

$$\frac{d\sigma}{d\Omega} = \frac{\alpha^2}{2s}\left\{\frac{q'^2}{q^2}|F(q^4)|^2 + \frac{q^2}{q'^2}|F(q'^4)|^2\right\} \qquad (4A.4a)$$

$$= \frac{d\sigma_{QED}}{d\Omega}(1+\delta_\Lambda(s,\theta)) \qquad (4A.4b)$$

$$\text{with } \delta_{\Lambda_\pm}(s,\theta) = \pm\frac{s^2}{2\Lambda_\pm^4}\,\frac{\sin^4\theta}{1+\cos^2\theta} + O(s^4/\Lambda^8)$$

(b) Heavy electron (E^+) exchange:
Here the interference of the normal (e) and heavy electron (E^+) is considered:

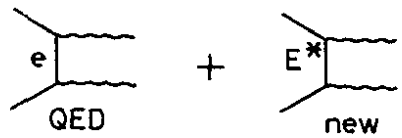

Current conservation allows only for a magnetic moment coupling between e, E^+ and γ. A quantitative calculation [404h] yields:

$$\delta_\Lambda = \frac{s^2}{2\Lambda^4}\cdot\sin^2\theta + O(s^4/\Lambda^8) \qquad (4.A.4c)$$

The parameter Λ is related to the mass M_E and to the coupling constant λ of the excited electron by $\Lambda^2 = M_E^2/\lambda$.

In both cases (a) and (b) the modifications are maximum at $\theta = 90^0$. They are numerically smaller than in the case of Bhabha scattering or lepton pair production (e.g. Λ = 100 GeV, $\sqrt{s}$ = 31 GeV: $\delta \sim 0.4\%$ at $\theta = 90^0$) which is reflected in correspondingly lower experimental limits on Λ.

A more detailed presentation can be found in refs. [404h, 419].

4 A.2 Electroweak cross sections

From the standard 1^{st} order Hamiltonian of the electroweak neutral current one can derive [420] the following differential cross sections (neglecting terms of the order m_e^2/s).

a) $e^+e^- \to e^+e^-$:

$$\frac{4s}{\alpha^2}\frac{d\sigma}{d\Omega} = \left\{\frac{3+x^2}{1-x}\right\}^2 + 2\frac{3+x^2}{(1-x)^2}\{(3+x)Q - x(1-x)R\}v^2 \qquad (4A.5)$$

$$- \frac{2}{1-x}\{7+4x+x^2)Q + (1+3x^2)R\}a^2$$

$$+ \frac{1}{2}\left\{\frac{16}{(1-x)^2}Q^2 + (1-x)^2R^2\right\}(v^2-a^2)^2$$

$$+ \frac{1}{2}(1+x)^2\left\{\left(\frac{2}{1-x}Q - R\right)\right\}^2 (v^4+6v^2a^2+a^4)$$

with $x = \cos\theta$, θ being the polar angle with respect to the beam axis

$$Q = g M_z^2 \frac{q^2}{q^2 - M_z^2} \to -g q^2 = \delta \cdot s\frac{1}{2}(1-x) \qquad (M_z^2 >> |q^2|)$$

$$R = g M_z^2 \frac{s}{s - M_z^2} \to -g s \qquad (M_z^2 >> s)$$

$$g = \frac{G_F}{8\sqrt{2}\,\pi\alpha} = 4.49 \cdot 10^{-5}\ (\mathrm{GeV}^{-2})$$

$\alpha = 1/137$, fine structure constant, G_F = Fermi coupling constant

M_Z = mass of the Z^0 boson

$$q^2 = -\frac{s}{2}(1 - \cos\theta) = -\frac{s}{2}(1 - x)$$

The coupling strengths of the vector and the axial weak current are expressed by v and a. Their normalization is such that

$a^2 = 1$, $v^2 = (1 - 4\sin^2\theta_w)^2$

in the standard electroweak model [403].

b) $e^+e^- \to \mu^+\mu^-$:

$$\frac{4s}{\alpha^2}\frac{d\sigma}{d\Omega} = (1+x^2)\{1 + 2v^2R + (v^2+a^2)^2R^2\} \qquad (4A.6a)$$

$$+ 4x\{a^2R + 2v^2a^2R^2\}$$

$$\sigma = \frac{4\pi\alpha^2}{3s}\{1 + 2v^2R + (v^2+a^2)^2R^2\} \qquad (4A.6b)$$

In equations (4A.5) and (4A.6) the terms independent of Q and R correspond to the pure QED contributions, the terms linear in Q, R describe the electroweak interference and the terms in Q^2, R^2 are pure weak contributions.

The interference term in ee → μμ produces a forward-backward asymmetry A, which is sensitive to a^2. If μ pairs are measured at production angles $|\cos\theta| < x_1$ eq. (4A.6) yields

$$A(x_1) = \frac{6x_1}{3 + x_1^2}\frac{a^2R(1 + 2v^2R)}{1 + 2v^2R + (v^2+a^2)^2R^2} \qquad (4A.7)$$

Appendix 4B: Data analysis in QED reactions

In this appendix we give details on the event selection - at the trigger level and in the off-line analysis - for the four QED reactions (4.1 - 4.4), and also on how the main background sources were removed. A few QED event pictures are shown in Fig. 4.11.

4 B.1 $e^+e^- \to e^+e^-$

At runs below 22 GeV, Bhabha events [413a, 421] were triggered by a coincidence of two opposite shower counters if more than 1.2 GeV was observed in each, or by a trigger sensitive to more than 3 GeV in the full shower counter. For runs at 27 - 31 GeV these threshold values were doubled. The efficiency of these triggers for Bhabha events was as high as 99.9 ± 0.1%. This could be measured by an independent track trigger for Bhabha events.

After shower reconstruction events with (at least) 2 showers with energies $E_{SH} > E_B/3$ each were accepted for the further analysis. The tracks were reconstructed and matched with the shower position. Events with no tracks pointing to the showers or with more than 4 tracks from a common vertex were rejected. Allowing for more than 2 tracks is necessary because some events start showering in the track detector. *The sample now consisted of* 2-prongs if both showers were associated with tracks, and of a few (~4%) 1-prongs. Within the acceptance (Table 4.1) the efficiency for recognizing an $e^+e^- \to e^+e^-$ event was determined to be 99.3 ±0.4%. The resolution of the scattering angle is $\sigma(\cos\theta) = 0.01$, independent of $\cos\theta$.

The main background source was the reaction $e^+e^- \to \gamma\gamma$, where one or both γ's started showering in the track detector. The 1-prong sample was cleared from this background in a visual scan. From the analysis of the reaction $ee \to \gamma\gamma$, and the number of $e^+e^- \to \gamma\gamma$ with 1γ converted, the contamination of the 2-prong Bhabha sample from this source was calculated to be 0.3 ±0.03%. All other backgrounds (beam gas, cosmic rays, $ee \to \tau\tau$, $ee \to ee + ee$, $ee + \mu\mu$) were less than 1% together.

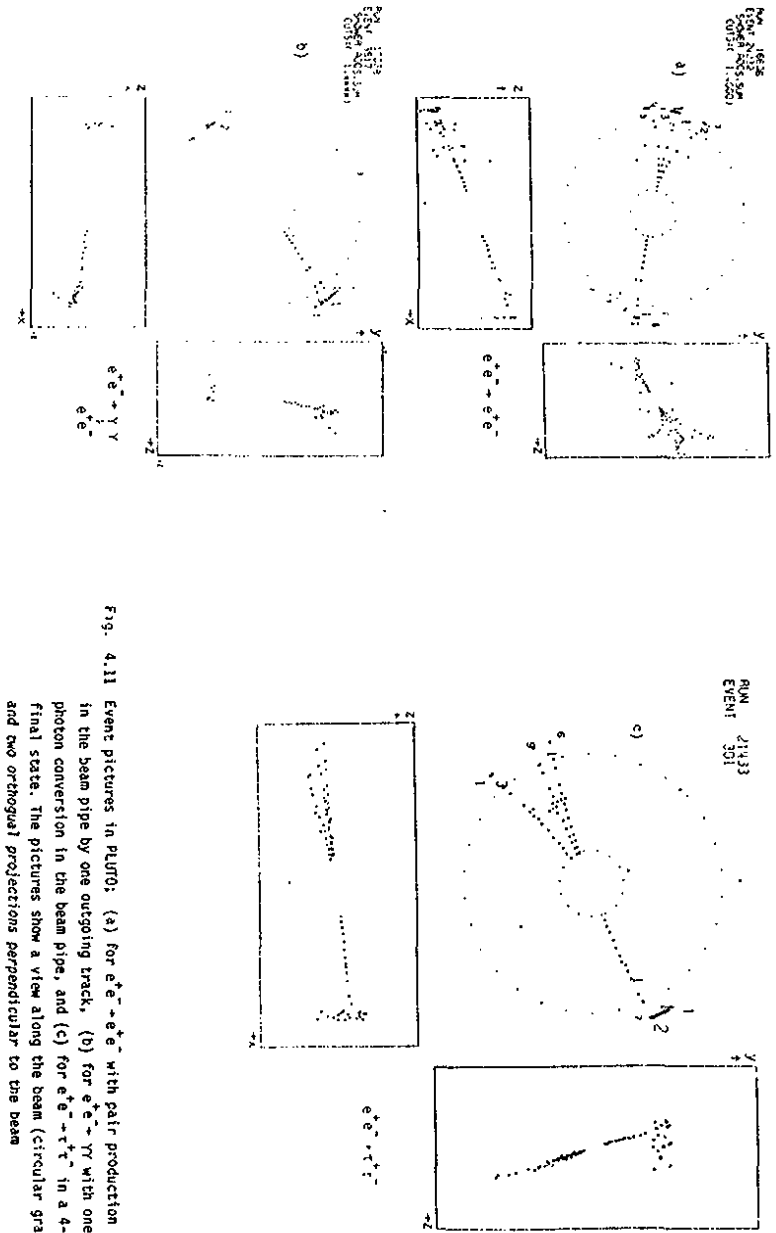

Fig. 4.11 Event pictures in PLUTO: (a) for $e^+e^- \to e^+e^-$ with pair production in the beam pipe by one outgoing track, (b) for $e^+e^- \to \gamma\gamma$ with one photon conversion in the beam pipe, and (c) for $e^+e^- \to \tau^+\tau^-$ in a 4-prong final state. The pictures show a view along the beam (circular graph), and two orthogonal projections perpendicular to the beam

The reliability of charge identification could be checked in the 2-prong Bhabha sample which contained a small fraction (~5%) of events with two same charge tracks. From this number we have determined the number of events with two wrong curvature tracks at each energy and cosθ interval for corrections. The same charge 2-prong events were divided according to the ratio of forward/backward scatters. Corrections of the few 1-prong Bhabhas could be neglected. In addition all backward scatters were checked in a visual scan. The separation of forward-backward Bhabha scattering does not affect the determination of the cut-off parameters Λ (eq. 4A. 1b), but is useful for the analysis of electroweak effects. Also it allowed a measurement of the modification of the photon propagator by hadronic vacuum polarization at the T resonance (see Sect. 7).

4 B.2 $e^+e^- \to \gamma\gamma$

Trigger and event preselection were similar as for Bhabha events (Sect. 4 B.1) with slightly different acceptance and acollinearity cuts (see Table 4.1) and by requiring $E_{sh} \geq 1/4\ E_B$ [413b,421]. In this sample γγ final states were separated from ee, eeγ and hadronic final states mainly by rejecting events where

(a) both clusters were associated with tracks
(b) more than 5 tracks were observed in the track detector
(c) the angle between any two reconstructed tracks exceeded 50^0.

The γγ candidates were then scanned visually. Among the events with no tracks in the track detector (~60% of the total sample) practically no background was found, in agreement with a Monte Carlo study. The remaining events could be separated into (i) γγ final states with one converted photon (~30% of the total γγ rate), and (ii) Bhabha scatters with one shower in the track detector without reconstructed tracks, eeγ final states and a small number of hadronic final states. The events from (ii) were rejected.

A total of 1034 events was accepted, with an estimated background of (1±1)%. Losses came from the selection cuts (5.5 ± 1.1%) and incorrectly analysed shower patterns (1.3%), leading to an overall efficiency of 93 ± 2%.

4.B.3 $ee \to \mu\mu$

The events were triggered by a track trigger sensitive to two coplanar tracks. In selecting this final state [413d, 422] the main problem is the rejection of cosmic ray background. All other backgrounds from $ee \to$ hadrons, $ee \to ee$, $ee \to ee + \mu\mu$ are negligible, or small (2% from $ee \to \tau\tau$) in 2 prong events which passed the following cuts:

(i) two tracks with $|\cos\theta| < 0.75$
(ii) collinear within 10^0
(iii) track momenta $p > 0.5\ (0.67) \cdot E_B$ for $E_B > 10\ (<10)$ GeV;
(for collinear tracks we find a momentum resolution of $\sigma_p \lesssim 0.01\ p^2$, see Fig. 3.5).

(iv) distance of tracks to the interaction point small:
$\Delta r\ (x,y) < 1.5$ mm, $\Delta z < 40$ mm
(v) total energy in shower counters $E_{SH} < 1$ GeV
(vi) time difference of < 20 (60) nsec between event time from barrel (end cap) and beam crossing.

After these cuts the cosmic ray background in the end cap region was 40% of the μ pair signal and was subtracted, using a side band in event time. In the barrel region ($|\cos\theta| < 0.6$) a time of flight separation was possible. Fig. 4.12 shows the time difference of the 2 back-to back tracks normalized to incidence perpendicular to the beam. Cosmic rays and μ-pairs are clearly separated by a cut at 2 nsec, leaving a cosmic ray background of less than 1.4%. After background subtractions we obtain 228 μ-pair events. The trigger efficiency is 98%, and the event selection cuts are associated with losses of 1.5%.

At the present level of statistics, errors in the asymmetry from uncertainties in charge sign identification are completely negligible. For W = 30 GeV, the sagitta in a collinear 2-track fit is different from zero by ~7 standard deviations.

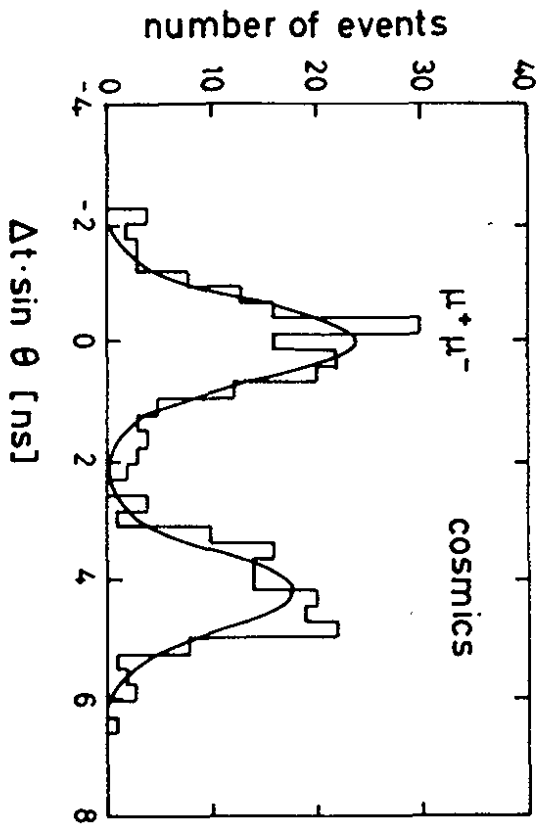

Fig. 4.12 TOF differenz for μ pairs and cosmics

4 B.4 $ee \to \tau\tau$

This reaction is new in the context of testing QED. In principle it provides the same information as $ee \to \mu\mu$, but in practice there are several drawbacks from the fact that τ's are not observed before they decay: cross sections have to be determined from decay channels using branching ratios which are known with a limited accuracy, and the production angle of τ's cannot exactly be reconstructed from the decay products.

On the other hand, at energies $W >> 2 \cdot m_\tau$ the signature of τ pair events becomes much clearer than at the low energies ($E_B \sim 2$ GeV), where the τ lepton was discovered (see section 5). The most distinctive features of τ pair events at PETRA energies are a low multiplicity (2-, 4- and a few 6-prongs, as compared to $\langle n_{CH} \rangle \sim 10$ for hadronic annihilation, see Fig. 6.24), and two almost collinear sets of decay products contained in very small solid angles (see Figs. 4.11c and 4.13). We have used final states in which at least one τ lepton decays into only one charged particle (e, μ, π) plus neutrals [413d, 423]. This way we accept ~90% of all decay modes [416]. The accepted events then consist of 2 prongs (~50% of all) and 4 prongs (~40%) which require different additional cuts for background rejection.

The main background problem in the 2-prong events is due to $ee \to ee$, $\mu\mu$, and to cosmic rays, and $\gamma\gamma$ reactions. 2-prong τ events were selected by applying the following selection criteria.

(1) 2 oppositely charged tracks, originating from the interaction point
(2) one momentum $p > 0.8$ GeV/c, the other $p > 0.5$ GeV/C (mainly against beam gas)
(3) production angle of each track $|\cos\theta| < 0.6$; (to have time of flight rejection of cosmic rays)
(4) no collinear fit possible (against μ-pairs and remaining cosmics)
(5) missing mass $>0.5\ E_{beam}$ (against $\mu\mu\gamma$, $ee\gamma$)
(6) an acoplanarity angle $\alpha > 18^0$, if both tracks are associated with showers of energies $E > 0.25\ E_{beam}$ (against radiative Bhabhas, see also Fig. 4.5 for α distribution of Bhabha events).
(7) 2-prong effective mass $M > 2$ (3) GeV at $E_{CM} \leq 13$ (≥ 17) GeV, and net momentum transverse to the beam >0.5 GeV/c (against $\gamma\gamma$ events).

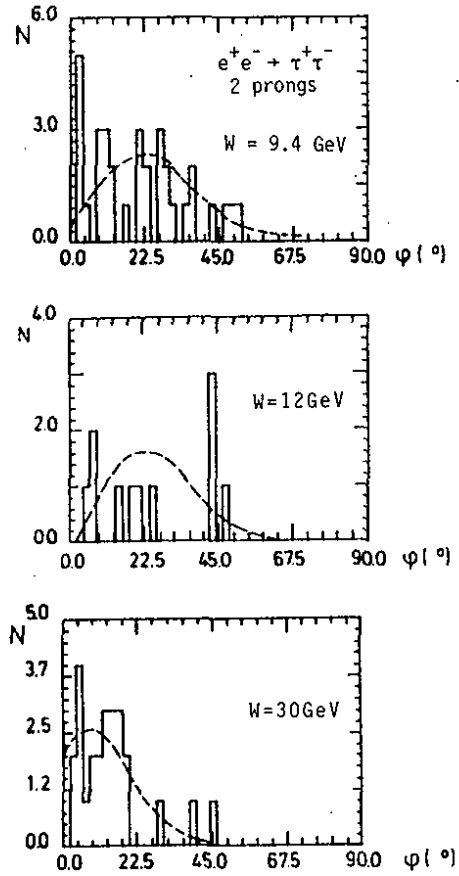

Fig. 4.13 Acolinearity angle distribution in $e^+e^- \to \tau^+\tau^-$ 2 prong events, at W = 9.4, 12, and 30 GeV

According to a simulation of reaction 4.4 17% of all 2-prong events passed these criteria [423]. 4-prong events are of the following type

$$ee \to \tau \quad \tau$$
$$\downarrow \quad \downarrow$$
$$\text{1 prong} \quad \text{3 prong}$$
$$\text{+ neutrals} \quad \text{+ neutrals}$$

with the 1- and 3-prong parts almost back to back. The main background in this topology is from $\gamma\gamma$ reactions and from degraded Bhabha events. To select τ events we required

(1) ≤ 6 observed charged tracks (to allow for one $\gamma \to e^+e^-$ conversion) with no charge excess

(2) all tracks with $|\cos\theta| < 0.75$

(3) at least 1 track with $p > 0.4$ (0.5) GeV at $E_{Cm} \leq 13$ (≥ 17) GeV, and with no other tracks within $\Delta\phi = \pm 90^o$ ('1-prong')

(4) the 3-prong mass consistent with τ decay

(5) cut (7) of 2-prongs with appropriate modifications to reject $\gamma\gamma$ events (in particular $\gamma\gamma \to \tau\tau$; two clear examples of such events have been observed).

20% of all 4-prongs passed these criteria.

After these cuts we find 73 2-prong events and 78 4-prong events. The remaining background, (3 2-prong and 9 4-prong events), due to $\gamma\gamma$ processes and multihadron events, was estimated by Monte Carlo simulations of these processes.

The efficiency of triggering and event selection, as well as the radiative corrections were determined from a Monte Carlo simulation which includes radiation in the initial state and τ production and decay into the various channels in the detector. We have checked [423] that the relative ratios of various subchannels with identified particles like e, μ, π, ρ, and the 2- and 4-prong ratio are consistent with the τ decay branching ratios [416].

References

401 A recent review of experimental QED tests can be found in: J.J.Sakurai, Conference on High Energy e^+e^- Interactions, (Vanderbilt, 1980), AIP Conference Proceedings No. 62 (1980), and preprint UCLA/80/TEP/14

402 R.P.Feynman, Phys.Rev. 76 (1949) 769

403 S.L.Glashow, Nucl.Phys. 22 (1961) 579; S.Weinberg, Phys.Rev.Lett. 19 (1967) 1264; A.Salam, Elementary Particle Theory, ed. N. Svartholm (Almquist and Wiksell, Stockholm, 1968), p. 367

404 (a) F. Bopp , Ann.Physik (5) 42 (1942) 573; R.P.Feynman, Phys.Rev. 74 (1948) 939

(b) H.Salecker, Zeits. Naturforsch. 8a (1953) 16; and 10a (1955) 349

(c) S.D.Drell, Ann.Phys. 4 (1958) 75

(d) F.E.Low, Phys.Rev.Lett., 14 (1965) 238

(e) J.A.McClure and S.D.Drell, Nuovo Cim. 37 (1965) 1638

(f) R.Gatto, Proceedings of the Intern.Symposium on Electron and Photon Interactions at High Energies, Hamburg 1965, Vol.1, p.106, Deutsche Physikalische Gesellschaft, 1965

(g) N.M.Kroll, Nuovo Cim. 45 (1966) 65

(h) A.Litke, Harvard University, Ph.D. Thesis (1970), unpublished

(i) K.Ringhofer, H.Salecker, Contribution to the 1975 Internat.Symposium on Lepton and Photon Interactions at High Energies, Stanford University, unpublished, and Contribution to the 19th International Conference on High Energy Physics, Tokyo 1978, unpublished

(j) Capdequi Peyranère M. et al., Nucl.Phys. B149 (1979) 243

405 For $\Gamma(T \to ee)$ see section 7; for $\Gamma(v \to ee)$, $v = \rho, \omega, \phi, J/\psi$ and ψ' see ref. 416

406 C.Y.Prescott et al., Phys.Lett. 77B (1978) 347; 84B (1979) 524

407 L.M.Barkov and M.S.Zolatosyov, Phys.Lett. 85B (1979) 308

408 J.E.Augustin et al., Phys.Rev.Lett. 34 (1975) 233; L.H.O'Neill et al., Phys.Rev.Lett. 37 (1976) 395

409 (a) G.Bonneau, F.Martin, Nucl.Phys. B27 (1971) 381

(b) F.A.Berends, K.J.F.Gaemers and R.Gastmans, Nucl.Phys. B57 (1973) 381
F.A.Berends, K.J.F.Gaemers and R.Gastmans, Nucl.Phys. B63 (1973) 381
F.A.Berends, K.J.F.Gaemers and R.Gastmans, Nucl.Phys. B68 (1974) 541
F.A.Berends and G.J.Komen, Phys.Lett. 63B (1976) 432
F.A.Berends and R. Kleiss, DESY 80/66

410 F.A.Berends, R.Gastman, Nucl.Phys. B61 (1973) 414

411 Weak interaction effects in reaction (4.2) have been discussed by many authors. Some of the earliest papers are:
N. Cabibbo and R. Gatto, Phys.Rev. 124 (1961) 1577;
T. Kinoshita et al., Phys.Rev. D2 (1970) 910, J. Godine and A. Hankey, Phys.Rev. D6 (1972) 3301; R. Budny, Phys.Lett. 45 (1973) 340.
For reviews see, e.g., L. Wolfenstein, AIP Proceedings 23 (1974) 84;
J.J. Sakurai, AIP Proceedings 51 (1979) 138

412 a) J.Takahashi, Nuov.Cim. 6 (1957) 370
b) F.E.Low, Phys.Rev. 110 (1958) 974

413 a) PLUTO Coll., Ch. Berger et al., Z.Phys. C4 (1980) 269
b) " " " " , Phys.Lett. 94B (1980) 87
c) " " " " , Z.Phys. C7 (1981) 289
d) " " " " , submitted to Phys.Lett.B, " 81/001

414 a) JADE Coll., W. Bartel et al., Phys.Lett. 92B (1980) 206, W. Bartel et al., DESY 80/123, to be published in Phys.Lett. B

b) MARK J Coll., D.P. Barber et al., Phys.Rev.Lett. 42 (1979) 1110; Phys.Rev.Lett. 43 (1979) 1915 and The MARK J Collaboration, Physics Reports 63 (1980) 337.

c) TASSO Coll., R. Brandelik et al., Phys.Lett.94B (1980) 259; Phys.Lett. 92B (1980) 199

d) For a summary as of June 1980 see:
P.Dittmann and V.Hepp, to be published in Z.Phys.C,
and DESY 81/030.

415 e.g. K. Winter, Proc. of the International Symposium on Lepton and Photon Interactions at High Energies, Fermilab (1979) 258

416 Particle Data Group, Rev.Mod.Phys. 52 (1980)

417 E.H. de Groot and D. Schildknecht, Phys.Lett. 90B (1980) 427;
E.H. de Groot and D. Schildknecht, University of Bielefeld Report, BI-TP 80/08

418 V. Barger et al., Phys.Rev.Lett. 44 (1980) 1169

419 V.Hepp, "Test of Quantum Electrodynamics at high momentum transfers", talk given at the Symposium on "Stand und Ziele der QED", Mainz, May 9-10, 1980, submitted for publication in "Lecture Notes on Physics", Springer Verlag

420 R. Budny, Phys.Lett. 55B (1975) 227; Phys.Lett. 45B (1973) 340

421 B. Koppitz, Ph. D. Thesis, Hamburg (1980)
and int. rep. DESY-PLUTO 80/05

422 W. Lührsen, Ph. D. Thesis, Hamburg, in preparation

423 Olivia Meyer, Ph. D. Thesis, Wuppertal (1980), internal report DESY PLUTO - 81/01

424 A.A.Sokolov and J.M.Ternov, Sov.Phys.Dokl. 8 (1964) 1203.
For a recent review see J.D.Jackson, Rev.Mod.Phys. 48 (1976) 417

Figure captions

4.1 First order QED diagrams for $e^+e^- \to l^+l^-$

4.2 First order QED diagrams for $e^+e^- \to \gamma\gamma$

4.3 Diagrams contributing to radiative corrections of order α^3, for $e^+e^- \to l^+l^-$

4.4 Diagrams contributing to radiative corrections of order α^3, for $e^+e^- \to \gamma\gamma$

4.5 Distribution of the acoplanarity angle α from the Bhabha event sample, at W = 9.4 GeV

4.6 Differential cross section $d\sigma^{CORR}/d\sigma_1^{QED}$ for (a) $e^+e^- \to e^+e^-$ and (b) $e^+e^- \to \mu^+\mu^-$; $d\sigma_1^{MOD}/d\sigma_1^{QED}$ for QED modifications by form factors (c,d) and by electroweak interference (e,f)

4.7 Total cross section σ^{CORR} for the reactions (a) $e^+e^- \to \mu^+\mu^-$ and $\tau^+\tau^-$, and (b) for $e^+e^- \to \gamma\gamma$ at $|\cos\theta| < 0.75$ as function of energy, after corrections for acceptance and radiative processes (see eq. 4.6). Curves are first order QED cross sections

4.8 Differential cross section $s d\sigma/d\cos\theta$ for $e^+e^- \to \gamma\gamma$, at 4 energies, not corrected for radiative effects and angular resolution. The curves are the corresponding QED prediction, with radiative corrections up to order α^3

4.9 95% c.l. contour plots from fits of v^2 and a^2 to the data of fig. 4.7a,b
(a) assuming Z^0 masses of 40 and 60 GeV
(b) assuming Z^0 masses of 80 and ∞ GeV.
Also shown are the two solutions for v^2 and a^2 as derived from elastic neutrino electron scattering [415]

4.10 95% c.l. limits on the masses in the two neutral vector boson models of refs. 417 (de Groot and Schildknecht) and 418 (Barger et al.). The dotted area is excluded by the models ($M_1 < M_Z < M_2$)

4.11 Event pictures in PLUTO; (a) for $e^+e^- \to e^+e^-$ with pair production in the beam pipe by one outgoing track, (b) for $e^+e^- \to \gamma\gamma$ with one photon conversion in the beam pipe, and (c) for $e^+e^- \to \tau^+\tau^-$ in a 4-prong final state. The pictures show a view along the beam (circular graph), and two orthogual projections perpendicular to the beam

4.12 TOF differenz for μ pairs and cosmics

4.13 Acolinearity angle distribution in $e^+e^- \to \tau^+\tau^-$ 2 prong events, at W = 9.4, 12, and 30 GeV

5 The heavy lepton τ

5.1 Introduction

It has been a long standing puzzle 'why' the muon existed as a second charged lepton without any appearant difference to the electron except for the mass and the lepton quantum number. The discovery of the τ particle by Perl and his collaborators in the SLAC-LBL collaboration [501, 502a] established the existence of a further charged lepton. The most interesting question concerning the nature of this new particle, and of the leptons in general was: is the τ related to the leptons e and μ in the same way as these two are related among each other, i.e. are their weak and electromagnetic interactions identical, and is the τ separated only by a new, third lepton quantum number (e-μ-τ universality)? Such a sequential heavy lepton would also have its own neutrino, ν_τ, to make up for a weak isodoublet. Furthermore, the τ gave rise to speculations on the existence of a third generation of quarks beyond the known (d, u) and (s,c) doublets, since there are good reasons to believe that there are equal numbers of quarks and leptons [503]. The experimental verification of this speculation is described in section 7.

As an implication of the sequential nature of the τ lepton its decay fractions are essentially determined by the universal weak current, depending mainly on its mass and open channels, and were largely predicted [504] as shown in table 5.1. The most characteristic final state from the decay of a τ pair event was

Table 5.1 Predictions for τ decays, with $\tan^2\theta_c = 0.05$ and $M_\tau = 1.784$ GeV.

	Γ/Γ(eνν)	B[%]	Input
νeν	1	16.1	
νμν	0.98	15.8	
νπ	0.58	9.4	Γ(π → νμ)
νK	0.025	0.4	Γ(π → νμ) + Cabbibo angle θ_c
$\nu\rho^-$	1.54	24.8	CVC
νK^{*-}	0.10	1.6	CVC + Cabbibo angle θ_c
$\nu A_1(1100)$	0.58	9.4	Weinberg sum rules
ν continuum (M > 1.1GeV)	~1.4	23	$\sigma(e^+e^- \to$ hadrons)

due to its leptonic decay modes $\tau \to \nu e \nu$, $\nu \mu \nu$, leading to final states containing a muon and an electron as the only observable particles:

$$\begin{array}{ccccc} e^+e^- & \to & \tau^+ & + & \tau^- \\ & & \downarrow & & \downarrow \\ & & e^+\nu_e\bar{\nu}_\tau & + & \mu^-\bar{\nu}_\mu\nu_\tau \\ & \text{or} & \mu^+\nu_\mu\bar{\nu}_\tau & + & e^-\bar{\nu}_e\nu_\tau \end{array} \qquad (5.1)$$

In fact, first evidence for the τ particle was already obtained in 1975 [502a] by the observation of so called 'μe events', and was supported by the 'anamalous muons' observed by the MPP collaboration [502b]. One year later improved statistics and the detailed kinematic properties of the μe events were sufficient to claim the discovery of a new heavy lepton [501].

To put the contribution of the PLUTO experiment to the confirmation of this discovery, and to the further verification of the τ particle as a sequential lepton, into perspectives we briefly review the experimental evidence for the τ as of the end of 1976.

The heavy lepton interpretation of the μe events was mainly based on the following two facts: (i) the momentum distribution of the μ and e tracks agreed with a 3-body weak decay of the parent particle [504], which was produced in pairs (with a pointlike QED cross section), and disagreed with a 2-body decay; and (ii) no other particles were observed even though (at least) 4 particles were missing per event. This pointed towards neutrinos as the 4 missing particles. Statement (ii) was important to exclude the hypothesis of charm production where only 2 neutrinos were expected per event. But it was not absolutely strict because of background problems. They came from a rather high hadron-lepton misidentification probability (up to 20% for muons and also for electrons) and from a gap of 36% of 4π in the solid angle coverage for charged particle and photon detection. As a result up to 39% of the μe events in the subtracted sample could still contain additional undetected photons or charged particles, at a confidence level of 90%. Such kind of events would rather hint towards charm production as the source of the μe events.

It was therefore very urgent to confirm this important discovery and to remove possible doubts by an independent experiment. Data taken by the PLUTO collaboration at DORIS were qualitatively complementary in their nature because of different features of the PLUTO detector, like

(1) the hadron absorbing iron was thicker (68 cm) leading to

$$P_{h \to \mu} = 2.8 \pm 0.7\%$$

$$\text{for} \quad p(\mu) \geq 1.0 \text{ GeV/c}$$

(2) the electron identification method was different, leading to

$$P_{h \to e} = 3.5 \pm 0.7\%$$

$$\text{for} \quad p(e) \geq 0.3 \text{ GeV/c}$$

(3) the solid angle not covered for charged particle and photon detection was 13% of 4π, only. The photon detection efficiency was 80% for $|\cos\theta| < 0.55$, and dropped to ≈ 50% at $|\cos\theta| = 0.87$.

Therefore background problems were considerably smaller. This made it possible to arrive at conclusive results even with a much smaller - but cleaner - sample of events [505, 507]. Thus the PLUTO experiment at DORIS could make important contributions to the confirmation of the τ discovery and to the measurement of its properties. Here in particular measurements of the leptonic decay modes, and of the semihadronic decays induced by the axial weak current, i.e. the decays $\tau \to \nu\pi$ and $\tau \to \nu\rho\pi$ were significant steps in verifying the sequential character of the τ lepton. The pointlike nature has been established by the PETRA experiments. The various results concerning the τ lepton are presented in sections 5.2 - 5.4. In section 5.5 we report the search for leptons heavier than the τ, at the PETRA storage ring.

5.2 Evidence for heavy lepton production

5.2.1 Search for heavy lepton events

In data taken in 1976 at CMS energies of $3.6 \leq W \leq 5.0$ GeV the PLUTO collaboration started searching for heavy lepton production by looking for events with a muon. For this purpose, all events with a muon candidate track ($p > 1.0$ GeV/c, $|\cos\theta| \leq 0.752$) and at least one further track with $p > 0.2$ GeV/c, $|\cos\theta| < 0.87$ were examined. First the events were required to pass kinematic cuts which removed

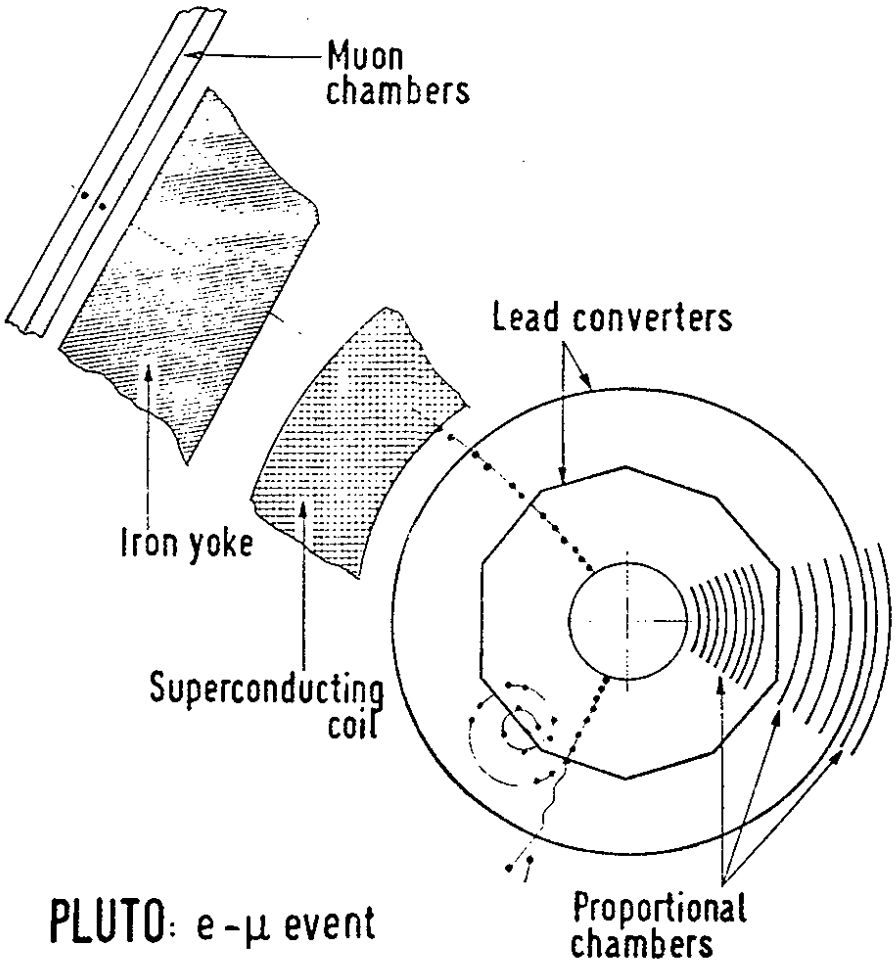

Fig. 5.1 μe event in the PLUTO detector

contributions from several background sources for muons:

cut:	background source	
$\Delta\phi > 10^0$	cosmics, $e^+e^- \to \mu^+\mu^-$	) 2-prongs
missing mass $M^2 > 0.11$ s	$ee \to \mu\mu\gamma$ (see Fig. 3.6)	)
$M(\mu + 1 \text{ track}) \neq M(J/\psi)$	$ee \to J/\psi + x$, $J/\psi \to \mu^+\mu^-$	multi-prongs

Muon events were observed in the channels listed in table 5.2. The μe channel (5.1) is a subchannel of (5.2). Fig. 5.1 shows a 'μe' event in the PLUTO detector. The background comes from (i) hadron lepton misidentification, in all

Table 5.2 Events found in the μ-search, and the expected background contributions.

	Channel	Events	Background
(5.1)	$\mu^- + e^+$ + 'nothing'	22	1.9
(5.2)	μ + 1 prong + any neutrals	273	52
(5.3)	μ + ≥ 2 prong + any neutrals	317	207

three reactions, (ii) from $ee \to \mu\mu\gamma\gamma$ in reaction (5.2), (iii) from $ee \to ee\mu\mu$ in reactions (5.1 and 5.3). The 'hadron' background (i) has been determined experimentally from corresponding hadronic events using the hadron-lepton misidentification probabilities [507]. The higher order QED background (ii and iii) has been calculated [508]. The QED background is smaller, typically less than half the 'hadron' background.

In Fig. 5.2 we show the observed inclusive μ momentum distribution at W = 5 GeV, for the 2 prong and the multiprong events, together with the expected background from hadron-muon misidentification. This figure shows that the (expected) background is substantially smaller than the observed numbers, typically 15%. Out of the 22 μe events in reaction (5.1) only 1.9 ± 0.5 are expected to be background due to hadron lepton misidentification.

Fig. 5.3 shows the differential cross section $d\sigma/dp_\mu$ after all background subtractions and acceptance corrections. The curves will be discussed in section 5.2.3. In Fig. 5.4 the electron momentum distribution of the μe events at all CMS energies is shown. The corrected total cross section, at $p_\mu > 1.0$ GeV/c, is shown in Fig. 5.5 for reactions (5.1 - 5.3). All 3 channels show a threshold behavior consistent with the pair production of a heavy spin 1/2 particle.

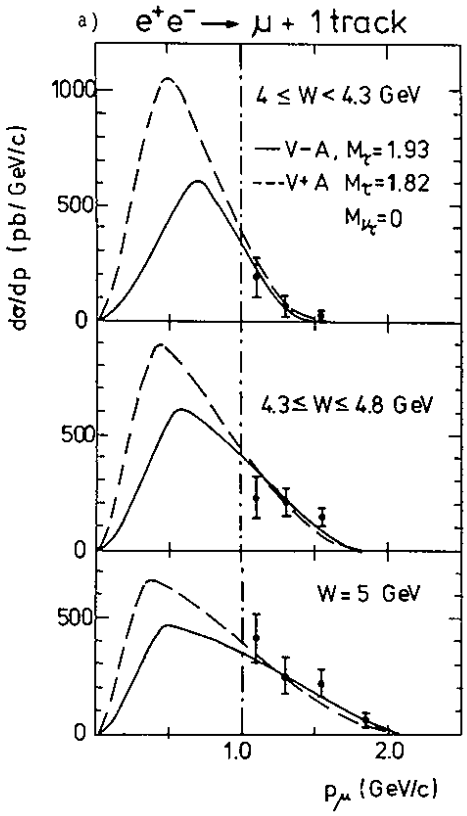

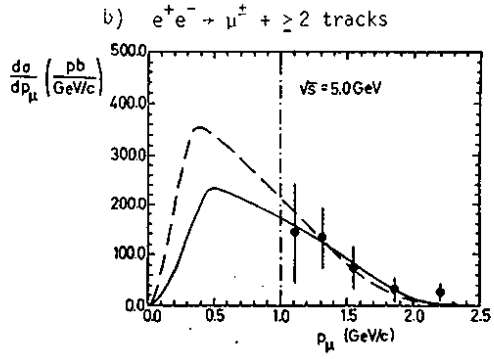

Fig.5.3 Differential cross section dσ/dp for muons (a) from 2-prong and (b) from multiprong events, corrected for acceptance, with QED contributions subtracted. Curves show the expectation for the standard model with V-A (full line) and V+A (broken line) decay interaction (see fit described in the text).

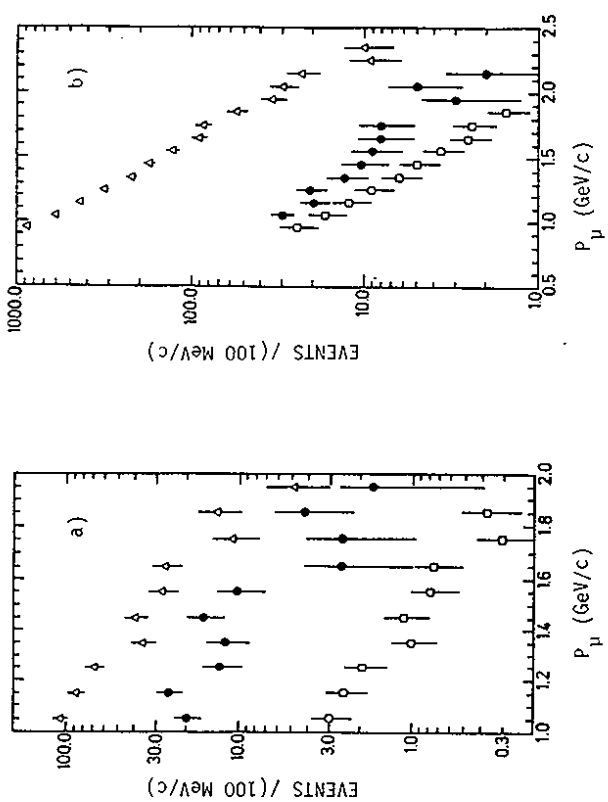

Fig. 5.2 Momentum distribution of muons (circles), hadrons (triangles) and the hadron punch through (squares) at W = 5 GeV; (a) from 2-prong and (b) from multiprong events.

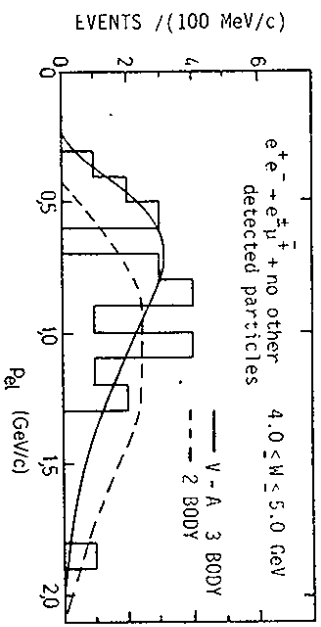

Fig. 5.4

Momentum distribution of electrons from μe events. Curves show the expectation for a V-A 3-body decay (full line) and for a 2-body decay (broken line) of a 1.9 GeV particle, including detection efficiency.

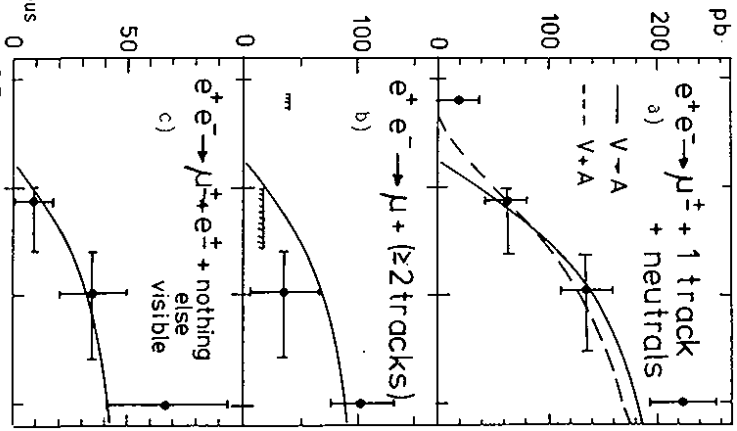

Fig.5.5

Cross section for production of muons with momenta $p > 1$ GeV/c, at various CMS energies, in (a) 2-prong events, (b) multiprong events and (c) μe events. Cross sections are corrected for acceptance and particle identification efficiencies. QED expectations are subtracted. Curves are from the fit described in text.

Cross section σ (pb) for $p_\mu > 1$ GeV/c

5.2.2 μe events from charm?

Can the μe events be explained 'conventionally' by charmed meson production and decay? Real 'μe + nothing' events can come from $D^+D^- \to \mu^+(e^+)\nu + e^-(\mu^-)\bar{\nu}$. This decay mode can safely be ruled out from the numbers in table 5.2. As in the leptonic decays of $\pi^\pm$ and $K^\pm$, the $D \to e\nu$ decay is severely suppressed relative to the $D \to \mu\nu$ decay, leading to $B(e\nu) = 2 \cdot 10^{-5} \cdot B(\mu\nu)$. Therefore we would expect many more 'μμ + nothing' events which would contribute to channel (5.2). The 273 events observed in channel (5.2) imply a conservative upper limit of 0.01 real 'μe + nothing' events from charm.

Appearant 'μe + nothing' events can come as contamination from charm events where the electron and the muon [+] originate from semileptonic decays. These events have additional photons or charged tracks. 2 ± 3 μe events of this type were found. They can be used to determine an upper limit on the amount of charm μe events were the additional photons or charged particles escaped detection. The result depends on the number of additional particles involved. The most conservative limit is achieved for the charm channel with the smallest number of additional observable particles. Assuming the 'elastic' production reaction $e^+e^- \to D^+D^-$ with the decay $D \to e(\mu)K^0\nu$ we expect to observe less than 2 'μe + nothing' events as partners of the observed 'μe + something' events, at 95% c.l. .

Therefore charm production was clearly ruled out to explain the 20.1 μe events. This was the cleanest evidence at that time that a new phenomenon different from charm production was observed in the μe events. Later, the observation of τ production below charm threshold [510, 512] confirmed this result in a particularly obvious way.

5.2.3 Results on Heavy Lepton Parameters

The data obtained in the analysis of reactions (5.1 - 5.3) can consistently be described in terms of the production and decay of a pair of sequential heavy leptons. For determining branching rations the τ production cross section and

---

[+] The leptonic width $\Gamma(D \to \mu\nu)$ is much smaller than the semileptonic width, by almost 2 orders in magnitude, for D-masses of ~1.8 GeV [509].

acceptance corrections were calculated with the following assumptions: τ pairs are produced like pointlike spin 1/2 particles, and they decay leptonically ($\tau \to \nu_\tau l \bar{\nu}_l$) by the standard V-A (or V+A) weak interaction, with a massless τ neutrino ν_τ. The following results were found [505, 506, 507] by a fit (see curves in Figs. 5.2 - 5.5).

	V-A		V+A			
M_τ	= 1.93	±0.05	1.82	±0.08	GeV	(5.4a)
B ($\tau \to$ 1 prong)	= 70	± 10%				(5.5a)
B ($\tau \to$ multiprong)	= 30	± 10%				(5.5b)
B_μ($\tau \to \mu\nu\nu$)	= 15	± 3%	19	± 4%		(5.6)
B_e($\tau \to e\nu\nu$)	= 15	± 5%	12	± 5%		(5.7)
χ^2/ND	= 7.5/8		11.7/8			

All branching ratios agree well with the predictions for a sequential heavy lepton of this mass [504] as listed in table 5.1. In particular the values of B($\mu\nu\nu$) and B($e\nu\nu$) were a further confirmation of the sequential lepton hypothesis which predicts both to be equal, in contrast to the paralepton picture [511], where the τ^+ has the lepton quantum number of $e^-(\mu^-)$ and requires no τ neutrino. Here the decay $\tau^- \to \nu e^- (\mu^-)$ is larger by a factor of 2 relative to the other modes. Also the possibility of a τ neutrino with neutron mass ('baryonic' τ) is inconsistent with the data. A V-A weak interaction is favoured, but a V+A type is not excluded.

The τ mass (5.4a) was determined from the threshold behaviour of the τ pair production cross section (Fig. 5.5). Unfortunately the acceptance for τ events drops to zero for the muon channels (5.1 - 5.3) at W ≈ 4 GeV, i.e. above the threshold energy, because of the momentum cut of $p \geq 1.0$ GeV/c for muon identification. By using identified electrons [512, 513] as a handle to select τ events also the data at W = 3.6 GeV could be used to search for τ events. In a later analysis [512] 6 $\tau\bar{\tau}$ events were found at W = 3.6 GeV. Fig. 5.6 shows the cross section for 2 prong events without photons. A determination of the τ mass from this data yields

$$M_\tau = 1.75 \pm 0.05 \text{ GeV} \qquad (5.4b)$$

in good agreement with the present world average of $M_\tau = 1.784 \pm 0.004$ GeV [514].

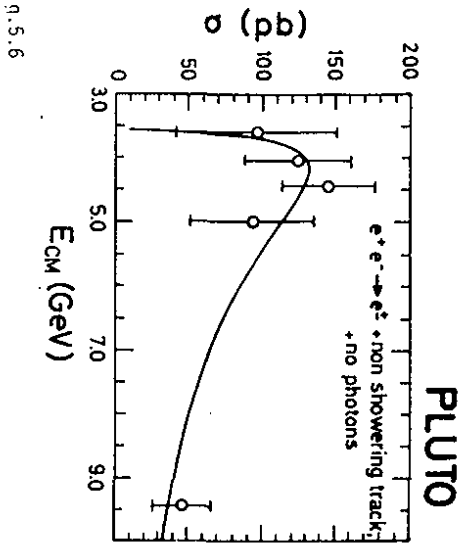

Fig.5.6 Cross section for 2-prong events with one electron and no photons, at various energies, corrected for acceptance and efficiency. The curve shows $\sigma_{\tau\tau} \cdot B(e\nu\nu)$. B(1 prong (not electron), no photons) = $\sigma_{\tau\tau} \cdot 0.039$ (see text), for $M_\tau = 1.782$ GeV.

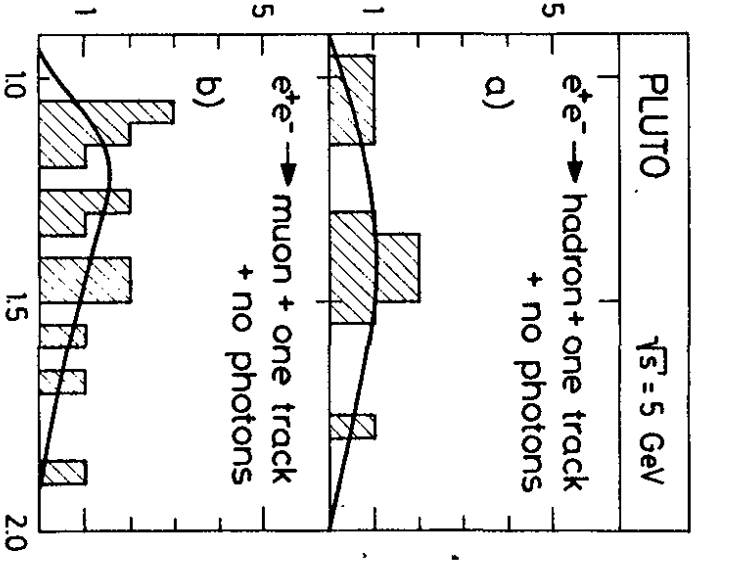

Fig.5.7 Momentum distribution of hadrons (a) from events of sample (5.11a), the [illegible] candidates for $\tau \to \nu\nu$ decay and of muons (b) in the control sample (5.11c). The curves show the spectra expected for V-A coupling.

From data taken after installation of shower counters the branching ratio for a subchannel of eq. (5.5a) could be determined (using $B(\tau \to \nu e \nu) = 17.5\%$):

$$B(\tau \to 1 \text{ prong (not electron)} + \text{no photons}) = 22.3 \pm 4.3\% \qquad (5.8)$$

which agrees with the predictions [504] for the combined branching ratios of the $\tau \to \nu\pi$ and $\tau \to \nu\mu\nu$ decay modes, as given in table 5.1. The latter decay fraction was also determined from the PETRA data [528, 529] to

$$B(\tau \to \mu\nu\nu) = 17.8 \pm 2.0 \text{ (stat.)} \pm 1.8 \text{ (syst.)} \qquad (5.6b)$$

5.3 The Hadronic Decay Modes of the τ

The sequential lepton hypothesis implies several (semi-) hadronic decay modes for the τ particle. The decay $\tau^- \to \pi^- \nu_\tau$ is an inversion of the decay $\pi^- \to \mu^- \nu_\mu$, and can be predicted without further assumptions. Using the CVC hypothesis the decay $\tau^- \to \nu\rho^-$ can be calculated and with Weinberg sum rules the decay mode $\tau^- \to \nu A_1^-$ was evaluated. The predicted branching ratios as evaluated for a τ mass, of m = 1.784 GeV [514] are listed in table 5.1. Also the widths relative to $\Gamma(e\nu\nu)$ are included since these ratios are not affected by changes in other decay channels.

The Cabbibo allowed semi-hadronic decay modes are sizeable and have, apart from the "continuum mode", clear final state signatures. The first specific hadronic decay mode identified at all was the $\tau \to \nu\rho\pi$ decay as reported by the PLUTO collaboration [515] in 1977. The 'crucial' decay $\tau \to \nu\pi$ was found in 1978 [516, 517].

5.3.1 The decay $\tau \to \nu\pi$

The width of this decay mode is uniquely given by the width of the $\pi \to \mu\nu$ decay [504]:

$$\Gamma(\tau \to \nu\pi) = \Gamma(\pi \to \mu\nu) \cdot \frac{M_\tau^3}{2 M_\pi M_\mu^2} \left(1 - \frac{M_\pi^2}{M_\tau^2}\right)^2 \cdot \left(1 - \frac{M_\mu^2}{M_\pi^2}\right)^{-2} \qquad (5.9)$$

The first preliminary result on a search for this decay was communicated by the DASP collaboration in summer 1977 [518] and indicated a substantial suppression of this decay mode. It was not before summer 1978 that this decay could be established and quantitatively measured. The measurement was first

published by the PLUTO collaboration [516], and briefly later by the DELCO [517] collaboration.

5.3.1.1 Event selection

The $\tau \to \nu\pi$ decay was looked for in events of the type

$$e^+e^- \to \tau\,\tau \;\begin{cases} \to \nu + \pi \\ \to \nu + (\nu e,\ \nu\mu,\ \pi) \end{cases} \qquad (5.10)$$

For this purpose we selected 2-prong events with no converted photons, a large missing mass, and one track being a hadron candidate. A track was a hadron candidate if it was in the acceptance for electron and muon identification. It was accepted as hadron if neither the electron nor the muon criteria (see section 3) were met. The inefficiency for electron identification was $(15 \pm 5)\%$, and for μ identification 2%.

To suppress background from ee, eeγ, $\mu\mu\gamma$, $\pi^+\pi^-\pi^0$, $\pi^+\pi^-\gamma$ final states, candidate events were required to have a missing mass of $MM^2 > 0.11 \cdot s$, an azimuthal angle difference between the two tracks of $10^0 < \Delta\phi < 170^0$ (acoplanar events), and an opening angle of $\cos\theta_{12} > -0.70$ (acolinear events).

The hadron candidate sample was split into 3 subsamples:

(a)	$e^+e^- \to$ hadron + charged track + no photon	(5.11)
(b)	$\to$ electron + charged track + no photon	
(c)	$\to$ muon + charged track + no photon	

Sample (a) contains the events of the reaction in question (5.10). Samples (b) and (c) were used to measure the background in sample (a) from e, μ identification inefficiency. Also events of the type

(d)	$e^+e^- \to$ hadron + charged track + photons	(5.11)

were selected to measure the contribution from events with unobserved photons in channel (a). Since sample (d) had sizeable contributions at $\cos\theta_{12} > 0.3$, this interval was also removed in all samples. Channels (b,c,d) contaminate sample (a) with 6.6 ± 0.7 events. In addition we expect 2.3 ± 0.7 events from $\tau \to \nu\rho$ decays without observed photons. Other contributions to sample (a) from 4-prong events, or from $\tau \to \nu(\pi\rho)$ 1 prong decays or from $\tau \to \nu K$ are negligible.

5.3.1.2 Evidence for $\tau \to \nu\pi$

In total 32 events were found in sample (a) after all cuts, and 8.9 ± 1.0 events were expected as background. The 32 events represent an excess of more than 5 s.d. The kinematic properties of the hadrons in sample (a) are consistent with reaction (5.10). The hadron momentum distribution agrees with the expectation for this process, as shown in Fig. 5.7 for the 5 GeV data. Also, the momentum cut for hadron selection does not accept τ pair events produced at $W = 3.6$ GeV, and no candidate events were found at this energy. The $\tau \to \nu\pi$ decay mode has thus been established.

5.3.1.3 Branching ratio

The detection efficiency of our event selection for reaction (5.10) has been determined under the assumption of V-A weak decay interaction and $m_\tau = 1.8$ GeV and $m_\nu = 0$. We find an average of the product branching ratio

$$B(\tau \to \nu\pi) \cdot B(\nu + 1 \text{ prong}) = 0.043 \pm 0.012 \qquad (5.12)$$

The 1 prong class contains $\nu\pi$, $\nu\mu$, νe events and a fraction of $\nu\rho^-$ ($\pi^-\pi^0$) where the π^0 induced no showers. This fraction was determined from simulated events to amount to $B(\nu e\nu)/3$ giving $B(\nu + 1 \text{ prong}) = 2.33\, B(\nu e\nu) + B(\nu\pi)$. With this value eq. (5.12) leads to

$$B(\nu\pi) = (9.0 \pm 2.9 \pm 2.5)\% \qquad (5.13)$$

in good agreement with the value of 9.4% derived from eq. (5.9). The second error is for systematic uncertainties.

5.3.2 The decay $\tau \to \nu\rho^0\pi$

As a further manifestation of the axial weak current the decay $\tau \to \nu A_1$ was predicted [504]. The PLUTO experiment has observed $\tau \to \nu\rho\pi$ decays, where the $\rho\pi$ system has the spin parity quantum numbers and other properties of the A_1 meson.

5.3.2.1 Event selection

This decay mode was identified in 4-prong events with a lepton and without converted photons [515, 519] :

$$e^+e^- \to \tau\bar{\tau} \begin{cases} \to \nu_\tau\, e\, \nu,\ \nu_\tau\, \mu\, \nu \\ \to \bar{\nu}_\tau\, \pi^+\, \pi^-\, \pi^+ \end{cases} \qquad (5.14)$$

54 events were found in which the 3 pion four-momentum was consistent with reaction (5.14), of which 24.5 events were estimated to be background: 18 from hadron-lepton misidentification and 6.5 from events with additional but unconverted photons. The hadron-electron misidentification probability in this analysis [512,513] was as low as 1.1%, for momenta of $p > 0.4$ GeV and the electron identification efficiency was near 50%.

The $\pi^+\pi^-$ mass distribution shows a clear ρ signal. Fig. 5.8 shows the distribution of both mass combinations possible in each event (open histogram), as well as the distribution of the higher mass combination. The circles indicate the expected background in the open histogram, due to hadron lepton misidentification. Out of 54 events, 40 events had at least one $\pi^+\pi^-$ mass combination in the ρ mass range ($0.68 < M(\pi\pi) < 0.86$ GeV) and 13 were expected as background. The other 14 events - with no ρ mass combination at all - were consistent with the 12 expected background events. In summary we found 27 $e(\mu) + \rho\pi$ events after background subtraction of 13 events.

The hypothesis that the $\rho\pi$ events are due to τ pair production has several further kinematic implications, which we have checked:

1) The electron momentum distribution (Fig. 5.9) is hard and compares well with the expectation for a V-A decay interaction.
2) The 3π system has a laboratory energy distribution which is consistent with the expected uniformity between the limits (Fig. 5.10) for reaction (5.14).
3) The invariant 3π mass (Fig. 5.11) is not correlated with the momentum of the lepton, which comes from the decay of the other τ.

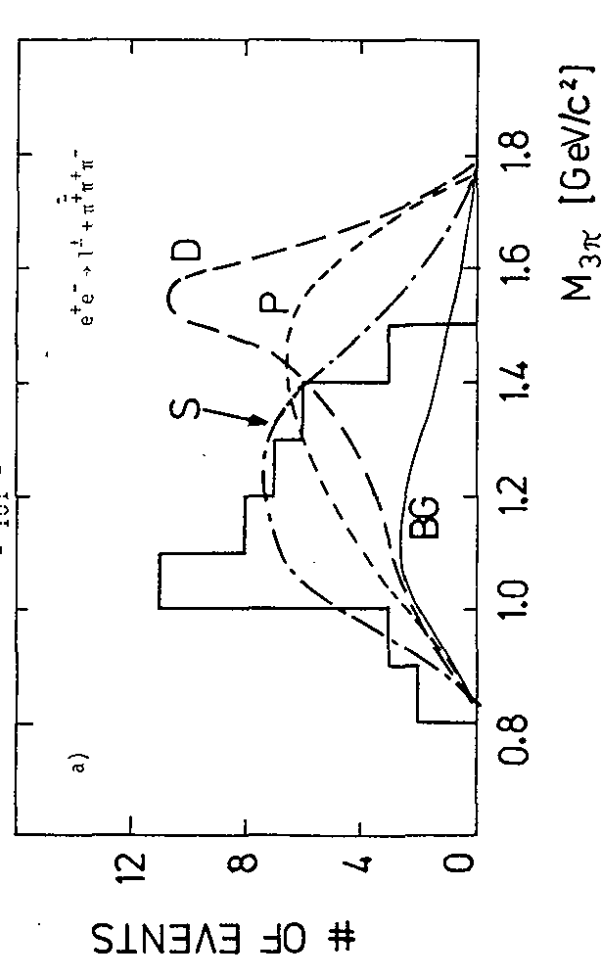

Fig.5.11

Invariant 3π mass distribution from events of reaction (5.14), after ρ-cut. Curves in (a) show the expectation for different partial waves of the $\rho\pi$ system, as indicated. Curves in (b) show the effect of an A_1 Breit-Wigner resonance. All curves are added to the expected background and normalized to the data.

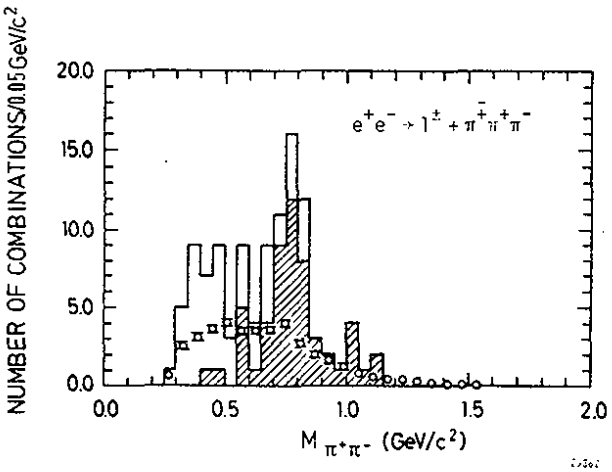

Fig.5.8

Distribution of the $\pi^+\pi^-$ masses (2 combinations per event) from the events of reaction (5.14). The shaded region gives the distribution of the higher mass combination. The circles represent the expected background from hadron-lepton misidentification.

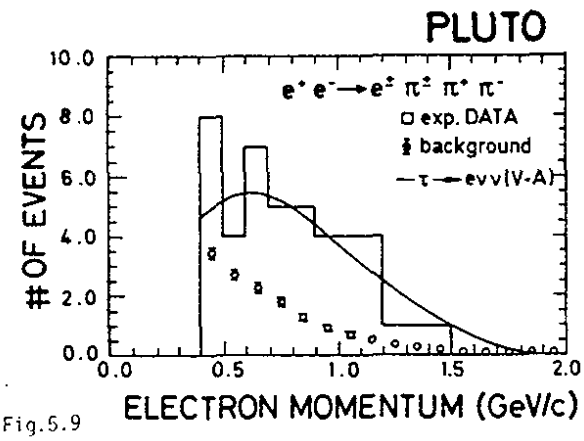

Fig.5.9

Momentum distribution of electrons from events of reaction (5.14). The curve shows the expectation for a sequential lepton, added to the expected background (circles).

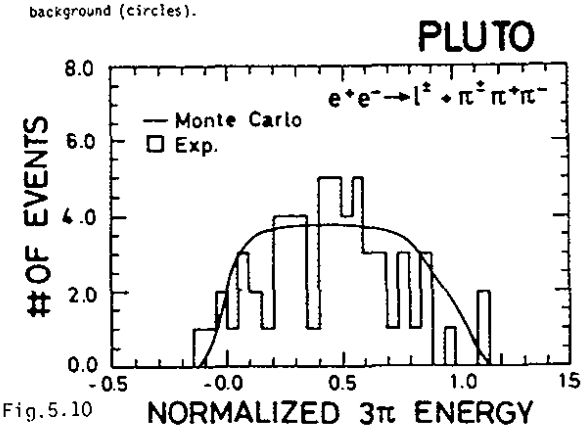

Fig.5.10

Distribution of the normalized energy, $E_3 = (E_{3\pi} - E_{min}) / (E_{max} - E_{min})$ for events of reaction (5.14). The curve shows the expectation for a sequential lepton, including resolution effects.

5.3.2.2 The branching ratio $\tau \to \nu\rho\pi$

The observed event numbers with mass combinations inside and outside the ρ mass band are consistent with 100% $\tau \to \nu\rho\pi$ decay mode. Using the QED production cross section for τ pairs with a τ mass of 1.80 GeV we find the following product branching ratio [519]

$$B(\tau^+ \to \ell^+ \nu \nu) \cdot B(\tau^- \to \nu \pi^- \rho^0) = 0.0093 \pm 0.0023. \qquad (5.15)$$

There is an additional relative systematic error of 16%. With an averaged leptonic branching ratio of $B(\tau \to \ell \nu \nu) = 0.173 \pm 0.013$, and assuming $B(\tau \to \nu \pi^- \rho) = B(\tau \to \nu \pi^0 \rho^-)$ we find

$$B(\tau \to \nu \pi \rho) = (0.108 \pm 0.026 \pm 0.021) \qquad (5.16)$$

The second error accounts for the systematic uncertainties.

The theoretical prediction [504] for the νA_1 decay of a sequential heavy lepton, of $B(\tau \to \nu A_1) = 0.094$, is in good agreement with the observed $\nu\rho\pi$ decay fraction.

We can determine an upper limit for a decay into 3 uncorrelated pions

$$\tau \to \nu \pi \pi \pi$$

from the fraction of events with no ρ combination. We find at 95% C.L.

$$\frac{\Gamma(\tau \to \nu + (3\pi \text{ uncorrelated}))}{\Gamma(\tau \to \nu + \tau\rho) + \Gamma(\tau \to \nu + (3\pi \text{ uncorrelated}))} < 0.20 \qquad (5.17)$$

This result rules out the hypothesis that the decay $\tau \to \nu\, 3\pi$ may be dominated by a contact term type diagram in the τ decay leading to 3 direct pions [520].

5.3.2.3 Spin parity of the ρπ system

If the ρπ system emerges from a weak decay it can carry the spin parity quantum numbers $J^P = 1^+$ (axial current) or 0^- (divergence of the axial current). The quantum numbers 2^- and 2^+ do not agree with the sequential nature of the τ, since they cannot emerge from a V-A decay. The state 1^- in $(\rho\pi)^\pm$ violates Bose statistics in an isospin I = 1 state and is therefore quite generally forbidden [521]. All these quantum numbers can be checked since the expected density distribution in the 3π Dalitz plot (Fig. 5.12) is different for various $J^P\ell$ assignments (ℓ = orbital angular momentum of the ρπ system, $P = (-1)^\ell$). We have

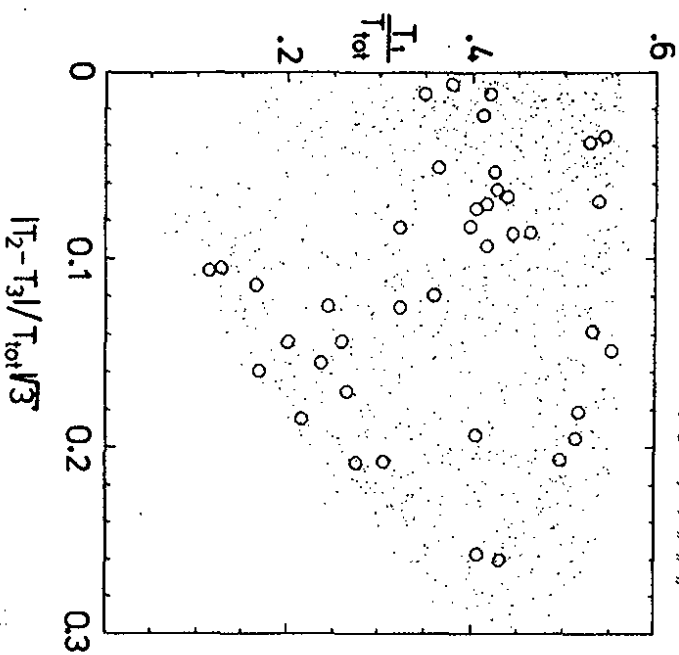

Fig.5.12 Triangle Dalitz plot T_i/T_{tot} vs $|T_2-T_3|/(\sqrt{3}\cdot T_{tot})$ for events of reaction (5.14) after ρ-cut (circles), and for simulated events with $J^P\ell = 1^+1$ (points). T_i are the kinetic energies of the pions, in the 3π rest frame. T_{tot} is the total kinetic energy.

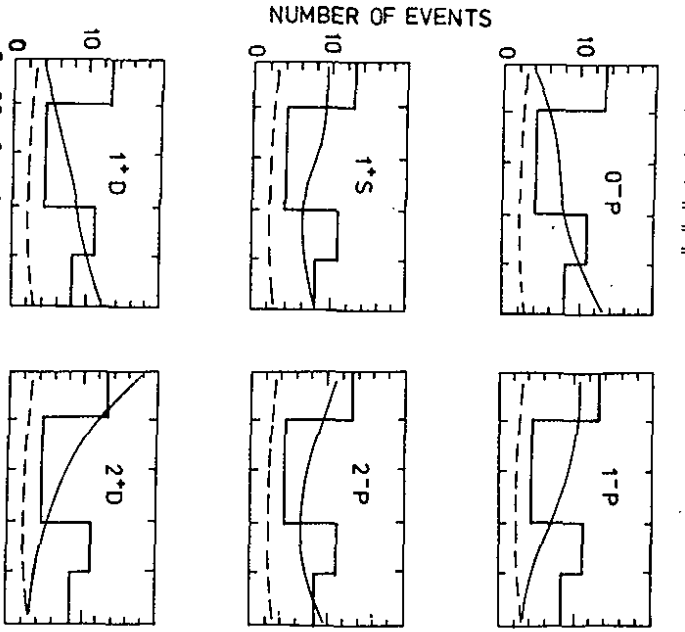

Fig.5.13 Distribution of the relative distance from the Dalitz plot center

$$\lambda = 1 - \frac{(\vec{p}_1 \times \vec{p}_2)^2}{3/4\,(1/9\,M_{3\pi}^2 - m_\pi^2)}$$

with $0 \le \lambda \le 1$. Experimental events (histograms), expected background (dashed line), and the distribution of various spin-parity states (solid lines) added to the background.

determined the probabilities to expect the observed Dalitz plot distribution, for several $J^P\ell$ states, by a likelihood analysis. The likelihood analysis of the Dalitz plot took into consideration the formation of a ρ^0 resonance, and eliminated all influences from the large spread of the $M(3\pi)$ distribution (see Fig. 5.11). This way only the symmetry properties of the different $J^P\ell$ densities [522] were exploited. The background distribution was determined from appropriate background source samples and subtracted from the Dalitz plot. For each $J^P\ell$ assignment we have evaluated the probability that the expected likelihood can be smaller than the measured value [513,519]. The expected likelihood distributions were determined from event samples simulated for each $J^P\ell$ assignment. The results are given in table 5.3.

Table 5.3 Probability to observe the measured distributions for several $J^P\ell$ assignments.

Probability (%)	$J^P\ell = 0^-1$	1^+0	1^+2	1^-1	2^-1	2^+2
3-dim Dalitz plot	<0.3	8.9	<0.7	0.6	3.7	<0.3
λ-distribution	1.6	16.2	<0.6	1.0	18.0	<0.6

In Fig. 5.13 we show the projection of the Dalitz plot distribution on the (normalized) distance from the center ($T_1 = T_2 = T_3$), the so called λ distribution [523], with $\lambda = 0$ at the center and $\lambda = 1$ at the boundary, for any $M(3\pi)$. It is compared to the expectation for the various $J^P\ell$ assignments, with the background expectation added. Table 5.3 gives the probabilities for agreement [512]. Only the axial current signature, $J^P\ell = 1^+0$, and the 2^-1 state are consistent with the Dalitz plot.

A further handle on the ℓ quantum number of the $\rho\pi$ system is provided by the $\rho\pi$ mass spectrum. The expected mass spectra for S, P and D waves [522] are shown as curves in Fig. 5.11a. The P and D waves show significant deviations. For a P-wave $\rho\pi$ system ($J^P\ell = 0^-1$, or 1^-1) in the τ decay we find an upper limit (95% C.L.) of

$$B(\tau \to \nu\rho^0\pi,\ \ell = 1) < 1.6\%. \qquad (5.18)$$

Only the S-wave resembles the experimental distribution.

In conclusion only the $J^P\ell = 1^+0$ assignment for the $\rho\pi$ system is consistent with the data.

5.3.2.4 Is there evidence for $\tau \to \nu A_1$?

The $\rho\pi$ mass spectrum is only marginally described by a τ decay into a non resonating $\rho\pi$ s-wave state (χ^2 probability = 1%). In particular the peak which is shown by the data at $M(\rho\pi) \approx 1.1$ GeV is not reproduced. If however a Breit Wigner resonance is included the peak can be well reproduced for parameters like $0.9 \lesssim M \lesssim 1.2$ GeV and $0.4 \lesssim \Gamma \lesssim 0.5$ GeV, all consistent with the somewhat uncertain A_1 resonance parameters [514]. In Fig. 5.11b we show the curve for M = 1.0 GeV and Γ = 0.475 GeV, which has a χ^2 probability of 44%. The $\rho\pi$ system therefore provides three independent pieces of evidence for an A_1 resonance: (i) the mass spectrum, (ii) the spin parity state and (iii) the τ branching fraction.

5.4 Some limits on τ parameters

5.4.1 Limit on the lifetime

Since in τ pair production by colliding beams the laboratory momenta of the τ's are known, in each event a finite lifetime T can be converted into a decay length d

$$d = T \cdot (P_\tau / M_\tau) \cdot c \qquad (5.19)$$

A finite decay length can be directly observed as a deviation of the intersecting point of the 3 pions in $\tau \to \nu\ 3\pi$, from the e^+e^- beam collision point, or indirectly as a broadening of the origin of single μ tracks from $\tau \to \mu\nu\nu$ decays, in the $r-\phi$ plane.

If the τ is a sequential lepton its lifetime T_τ^S is related to the μ lifetime T_μ by [504]

$$T_\tau^S = B(\tau \to \ell\nu\nu) \cdot \left(\frac{M_\mu}{M_\tau}\right)^5 \cdot T_\mu \qquad (5.20a)$$

which yields $T_\tau^S = 2.6 \cdot 10^{-13}$ sec.

In the PLUTO experiment we have $\langle E_\tau \rangle \approx 2.25$ GeV and expect an average decay length of 0.07 mm. This is clearly below the resolution. The average minimal distance of single direct tracks from the beam line is $\sigma(r_{min}) = 2.8$ mm in the $r-\phi$ plane, because of beam width, multiple scattering and tracking resolution.

From our 2 prong and 4 prong τ pair events we have determined [524] an upper limit of the τ lifetime of

$$T_\tau < 9 \cdot 10^{-12} \text{ sec} = 35 \cdot T_\tau^S \quad [95\% \text{ c.l.}] \qquad (5.20b)$$

This result excludes models where the τ neutrino is heavier than the τ and the τ decays through mixing of ν_τ with μ and e neutrinos, since from experimental limits on violation of μ-e universality, limits on the mixing parameters can be inferred leading to a predicted lifetime of $T > 50\ T_\tau^S$ [525].

5.4.2 Limit on the τ neutrino mass

The best value that can be inferred from the PLUTO data came from the decay mode $\tau \to \nu + 3\pi$:

$$M_\nu^2 = (E_\tau - E_{3\pi})^2 - (P_\tau^2 + P_{3\pi}^2) + 2P_\tau P_{3\pi} \cdot \cos\theta_{\tau,3\pi} \qquad (5.21)$$

The only unknown quantity here is the decay angle $\theta_{\tau,3\pi}$. Choosing the maximum value $\cos\theta = 1$ in each event we find [526]

$$M_\nu < 360 \text{ MeV} \qquad (5.22)$$

at 95% c.l.

5.4.3 Limit on the τ charge radius

The energy dependence of the τ cross section measured from threshold to $s = 1000\ \text{GeV}^2$ (see Figs. 5.6 and 4.6) excludes spin values of $j = 0$, 1, and 3/2 [504a], and agrees very well with $j = 1/2$. Using QED production cross section for spin 1/2 pairs (see section 4), and allowing for extended τ leptons in the QED formulae, we find from the total τ pair cross section at $W \approx 31$ GeV an upper limit on the τ charge radius of

$$\langle r^2 \rangle^{1/2} < 6 \cdot 10^{-13} \text{ cm} \qquad (95\% \text{ c.l.}] \qquad (5.23)$$

This limit is of the same magnitude as the present limits for μ and e leptons (see section 4.4).

5.5 Search for leptons heavier than the τ

Since the QED cross section for the pair production of point like spin = $^1/_2$ heavy leptons L in e^+e^- annihilation is well known to be

$$\frac{\sigma(L\bar{L})}{\sigma(\mu\bar{\mu})} = R(L\bar{L}) = \sqrt{1 - \frac{M_L^2}{E^2}} \cdot \left(1 - \frac{M_L^2}{2E^2}\right) \qquad (5.24)$$

we can perform a clear cut investigation on the existence of a heavy lepton with a mass M_L heavier than the τ mass, up to some mass limit very close to the maximum beam energy.

There are no firm predictions on the existence of a fourth lepton doublet, or on a fourth quark-lepton generation, but there are some speculations on its mass value [527], in the range of ~10 to 22 GeV. With the data from PETRA some of these speculations can be ruled out.

Here we describe our search [528, 529] for such a new heavy lepton in the mass range $M_\tau < M_L < 15$ GeV, assuming decays mediated by the standard weak current. For a mass of $M_L \sim 14$ GeV we expect [504] branching ratios of 10% for each $e\nu$, $\mu\nu$ and $\tau\nu$, and of 35% for $u\bar{d}$, and for $c\bar{s}$ current transitions.[+] Appropriate event selection criteria, and their respective efficiencies in the 2 steps of the search described below have been determined from simulated heavy lepton events, with masses of M_L = 4, 6, 10, 12, 14 and 14.5 GeV, at W = 30 GeV. The fragmentation of the quarks was treated according to the prescription of Feynman and Field [530], with an appropriate inclusion of c-quarks. The search was done separately for the 'low' mass range ($M_\tau < M_L < 10$GeV) and for the 'high' mass range (10 GeV $< M_L < E_B$) making use of different topological properties. For the search we used the data taken in the energy range of $30 \leq W \leq 31.6$ GeV.

[+] For simplification we included the small contributions from currents which mix quark generations, into the $u\bar{d}$ and $c\bar{s}$ branching ratio.

5.5.1 Search for 'low' mass leptons: $M_\tau < M_L < 10$ GeV

The τ event selection chain (see section 4) has an acceptance for heavy leptons in this mass range through the multiprong category which is similar in size as for the τ itself. Fig. 5.14 shows as a function of M_L the number of expected heavy lepton multiprongs relativ to the observed τ multiprongs. The number of observed τ multiprongs, (20 ± 4.8), agrees with the expected QED rate of 21 events. For a heavy lepton with $m_L \leq 10$ GeV we would expect an excess of events beyond the observed τ yield by more than 2 s.d. . This excludes the production of a new heavy lepton pair with a mass $m_L < 10$ GeV at the 95% conficence level, or better.

5.5.2 Search for 'high' mass leptons: $10 \text{ GeV} < M_L < E_B$

At these high masses heavy lepton pairs will be accepted by the criteria for multihadron events from e^+e^- annihilation into quark pairs, if at least one of the two leptons has a hadronic decay mode (~90% of all events). Their topology, however, will be different from $q\bar{q}$ multihadron events in the following respects:

(i) because of the high mass M_L the velocity of the new lepton is small, and the thrust T of these events will be lower;

(ii) because of missing neutrinos there is a larger momentum imbalance. To account for track's lost near the beam direction, we consider the missing momentum perpendicular to the beam, normalized to the sum of all measured momenta: $x_\perp = |\Sigma \vec{p}_\perp| \,/\, \Sigma|\vec{p}|$

(iii) in a subset of ~20% of $L\bar{L}$ events we expect a final state of the type

$$(\mu\nu\nu) + (\nu + \text{hadrons}) \qquad (5.25)$$

with an isolated high momentum muon.

(iv) in subset (iii) the multiplicity will be lower.

We have searched for $L\bar{L}$ events by requiring (i) $T < 0.95$, (ii) $x_\perp > 0.3$, (iii) a muon with momentum $p > 1.4$ GeV/c and no other track nearer than 20^0, and (iv) the number of charged tracks in the range $2 \leq n_{CH} \leq 12$.

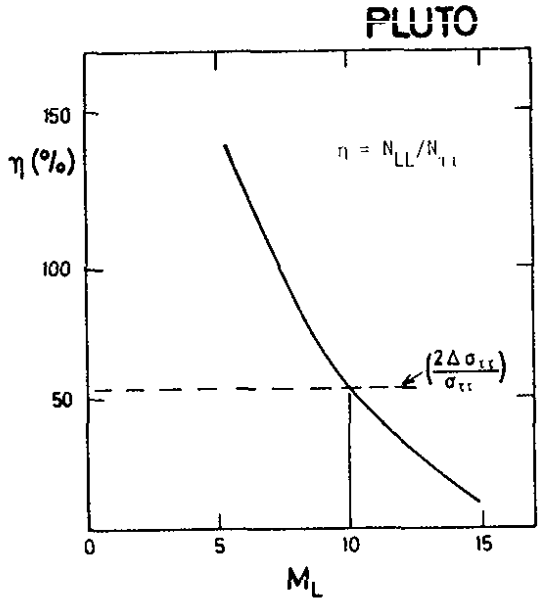

Limits on the mass M_L of a new sequential heavy lepton L with standard coupling to leptons and quarks;
(a) expected ratio for ('observed') 4-prong events, $N_{LL}/N_{\tau\tau}$, as solid curve. The dashed line indicates the 2 standard deviation limit of this ratio from a statistical fluctuation in the τ yield, $2 \cdot \Delta N_{\tau\tau}/N_{\tau\tau}$, with $N_{\tau\tau}$ the QED expectation.
(b) 95% c.l. upper limit of the number of heavy lepton events with at least one detectable muon (dashed line). The shaded band is the expected signal as a function of heavy lepton mass from the Monte Carlo program. The event selection cuts are described in the text.
(c) Potential lepton signal with multihadronic decays (dash-dotted line with 2σ error limits); the shaded band is the expected signal as a function of heavy lepton mass from the Monte Carlo program. The width of the band indicates the statistical error plus the systematic uncertainty of the Monte Carlo simulation.

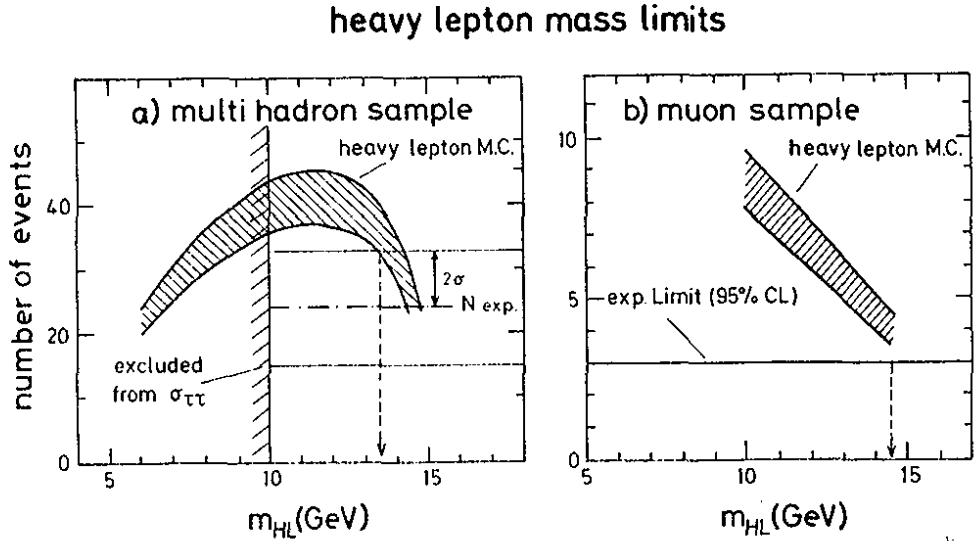

Fig. 5.14

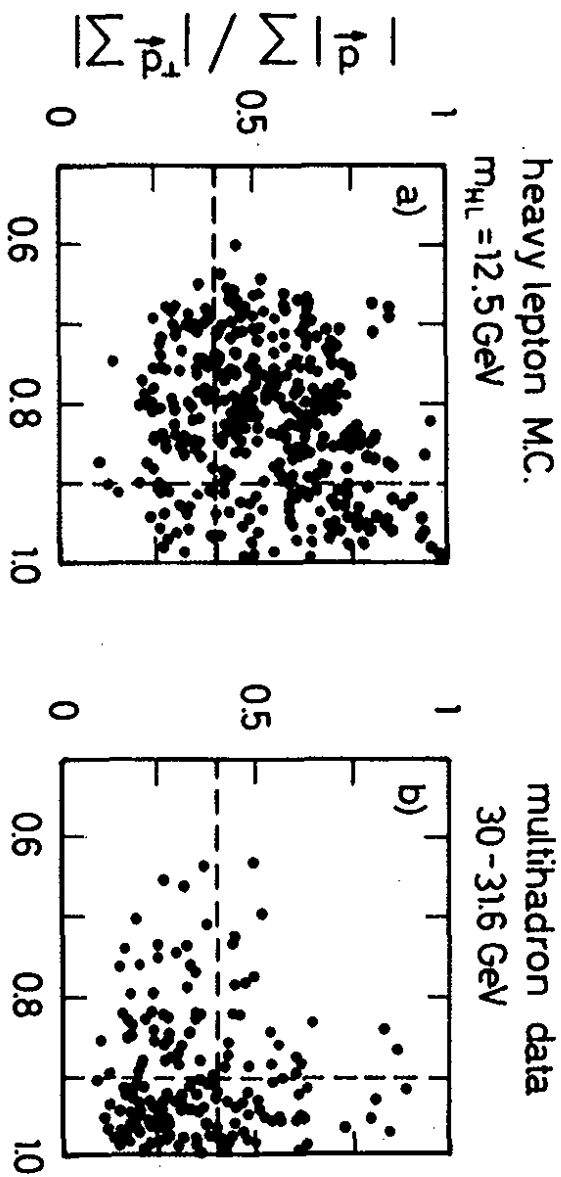

Fig.5.15 Sum of the normalized transverse momenta vs. the thrust for charged particles from multiparticle final states. a) Heavy lepton Monte Carlo (M_L = 12.5 GeV); b) data at E_{cm} = 30 - 31.6 GeV. $P_\perp$ is measured relative to the beam axis. The events were selected with the excess of positive charged tracks < 3 and the total energy > 3 GeV.

The discriminating effect of cuts (i) and (ii) is shown in Fig. 5.15, where we plot $x_\perp$ vs. T for simulated heavy lepton and real (multihadron) events. We found no real event passing the criteria (i - iv). The number of heavy lepton events expected to pass these criteria is shown in Fig. 5.14b, as a function of M_L. At M_L = 14.5 GeV we expect 4 ± 0.5 such events. Therefore we can exclude the existence of heavy sequential leptons with masses

$$M_L \leq 14.5 \text{ GeV} \qquad (5.26)$$

at a confidence level of 95%.

A similar analysis was performed with a larger sample of events which was selected without asking for a muon, but by stronger cuts on thrust (T < 0.90) and missing transverse momentum ($x_\perp > 0.4$), excluding all $M_L < 13.5$ GeV. Therefore, our conclusions change little if the ratio of leptonic to hadronic decay fractions of the heavy lepton L changes. Similar limits have been found in the other PETRA experiments [531].

5.6 Summary on heavy leptons +

(1) The PLUTO experiment has confirmed the evidence for the new heavy lepton τ through the observation of a very clean sample of μ-e events, for which an explanation by charm production was definitely ruled out.

(2) Significant evidence for the sequential nature of the τ lepton was provided by
(i) measuring both of the leptonic branching ratios, in agreement with the prediction and confirming their equality
(ii) the first observation and measurement of a specific hadronic decay mode, $\tau \to \nu\rho^0\pi$, the rate and kinematic properties of which agree with the predicted decay $\tau \to A_1$

and finally by

(iii) the measurement of the decay mode $\tau \to \nu\pi$, with a coupling strength in agreement with the inverse decay $\pi \to \nu\mu$.

+ For a complete summary on the present knowledge on the τ we refer to recent review papers [532] and to the compilations of the particle data group [514].

None of the many details of the observed decay modes deviates from the sequential lepton picture.

(3) The pointlike nature of the electric charge of the τ lepton was probed to be valid down to $< 6 \cdot 10^{-16}$ cm, comparable to the respective limits of μ and e leptons.

(4) There is no further sequential heavy lepton in the mass range $M_\tau < M_L \leq 14.5$ GeV.

References

501 M.L.Perl et al., Phys.Lett. 63B (1976) 466

502 a M.L.Perl et al., Phys.Rev.Lett. 35 (1975) 1489
b H.Cavalli-Sforza et al., Phys.Rev.Lett. 36 (1976) 558

503 S.L.Adler, Phys.Rev. 177 (1969) 2426; J.S.Bell and R.Jackiw, Nuovo Cim. 51 (1969) 47; C.Bouchiat, J.Illiopoulos and Ph.Meyer, Phys.Lett 38B (1972) 519; D.J.Gross and R.Jackiw, Phys.Rev. D6 (1972) 477

504 a Y.S.Tsai, Phys.Rev. D4 (1971) 2821; and SLAC PUB 2105 (1978)

b H.B.Thacker, J.J.Sakurai, Phys.Lett. 36B (1971) 103

505 PLUTO Coll., J.Burmester et al., Phys.Lett. 68B (1977) 301

506 PLUTO Coll., J.Burmester et al., Phys.Lett. 68B (1977) 297, and H.Meyer in Proceedings of the Orbis Scientiae (Coral Gables Conference 1977), DESY 77/19

507 M.Rössler, Thesis (1977), University of Hamburg, and DESY F14-78/01

508 F.Gutbrod, Z.J.Rek, Z.Physik C1 (1979) 171, and private communication

509 M.K.Gaillard, B.W.Lee and J.L.Rosner, Rev.Mod.Phys. 47 (1975) 277

510 DASP Coll., R.Brandelik et al., Phys.Lett 73B (1978) 109; DELCO Coll., W.Bacino et al., Phys.Rev.Lett. 41 (1978) 13; DESY-HD Coll., W.Bartel et al., Phys.Lett. 77B (1978) 331

511 J.D.Bjorken and C.H.Llewellyn Smith, Phys.Rev. D7 (1973) 887

512 E.Lehmann, Thesis (1980). University of Hamburg, and internal report DESY-PLUTO 81/02

513 W.Wagner, Thesis (1978), RWTH Aachen, and PITHA 78/01

514 Particle Data Group, Rev.Mod.Phys. 52 (1980)

515 PLUTO Coll., G.Alexander et al., Phys.Lett. 73B (1978) 99, and G.Knies, Proc. of the 1977 Intern.Symp. on Lepton and Photon Interactions at High Energies, Hamburg (1977)

516 PLUTO Coll., G.Alexander et al., Phys.Lett. 78B (1978) 162

517 W.Bacino et al., Phys.Rev.Lett. 42 (1979) 6

518 S.Yamada, Proc. of the 1977 International Symp. on Lepton and Photon Interactions at High Energies, Hamburg (1977)

519 PLUTO Coll., W.Wagner et al., Z.Physik C3 (1980) 193

520 H.Goldberg, R.Aaron, Phys.Rev.Lett. 42 (1979) 339

521 F.Gutbrod, private communication

522 W.R.Frazer, J.R.Fulco and F.R.Halpern, Phys.Rev. 136B (1964) 1207 and N.Kawamoto, Z.Rek, private communication

523 R.H.Dalitz, Phil.Mag. 44 (1953) 1068

524 PLUTO Coll., G.Alexander et al., Phys.Lett. 81B (1979) 84

525 H.Fritzsch, Phys.Lett. 67B (1977) 451
D.Horn and G.G.Ross, Phys.Lett. 67B (1977) 460
G.Altarelli et al., Phys.Lett. 67B (1977) 463
J.F.Donoghue and L.Wolfenstein, Phys.Rev. D17 (1978) 224

526 G.Knies, Proc. of the Sixth Trieste Conference on Particle Physics, Trieste (1978), unpublished

527 T.F.Walsh, Proc. New Phenomena in Lepton-Hadron-Physics, Karlsruhe 1978, 99; S.Iwao Kanazawa University, preprint HPICK-077, Oktober 1979; J.D.Bjorken, SLAC-PUB-2195 (September 1978)
A.O.Barut, Phys.Rev.Lett 42 (1979) 1251

528 PLUTO Coll., Ch.Berger et al., Phys.Lett. 99B (1981) 489

529 Olivia Meyer, Thesis, Wuppertal (1980), WU B 80-32

530 R.D.Field, R.P.Feynman, Nucl.Physics B 136 (1978) 1

531 a Mark J Coll., D.P.Barber et al., Phys.Rev.Lett. 45 (1980) 1904
b TASSO Coll., R.Brandelik et al., Phys.Lett. 92B (1980) 199

532 a G.Flügge, Z.Physik C1 (1979) 121
b J.Kirkby, Proc. of the 1979 Int. Symp. on Lepton and Photon Interactions at High Energies, FNAL (1979) 107
c K.G.Hayes and M.L.Perl, SLAC-PUB-2699 (1981)

Figure captions

5.1 μe event in the PLUTO detector

5.2 Momentum distribution of muons (circles), hadrons (triangles) and the hadron punch through (squares) W = 5 GeV. (a) from 2-prong and (b) from multiprong events.

5.3 Differential cross section $d\sigma/dp$ for muons, (a) from 2-prong and (b) from multiprong events, corrected for acceptance, with QED contributions subtracted. Curves show the expectation for the standard model with V-A (full line) and V+A (broken line) decay interaction (see fit described in the text).

5.4 Momentum distribution of electrons from μe events. Curves show the expectation for a V-A 3-body decay (full line) and for a 2-body decay (broken line) of a 1.9 GeV particle, including detection efficiency.

5.5 Cross section for production of muons with momenta $p > 1$ GeV/c, at various CMS energies, in (a) 2-prong events, (b) multiprong events and (c) μe events. Cross sections are corrected for acceptance and particle identification efficiencies. QED expectations are subtracted. Curves are from the fit described in text.

5.6 Cross section for 2-prong events with one electron and no photons, at various energies, corrected for acceptance and efficiency. The curve shows $\sigma_{\tau\tau} \cdot B(e\nu\nu)$. B(1 prong (not electron), no photons) = $\sigma_{\tau\tau} \cdot 0.039$ (see text), for $M_\tau = 1.782$ GeV.

5.7 Momentum distribution of hadrons (a) from events of sample (5.11a), the candidates for $\tau \to \pi\nu$ decay and of muons (b) in the control sample (5.11c). The curves show the spectra expected for V-A coupling.

5.8 Distribution of the $\pi^+\pi^-$ masses (2 combinations per event) from the events of reaction (5.14). The shaded region gives the distribution of the higher mass combination. The circles represent the expected background from hadron-lepton misidentification.

5.9 Momentum distribution of electrons from events of reaction (5.14). The curve shows the expectation for a sequential lepton, added to the expected background (circles).

5.10 Distribution of the normalized energy, $E_3 = (E_{3\pi} - E_{min}) / (E_{max} - E_{min})$ for events of reaction (5.14). The curve shows the expectation for a sequential lepton, including resolution effects.

5.11 Invariant 3π mass distribution from events of reaction (5.14), after ρ-cut. Curves in (a) show the expectation for different partial waves of the $\rho\pi$ system, as indicated. Curves in (b) show the effect of an A_1 Breit-Wigner resonance. All curves are added to the expected background and normalized to the data.

5.12 Triangle Dalitz plot T_1/T_{tot} vs $|T_2-T_3| / (\sqrt{3} \cdot T_{tot})$ for events of reaction (5.14) after ρ-cut (circles), and for simulated events with $J^P\ell = 1^+1$ (points). T_i are the kinetic energies of the pions, in the 3π rest frame. T_{tot} is the total kinetic energy.

5.13 Distribution of the relative distance from the Dalitz plot center

$$\lambda = 1 - \frac{(\vec{P}_1 \times \vec{P}_2)^2}{3/4\,(1/9\,M_{3\pi}^2 - m_\pi^2)}$$

with $0 \leq \lambda \leq 1$. Experimental events (histograms), expected background (dashed line), and the distribution of various spin-parity states (solid lines) added to the background.

5.14 Limits on the mass M_L of a new sequential heavy lepton L with standard coupling to leptons and quarks;

a) expected ratio for ('observed') 4-prong events, $N_{LL}/N_{\tau\tau}$, as solid curve. The dashed line indicates the 2 standard deviation limit of this ratio from a statistical fluctuation in the τ yield, $2 \cdot \Delta N_{\tau\tau}/N_{\tau\tau}$, with $N_{\tau\tau}$ the QED expectation.

b) 95% c.l. upper limit of the number of heavy lepton events with at least one detectable muon (dashed line). The shaded band is the expected signal as a function of heavy lepton mass from the Monte Carlo program. The event selection cuts are described in the text.

c) Potential lepton signal with multihadronic decays (dash-dotted line with 2σ error limits); the shaded band is the expected signal as a function of heavy lepton mass from the Monte Carlo program. The width of the band indicates the statistical error plus the systematic uncertainty of the Monte Carlo simulation.

5.15 Sum of the normalized transverse momenta vs. the thrust for charged particles from multiparticle final states. a) Heavy lepton Monte Carlo (M_L = 12.5 GeV); b) data at E_{cm} = 30 - 31.6 GeV. $P_\perp$ is measured relative to the beam axis. The events were selected with the excess of positive charged tracks < 3 and the total energy > 3 GeV.

6. Hadron production in the continuum

Hadron production in e^+e^- annihilation is a direct and beautifully simple means of looking for partons, that is for pointlike constituents of the hadrons. The existence of such partons reduces hadron production to the creation of parton-antiparton pairs, and their subsequent fragmentation into hadrons [601, 602]. The parton pair creation is, to lowest order in the fine structure constant α, proportional to the asymptotic muon pair cross section,

$$\sigma_{\mu\mu} = 4\pi\alpha^2 \hbar^2 / 3E_{CM}^2 , \qquad (6.1)$$

multiplied with the square of the parton charge, e_q^2, and a spin factor which at high energies approaches 1 for spin $^1/_2$ partons, or $^1/_4$ if they have spin zero.

In the limit of these asymptotic spin factors the ratio R between the total hadronic and the muon cross section is therefore simply given by the number and charges of the partons as:

$$R = \frac{\sigma(e^+e^- \to \text{hadrons})}{\sigma(e^+e^- \to \mu^+\mu^-)} = \sum_q e_q^2 + \frac{1}{4}\sum_{q'} e_{q'}^2 , \qquad (6.2)$$

where the sum extends over all possible kinds q (flavor, colour) of spin $^1/_2$ partons (or q' in case of spin zero) that contribute to the hadronic final state.

An energy independent ratio R will thus verify that the partons behave indeed pointlike. The value of R provides a test of their multiplet structure.

The following sections will describe the measurement and interpretation of the total hadronic cross section, some effects of a new parton threshold ('charm'), and deal extensively with hadron jets as a particularly impressive manifestation of the underlying parton dynamics.

6.1 The total hadronic cross section

According to the quark-parton model the hadron constituents are fractionally charged spin $\frac{1}{2}$ quarks occurring in n_F flavours and 3 (suggested by QCD) colours. The corresponding prediction for R is given in Table 6.I.

n_F	3	4	5	6
quarks	u,d,s	u,d,s,c	u,d,s,c,b	u,d,s,c,b,t
R	2	3 1/3	3 2/3	5

Table 6.I R as predicted by the quark-parton model for different numbers n_F of quark flavours.

QCD adds a small (5-10%) correction to the quark-parton model prediction. In the $\overline{MS}$ renormalization scheme the correction factor is [603-607]

$$1 + \frac{\alpha_s}{\pi} + (1.98 - 0.115\, n_F)\left(\frac{\alpha_s}{\pi}\right)^2 . \qquad (6.3)$$

The 'running' strong coupling constant α_s is given by

$$\alpha_s(Q^2) = \frac{4\pi}{\beta_0 \ln(Q^2/\Lambda^2) + (\beta_1/\beta_0)\ln\ln(Q^2/\Lambda^2)} , \qquad (6.4)$$

evaluated at $Q^2 = E_{cm}^2$ with $3\beta_0 = 33 - 2n_F$, $3\beta_1 = 306 - 38n_F$, and the QCD scale constant Λ.[++]

Table 6.II gives R as measured by PLUTO[+] between 3.6 and 31.6 GeV [608-615]. The contribution of the heavy lepton τ (see Sect.5) is excluded. Fig.6.1 displays the data in the low and Fig.6.2 in the high energy range.

We observe a step in R around 4 GeV, and, after some oscillations, an almost constant level up to the highest energies. The level extends over a range where the reference cross section $\sigma_{\mu\mu}$ falls by a factor of 50, and thus beautifully demonstrates the point-like nature of the constituents. The quantitative prediction of the quark-parton model is given by the dashed and the QCD corrected one by the solid curves. The agreement is excellent, and argues against different constituents like colourless quarks or integer-charged partons.

For energies above 10 GeV the average R values of PLUTO and the other PETRA experiments [616-618] all lie above the value 3 2/3 predicted by the quark-parton model, and are in fact closer to the QCD prediction (solid curve in Fig. 6.2). While the estimated systematic errors of typically 10 - 15% have so

[+] The analysis procedure is described in Sect. 3.8.4.

[++] Λ is chosen such as to yield $\alpha_s(900\,\text{GeV}^2) \approx 0.15$ (6.16), which in first order ($\beta_1 = 0$) gives ≈ 200 MeV.

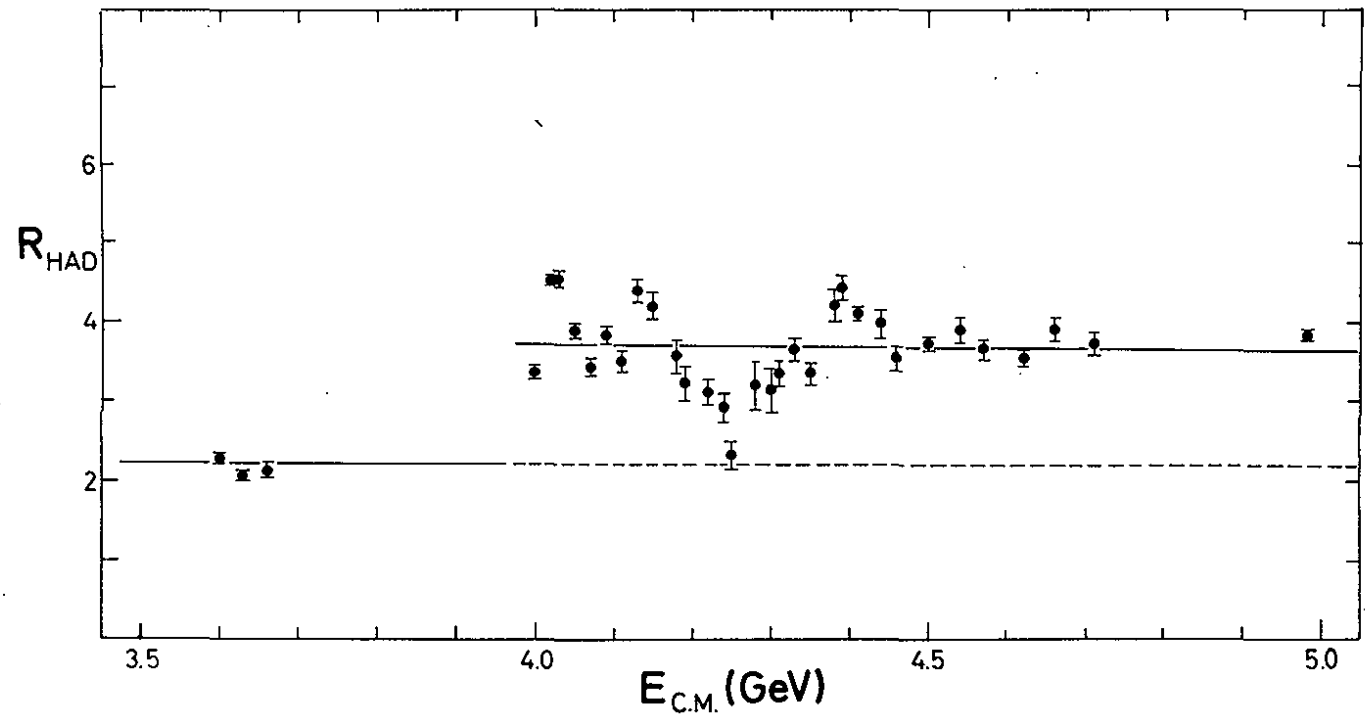

Fig. 6.1 R (e^+e^- → hadrons) vs. c.m. energy acc. to Refs. [608, 609]
Full line: asymptotic prediction of quark model including QCD correction. Dashed line : 3 quarks only.

TABLE 6.II: R_{HAD} after radiative corrections

E_{cm} (GeV)	R	Δ R	E_{cm} (GeV)	R	Δ R	E_{cm} (GeV)	R	Δ R
3.60	2.29	0.03	4.28	3.21	0.29	7.70	3.92	0.26
3.63	2.07	0.08	4.30	3.15	0.28	9.30	3.45	0.62
3.66	2.13	0.09	4.31	3.34	0.15	9.35	3.82	0.75
4.00	3.38	0.08	4.33	3.66	0.16	9.37	4.68	0.82
4.02	4.52	0.05	4.35	3.35	0.13	9.38	5.04	0.89
4.03	4.54	0.09	4.38	4.19	0.21	9.39	3.88	0.47
4.05	3.88	0.11	4.39	4.43	0.14	9.40	3.16	0.63
4.07	3.42	0.11	4.41	4.10	0.06	9.41	3.58	0.70
4.09	3.83	0.11	4.44	3.97	0.17	9.42	3.93	0.64
4.11	3.50	0.13	4.46	3.54	0.16	9.43	4.05	0.64
4.13	4.40	0.15	4.50	3.72	0.07	9.44	2.92	0.82
4.15	4.19	0.17	4.54	3.90	0.15	12.0	4.29	0.29
4.18	3.57	0.20	4.57	3.66	0.13	13.0	4.10	0.45
4.19	3.22	0.23	4.62	3.55	0.11	17.0	3.60	0.37
4.22	3.12	0.16	4.66	3.91	0.14	22.0	3.47	0.60
4.24	2.92	0.18	4.71	3.73	0.16	27.6	4.07	0.29
4.25	2.32	0.17	4.98	3.85	0.04	$^{30.0}_{31.6}$	4.10	0.13

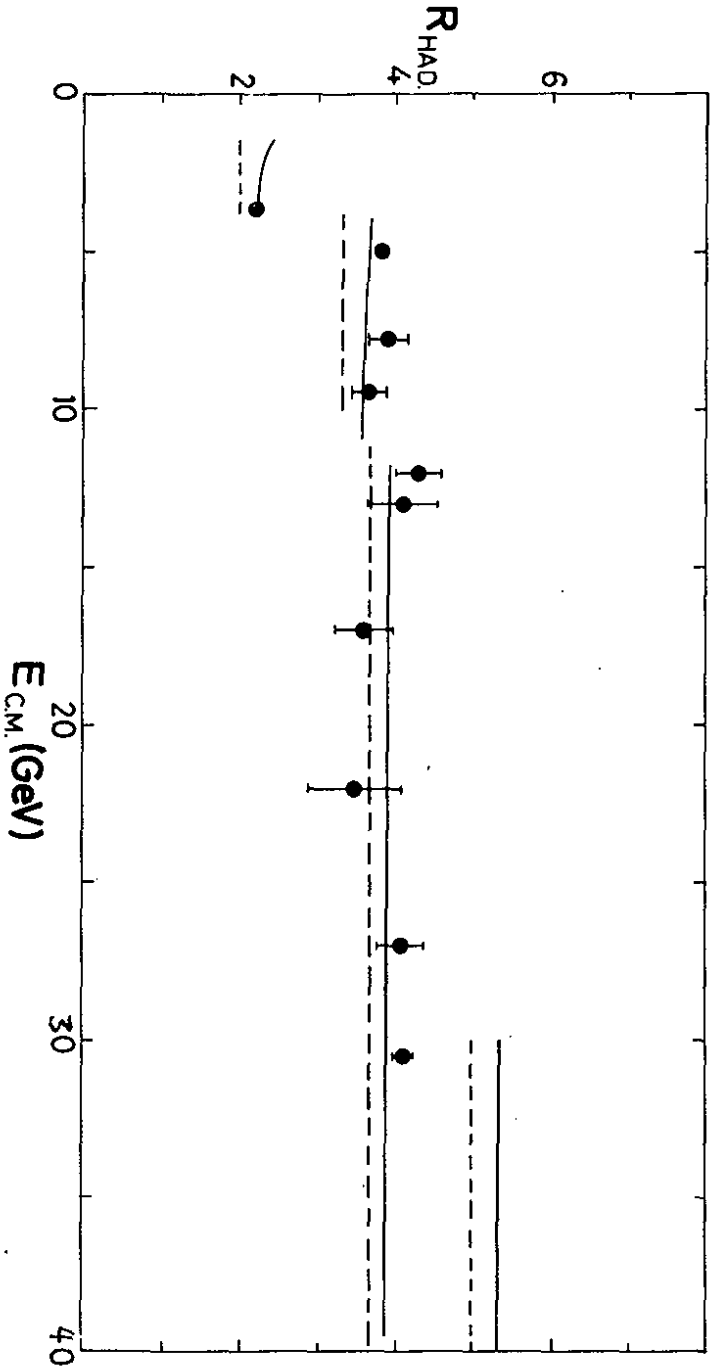

Fig. 6.2 R (e^+e^- → hadrons) vs. c.m. energy acc. to Refs [610-615]
Dashed and full lines give quark model predictions without and with QCD correction.

far prevented quantitative conclusions, a recent detailed investigation of all uncertainties in acceptance, $\gamma\gamma$ background, monitoring, and radiative corrections, has reduced the systematic uncertainty of PLUTO cross sections below 6%, and thus established a 2.5 σ deviation from the quark-parton model in the direction predicted by QCD [615].

The contribution of a 6^{th} quark of charge 2/3 ('top'), as indicated by the upper lines in Fig. 6.2, can safely be excluded. Also the rate of inclusive muons observed [619], and in particular the investigations of the final state topology (see Sects. 6.3.2, 6.3.3) argue against a new threshold. Between 30.0 and 31.6 GeV the cross section was 'scanned' in small steps of 20 MeV, in order to check for a narrow $t\bar{t}$ resonance [614]. The data are shown in Fig. 6.3. If the $t\bar{t}$ ground state lies in this scan range, one expects a resonance signal of about 12 units in R with an rms width of 20 MeV as indicated by the dashed curve. This expectation is based on the energy width of the stored e^+ and e^- beams (calculated from quantum fluctuations in the synchrotron radiation, and verified at several resonances and storage rings) and an empirical relation (also suggested by generalized vector dominance [620 - 624] which connects the leptonic branching ratios of the vector mesons to the squares of their average quark charges like

$$\Gamma_{ee}(\rho):\Gamma_{ee}(\omega):\Gamma_{ee}(\phi):\Gamma_{ee}(J/\psi):\Gamma_{ee}(\Upsilon) = \tfrac{1}{2} : \tfrac{1}{18} : \tfrac{1}{9} : \tfrac{4}{9} : \tfrac{1}{9} \qquad (6.5)$$

This sequence 'predicts' for the t quark of charge $^2/_3$:

$$\Gamma_{ee}\ (t\bar{t}) = 5\ \text{keV}. \qquad (6.6)$$

The PLUTO data, on the other hand, result in an upper limit of

$$\Gamma_{ee} < 2.0\ \text{keV at 95\% C.L.}, \qquad (6.7)$$

and therefore exclude existence of a $t\bar{t}$ ground state between 30 and 31.6 GeV.

6.2 Charm effects

Figs. 6.1 and 6.2 show a higher level of R above 4 GeV, as compared to 3.6 GeV, (in agreement with the data of other experiments [625-627]). This is quite naturally attributed to the production of 'open charm', that is heavy mesons

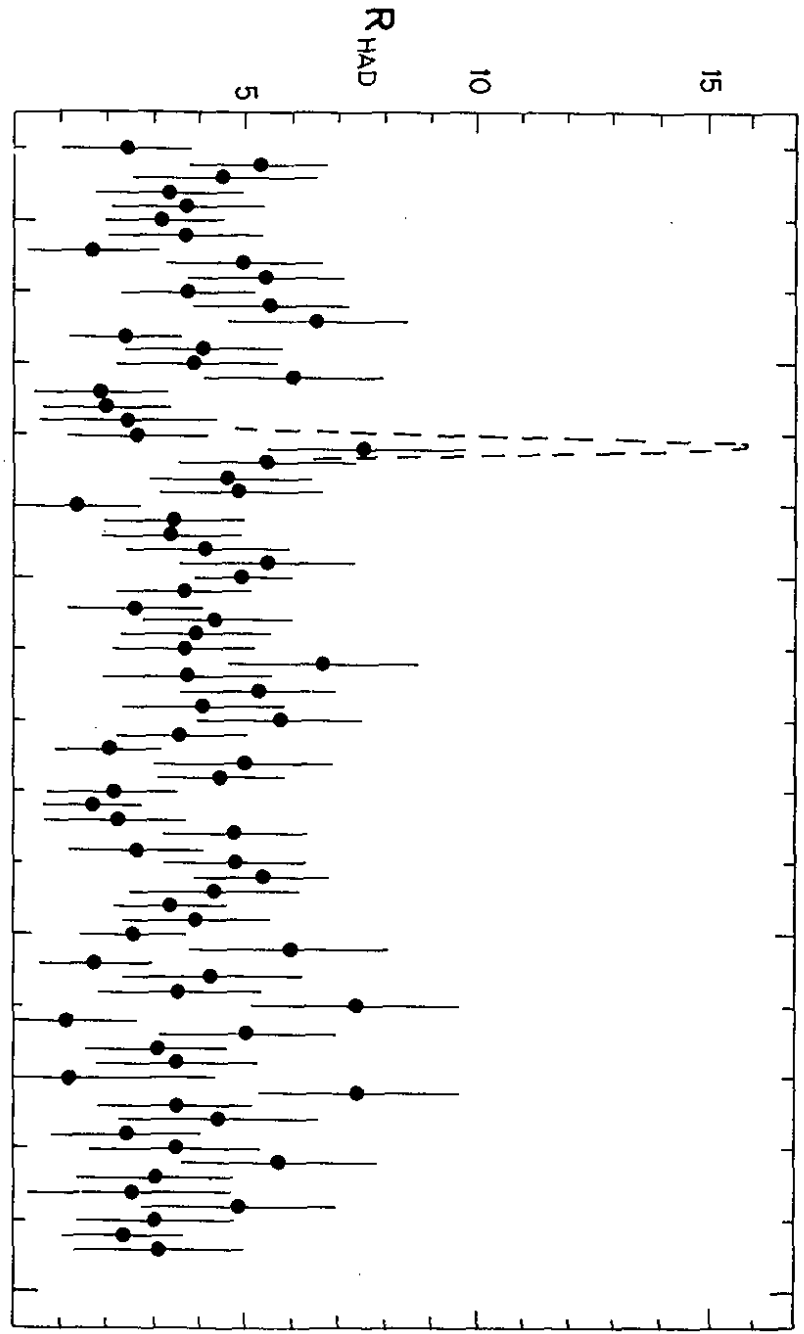

Fig. 6.3 R (e^+e^- → hadrons) in the scan range 30-31.6 GeV. The dashed line indicates the resonance signal expected for a $t\bar{t}$ ground state.

containing one charmed and one light quark [628-630]. Since the charm quantum number is conserved in strong and electromagnetic interactions the charmed states have to decay via weak interactions. According to the GIM scheme [631] these decays will predominantly lead to strange quarks and therefore to kaons. This enhanced kaon production as well as the possibility of Zweig - forbidden [632-634] charm-anticharm annihilation will be discussed in the following sections.

6.2.1 Inclusive K^0 production

The charmed quark c had originally been postulated in order to explain the absence of the strangeness-changing neutral transition s→d→u, which originates from the product of two charged currents, through the (completely) destructive interference with the amplitude for s→c→d [631]. This scheme uniquely connects the weak coupling of the charmed quark with the Cabbibo angle [635, 636] Θ_c, such as to produce 2 $\cos^2\Theta_c = 1.9$ kaons for every charm-anticharm event. One quarter of these will appear as K^0_s mesons and can be idendified in the PLUTO detector.

PLUTO's first evidence for charm was a suggestive but statistically marginal signal of K^0_s mesons associated with prompt electrons [637], as expected from the simultaneous non- and semileptonic decay of a pair of charmed particles.

More quantitative evidence for charm was subsequently obtained from the cross section for inclusive K^0_s production [638] as shown in Fig. 6.4a.[+] Above 4 GeV the cross section is clearly higher than the reference value at 3.6 GeV. If the difference is divided by the corresponding difference of the total hadronic cross section, one obtains the number of 'new' kaons per 'new' event. It is consistent with the expected number, as shown in Fig. 6.4b, and demonstrates that the identification of the new quantum number with the GIM-charm is correct.

A kinematical check that the kaons are indeed due to the opening of a new threshold is given by their energy spectrum as shown in Fig. 6.5, for 3.6 and $\geq$ 4.03 GeV. Since at threshold the charmed mesons are produced at rest, their decay particles will be mostly below half the beam energy. Indeed, all the 'new' kaons are found at $x_E = E_K/E_B < 0.5$, while the cross section for

[+] The measurements have recently been extended up to 32 GeV [6908].

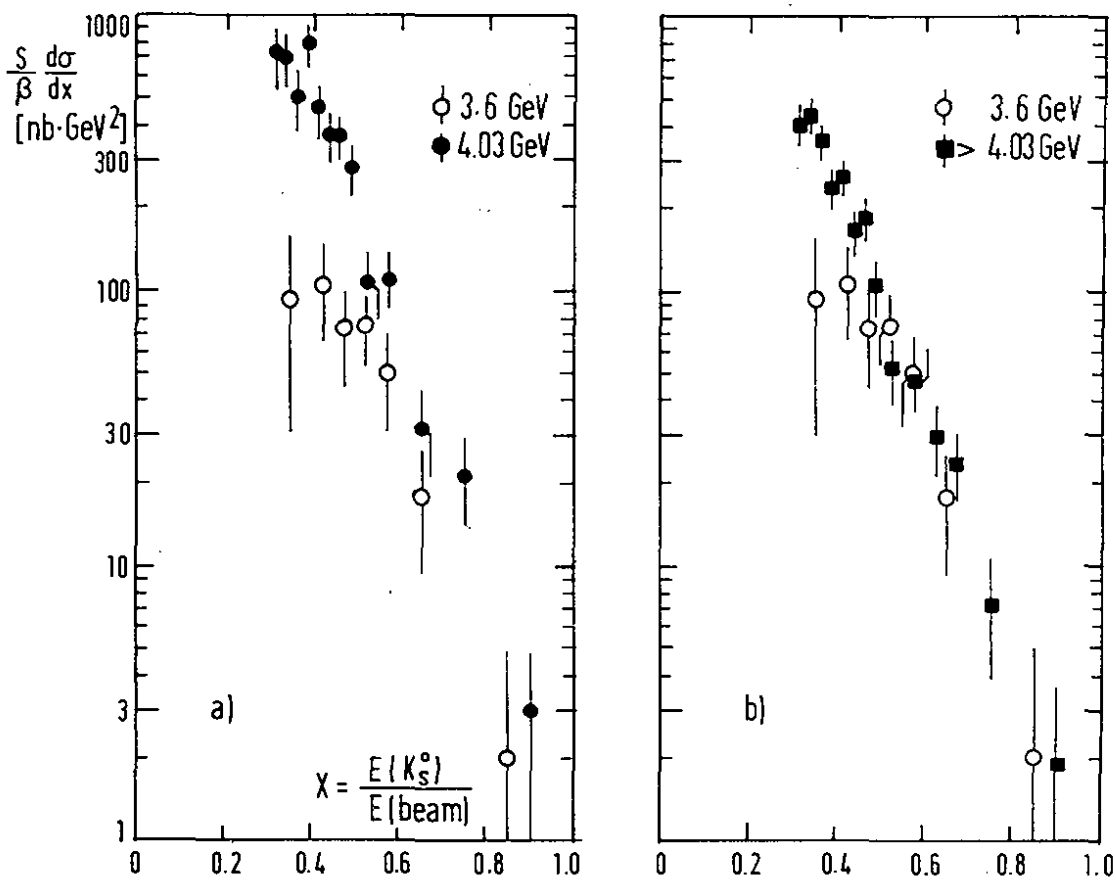

Fig. 6.5 Invariant cross section for K^0_S production $(s/\beta)\, d\sigma/dx$ vs. x above and below charm threshold.

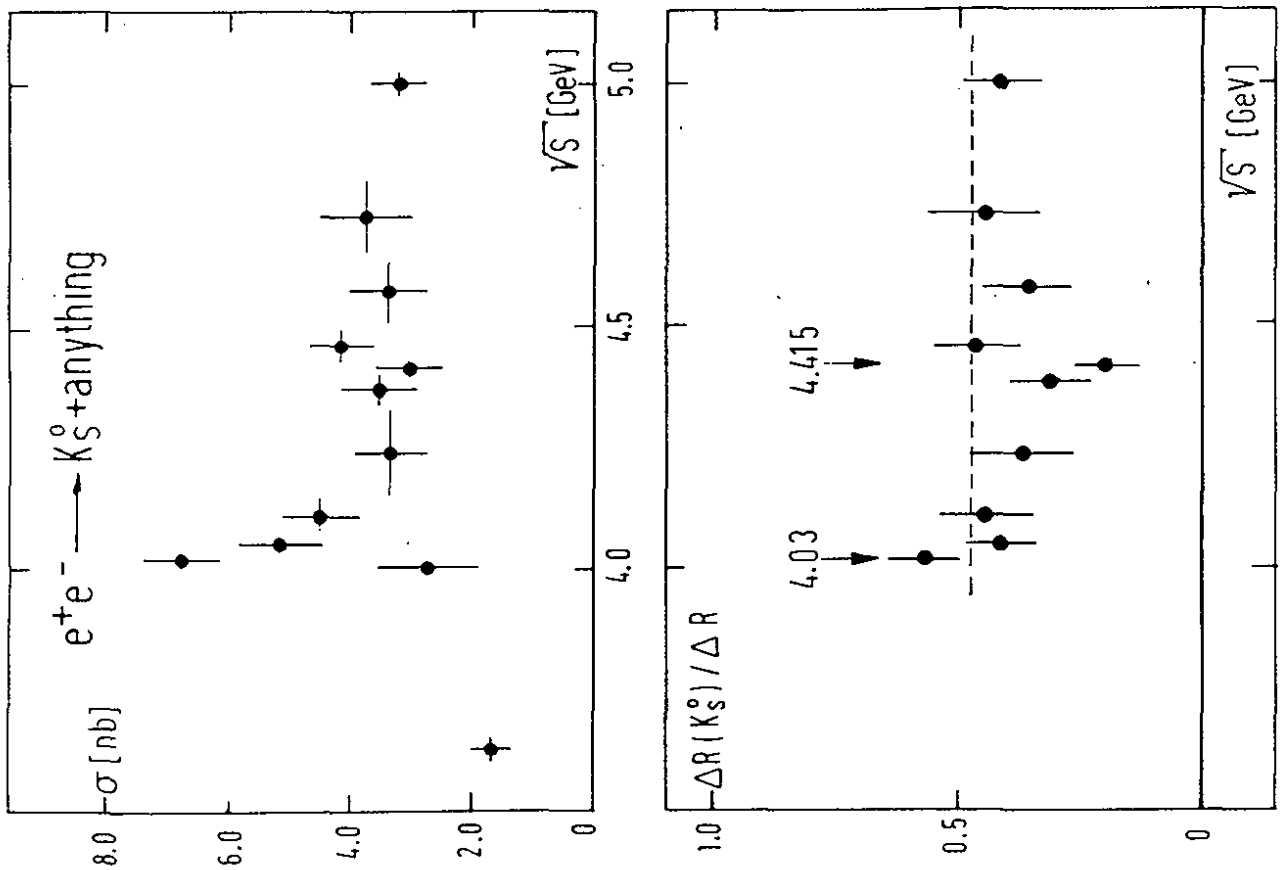

Fig. 6.4a Total K^0_S production [638] vs. c.m. energy.

Fig. 6.4b Ratio of charm induced K^0_S to charm induced hadron production [638].

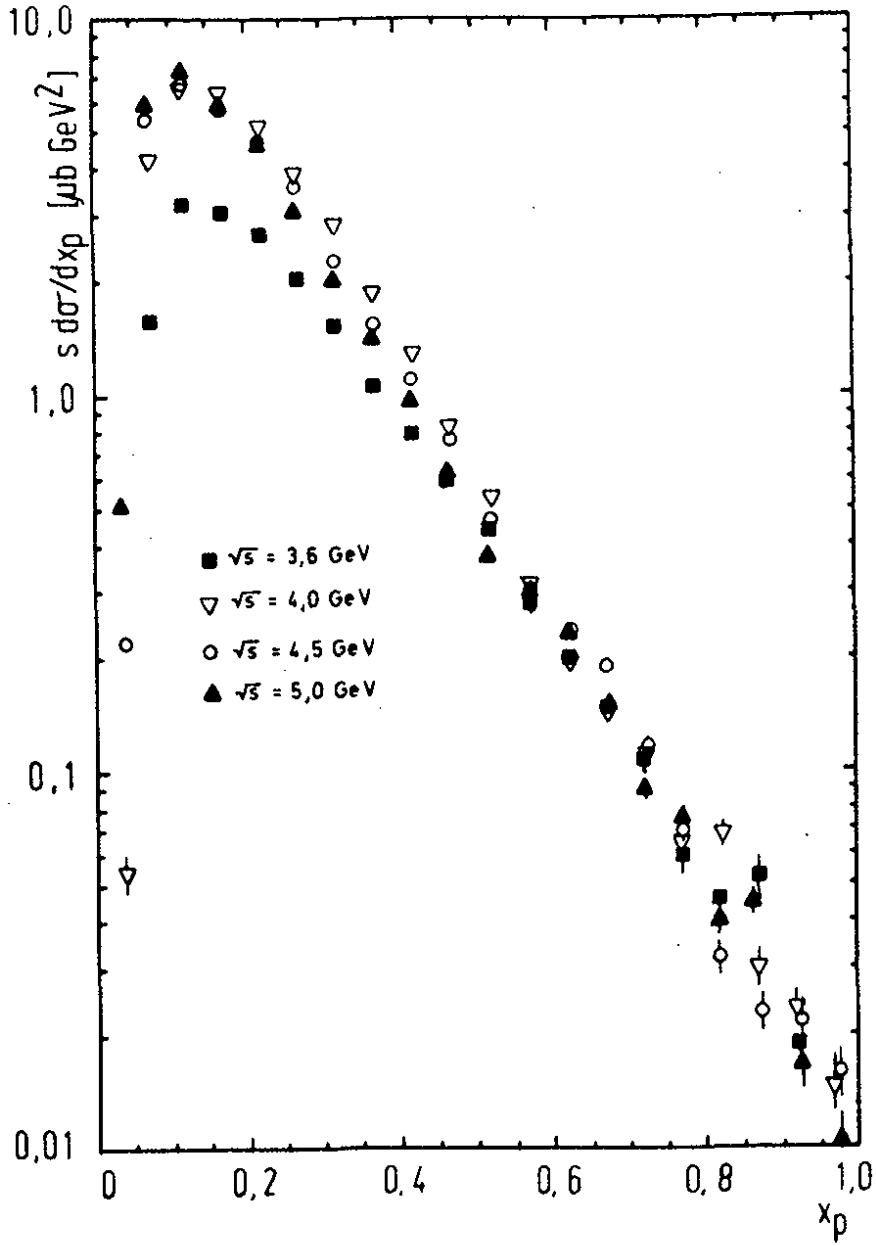

Fig. 6.6 Invariant cross section for hadron production $sd\sigma/dx$ vs. $x_p = p/E_{cm}$ for different c.m. energies.

higher x_E appears to scale. A similar behavior is observed [609] in the inclusive momentum spectra of all charged particles (mostly π^+ and π^-) in Fig. 6.6: A threshold effect at low and scaling at high values of $x_p = p/E_B$.

6.2.2 Inclusive J/ψ production

In order to explain the resonance structure of the cross section between 4 and 4.5 GeV, the production of 'charm molecules', consisting of two charmed and two light quarks, has been proposed [639 - 641]. Within such molecules, rearrangements should lead to a sizeable branching into a $c\bar{c}$ state and a light meson. This 'charm burning' process would be visible not only in a reduction of the inclusive K yield shown above, but more distinctly also as a sizeable signal of inclusive J/ψ mesons.

Inclusive J/ψ mesons were indeed observed in the PLUTO detector [642]. Most of these events were identified as originating from the decay of the ψ'(3.7) resonance which was formed after a hard radiation in the initial state. Their cross section, as shown in the left part of Fig. 6.7, agrees with the expectation. The remaining 'direct' J/ψ production, shown in the right part of the figure, amounts to 0.13% of the total cross section, as expected from small violations of the OZI rule [632 - 634]. No indication of enhanced production due to charm molecules is observed, in particular no single event at the position of the 4.03 and 4.44 resonances.

6.3 Jets

As shown in sect. 6.1, the quark-parton model successfully describes the total hadronic cross section by reducing hadron production to the electromagnetic creation of quark pairs. These quarks should therefore be considered the 'elementary' particles of the reaction. Although not directly observable, they are expected to manifest themselves through a jet of hadrons into which each of them fragments [601, 602], so that the elementary reaction can be investigated by identifying and measuring the hadron jets.

Sec. 6.3.1 will describe some methods of the jet analysis. 6.3.2 will deal with the dominant two-jet final state, and 6.3.3 will present the evidence for the

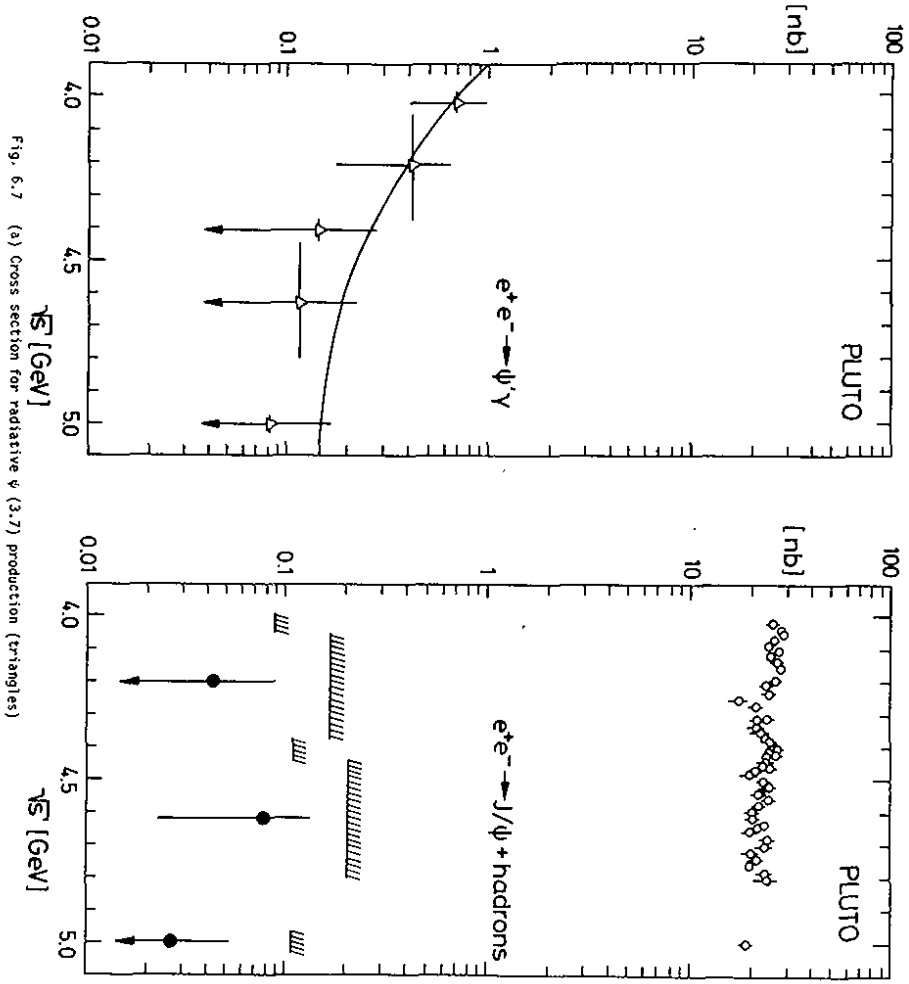

Fig. 6.7 (a) Cross section for radiative ψ(3.7) production (triangles) together with expectation (full line), (b) Cross section for direct J/ψ production (full circles) and upper limits (90% C.L.), together with total hadronic cross section (open circles, (not corrected for radiation)).

emission of a third jet which is attributed to the gluon, the field quantum of the strong interactions [603, 604] Sect. 6.3.4 will compare some attempts to describe the fragmentation process itself by high-order quark-gluon dynamics to the data.

6.3.1 Jet analysis

The event analysis should ideally characterize a given system of N particles by the number of jets it contains, and associate each particle with one of the jets. If the jets are well collimated and separated, this can be achieved by a cluster finding mechanism as described below.

For the general case in which the jets may be wide and even overlap, no general solution exists. Instead one defines one or several observables which specify the deviations from a predefined simple topology, like for instance from two very narrow collinear jets. In case of the most popular observable, sphericity S, such a needle-shaped state gives S = 0 (see below). However, S > 0 specifies no unique topology, but may be due to the width or acollinearity of two jets, to additional jets, or a combination of several effects. Additional observables are then needed for describing even such basic characteristics of the reaction.

'Sphericity' S [602] and the corresponding 'sphericity axis' $\hat{n}_3$ are obtained from the momenta $\vec{p}_j$ of N particles by maximizing the quadratic sum of the parallel momenta $p_{\parallel j} = (\vec{p}_j, \hat{n}_3)$, or by minimizing it for the transverse momenta $p_{\perp j}$:

$$S = \frac{3}{2} \min \left(\sum_{j=1}^{N} p_{\perp j}^2 \right) / \left(\sum_{j=1}^{N} p_j^2 \right)$$

$$= \frac{3}{2} \left\{ 1 - \max \left(\sum_{j=1}^{N} p_{\parallel j}^2 \right) / \left(\sum_{j=1}^{N} p_j^2 \right) \right\} \qquad (6.8)$$

The problem and its solution are equivalent to finding the axes and moments of inertia in a mechanical system:

Diagonalizing the tensor $T_{LK} = \sum_{j=1}^{N} p_{Lj} p_{Kj}$ (L,K = x,y,z) yields three principal axes $\hat{n}_K$ (K = 1,3) which give the orientation of the system, together with three

normalized eigenvalues Q_K

$$Q_K = \sum_{j=1}^{N} (\vec{p}_j \cdot \hat{n}_K) \Big/ \sum_{j=1}^{N} p_j^2 \qquad (K = 1,3) \qquad (6.9a)$$

which describe its shape [643, 644]. Distributions of event shapes are commonly given as scatter plots in two linear independent combinations of the Q_K. If the Q_K are ordered as

$$Q_1 \leq Q_2 \leq Q_3, \qquad (6.9b)$$

$\hat{n}_3$ becomes the sphericity axis, with

$$S = 3/2\ (1-Q_3). \qquad (6.9c)$$

If this formalism is used to describe planar event shapes, Q_2 and Q_1 are measures of the relative transverse momenta "in" and "out of" the plane, and $Q_2 - Q_1$ or Q_1/Q_2 measure the 'flatness' of the events.

While the sphericity S and the event shape parameters Q_K are very convenient measures obtained by a straightforward algorithm, they suffer from a basic shortcoming. The squared momenta used in the calculation are sensitive to the dissociation of particles in the jet: A π^0 measured in shower counters will contribute differently depending on whether the two decay photons are separated or not. Likewise, QCD predictions for sphericity are sensitive to the emission of collinear gluons, and actually diverge [647]. Therefore, several measures have been proposed which depend only on linear sums of momenta, and are therefore insensitive to collinear dissociations. The most popular one is 'thrust', defined as [645-647]

$$T = \max \sum_{j=1}^{N} |p_{\parallel j}| \Big/ \sum_{j=1}^{N} |p_j| \qquad (6.10)$$

with the maximizing direction called 'thrust axis'. The computation of T is less straightforward than that of S, because the derivative of T has discontinuities. Ref.[648] discusses the problems of finding the axis and presents a general solution.

A generalization of thrust to a 3-jet measure is 'triplicity' T_3 [648]. It is obtained by subdividing the particles of an event in three non-empty classes, C_K, calculating the total momentum

$$\vec{P}_K = \sum_{j \in C_K} \vec{p}_j \qquad (6.11)$$

for each class and finding that particular partition for which the sum of the three linear momenta is maximal. This defines triplicity as

$$T_3 = \max\ (|\vec{P}_1| + |\vec{P}_2| + |\vec{P}_3|) \Big/ \sum_{j=1}^{N} |\vec{p}_j| \qquad (6.12a)$$

One obtains $T_3 = \sqrt{27}/8 \simeq 0.65$ for a completely spherical event, and $T_3 = 1$ for any configuration of three very narrow jets. The jet configuration itself is then specified by two additional variables: either two of the angles θ_K between the jet momenta P_K (convention: θ_1 is measured between $\vec{P}_2$ and $\vec{P}_3$; $\theta_1 \leq \theta_2 \leq \theta_3$) or two of the normalized jet momenta

$$x_K = 2|\vec{P}_K| \Big/ \sum_{j=1}^{3} |\vec{p}_j| = \frac{2 \sin \theta_K}{\sum_j \sin \theta_j} \qquad (6.12b)$$

with $x_1 \geq x_2 \geq x_3$. For the case of real hadron jets with internal transverse momenta one obtains $T_3 < 1$, but can hope - and partly verify in Monte Carlo studies - that the measured x_K and θ_K still reproduce the kinematics of the original partons, thus unfolding the fragmentation process. The dynamics of the parton system can then be represented by scatter plots in the θ_K or x_K (*Dalitz plot*).

Several authors [649-652] have proposed more general measures of the event shape which do not depend on imposing an assumed structure and axis upon the event. Fox and Wolfram [652] suggest spherical moments H_l defined as

$$H_l = \sum_{i,j}^{N} \frac{|\vec{p}_i| \cdot |\vec{p}_j|}{E_{CM}^2} \cdot P_l(\cos \theta_{ij}) \qquad (6.13)$$

where the P_l are Legendre polynomials, and θ_{ij} is the angle between particle i and j. Due to the weighting with the particle momenta the H_l are insensitive

to collinear dissociations of particles. While H_0 and H_1 are constants for a completely measured event, H_2 is sensitive to a collinear two-jet-structure.

A related quantity which is important for studying the shape of jets is the two-particle or energy-energy correlation [650-651]. It is defined as

$$f(\theta) = \frac{d\Sigma}{d\theta} = 2 \sum_{ij}^{N} \frac{d^3\sigma}{dz_i\, dz_j\, d\theta_{ij}}\, z_i\, z_j\, dz_i\, dz_j \Big|_{\theta = \theta_{ij}}$$

$$= \left\langle 2 \sum_{ij}^{N} z_i\, z_j\, \delta(\theta - \theta_{ij}) \right\rangle \qquad (6.14)$$

where $z_i = E_i / E_{CM}$ and z_j are the fractional energies of particles i and j, and is θ_{ij} the angle between them.[+] $f(\theta)$ can be considered as the product of the energy flows seen by two spectrometers with fixed spacing θ, averaged over all orientations. For a collinear two-jet structure $f(\theta)$ is large if the spacing θ is either small, or close to 180^0. [++]

The correlation again is insensitive to collinear particle dissociations. The correlation can be separated into a 'same-side' correlation, where particles i and j belong to the same jet, and an 'opposite-side' one where they are taken from different jets. In this case the jets have to be artificially separated by a plane perpendicular to the jet axis, which complicates the interpretation of the $\theta \approx 90^0$ region as compared to the full correlation (6.14).

In the jet analysis methods described so far the multijet states are largely parameterized as deviations from an assumed ideal geometry, usually two narrow

[+] In order to have a normalization which is independent of collinear particle dissociations, the self-correlation terms j = i cannot be omitted in equ. (6.14). The normalization to 2 (instead of unity) is maintained for historical reasons.

[++] The variable θ appears most appropriate to present the complete function of such a structure, while cos θ would grossly contract the interesting forward and backward peaks, and ln (tan θ/2) [650] spreads them very much.

collinear jets. Most parametrizations are insensitive to the nature of these deviations and not very useful for a general investigation of multi-jet topologies.

On the other hand, it is possible to recognize high-energy jets visually just from the clustering of the particle flight directions. Starting from this experience, members of the PLUTO group have recently succeeded in developing, testing and applying a simple effective jet-finding algorithm [653]. In a first step, the particles [+] are grouped into 'preclusters' in which each particle has at least one neighbour closer than α_{max} (typically 30^0), or which consists of a single particle without such neighbour. Energy E and direction $\tilde{n}$ of a precluster are obtained by summing energies and momenta of the particles.

By the same procedure preclusters are grouped to 'clusters', defined by a corresponding collecting angle β_{max} (typically 45^0) between the directions of the preclusters. This and the following steps are necessary to minimize spurious results arising from particle fluctuations in the jets. The least energetic clusters are removed up to a maximum fraction ε (typically 10%) of the total observed energy. All remaining clusters whose energy exceeds a given threshold, typically 2 GeV, are then called jets. The momentum vector of a jet is defined as $E_{JET} \cdot \tilde{n}_{JET}$ (zero mass kinematics!). The algorithm was optimized with the help of a Monte Carlo simulation of typical reactions at 30 GeV, including fragmentation [656, 657].

Figs. 6.8 a-c give the Monte Carlo simulated distributions of n_J, the resulting number of jets, for different two- and three-parton mechanisms. The probability is highest for detecting the same number of jets as partons, and drops considerably for smaller n_J, as produced by merging jets, and for larger n_J as resulting from fluctuations and heavy quark decays (shaded area in Fig. 6.8a). An observed n_J-distribution can therefore efficiently be decomposed into the contributions from different parton reactions. Monte Carlo simulations of the $q\bar{q}g$ reaction show in the subsample of generated 3-jet events strong correlations between the kinematics of the jets and the partons [653]. Fig. 6.9 shows the close correspondence between the thrust $T_J = \max \sum_{i=1}^{3} E_i \tilde{n}_i / \Sigma E_i$

[+] charged as well as neutral ones

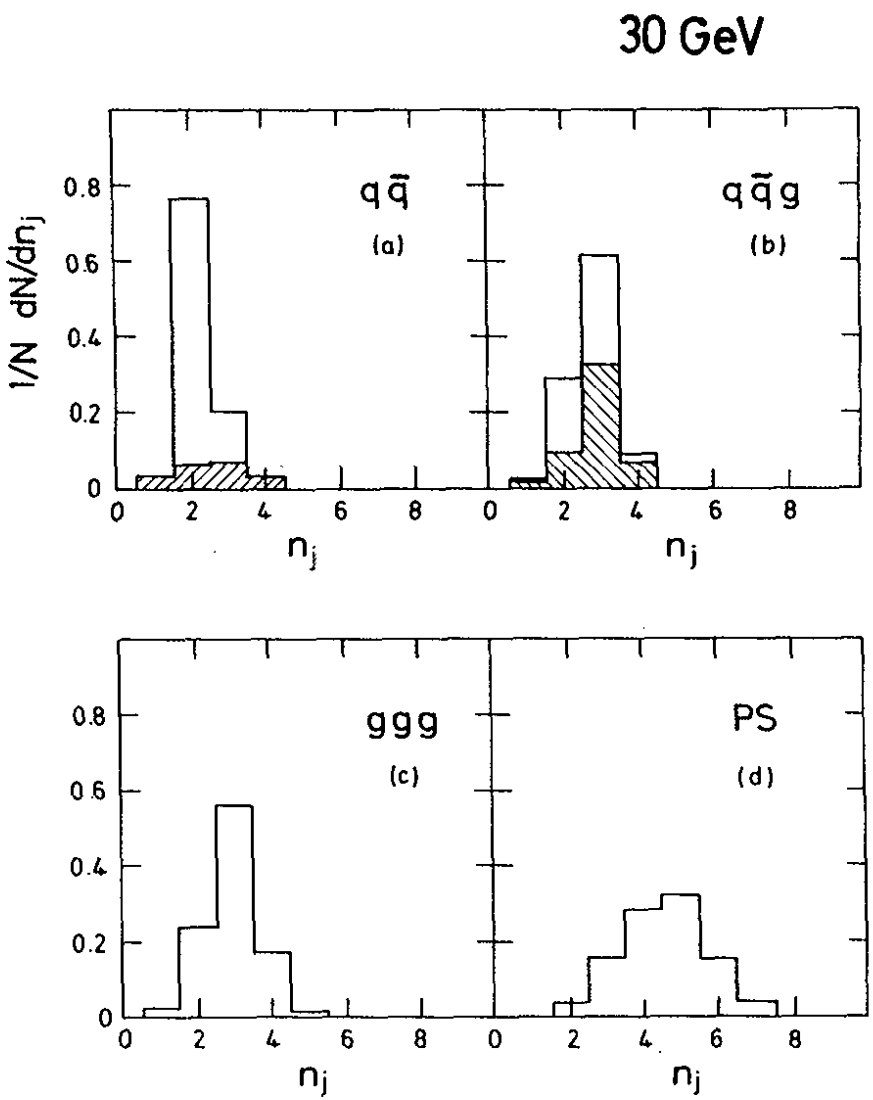

Fig. 6.8 Expected number of jets as reconstructed by the cluster algorithm for different production mechanismus: (a) $q\bar{q}$ = $u\bar{u}$ + $d\bar{d}$ + $s\bar{s}$ + $c\bar{c}$ + $b\bar{b}$. Shaded area: $b\bar{b}$ contribution. (b) $q\bar{q}g$ (gluon). Shaded area: events selected with thrust cut ($T < 0.90$). (c) 3-gluon. (d) Phase space.

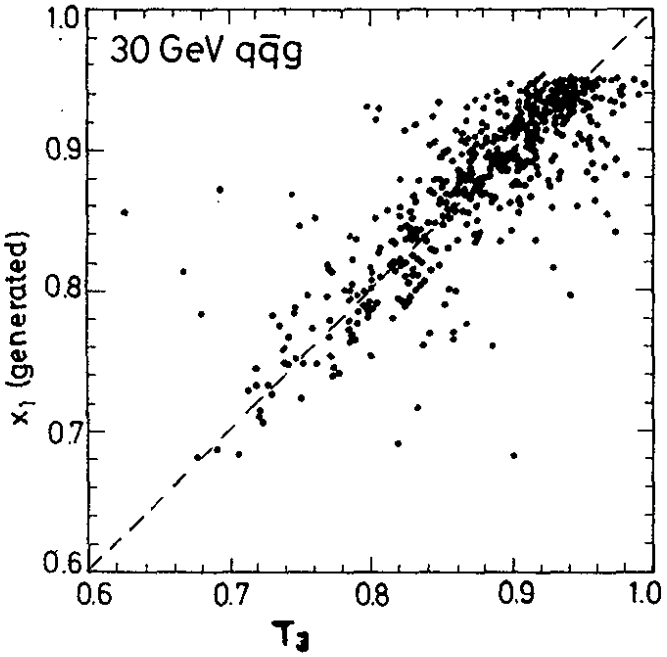

Fig. 6.9 Correlation between 'jet thrust' T_J and parton thrust x_1.

of the three jets and the parton thrust x_t which is just the fractional energy of the most energetic parton. [+]

When applied to phase space events the algorithm produces a broad distribution (Fig. 6.8d) extending to large n_J, which (although the n_J themselves are artefacts) provides a sensitive handle for detecting small isotropic contributions to the cross section, like expected at new particle thresholds.

6.3.2 Two-jet topologies

While at lower energies the jet structure of the hadronic events is not directly visible, but has to be inferred from a comparison of the observed and the Monte Carlo simulated sphericity distributions [654], it becomes more and more striking as the energy increases. Fig. 6.10 displays the reconstructed charged and neutral particles (full and dashed, rsp.) of a typical event observed at 30 GeV c.m. energy. The PLUTO detector could demonstrate for the first time that the neutral energy flow is collimated in the same direction as the charged particles [655]. Fig. 6.11 shows that the angular distributions of the charged (histogram) and of the neutral energy (full points) around the thrust axis are quite similar. (As the charged particles have been used to determine the axis, they appear to cluster somewhat closer). So both the charged and neutral energy consistently indicate the origin of all hadrons from just two parent particles. The spin of the parent particles can be read off the angular distribution of the jet axis with respect to the beam line: it should be $\sim 1 + a\cos^2\theta$ with $a = +1$ or -1 for spin 1/2 or 0. Fig. 6.12 clearly verifies spin 1/2, as expected from the quark-parton model.

e^+e^- annihilation thus constitutes a source of quark jets which, in contrast to inelastic lepton hadron scattering, is free of the problems of spectator particles. It can be used to study various aspects of the quark fragmentation, in particular anomalies which are expected at new particle thresholds and through hard gluon bremsstrahlung as predicted by QCD. An invaluable help for these investigations is the quark fragmentation model of Field and Feynman [656] (see 3.8.5.1) which allows a Monte-Carlo computation of all observables with full account of detector biases. The $q\bar{q}$ model has been extended by including hard gluon emission to first ($q\bar{q}g$) [657] and second order ($q\bar{q}gg + q\bar{q}q\bar{q}$) [658] in QCD,

[+] The corresponding error made by setting $x_1 = T_J$ is $\sigma(x_1)/x_1 = 0.03$ (at E_{CM}=30 GeV, $T_J < 0.95$; detector effects included)

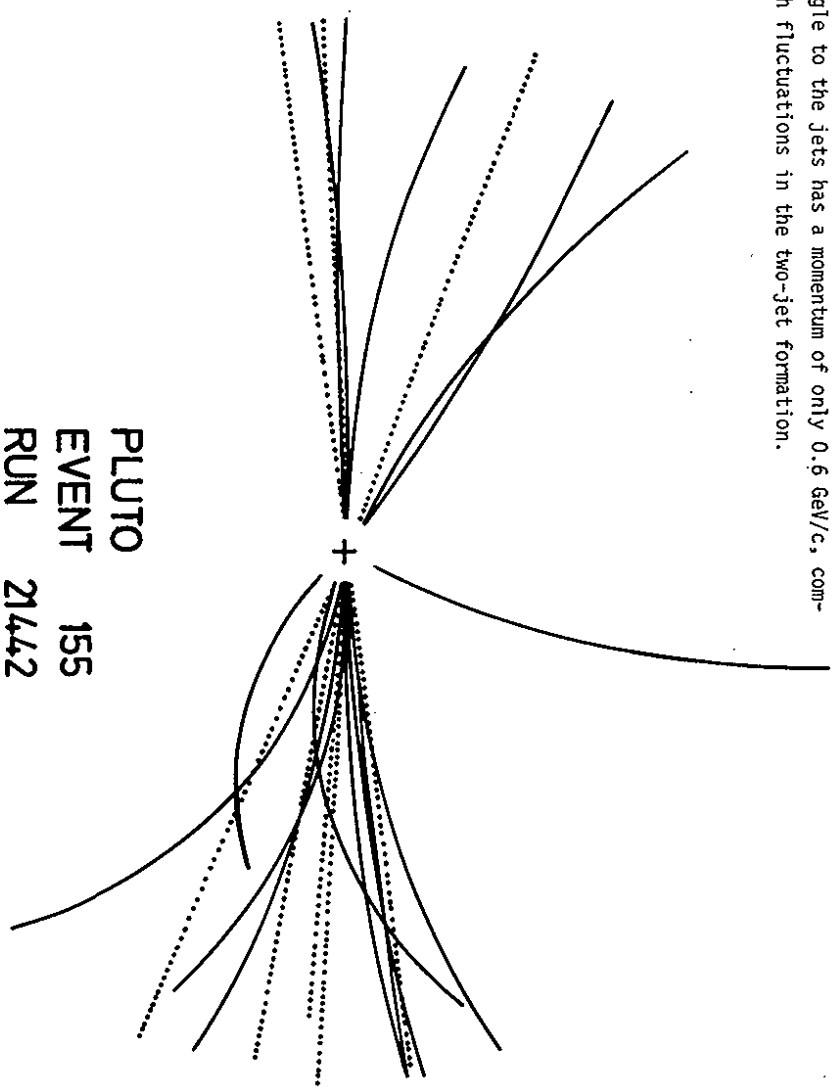

Fig. 6.10 Typical event observed at 30 GeV with reconstructed charged (full lines) and neutral particles (dashed). The single particle emitted at right angle to the jets has a momentum of only 0.6 GeV/c, compatible with fluctuations in the two-jet formation.

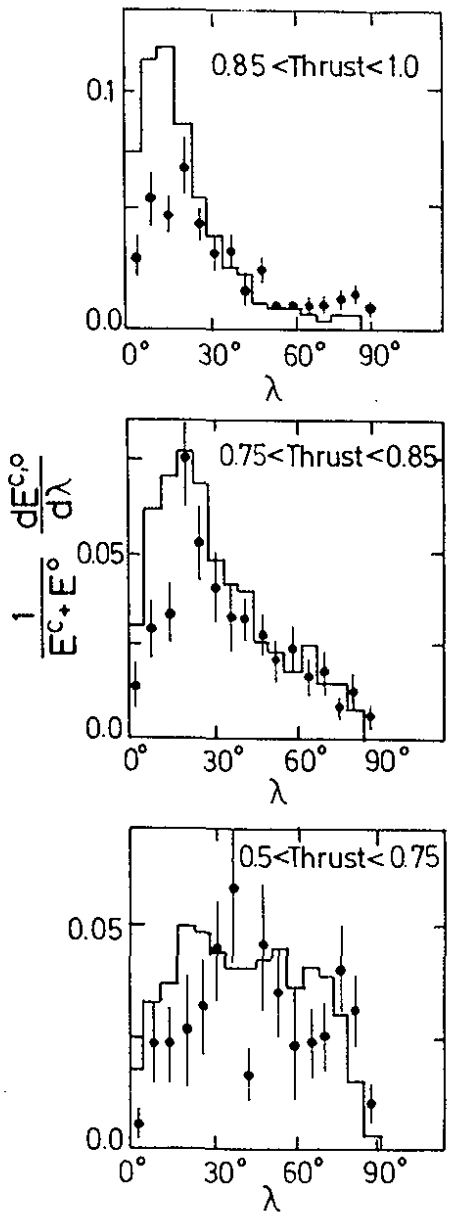

Fig. 6.11 Distribution of the charged (histogram) and neutral (full points) energy flow vs. λ, the angle to the thrust axis, as observed at 9.4 GeV in different thrust bins.

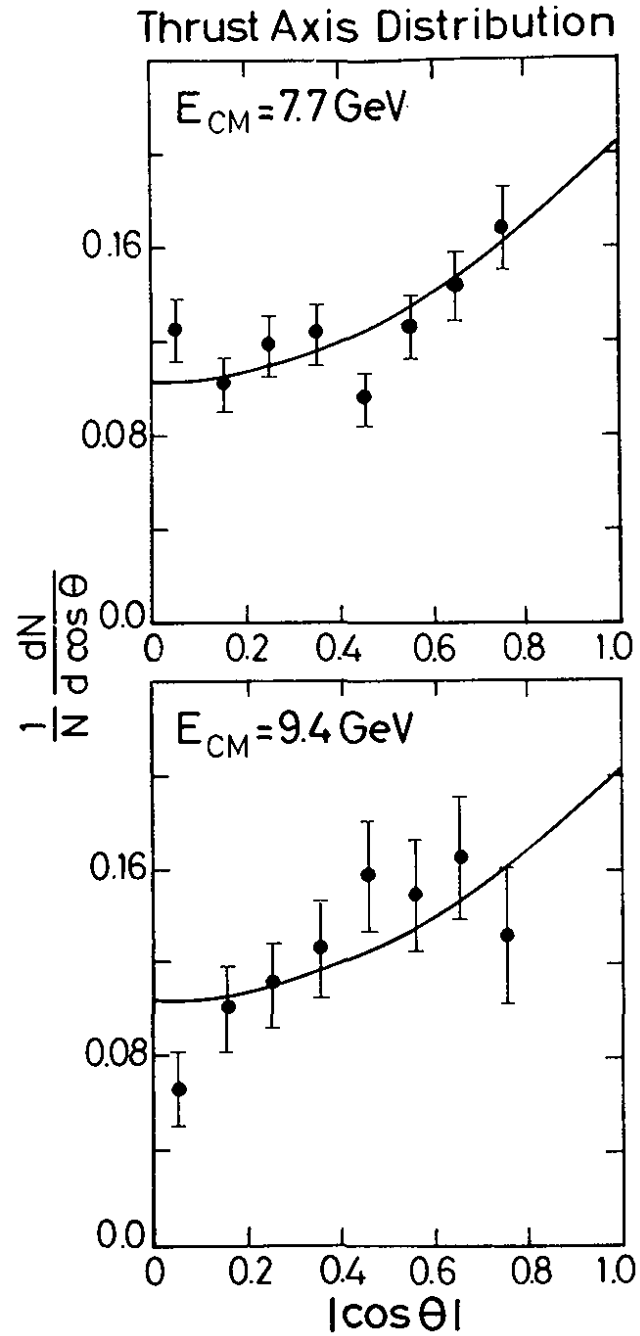

Fig. 6.12 Angular distribution of the thrust axis with respect to the e^+e^- beam. Full line is ~ $1 + \cos^2\theta$, the quark model prediction.

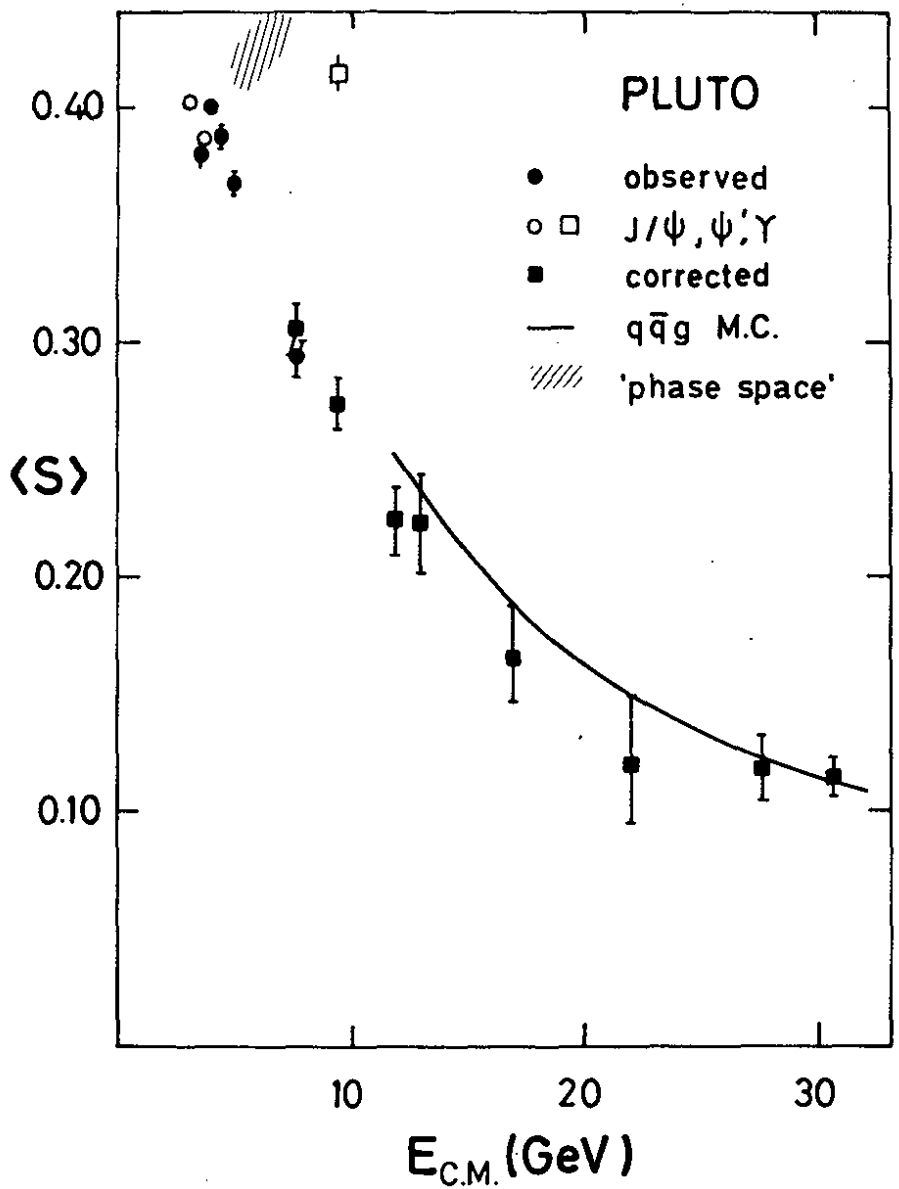

Fig. 6.13 Mean sphericity as observed from charged particles (dots), and corrected for all missing particles, detector effects and initial state radiation (squares). Open symbols show resonance values.

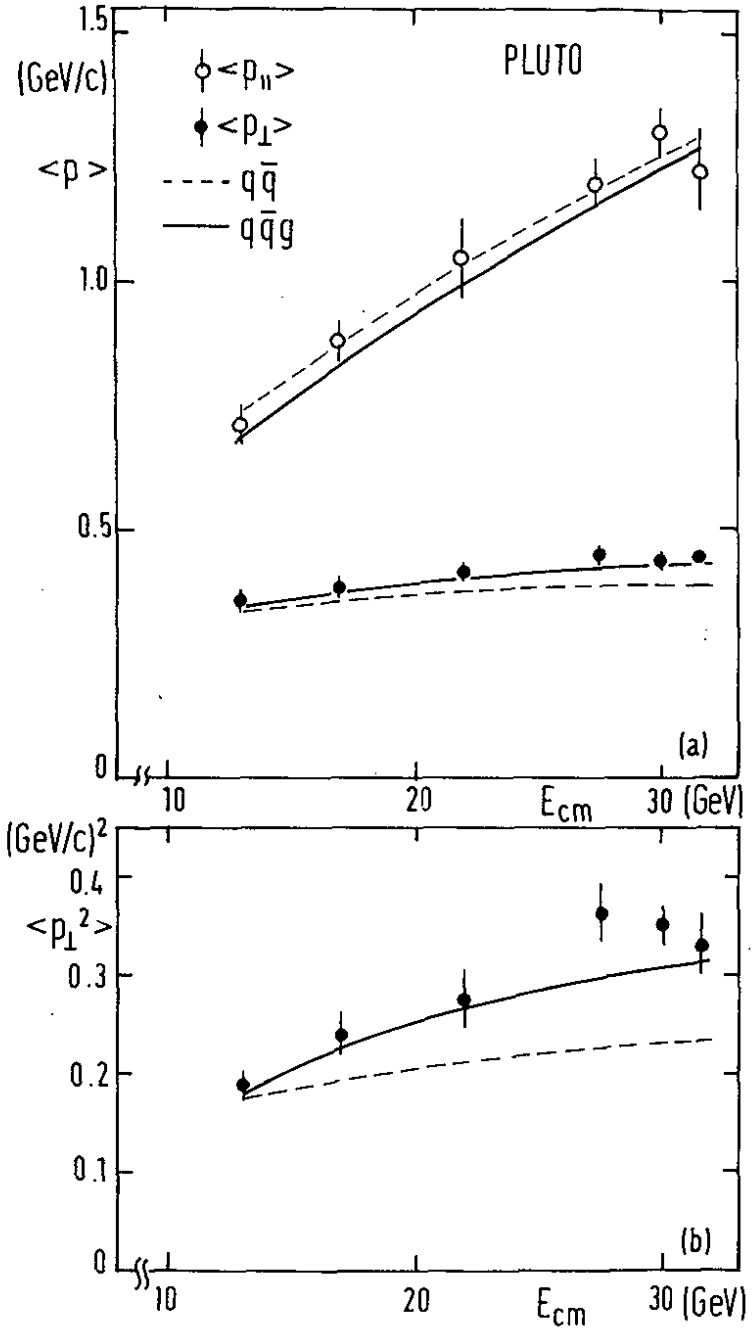

Fig. 6.14 Average particle momenta parallel and perpendicular to the jet axis vs. c.m. energy (a) $\langle p_{\parallel} \rangle$ and $\langle p_{\perp} \rangle$, (b) $\langle p_{\perp}^2 \rangle$.

as well as the production and weak decays of new mesons [659], and will be used to search for these effects +. Fig. 6.13 shows the energy dependence of the mean sphericity [643, 6925]. Apart from the values at the resonances (open symbols, see Sect.7), the sphericity falls very rapidly with increasing energy, and is distinctly different from the large, slowly rising one that would be expected from an uncorrelated particle emission ('phase space'). The fragmentation model ($q\bar{q}g$ acc. to [657]), on the other hand, describes the trend of the non-resonance data very well. No increase indicating the production of slow heavy particles is observed at high energies, thus excluding a 'top' meson threshold up to 31 GeV, provided the top quark has charge 2/3. The effect of the 'bottom' (quark charge -1/3) threshold around 10.5 GeV is too small to be visible within present statistics.

The decrease of <S> corresponds to an almost constant momentum $\langle p_\perp \rangle$ transverse to the jet axis [660], as shown in Fig. 6.14a. Most of $\langle p_\perp \rangle$ can be accounted for by the $q\bar{q}$ model which parameterizes the transverse momenta by one energy-independent constant σ_q. Using the cluster algorithm described above, this constant has been determined from a clean sample of $q\bar{q}$ events (corrected for $q\bar{q}g$ admixtures) as [661]

$$\sigma_q = (290 \pm 20)\ \text{MeV}/c \qquad (6.15)$$

6.3.3 Evidence for hard gluons

QCD predicts deviations from the quark-parton model ($q\bar{q}$) due to the emission of a single hard gluon ($q\bar{q}g$). While at PETRA energies this has little influence on the average linear momenta $\langle p_\perp \rangle$ and $\langle p_{in} \rangle$, a large effect can be seen in the average squared transverse momentum $\langle p_\perp^2 \rangle$ (Fig. 6.14b). The gluon emission in the $q\bar{q}g$ models can describe this deviation very well. However, a thorough check is required on whether it explains other, more crucial features of the data as well, and on how far alternative explanations like a general broadening of quark jets can be excluded.

+ Quite recently the 'Lund' model [6901] which relates the hadron production to colour flow rather than the parton flight directions has also been applied. Within the present measurement errors its predicted hadron distributions are consistent with those of the 'standard' $q\bar{q}g$ [657] and the $q\bar{q}gg$ [658] model.

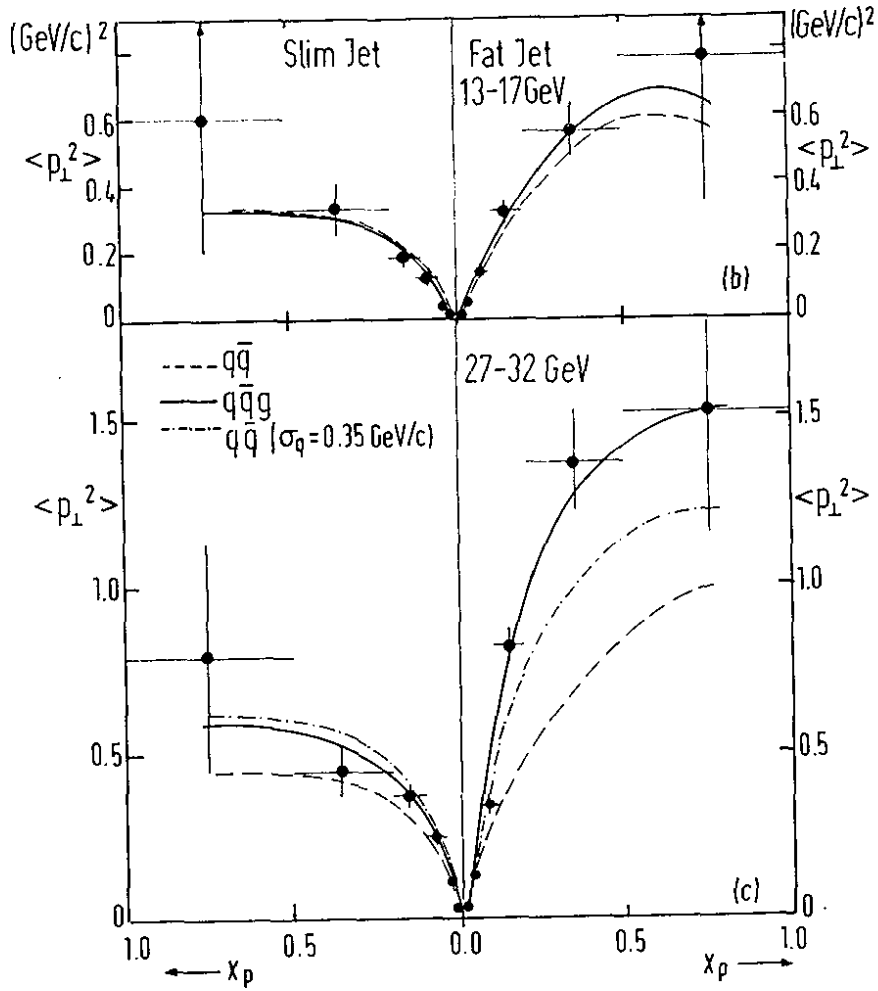

Fig. 6.15 'Seagull' plot: Average $p_\perp^2$ of charged particles vs. scaled momentum $x_p = 2p/E_{cm}$ for different c.m. energies, separated into 'slim' jet (left) and 'fat' jet (right). Dashed and solid curves show $q\bar{q}$ and $q\bar{q}g$ expectations.

QCD predicts that the probability for hard gluon emission is small ($\sim\alpha_s$), and decreases with increasing gluon energy and emission angle. Three striking phenomena should therefore be observed [657 - 665]

(i) asymmetric 2-jet configurations in which one jet, originating from a quark plus a gluon, is wider than the other,

(ii) 'clear' 3-jet events in which the gluon energy and emission angle are large enough that a separated third jet can be created, and

(iii) planar event structures due to the underlying three-body kinematics.

The asymmetry of the jets (i) is studied as a function of the scaled particle momentum $x_p = 2 \cdot p/E_{cm}$ in the so-called 'seagull' plot (6.15). Every event is divided into a 'fat' and a 'slim' jet depending on the average $p_\perp$ [660]. The average $p_\perp^2$ of the charged particles are then plotted separately, with the x_p axis pointing right (left) for the particles of the fat (slim) jet.

Due to statistical fluctuations in the transverse momenta even the symmetric Field-Feynman-model predicts some asymmetry. It is too small, however, to fit the data, *even if the transverse momentum parameter of the model is taken* as high as σ_q = 350 MeV (compare to (6.15)). The inclusion of gluon bremsstrahlung, on the other hand, quantitatively reproduces the observed asymmetry.

The second evidence is given by the events with a clear three-jet topology. One example is shown in Fig. 6.16. The neutral particles, indicated by the dotted lines, are aligned with the direction of the charged particle jets. Such a correlation strongly supports the idea that the structure originates from three and only three parent particles.

A quantitative analysis has been based on the triplicity method as described in section 6.3.1. Thrust T and triplicity T_3 are calculated using both charged and neutral particles. Three-jet structures are characterized by low T and *high* T_3. *Requiring* $T < 0.8$ *and* $T_3 > 0.9$ *leaves 48 three-jet candidates, very* close to the 43 expected from the $q\bar{q}g$ model.

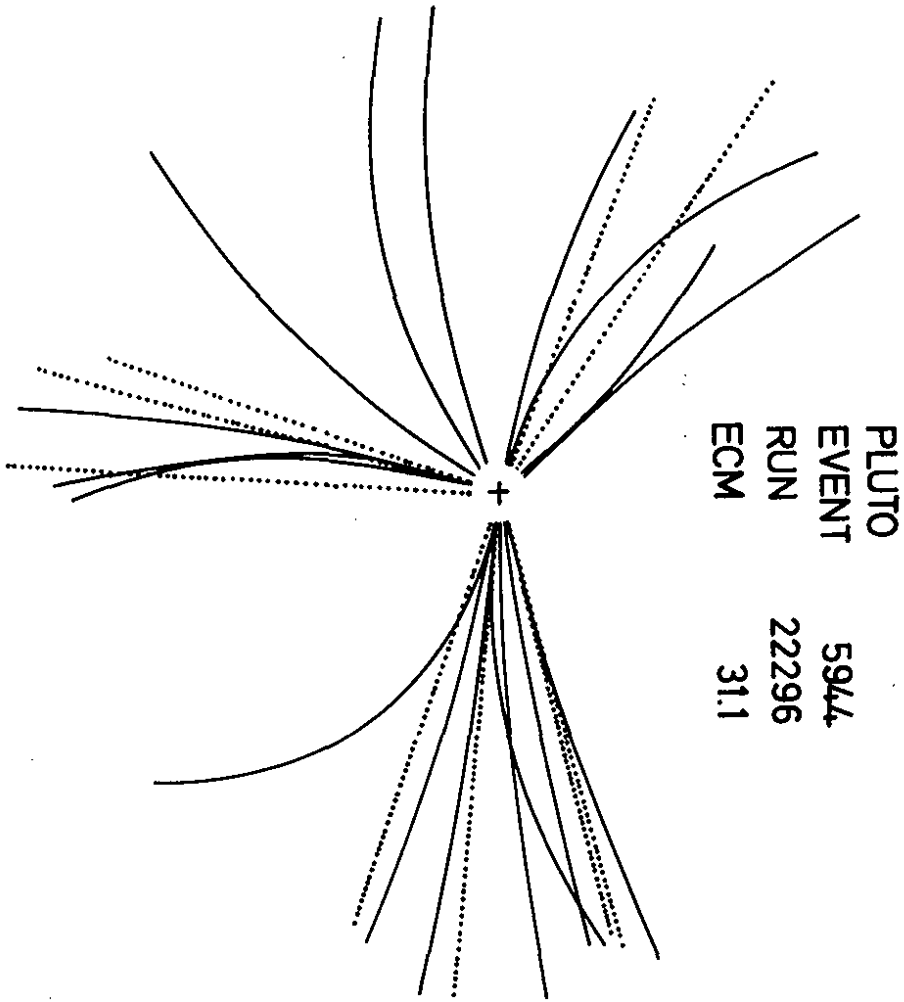

Fig. 6.16 Three-jet event observed at 31.1 GeV with reconstructed charged and neutral particles (full and dashed lines).

Table 6.III: Observed and expected numbers of events obeying different selection criteria [660]

E_{cm} (GeV)	selected region	events observed	events expected (σ_q = 250 MeV) $q\bar{q}$	events expected (σ_q = 250 MeV) $q\bar{q}g$	events expected (σ_q = 300 MeV) $q\bar{q}$	events expected (σ_q = 300 MeV) $q\bar{q}g$	events expected (σ_q = 350 MeV) $q\bar{q}$
13 - 17	$T_3 > 0.9$, $T < 0.8$ (3-jet events)	24	11	15	15.5	17.5	20
	$\theta_3 < 150^0$	32	25	32	27	33	29
	$\langle p_{\perp in}^2 \rangle > 0.5$ GeV^2/c^2	5	5	5	7	10	9
	$S > 0.25$, $Q_1 < 0.03$ (planar events)	7	8	8	9	9	11
27 - 32	$T_3 > 0.9$, $T < 0.8$ (3-jet events)	48	11	43	23.5	48.5	36
	$\theta_3 < 150^0$	52	19	51	25	50	31
	$\langle p_{\perp in}^2 \rangle > 0.5$ GeV^2/c^2	68	23	56	30	61	37
	$S > 0.25$, $Q_1 < 0.03$ (planar events)	35	12	30	17	30	22

The 48 events observed at 30 GeV are incompatible, on the other hand, with the 11 expected from a standard $q\bar{q}$ model, and also, as shown in Table 6.III with modified $q\bar{q}$ models. At 13 and 17 GeV the data favour the $q\bar{q}g$ model, too, although the difference to the $q\bar{q}$ prediction is smaller. The table also presents the evidence that can be obtained with different selection criteria. The second method identifies the triple structure by demanding that the largest of the separation angles between the three axes be smaller than 150^0, with no cut in thrust nor triplicity. The event numbers satisfying this condition (6^{th} line) again are consistent with the expectations of the $q\bar{q}g$ and inconsistent with various $q\bar{q}$ models.

The same is true for two selections based on the expected planar event shape. The analysis uses the momentum components along the three ordered orthogonal directions found by the sphericity method, $\vec{n}_1$, $\vec{n}_2$, $\vec{n}_3$, of which the last two define the event plane. Planar events are characterized by a large squared average momentum component <u>in</u> the plane, $\langle p_{\perp in}^2 \rangle = \langle (\vec{p}\vec{n}_2)^2 \rangle$, and a small one $\langle p_{\perp out}^2 \rangle = \langle (\vec{p},\vec{n}_1)^2 \rangle$ <u>out</u> of the plane. A similar condition in terms of the normalized shape parameters is $Q_2 \gg Q_1$. The third line of table 6.III shows the results of a selection requiring $\langle p_{\perp in}^2 \rangle \geq 0.5$ GeV^2/c^2 while the last one is based on $S = 3/2\ (Q_1 + Q_2) < 0.25$, and $Q_1 < 0.03$. For both selections the data agree with expectations from the $q\bar{q}g$ model, and cannot be explained by $q\bar{q}$ alone.

The third evidence rests on a comparison of the distributions of $\langle p_{\perp in}^2 \rangle$ and $\langle p_{\perp out}^2 \rangle$, as displayed in Fig. 6.17. While the $\langle p_{\perp}^2{}_{out} \rangle$ distribution does not change very much between 13 and 30 GeV, the average momenta <u>in</u> the plane $\langle p_{\perp in}^2 \rangle$ develop a long tail up to 1.5 GeV^2/c^2, corresponding to distinct planar structures. All distributions are well described by the $q\bar{q}g$ model (solid curve), both in the average values as in magnitude of the tail, and cannot be explained by any of the $q\bar{q}$ models considered.

Strong evidence for hard gluon bremsstrahlung has also been obtained by other PETRA experiments [666-668]. Their conclusions are similarly based on comparing the distribution in various planarity observables to the predictions of $q\bar{q}$ and $q\bar{q}g$ (+ higher order) models.

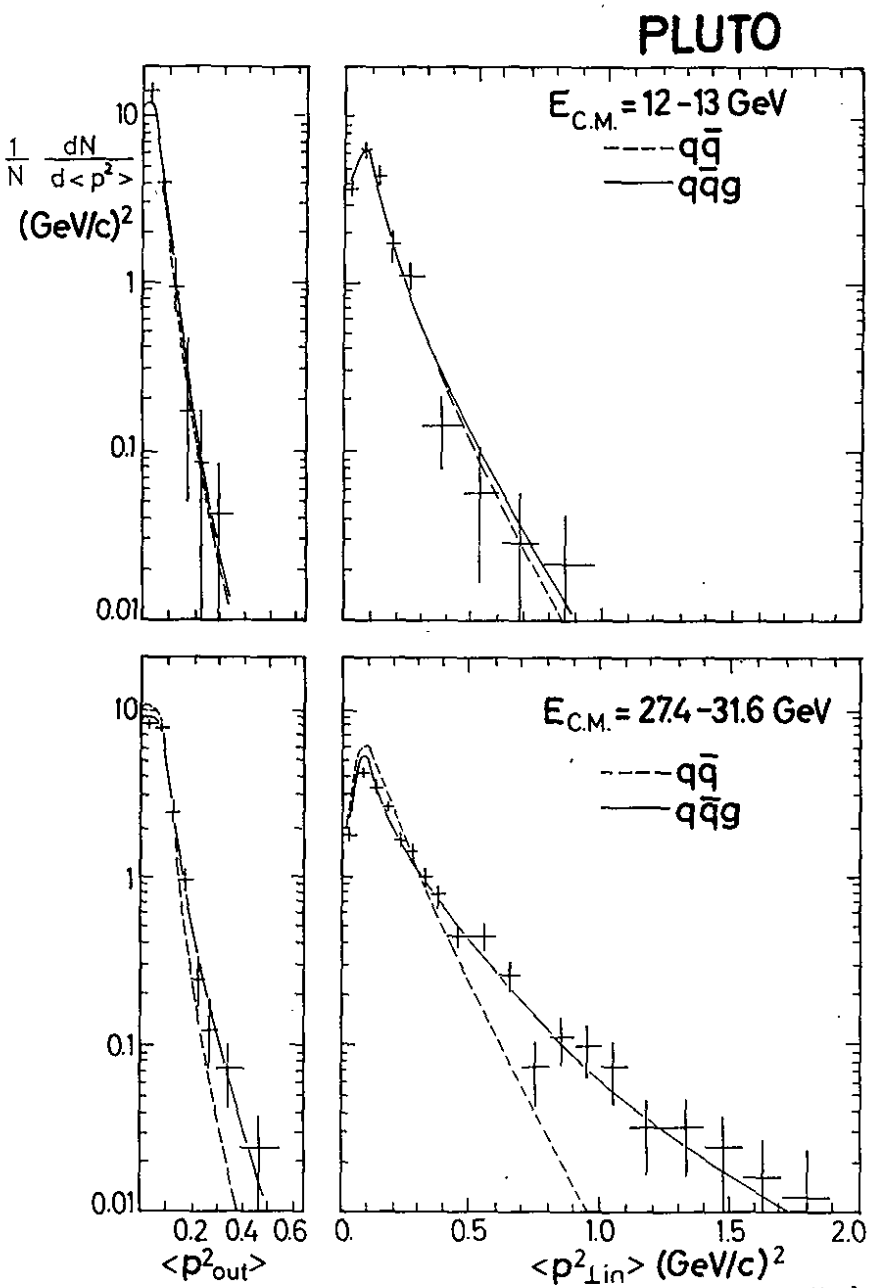

Fig. 6.17 Distribution of the average squared momentum components perpendicular to the jet axis. Left: *out* of the event plane $<p_{\perp out}^2>$. Right: *in the event plane* $<p_{\perp in}^2>$. Dashed and solid curves give expectation from $q\bar{q}$ and $q\bar{q}g$ model.

As an independent approach, the PLUTO group has recently analysed all hadronic events in terms of separated hadron jets as obtained by a new cluster method [653], and used the jets to reconstruct the number and kinematics of the hard parent partons [661, 6909]. This procedure appears to be quite insensitive to details of the fragmentation process, in particular to the mean transverse momentum of the jets (σ_q).

The cluster algorithm uniquely assigns a 'number of jets', n_J, to every event. The observed distribution in n_J, as given in Fig. 6.18 for the combined 27 - 32 GeV data, can then be decomposed into the (Monte-Carlo determined) contributions of several competing reactions, as shown in table 6. IV. The observed distribution is clearly dominated by the 2-jet topology, but contains too many multijet events as to be explained by the $q\bar{q}$ model alone, even if the primordial transverse momentum σ_q is raised as high as 350 MeV (compare to (6.15)). The distribution can be saturated, however, by adding the amount of 'hard $q\bar{q}g$' which corresponds to $\alpha_s = 0.16$. This value of the strong coupling constant is consistent with the results of other PETRA [666-668] and also lepton scattering experiments [669-672], and in particular agrees with the result of the refined determination as outlined below.

The $q\bar{q}g$ = '$q\bar{q}$ + hard $q\bar{q}g$' prediction also accounts for most of the events with $n_j = 4$, allowing only for a very few events originating from four separated hard partons, in agreement with recent QCD calculations to order α_s^2 [673]. The absence of events with $n_j = 6,7$ limits an isotropic component which may arise from the threshold production and isotropic decay of new heavy particles to less than 3% of the total cross section (99% C.L.).

The 3-jet class can now be used for investigating the dynamics of the $q\bar{q}g$ system. In order to reduce the contamination of $q\bar{q}$ events, the three jets are required (i) to have two or more particles each, (ii) to contain more than 90% of the visible energy together, (iii) to be spaced by less than 165^0, and (iv) to be planar within 45^0 (see[661]). Fig. 6.19 gives the distribution of the jet thrust T_J (see 6.3.1), corrected for the estimated contribution of $q\bar{q}$ events.

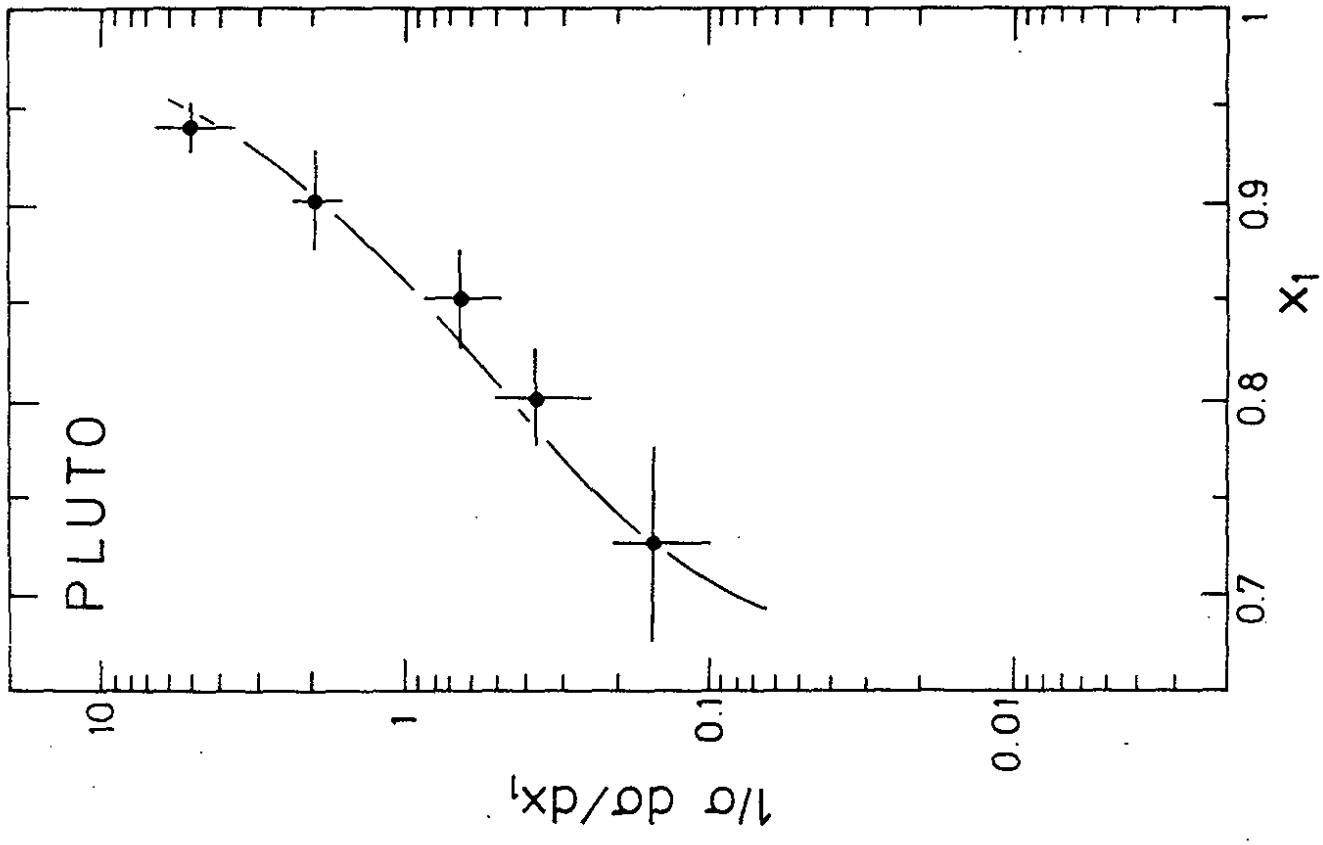

Fig. 6.19 Distribution of parton thrust x_1 for the 3-jet event class. Solid curve gives expectation from 1st order QCD.

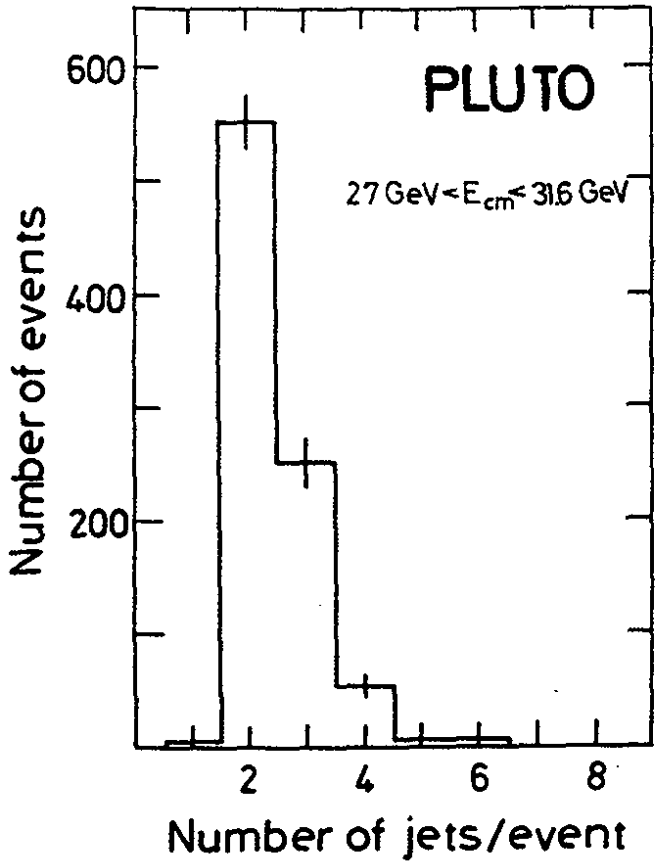

Fig. 6.18 Distribution of number of jets as reconstructed by the cluster algorithm from the combined 27 - 32 GeV data.

Table 6.IV

n_j=	1	2	3	4	5	6	7
Data	2	551	249	53	3	1	
$q\bar{q}$	3	680	152	23	1		
$q\bar{q}g$	2	229	509	113	5	1	
$q\bar{q}+q\bar{q}g$	3	567	247	46	2		
PS	1	30	154	306	268	86	14

Distributions of the observed numbers of jets per event (n_j) for data and different models, all normalized to the number of observed events. For the $q\bar{q}+q\bar{q}g$ -model $\alpha_s = 0.15$ is assumed.

Because of the close correspondence between T_J and x_1, the scaled energy of the most energetic parton (Fig. 6.9), the T_J-distribution can be directly compared to theoretical predictions in x_1. The data agree well with the first order QCD curve [662] over the full range $0.7 \leq x_1 \leq 0.95$. Second order QCD corrections to the 3 jet cross sections are discussed by several authors [674, 675], with controversial conclusions at present.

It is pointed out in [6909] that the data are not consistent with the distribution predicted from scalar gluons [662], and also disagree with the prediction of the constituent interchange model CIM [663].

By adjusting the first order QCD prediction to the data in the restricted range $x_1 < 0.925$ one obtains the strong coupling constant at 30 GeV as [6909]

$$\alpha_s = 0.16 \pm 0.02 \text{ (stat.)} \pm 0.02 \text{ (syst.)} \qquad (6.16)$$

The systematic error resulting from the fragmentation parameter σ_q is particularly small in this method, namely less than 0.01 for $250 \leq \sigma_q \leq 350$ MeV/c (compare to (6.15)).

In conclusion, with the help of the cluster method 3-parton events can efficiently be selected, and the parton kinematics be reconstructed. The QCD predicted energy distribution of the partons in the process $e^+e^- \to q\bar{q}g$ has been verified, and the strong coupling constant has been determined with a small systematic error.

6.4 Multiparton effects

As demonstrated in the previous section the fragmentation model [656] with single gluon emission added [657] is quite successful in describing the observed 2- and 3-jet topologies in great detail, and can be used to clearly establish effects of hard gluons. In this description the fragmentation part as determined by the empirical constant σ_q dominates most of the global jet properties like $\langle p_{\parallel} \rangle$ and $\langle p_{\perp} \rangle$ (Fig. 6.14), at least up to 30 GeV.

Several authors [650, 676-678] have developed an alternative description in which not just a small correction, but the dominant part of the jet formation is predicted from first principles of QCD. The process is split in two steps, as sketched in Fig. 6.20: First the evolution of a cascade of partons (quarks and gluons) out of the initial quarks, and then the conversion of the partons into hadrons. The cascade part is described by perturbative QCD. Since the probability for the emission of soft gluons is not small at all, the contributions of high-order diagrams cannot be neglected, and are summed up in 'leading log approximation' (LLA). The underlying hope is that the second step, the conversion of the final partons into hadrons, has little effect on the calculated observables ('soft hadronization'), so that at sufficient high energies these parton predictions can be directly compared to the hadron data. In the following sections LLA predictions on energy-energy correlations, transverse momenta, and multiplicity distributions will be confronted with PLUTO data taken in the energy range from 7 to 32 GeV.

6.4.1 Energy-energy correlations

The first LLA calculations predicted the energy-energy correlation (6.14) for angles close to 180^0 [650], as well as close to 0^0 [678]. Later papers basically confirmed the early predictions, but also introduced corrections and modifications [679 - 686]. For angles around 90^0, the correlation was predicted from first order QCD [651].

Measurements of the correlation were presented by the PLUTO group first for both angular regimes separately [687], and then with improved statistics for the full angular range [688]. Fig. 6.21 shows the data over the full range, corrected for initial state radiation, particle losses, and detector resolution.

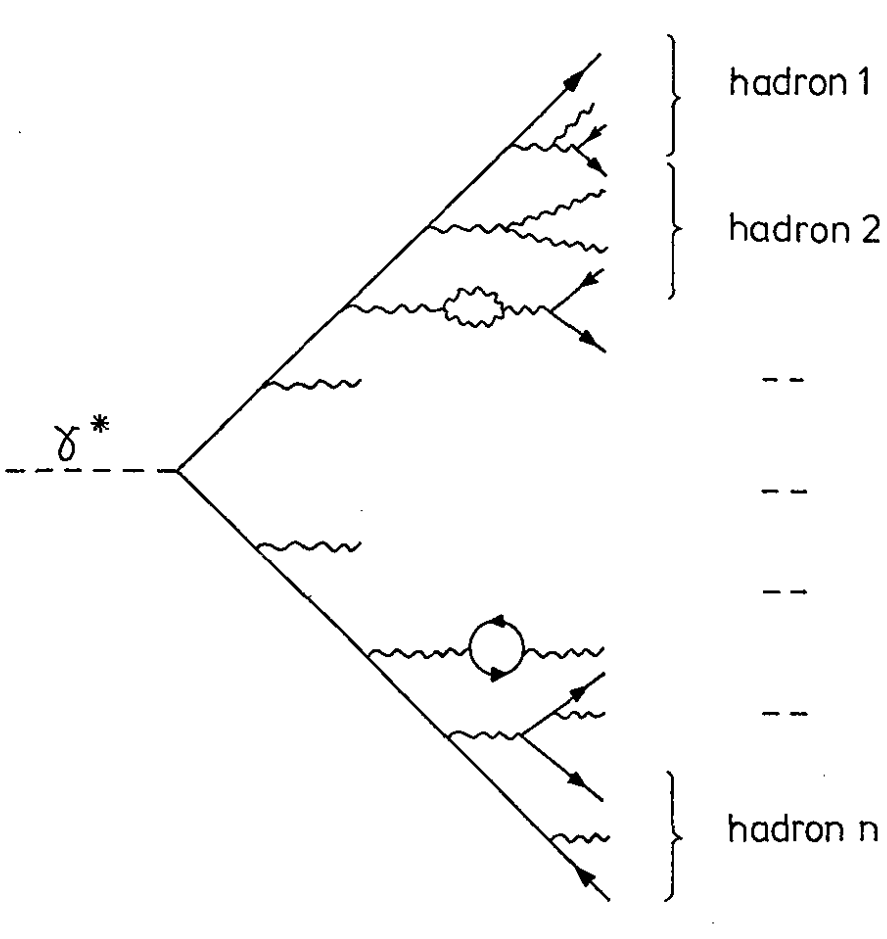

Fig. 6.20 Quark-gluon cascade.

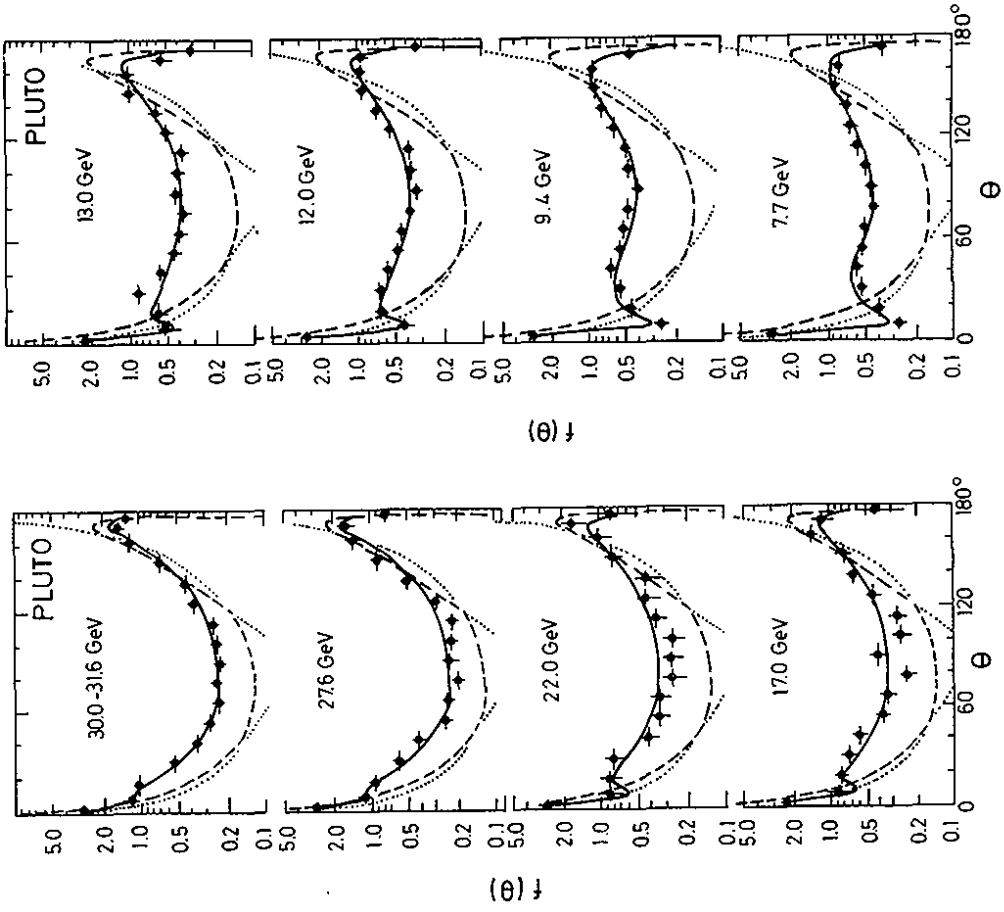

Fig. 6.21 Energy-energy correlation vs. particle-particle angle for different c.m. energies. Full line shows fragmentation model ($q\bar{q}$ below 10 GeV, $q\bar{q}g$ above). Dashed lines give pure QCD predictions acc. to Ref.[678](0-50°), Ref.[651] (50°-120°), and Ref.[679] (120°-180°), all with Λ = 200 MeV. Dotted lines indicate continuation of QCD predictions.

At low energies the distribution is flat, corresponding to a weakly visible two-jet structure. (Isotropy would lead to $f(\theta) \sim \sin\theta$). With increasing energy the two-jet structure becomes more pronounced in form of two peaks at particle-particle angles close to zero and to 180 degrees. All these features are very well reproduced by the $q\bar{q}$ fragmentation model, with hard gluons added at the higher energies ($q\bar{q}g$). (Full lines in Fig. 6.21)

A 'pure QCD' prediction (dashed lines in Fig. 6.21) can be constructed by smoothly connecting the results of 'KUV' [678], 'BBEL' [651], and 'PP' [679] at 50^0 and 120^0. As a typical feature of QCD, this prediction varies only slowly with the energy. It completely fails at low energies, but approaches the data with increasing energy. Good qualitative agreement is reached in the backward direction.

In contrast, most of the forward and central region is predicted about a factor two too low. This discrepancy could be cured by inserting a larger coupling constant α_s into the QCD expressions, but is more naturally attributed to the final conversion of the partons into hadrons. With increasing energy such 'non-perturbative' effects should die away like powers of $1/E_{CM}$. As an example, the energy dependence in the central region can be written as [651]

$$f(\theta,E_{cm}) = \alpha_s\,(E_{cm}^{\,2}) \cdot g(\theta) + \frac{\langle p_\perp \rangle \cdot C}{E_{cm}} \sin^{-2}\theta \qquad (6.17)$$

The first term is the first order QCD result shown in Fig. 6.21, and the second one (with $C \cdot \langle p_\perp \rangle \sim 1$ GeV) accounts for the spillover of the fragmentation from the forward and backward region. Fig. 6.22 demonstrates that the correlation integrated over the central region indeed follows the expected energy dependence. At 30 GeV the QCD term (dashed curve, with Λ = 200 MeV) accounts for more than half of the correlation, but still does not dominate.

A different method of separating the QCD effect consists in looking at the asymmetry $f(\pi-\theta) - f(\theta)$, thereby eliminating the fragmentation term [651]. Ref. [688] shows that one can indeed observe a fragmentation-free asymmetry at 30 GeV (not at 9.4), however with too poor statistics to exploit it.

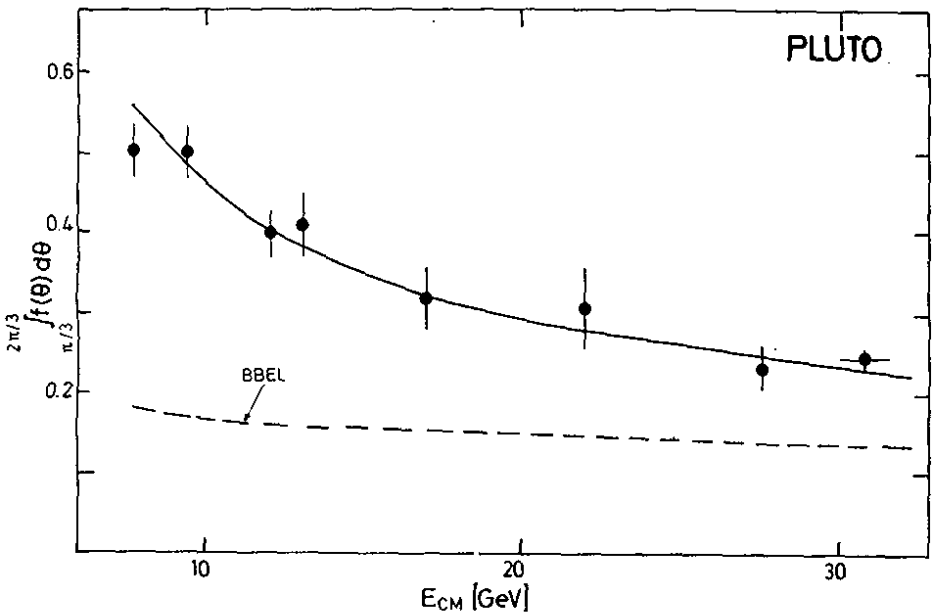

Fig. 6.22 Central (60-120^0) energy-energy correlation vs. c.m. energy. Dashed line: pure QDC. Full line: fragmentation added.

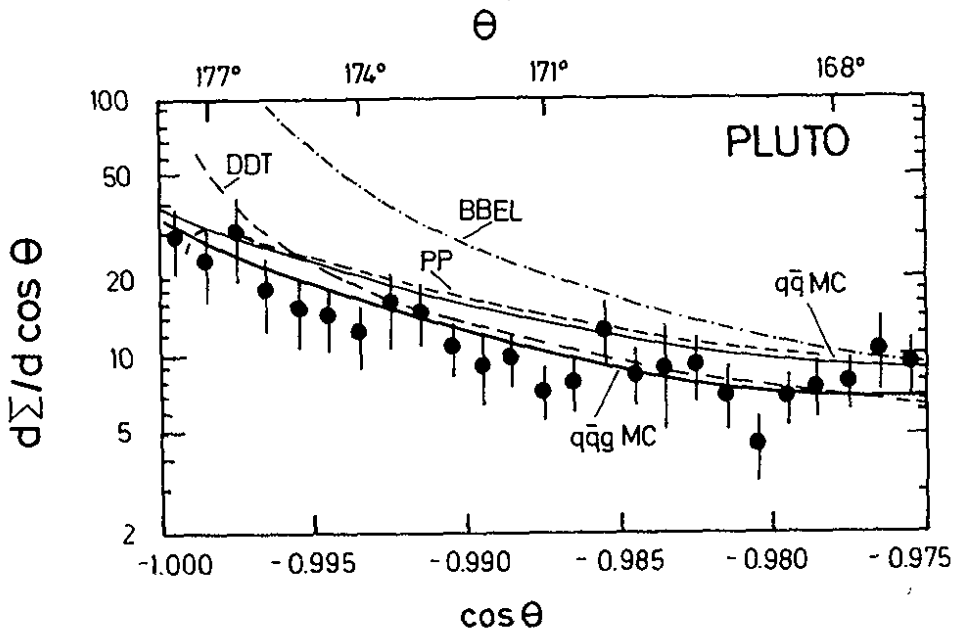

Fig. 6.23 Energy-energy correlation in extreme backward directions as measured between 27 and 32 GeV. Fragmentation models: upper full line $q\bar{q}$, lower full line $q\bar{q}g$. Pure QCD predictions are labelled: DDT [650], BBEL [651], and PP ([679], Equ. (3.3); which results from the exponentiation in momentum and not in impact space).

Fig. 6.23 shows the backward region of the 30 GeV data, plotted as $d\Sigma/d\cos\theta$, because $f(-\pi)$ is zero from phase space. The data approach a non-zero limit for $\cos\theta \to -1$, in accordance with the $q\bar{q}g$ fragmentation model. The LLA calculations (DDT, PP) successfully reproduce the data over most of the range.[+] This means that the back-to-back correlation of hadrons can qualitatively be understood as dominated by parton branching process (Fig. 6.20), calculable from perturbative QCD alone.

It thus appears that energy-energy correlations are indeed, as proposed, a sensitive measure for QCD effects.[++] First order effects can be separated in the central region, and agree with expectations. The description of the forward and backward peaks in terms of high-order parton cascades (LLA) improves with increasing energy. At 30 GeV it qualitatively reproduces the backward data, while the prediction in the forward region still stays a factor of 1.5 too low. There are several proposals to improve the leading-log order of the jet calculus by next-to-leading orders [689 - 6901], by better accounting for finite energy kinematics in Monte-Carlo calculations [6902 - 6905], and by phenomenologically accounting for effects of the parton-hadron conversion [679, 686]. It will be interesting to see whether these efforts succeed, or whether the hope of describing the jet features at present energies by QCD alone is altogether premature.

[+] One should note that the limit $\cos\theta \to 1$ cannot be covered by perturbative QCD, because the expansion parameter α_s diverges at $\sin(\theta/2) = \Lambda/E_{CM}$. Refs. [679, 686] propose to treat this region by exponentiating the gluon emission in impact space.

[++] Basically, the same information is contained in the Fox-Wolfram moments which according to (6.13) are just the Legende coefficients of the correlation function. A detailed investigation of the different angular regions, however, would have to resort to a fairly large number of such moments.

6.4.2 Multiplicity distributions

Additional insight into the mechanism of hadron production may be obtained from a study of the average and the distribution of the multiplicity. General scaling arguments [6910] as well as specific fragmentation models [656, 657] lead to a logarithmic increase of the average multiplicity $\langle n \rangle$ with the energy like

$$\langle n \rangle = a + b \ln s \qquad (6.18)$$

A stronger rise with s is suggested by perturbative QCD calculations of a parton cascade, namely [6911 - 6914]

$$\langle n \rangle = A + B \exp\left(C \sqrt{\ln(s/\Lambda^2)}\right) \qquad (6.19)$$

with $C = 2.4$ for $n_F = 4$ flavours. In addition, the QCD calculations yield two interesting predictions about the distribution of the multiplicities, namely

(i) KNO - scaling, meaning an energy-independent distribution which depends only on the ratio $n/\langle n \rangle$ [6915] and

(ii) a large relative dispersion, namely

$$D/\langle n \rangle = \sqrt{\langle n^2 \rangle / \langle n \rangle^2 - 1} = \sqrt{3/4} \qquad (6.20)$$

for one quark-initiated jet.

An even stronger asymptotic rise like $s^{0.25}$ is expected in the thermodynamic model [6916]. Still higher power laws up to $s^{1/2}$ occur in statistical models [602].

The energy dependence of the average charged multiplicity [615], corrected for detector effects, is shown in Fig. 6.24. For comparison with the data from ADONE [6918], SPEAR [625], and the JADE [618] and TASSO [6919] experiments at PETRA, the pions from the decay $K_s^0 \to \pi^+\pi^-$ (≈ 0.6 units around 10 and ≈ 1.0 units around 30 GeV) have been included in the figure. Recent results of the LENA experiment [6907] at DORIS are also shown. The data points scatter by about 10%, consistent with the estimated systematic errors from track recognition in dense jets and unfolding detector effects. The general conclusions, however, are independent of these differences.

The multiplicity appears to follow one straight line (6.18) at low energies (fitted by [6918]), and then to rise much more rapidly above 10 GeV. This rapid rise agrees with the one expected from the quark fragmentation models

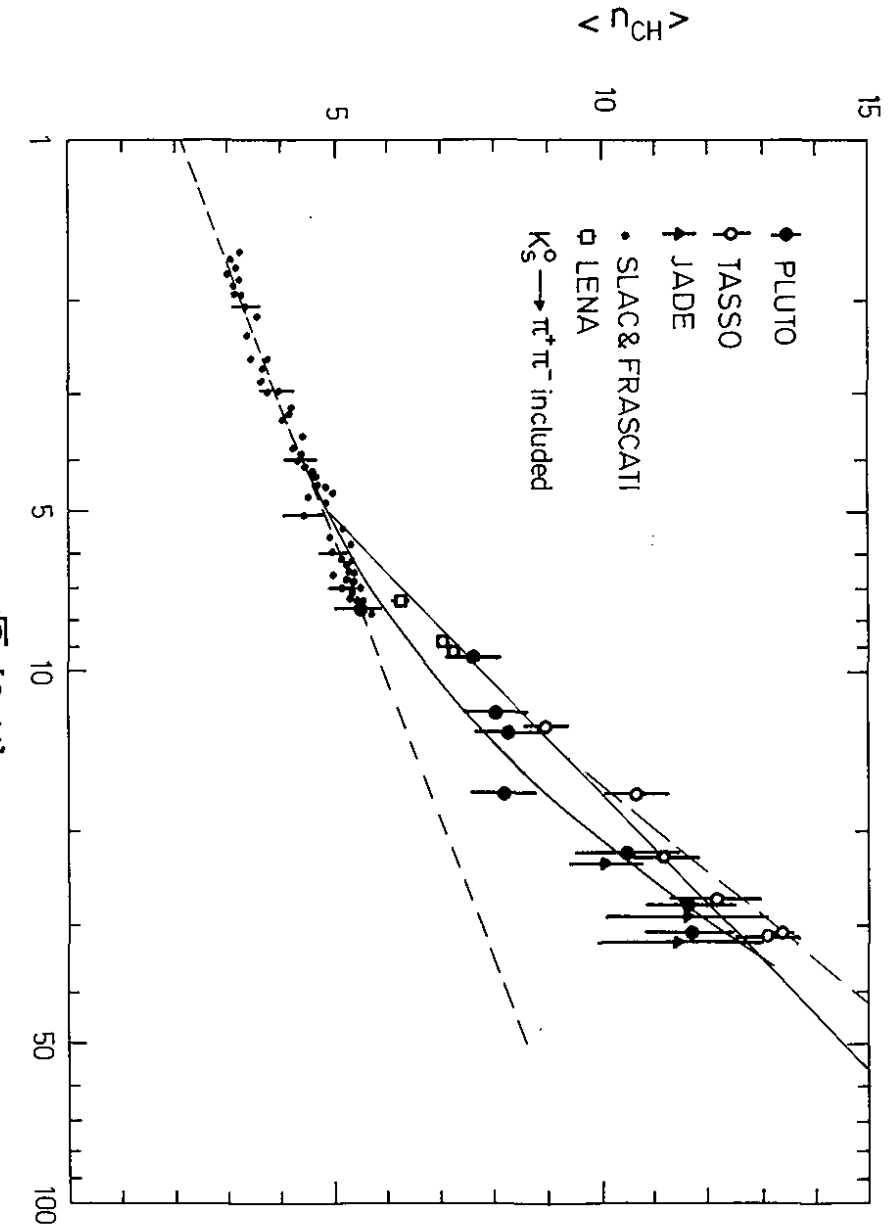

Fig. 6.24 Energy dependence of the average charged multiplicity for e^+e^- - annihilations.

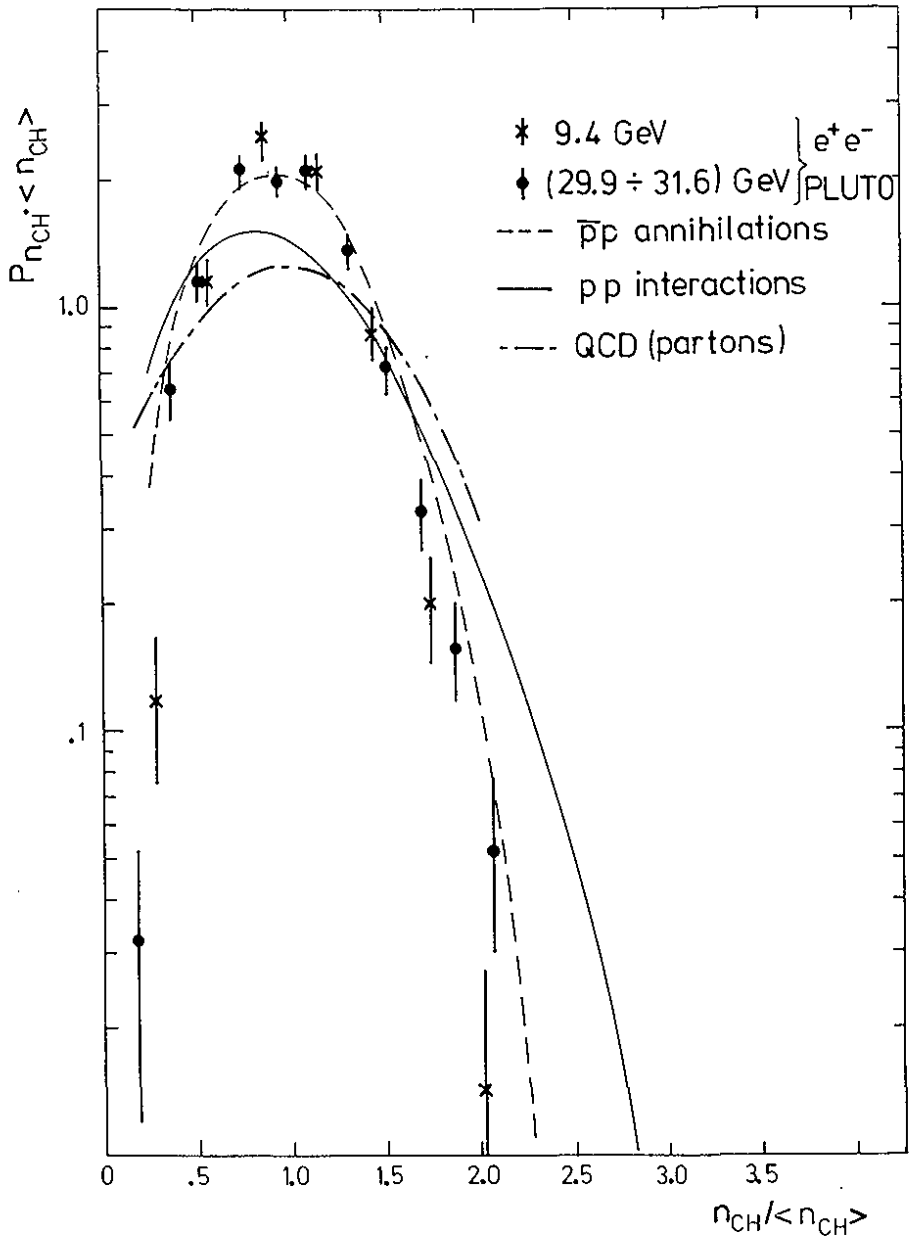

Fig. 6.25 KNO plot for e^+e^- PLUTO data at 9.4 and 30.7 GeV. The dashed-dotted curve gives the analytic QCD prediction as explained in the text.

[656,657], indicated by the two steeper straight lines. The difference between the two shows that the contribution of the gluon jet is still very small at these energies.

Smooth curves describing the multiplicity over a larger energy range are given by the thermodynamic model with $\langle n \rangle = (2.2 \pm 0.1)\, s^{(0.25 \pm 0.01)}$, and by the QCD cascade predictions (6.19) with $\Lambda = 200$ MeV, $A = 2.16 \pm 0.16$, $B = 0.010 \pm 0.004$, and $C = 2.20 \pm 0.11$ [+]. The data on $\langle n_{ch} \rangle$ thus cannot distinguish between general cascading models and the special dynamics of QCD, but only exclude models with higher powers of s.

A special prediction of QCD, KNO scaling of the multiplicity distribution, works well between 9.4 and 30 GeV, as shown in Fig. 6.25. The observed dispersion of $D/\langle n \rangle \approx 0.36 \pm 0.02$, however, is much smaller than the value 0.61 predicted for two quark jets (dashed line). The discrepancy in the dispersion indicates that the analytic LLA expression (6.19) should only be applied, if at all, at much higher energies.

On the other hand, the $q\bar{q}g$ fragmentation model [657] gives a relative dispersion $D/\langle n \rangle$ which varies slowly from 0.38 to 0.32 between 10 and 30 GeV, quite consistent with the data. Similarly, LLA Monte Carlo calculations which, after a very few hard parton branchings [6907], also resort to the Field-Feynman fragmentation algorithm, or alternatively to experimental fragmentation data directly [6902], lead to approximate KNO scaling and to dispersions consistent with the data [6906, 6920].

It thus appears that the multiplicity data at these energies cannot be related to calculable fundamental QCD processes, but are dominated by the (at present uncalculable) fragmentation processes.

[+] As the data with their quoted statistical errors only are inconsistent with any smooth energy dependence, a systematic error of 5% has been added in quadrature to every point, resulting in a good probability for the fit (~ 70%). Similary good fits are obtained with $\Lambda = 500$, and also with C fixed to 2.4.

6.4.3 Transverse momenta

The transverse hadron momenta relative to the flight direction of the initial quark can either be parametrized by the fragmentation constant σ_q, or perhaps be understood as the result of multiple gluon emission, leading to a quark-gluon cascade. As a variable which can be calculated from perturbative QCD the transverse momentum $K_\perp$ has been proposed [6921]. It is obtained by summing the transverse momentum vectors within one hemisphere like:

$$K_\perp = \Big| \sum_{\text{one jet}} \vec{p}_{i\perp} \cdot \Theta\,(p_i \cdot \hat{n}_\perp) \Big|, \qquad (6.21)$$

where $\hat{n}_\perp$ is an arbitrary vector perpendicular to the jet axis, and $\Theta\,(x) = 0,1$ for $x \leq 0$, >0.

A QCD prediction for the probability distribution $P\,(K_\perp)$ ([6921, 6922]) has been obtained from a LLA summation of multiple gluon emission. This summation extends over gluon momenta $k_\perp$ down to zero, clearly outside the range of perturbative QCD. This non-perturbative region which contributes the major part of the prediction is globally treated by replacing the 'running' coupling constant α_s by a fixed value α_{eff} [6923]. The resulting formula gives an interesting scaling distribution which depends only on the ratio $K_\perp/\langle K_\perp\rangle$ [6921,6924].

The data were evaluated by summing (6.21) over charged particles only, and were corrected for the detector acceptance and resolution, and for initial state radiation.

Fig. 6.26 shows that the measured distributions indeed scale, not only for the reduced summed momenta $K_\perp/\langle K_\perp\rangle$, but surprisingly also for the reduced single particle momenta $p_\perp/\langle p_\perp\rangle$. Figs. 6.27 and 6.28 show the data separately for different c.m. energies. The LLA prediction (solid curves, scaled from $K_\perp/\langle K_\perp\rangle$ to $K_\perp$) fits the major part of the distributions very well. At the highest $K_\perp$, however, the data show an excess which strongly grows with increasing c.m. energy. It is attributed to the emission of single hard gluons, and very well described by 1st order QCD [663, 664] (dashed curves).

The LLA summation of soft gluon emission can thus reproduce the major part of the $K_\perp$ distributions very well, including the scaling property. In addition, the distributions show clear evidence for hard gluon emission in form of a pronounced large $K_\perp$ tail.

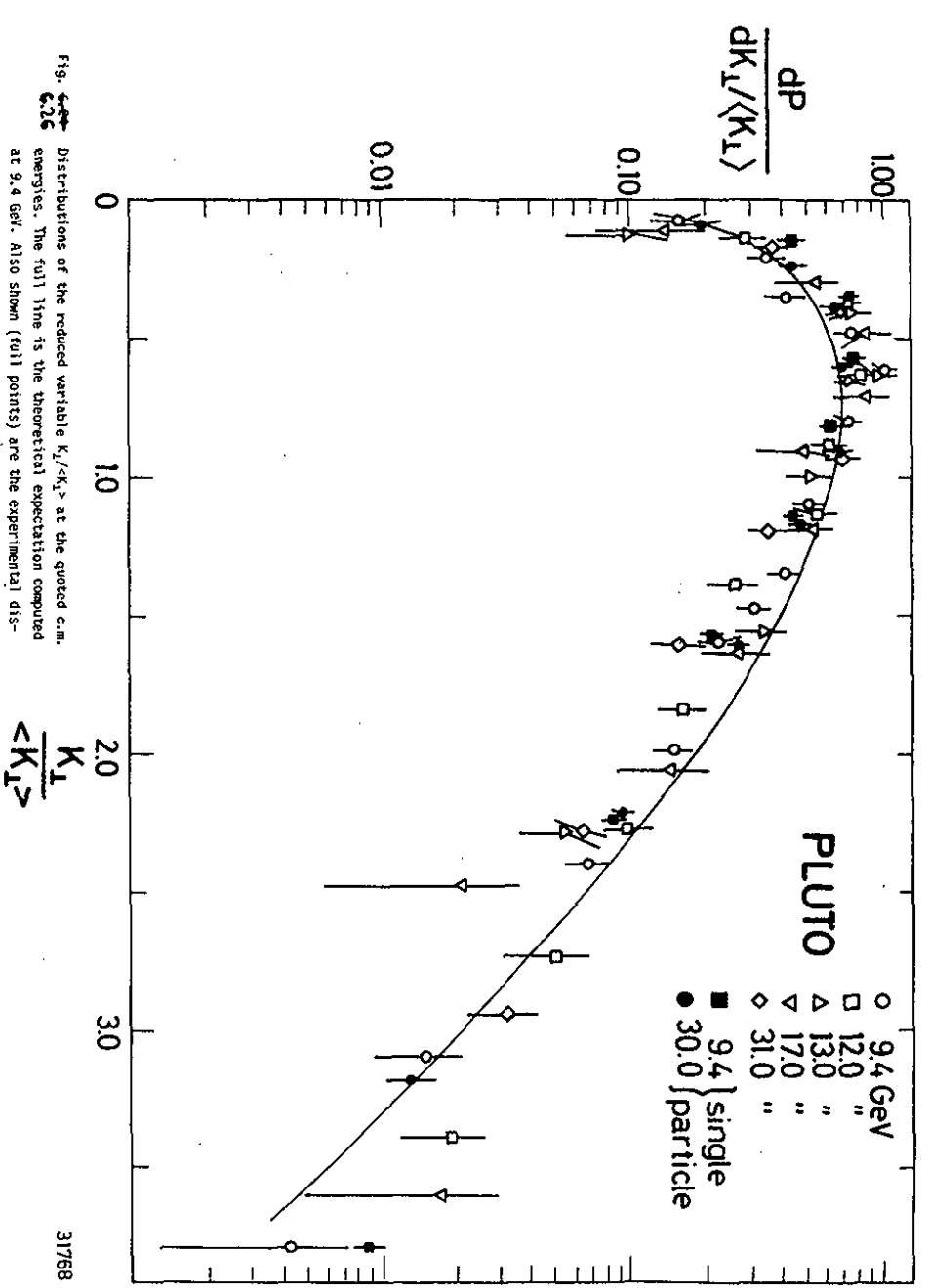

Fig. 6.26 Distributions of the reduced variable $K_\perp/\langle K_\perp\rangle$ at the quoted c.m. energies. The full line is the theoretical expectation computed at 9.4 GeV. Also shown (full points) are the experimental distributions of the corresponding single particle reduced variable $p_\perp/\langle p_\perp\rangle$ at 9.4 and 30 GeV. (In order not to overload the figure, we show here only one of our high energy distributions, which are reported in Fig. 6.28).

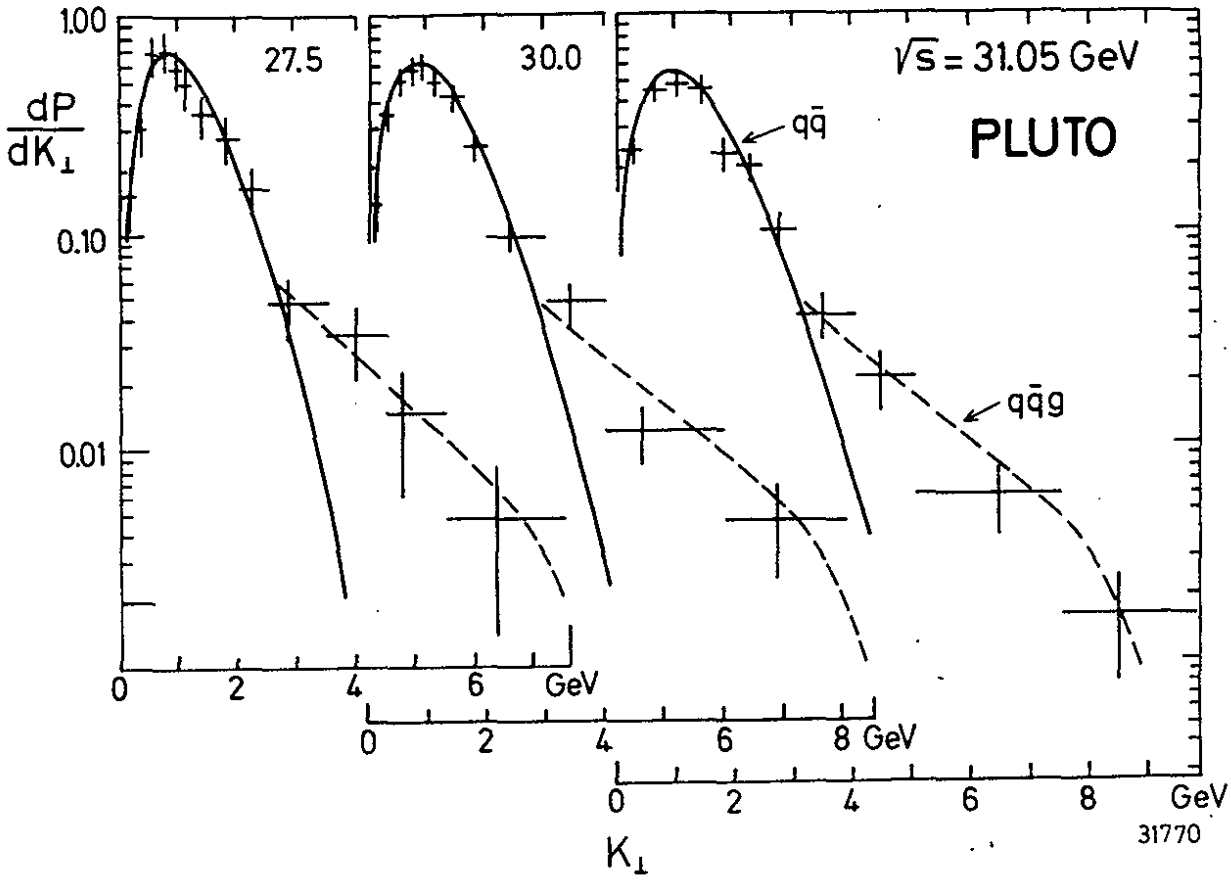

Fig. 6.28 Same as Fig. 6.25 for 27.5, 30 and 31.05 GeV average c.m. energies. (The two last points for 30 GeV do not appear in Fig.6.24, being out of range).

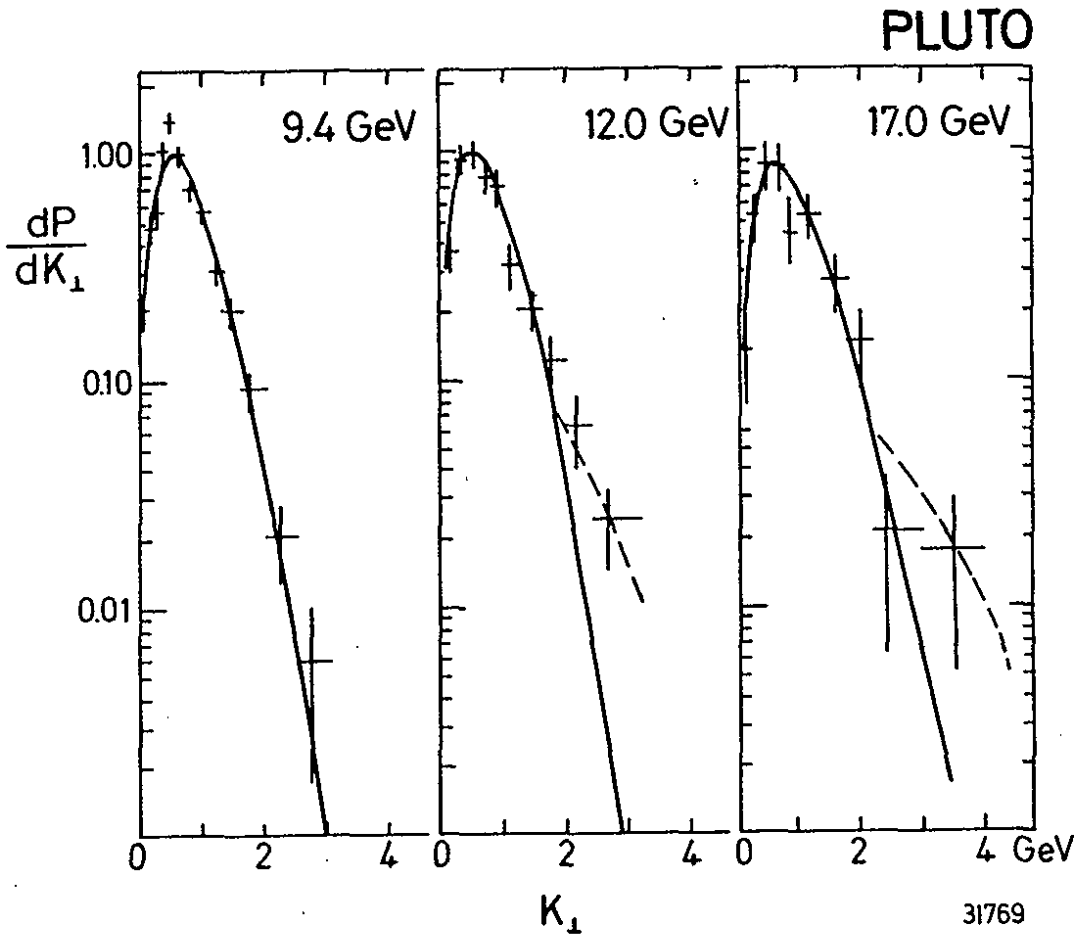

Fig. 6.27 Distributions of the jet transverse momentum $K_\perp$ at 9.4, 12 , 17 GeV compared with QCD expectation (see text).

6.4.4 Conclusions

As general conclusions to be derived from the e^+e^- induced hadron production both the total cross section and particularly the formation of 2-jet final states demonstrate very clearly the role of quarks as the underlying 'elementary' particles.

All observed features are well consistent with the emission of gluons as postulated by QCD. These first order QCD effects have been isolated in energy-energy correlations and particularly well in three-jet studies, and have been used to confirm the QCD predicted dynamics of the $q\bar{q}g$ system and to fix the strong coupling constant α_s.

LLA predictions of the jet evolution are successful in opposite-side energy-energy correlations, but less so in same-side correlations and multiplicity distributions, and appear to need some more refinements, at least for applications at presently available energies.

References

[601] S.D.Drell, D.Levi and T.Yan, Phys.Rev. 187 (1969) 2159

[602] J.D.Bjorken and S.J.Brodsky, Phys.Rev. D1 (1970) 1416

[603] T.Appelquist and H.Georgi, Phys.Rev. D8 (1973) 4000

[604] A.Zee, Phys.Rev. D8 (1973) 4038

[605] M.Dine and J.Sapirstein, Phys.Rev.Lett. 43 (1979) 668

[606] K.Khetyrkin, A.L.Kataev and F.V.Tkakov, Phys.Lett. 85B (1979) 277

[607] W.Celmaster and R.J.Gonsalves, Phys.Rev.Lett 44 (1980) 560, Phys.Rev. D21 (1980) 3312

[608] PLUTO Collaboration J.Burmester et al., Phys.Lett. 66B (1977) 395

[609] " " A.Bäcker, thesis, DESY F33-77/03 (1977)

[610] " " Ch.Berger et al., Phys.Lett. 76B (1978) 243

[611] " " Ch.Gerke, thesis, report PLUTO 80/03

[612] " " Ch.Berger et al., Phys.Lett. 81B (1979) 410

[613] " " Ch.Berger et al., Phys.Lett. 86B (1979) 413

[614] " " Ch.Berger et al., Phys.Lett. 91B (1980) 148

[615] " " W.Lackas, thesis

[616] TASSO " R.Brandelik et al., Phys.Lett. 88B (1979) 199, and Z. Physik C4 (1980) 87

[617] D.P.Barber et al., Phys.Rev.Lett. 43 (1979) 830 and 44 (1980) 1722 Phys.Lett 85B (1979) 463, Phys.Rep. 63C (1980) 337

[618] JADE Collaboration, W.Bartel et al., Phys.Lett. 88B (1979) 171; 89B (1979) 136 ; 91B (1980) 152

[619] PLUTO " Ch.Berger et al., Phys.Rev.Lett. 45 (1980) 1533

[620] M.Böhm, H.Joos and M.Krammer, Acta Phys. Austr. 38 (1973) 123

[6201] J.J.Sakurai, Phys.Lett. 46B (1973) 207

[6202] D.R.Yennie, Phys.Rev.Lett. 34 (1975) 239

[621] F.E.Close, D.M.Scott, D.Sievers, Phys.Lett. 62B (1976) 213

[622] T.Walsh, DESY report 76/13 (1976)

[623] G.J.Gournaris, Phys.Lett. 72B (1977) 91

[624] M.Greco, Phys.Lett. 77B (1978) 84

[625] J.Siegrist et al., Phys.Rev.Lett. 36 (1976) 700;
SLAC 225 (1980) (thesis)

[626] DASP Collaboration, R.Brandelik et al., Phys.Lett. 70B (1977) 125;
73B (1978) 109

[627] For a review of the low energy data see
G.Feldman, Proceedings of the 1978 Tokyo Conference

[628] G.S.Goldhaber et al., Phys.Rev.Lett. 37 (1976) 255

[629] I.Peruzzi et al., Phys.Rev.Lett. 37 (1976) 569

[630] G.Trilling, Phys.Reports C, to be published

[631] S.L.Glashow, J.Illiopoulos, and L.Maiani, Phys.Rev. D2 (1970) 1285

[632] S.Okubo, Phys.Lett. 5 (1963) 105

[633] G.Zweig, CERN Rep. TH-401, 412 (1964)

[634] J.Iizuka, K.Okada and O.Shito, Progr.Theor.Phys. 35 (1966) 1061

[635] N.Cabbibo, Phys.Rev.Lett. 10 (1963) 531

[636] M.Roos, Phys.Lett. 36B (1971) 130

[637] PLUTO Collaboration, J.Burmester et al., Phys.Lett. 64B (1976) 369

[638] " " J.Burmester et al., Phys.Lett. 67B (1977) 367

[639] M.Bander et al., Phys.Rev.Lett. 36 (1976) 695

[640] C.Rosenzweig, Phys.Rev.Lett. 36 (1976) 697

[641] A.de Rújula, H.Georgi and S.L.Glashow, Phys.Rev.Lett 38 (1977) 317

[642] PLUTO Collaboration, J.Burmester et al., Phys.Lett. 68B (1977) 283

[643] " " Ch.Berger et al., Phys.Lett. 82B (1979) 449

[644] S.L.Wu and G.Zobernig, Z.Physik C2 (1979) 107

[645] S.Brandt, Ch.Peyrou, R.Sosnowski and A.Wroblenski, Phys.Lett. 12 (1964) 57

[646] E.Farhi, Phys.Rev.Lett. 39 (1977) 1587

[647] A.de Rújula, J.Ellis, E.G.Floratos and M.K.Gaillard,
Nucl.Phys. B 138 (1978) 387

[648] S.Brandt and H.D.Dahmen, Z.Physik C1 (1979) 61

[649] P.Grassberger and E.H.De Groot, Nucl.Phys. B 102 (1976) 297

[650] Yu.L.Dokshitser, D.I.D'yakonov and S.I.Trojan,
Phys.Lett. 78B (1978) 290, and Phys.Rep. C58 (1980) 269

[651] C.L.Basham, L.S.Brown, S.D.Ellis and S.T.Love,
Ph.R.Lett. 41 (1978) 1585, and Phys.Rev. D17 (1978) 2298; D19 (1979)

[652] G.C.Fox and S.Wolfram, Phys.Rev.Lett. 41 (1978) 1581, and
Nucl.Phys. B 149 (1979) 413

[653] H.J.Daum, H.Meyer and J.Bürger, Z.Physik C8 (1981) 167

[654] G.Hanson et al., Phys.Rev.Lett. 35 (1975) 1609;
13. Rencountre de Moriond (1978), ed. by J.Tran Tranh Van, Vol. III

[655] PLUTO Coll., Ch.Berger et al., Phys.Lett. 78B (1978) 176

[656] R.D.Field and R.P.Feynman, Nucl.Phys. B 136 (1978) 1

[657] P.Hoyer, P.Osland, H.G.Sander, T.F.Walsh, P.M.Zerwas,
Nucl.Phys. B 161 (1979) 349

[658] A.Ali, E.Pietarinen, G.Kramer, J.Willrodt, Phys.Lett. 93B (1980) 155

[659] A.Ali, J.G.Körner, G.Kramer, J.Willrodt, Z.Phys. C1 (1979) 203

[660] PLUTO Coll., Ch.Berger et al., Phys.Lett. 86B (1979) 418

[661] " " Ch.Berger et al., Phys.Lett. 97B (1980) 459, see also [6909]

[662] J.Ellis, M.K.Gaillard, G.Ross, Nucl.Phys. B 111 (1976) 253
B 130 (1977) 516

[663] T.A.De Grand, Y.J.Ng, S.-H.H.Tye, Phys.Rev. D16 (1977) 3251

[664] A.J.De Rujula, J.Ellis, E.G.Floratos, M.K.Gaillard,
Nucl.Phys. B 138 (1978) 387

[665] G.Kramer and G.Schierholz, Phys.Lett. 82B (1979) 108

[666] TASSO Coll., R.Brandelik et al., Phys.Lett. 86B (1979) 243
and 94B (1980) 437

[667] D.P.Barber et al., Phys.Rev.Lett. 43 (1979) 830; Phys.Lett. 89B (1980) 139

[668] JADE Coll., W.Bartel et al., Phys.Lett. 91B (1980) 152

[669] P.C.Bosetti et al., Nucl.Phys. B142 (1978) 1 and Z.Physik C1 (1979) 143

[670] J.G.H.De Groot et al., Phys.Lett. 82B (1979) 292

[671] J.J.Aubert et al., preprint (Madison Conf. 1980)

[672] H.E.Montgomery, CERN-EP/80 - 177 (1980)

[673] A.Ali et al., Phys.Lett. 82B (1979) 285 and Nucl.Phys. B167 (1980) 454

[674] K.Fabricius, G.Kramer, G.Schierholz and I.Schmidt, DESY 80/91

[675] R.K.Ellis, D.A.Ross and A.E.Terrano, Phys.Rev.Lett. 45 (1980) 1226

[676] G.Altarelli and G.Parisi, Nucl.Phys. B123 (1977) 298

[677] D.Amati and G.Veneziano, Phys.Lett. 83B (1979) 87

[678] K.Konishi, A.Ukawa and G.Veneziano, Phys.Lett. 80B (1979) 259

[679] G.Parisi and R.Petronzio, Nucl.Phys. B154 (1979) 427

[680] C.L.Basham, L.S.Brown, S.D.Ellis and S.T.Love, Phys.Lett. 85B (1979) 279

[681] G.Y.Lo and J.D.Sullivan, Phys.Lett 86B (1979) 327

[682] G.C.Fox and S.Wolfram, Caltech preprint CALT-68-723, 68-740 (1979)

[683] W.Marquardt and F.Steiner, Phys.Lett. 93B (1980) 480)

[684] F.Halzen and D.M.Scott, Phys.Lett. 94B (1980) 405

[685] S.D.Ellis and W.J. Sterling, Univ. of Washington preprint (1980)

[686] R.Baier and K.Fey, Univ. of Bielefeld preprint - BI-TP-80/10 (1980)

[687] PLUTO Coll., Ch.Berger et al., Phys.Lett. 90B (1980) 312

[688] " " Ch.Berger et al., Phys.Lett. 99B (1981) 292

[689] K.Kalinowski, K.Konishi and T.R.Taylor, TH. 2902-CERN (1980)

[690] J.Kirschner, Phys.Lett. 91B (1980) 459, and Univ. of Leipzig preprint

[6901] B.Anderson, G.Gustafson and T.Sjöstrand, Phys.Lett. 94B (1980) 211 and earlier references quoted therein

[6902] G.C.Fox and S.Wolfram, Nucl.Phys. B168 (1980) 285

[6903] K.Kajantie and E.Pietarinen, Phys.Lett. 93B (1980) 269

[6904] R.Odorico, Nucl.Phys. B172 (1980) 257

[6905] P.Mazzanti and R.Odorico, Phys.Lett. 95B (1980) 133, and Z.Physik C7 (1980) 61

[6906] R.Odorico, Bologna Preprint IFUB 81/4.
We thank Dr. R. Odorico for making his Monte Carlo program available to us. In a pilot run the mean parton multiplicity was found to be about 5, and the relative dispersion $D/\langle n \rangle = 0.31$ at 30 GeV.

[6907] LENA Collaboration, B.Niczyporuk et al., DESY 81-008

[6908] PLUTO Collaboration, Ch.Berger et al., DESY 81-018

[6909] H.J.Daum, thesis 1981

[6910] R.P. Feynman, Phys.Rev.Lett. 23 (1969) 1415

[6911] W.Furmanski and S.Pokorski, Nucl.Phys. B155 (1979) 253

[6912] M.Ciafaloni and G.Marchesini, Phys.Lett. 83B (1978) 207

[6913] A.Bassetto, M.Ciafaloni and G.Marchesini, Nucl.Phys. B163 (1980) 447 and Phys.Lett. 83B (1979) 207

[6914] K.Konishi, Rutherford preprint RL-79-035 (1979) and Ref. TH. 2897 -CERN (1980)

[6915] Z.Koba, H.B.Nielsen and P.Olesen, Nucl.Phys. B40 (1972) 317

[6916] E.Fermi, Elementary Particles, Yale University Press, New Haven, p.86 (1951)

[6917] PLUTO Collaboration, Ch.Berger et al., Phys.Lett. 95B (1980) 313

[6918] C.Bacci et al., Phys.Lett. 86B (1979) 234

[6919] TASSO Collaboration, R.Brandelik et al., Phys.Lett. 89B (1980) 418

[6920] S.Wolfram in Proceedings of the XV Rencontre de Moriond (1980)

[6921] G.Curci, M.Greco and Y.Srivastava, Phys.Rev.Lett. 43 (1979) 834 and Nucl.Phys. B159 (1979) 451

[6922] PLUTO Collaboration, Ch.Berger et al., Phys.Lett.100B (1981) 351

[6923] M.Greco, G.Penso and Y.Srivastava, Phys.Rev. D21 (1980) 2520

[6924] G.Pancheri-Srivastava and Y. Srivastava, Phys.Rev. D21 (1980) 95

[6925] PLUTO Collaboration, Ch.Berger et al., to be published

Figure Captions

Fig. 6.1 R (e^+e^- → hadrons) vs. c.m. energy acc. to Refs. [608, 609]
Full line: asymptotic prediction of quark model including QCD correction. Dashed line : 3 quarks only.

Fig. 6.2 R (e^+e^- → hadrons) vs. c.m. energy acc. to Refs [610-615]
Dashed and full lines give quark model predictions without and with QCD correction.

Fig. 6.3 R (e^+e^-→ hadrons) in the scan range 30-31.6 GeV. The dashed line indicates the resonance signal expected for a $t\bar{t}$ ground state.

Fig. 6.4a Total K^0_S production [638] vs. c.m. energy.

Fig. 6.4b Ratio of charm induced K^0_S to charm induced hadron production 638 . Dashed line: $\frac{1}{2} = \sin^2 \theta_C$ according to GIM scheme.

Fig. 6.5 Invariant cross section for K^0_S production $(s/\beta)\, d\sigma/dx$ vs. x above and below charm threshold.

Fig. 6.6 Invariant cross section for hadron production $sd\sigma/dx$ vs. $x_p = p/E_{cm}$ for different c.m. energies.

Fig. 6.7 (a) Cross section for radiative ψ (3.7) production (triangles) together with expectation (full line). (b) Cross section for direct J/ψ production (full circles) and upper limits (90% C.L.), together with total hadronic cross section (open circles, (not corrected for radiation)).

Fig. 6.8 Expected number of jets as reconstructed by the cluster algorithm for different production mechanismus: (a) $q\bar{q} = u\bar{u} + d\bar{d} + s\bar{s} + c\bar{c} + b\bar{b}$. Shaded area: $b\bar{b}$ contribution. (b) $q\bar{q}g$ (gluon). Shaded area : events selected with thrust cut ($T < 0.90$). (c) 3-gluon. (d) Phase space.

Fig. 6.9 Correlation between 'jet thrust' T_J and parton thrust x_1.

Fig. 6.10 Typical event observed at 30 GeV with reconstructed charged (full lines) and neutral particles (dashed). The single particle emitted at right angle to the jets has a momentum of only 0.6 GeV/c, compatible with fluctuations in the two-jet formation.

Fig. 6.11 Distribution of the charged (histogram) and neutral (full points) energy flow vs. λ, the angle to the thrust axis, as observed at 9.4 GeV in different thrust bins.

Fig. 6.12 Angular distribution of the thrust axis with respect to the e^+e^- beam. Full line is ~ $1 + \cos^2 \Theta$, the quark model prediction.

Fig. 6.13 Mean sphericity as observed from charged particles (dots), and corrected for all missing particles, detector effects and initial state radiation (squares). Open symbols show resonance values.

Fig. 6.14 Average particle momenta parallel and perpendicular to the jet axis vs. c.m. energy (a) $\langle p_\parallel \rangle$ and $\langle p_\perp \rangle$, (b) $\langle p_\perp^2 \rangle$.

Fig. 6.15 'Seagull' plot: Average $p_\perp^2$ of charged particles vs. scaled momentum $x_p = 2p/E_{cm}$ for different c.m. energies, separated into 'slim' jet (left) and 'fat' jet (right). Dashed and solid curves show $q\bar{q}$ and $q\bar{q}g$ expectations.

Fig. 6.16 Three-jet event observed at 31.1 GeV with reconstructed charged and neutral particles (full and dashed lines).

Fig. 6.17 Distribution of the average squared momentum components perpendicular to the jet axis. Left: out of the event plane $\langle p_{\perp_{out}}^2 \rangle$. Right: in the event plane $\langle p_{\perp_{in}}^2 \rangle$. Dashed and solid curves give expectation from $q\bar{q}$ and $q\bar{q}g$ model.

Fig. 6.18 Distribution of number of jets as reconstructed by the cluster algorithm from the combined 27 - 32 GeV data.

Fig. 6.19 Distribution of parton thrust x_1 for the 3-jet event class. Solid curve gives expectation from 1st order QCD.

Fig. 6.20 Quark-gluon cascade.

Fig. 6.21 Energy-energy correlation vs. particle-particle angle for different c.m. energies. Full line shows fragmentation model ($q\bar{q}$ below 10 GeV, $q\bar{q}g$ above). Dashed lines give pure QCD predictions acc. to Ref.[678](0-50°), Ref.[651] (50°-120°), and Ref.[679] (120°-180°), all with Λ = 200 MeV. Dotted lines indicate continuation of QCD predictions.

Fig. 6.22 Central (60-120°) energy-energy correlation vs. c.m. energy. Dashed line: pure QDC. Full line: fragmentation added.

Fig. 6.23 Energy-energy correlation in extreme backward directions as measured between 27 and 32 GeV. Fragmentation models: upper full line $q\bar{q}$, lower full line $q\bar{q}g$. Pure QCD predictions are labelled: DDT [650], BBEL [651], and PP ([679], Equ. (3.3); which results from the exponentiation in momentum and not in impact space).

Fig. 6.24 Energy dependence of the average charged multiplicity for e^+e^- - annihilations.

Fig. 6.25 KNO plot for e^+e^- PLUTO data at 9.4 and 30.7 GeV. The dashed-dotted curve gives the analytic QCD prediction as explained in the text.

Fig. 6.26 Distributions of the reduced variable $K_\perp/\langle K_\perp\rangle$ at the quoted c.m. energies. The full line is the theoretical expectation computed at 9.4 GeV. Also shown (full points) are the experimental distributions of the corresponding single particle reduced variable $p_\perp/\langle p_\perp\rangle$ at 9.4 and 30 GeV. (In order not to overload the figure, we show here only one of our high energy distributions, which are reported in Fig. 6.26).

Fig. 6.27 Distributions of the jet transverse momentum $K_\perp$ at 9.4, 12 , 17 GeV compared with QCD expectation (see text).

Fig. 6.28 Same as Fig. 6.25 for 27.5, 30 and 31.05 GeV average c.m. energies. (The two last points for 30 GeV do not appear in Fig.6.24, being out of range).

7. The T and J/ψ resonances

The production and decay of $q\bar{q}$ resonances below $q\bar{q}$ threshold ('quarkonia') in e^+e^- annihilation has provided a rich spectroscopy of $q\bar{q}$ bound states. These states allow (i) for studies of the dynamics of the $q\bar{q}$ bound system, e.g. in terms of a $q\bar{q}$ potential, via the level spacing and the electromagnetic (cascade-) decays of excited states, and (ii) for an investigation of the strong (gluonic) $q\bar{q}$ annihilation in decays of the ground states. In addition, after the discovery of the T [701] its verification as a quarkonium state of a new heavy quark, and the measurement of the quark charge was of considerable interest. Since the observation of the τ as a third lepton the identification of the first member of a third quark doublet was of great significance for our present understanding of the fundamental fermions (quark-lepton symmetry, see also section 5.1).

The main work of the PLUTO experiment on quarkonium physics is the measurement and analysis of the T ground state production and decay properties. The analysis is focussed on the determination of the constituents, and on a search for evidence for a 3-gluon decay mode in the topology of events. In sections 7.1 - 7.7 we give a full account of the PLUTO work on the T resonance. At the J/ψ and ψ' most of the physics came from the study of exclusive decay modes, and from the single photon spectroscopy of ψ' cascade decays. Data on these resonances were taken by PLUTO before shower counters were installed, without particle identification, later than by other experiments at SPEAR and DORIS, and with a modest integrated luminosity. For these reasons, only a few interesting results were achieved. They are described in section 7.8.

7.1 T discovery and open questions

The T was discovered in summer 1977 at Fermilab [701a] as a broad bump at 9.5 GeV in the mass spectrum of $\mu^+\mu^-$ pairs produced in proton-nucleus collisions. Briefly later [701b] the bump was resolved into two peaks (Fig.7.1) whose widths were consistent with the resolution of 200 MeV/c^2 (rms). The T states appeared to be hadrons because of their production process. The fact that they were observed in an electromagnetic decay mode indicated that their hadronic decay widths were much smaller than a few hundred MeV as expected for Zweig-allowed strong decays. The Fermilab experiment left open many questions, like

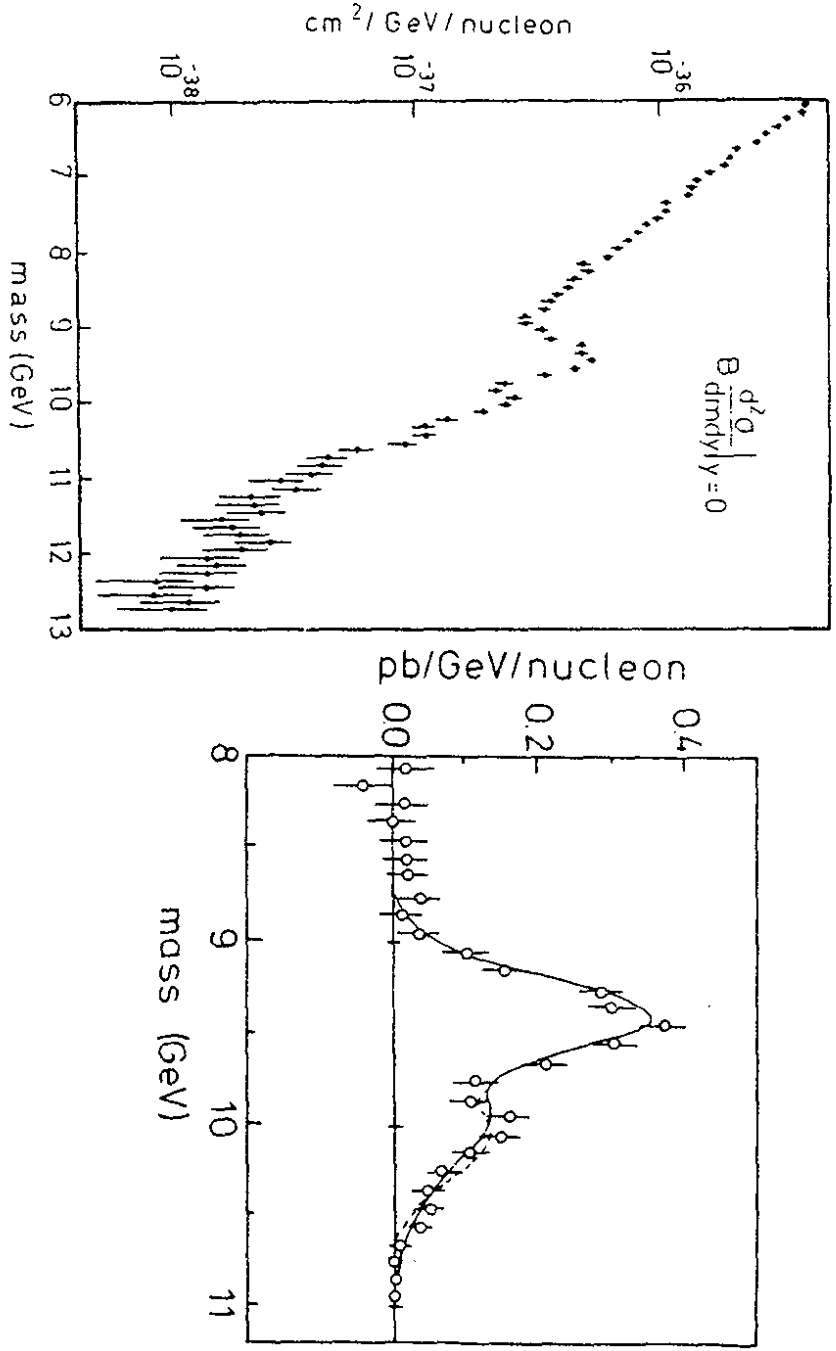

Fig.7.1 Columbia-Fermilab-Stony Brook: invariant mass distribution of $\mu^+\mu^-$ from $p+Be \to \mu^+\mu^- + X$: evidence for T and T' [701].

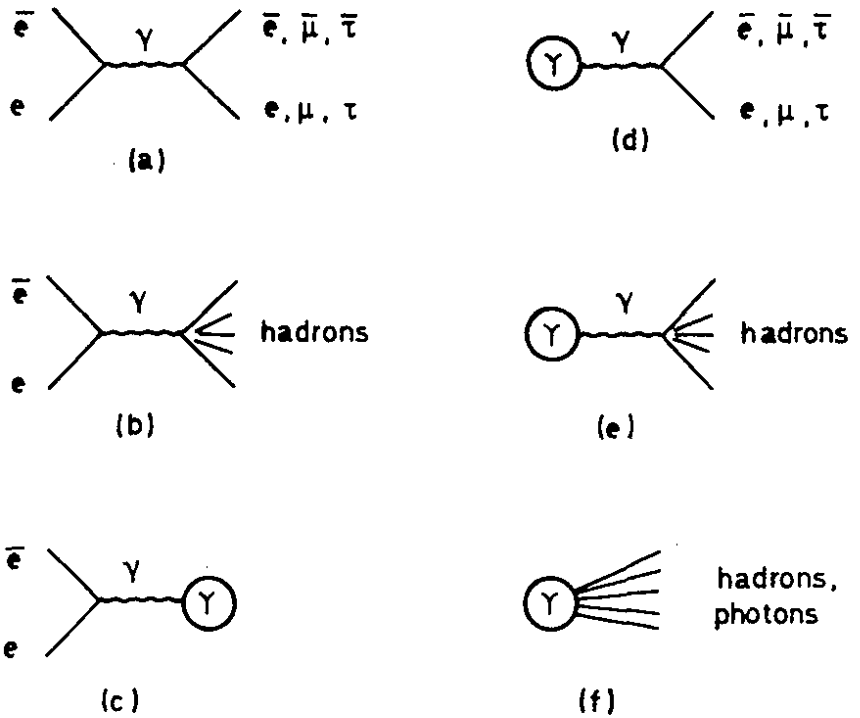

Diagrams for lepton pair (a) and hadron (b) and Υ (c) production in e^+e^- annihilation. Diagrams for electromagnetic (d,e) and direct (f) Υ decays. QCD diagrams for Υ decays (g,h).

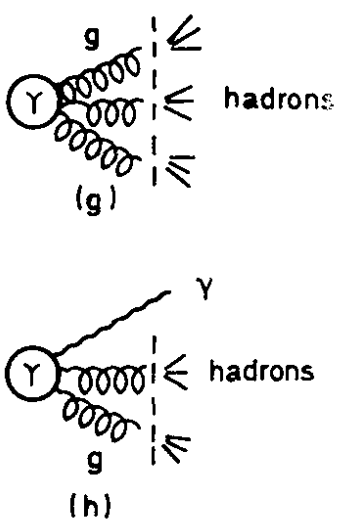

Fig. 7.2

(1) Is the Υ resonance significantly narrower than a few hundred MeV? Is its width similar to the charmonium ground state, the J/ψ?

(2) Are there two or more narrow resonance states observed? The μ pair mass spectrum was suggestive for 2 or 3 states (Fig. 7.1).

(3) Does the electronic width Γ_{ee} (Fig. 7.2c) conform with the expectations [702] for a $q\bar{q}$ bound state? Does Γ_{ee} correspond to the charge of a bottom quark b ($e_b = -1/3$) or to a top quark t ($e_t = 2/3$) ?

Because the mass of the Υ was high enough for jet formation in hadronic final states it was of great interest to learn whether the topological properties of non-electromagnetic ('direct') decays (Fig. 7.2f)

(4) exclude a dominant (one gluon-) annihilation into a light $q\bar{q}$ pair? An one gluon decay mechanism is forbidden by the colour octet nature of gluons or, in other words, by the non-Abelian character of QCD;

(5) exclude a dominant 2-gluon decay? This mode is forbidden by the vector nature (or C-parity) of the gluon quanta.

(6) confirm the expected [703,704] 3 gluon decay (Fig.7.2g) to be dominant? This is the strong decay mechanism with the lowest possible order in α_s.

Sensitive topological properties relevant for these questions are the jet character of the direct decays, the angular distribution of the thrust (or sphericity) axis, and also the particle multiplicity.

All of these questions could be checked with measurements at e^+e^- storage rings, but there was no one that could be operated at the Υ energy. The storage rings SPEAR and DORIS were not designed for energies of 9.5 GeV, and PETRA, CESR and PEP construction schedules were 2 years or more away from completion.

7.2 The T search at DORIS

Even though the original DORIS proposal forsaw a 3 GeV storage ring, the magnets were designed to allow for a later extension of the beam energy to 4.5 GeV. For higher beam energies the iron begins to saturate. Since DORIS was already in the process of being converted to a single ring machine, which allowed for higher energies than the double ring scheme by concentrating all magnet and RF power to one ring, the PLUTO collaboration immediately made the proposal to push the DORIS energies beyond the planned 8.6 GeV into the T region. The DORIS machine physics group [705] was daring enough to embark on this proposal.

On April 12, 1978, the conversion and upgrading process was completed, and an energy scan for a narrow resonance was started. The FNAL group had reevaluated their estimate for the mass as 9.45 GeV, with an uncertainty of ± .10 GeV. [70lc]. The scan started at 9.35 GeV and proceeded in steps of 5 or 10 MeV, with integrated luminosities of ~20 nb^{-1} per 10 MeV. A fast analysis chain, based on events with an energy signal of more than 2 GeV in the shower counters, returned cross section results within a day. On April 29 a narrow resonance was hit and completely established on May 2 [706a, b] as shown in Fig. 7.3a. The DORIS machine group [705a] deserves high credit for their enthusiasm and hard work that made this result possible.

PLUTO continued to take data at and around the T peak until May 15 when it was scheduled to be removed from DORIS for getting transferred to PETRA. During the T experiment integrated luminosities of 177 nb^{-1} below ("off") the resonance ($9.30 < W < 9.44$ GeV) and 190 nb^{-1} on the resonance ($9.45 < W < 9.47$ GeV) were accumulated.

7.3 Parameters of the T resonance

From the cross section curve in Fig. 7.3 the values for the T mass and the upper limit of the width could be considerably improved, and from this and other data the electric charge of the constituents could be determined.

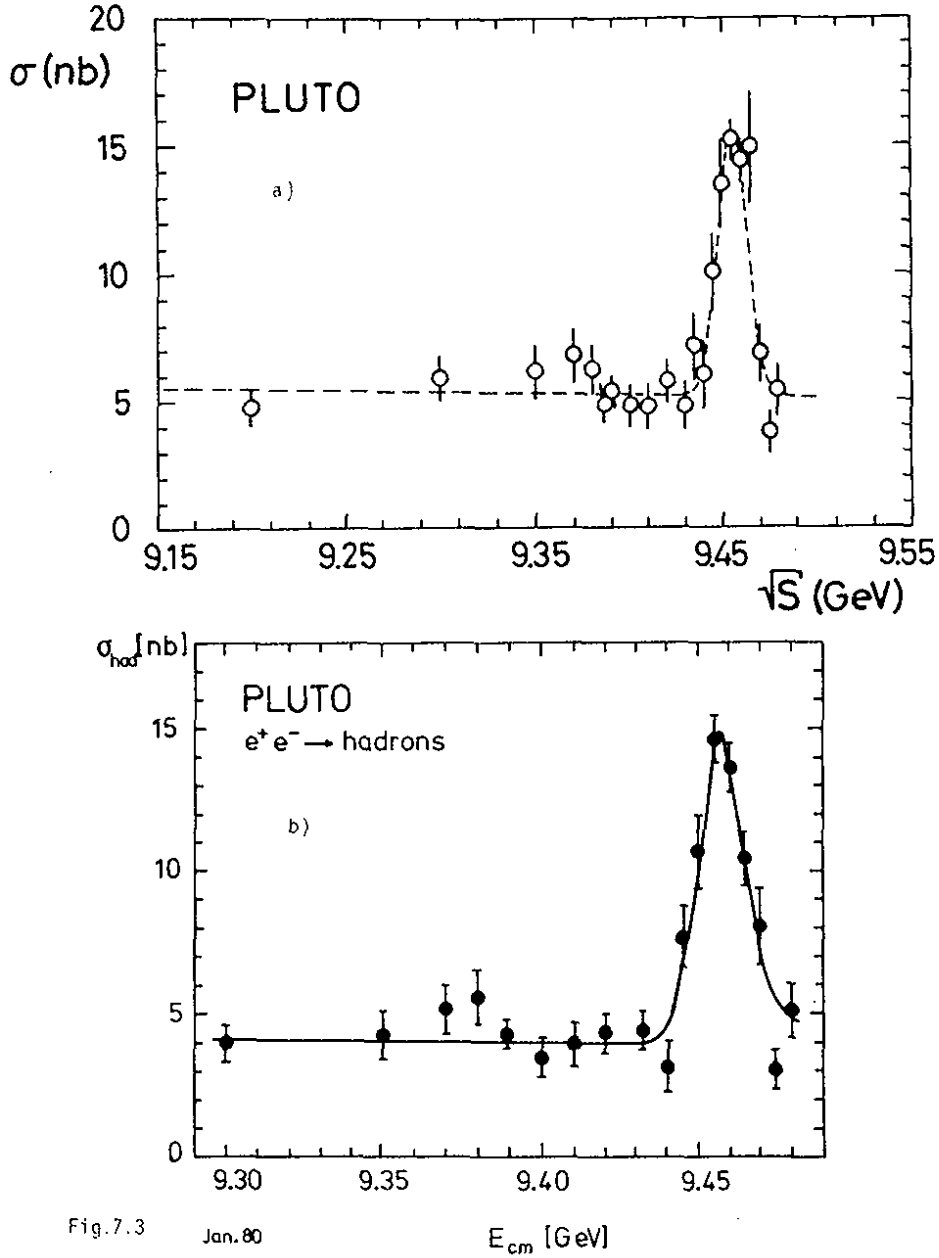

Fig.7.3 Jan.80

Total cross section for $e^+e^- \rightarrow$ hadrons at T energies, (a) as from the fast analysis chain used during the T search and (b) after final evaluation. The curves are a fit of the continuum and the T cross section, to the data. They include the radiative corrections and the machine energy width.

7.3.1 Mass and width of the T

The T excitation curves in Fig. 7.3a had three immediate implications:

(i) The precise mass value of the T resonance is

$$M(T) = 9456 \pm 10 \text{ MeV} \qquad (7.1)$$

where the error comes completely from the absolute energy calibration in the DORIS storage ring.

(ii) The "resonance" curve is a Gaussian with the width

$$\Delta = 7.3 \pm 0.1 \text{ MeV} \qquad (7.2)$$

which is quantitatively in agreement with the expectations for the energy spread of the DORIS beams at this central energy [705b]. This implies that the width of the T is small, actually

$$\Gamma_{tot}^{T} < 18 \text{ MeV} \quad (95\% \text{ c.l.}) \qquad (7.3)$$

This limit is significantly smaller than the usual widths of hundred MeV and more, found for resonances with Zweig allowed strong decays and large Q values. Thus the hypothesis of a $q\bar{q}$ bound state is strongly supported by this result. We will come back to the determination of Γ_{tot} in section 7.4.

(iii) These results on M_T and Γ_T confirmed the interpretation that the broad T bump in hadronic μ-pair production was due to at least three narrow resonance states [701].

Within potential models for $q\bar{q}$ bound states, masses of the constituent quarks can be defined and related to the bound state masses. For instance the Richardson potential [707], which yields an excellent description of the mass levels of the J/ψ and T family leads to a constituent quark mass of

$$m_b = 4883 \text{ MeV}. \qquad (7.4)$$

7.3.2 Production cross section, electronic width and constituent charge

The electronic width of the T, Γ_{ee}, is proportional to the squares of the constituent quark electric charges e_q. It can be measured by the T production cross section in e^+e^- collisions. There are two approaches for a quantitative relation of the electronic width of vector mesons to the quark charges. The first one is the Matveev, Shuminskii and Tavkhelidze formula [702]:

$$\Gamma_{ee} = \frac{16\pi\alpha^2}{M^2(T)} |\psi(0)|^2 e_q^2 \qquad (7.5)$$

There are 2 unknown quantities in (7.5), the quark charge in question, and the $q\bar{q}$ bound state wave function at the origin, $|\psi(0)|^2$. The latter can be calculated in potential models. There are, however, uncertainties in extrapolating the potential to the origin, and also substantial QCD radiative corrections, as pointed out by Celmaster [708] and Barbieri et al. [709]. The first order term (in α_s) modifies the r.h.s. of (7.5) by the factor $(1-16\cdot\alpha_s/3\pi) \approx {}^2/_3$. To some extent, one can avoid these problems by comparing the widths of the T and of the ψ/J state, and by using a relation between their wave functions valid for a large class of potentials [710]. This yields the inequality

$$\Gamma_{ee}(T) \geq \frac{e_q^2}{e_c^2} \cdot \frac{m_q}{m_c} \cdot \frac{M^2(J/\psi)}{M^2(T)} \cdot \Gamma_{ee}(J/\psi) \qquad (7.6)$$

Another quantitative relation between e_q and Γ_{ee} of vector mesons has been derived from the conjecture of 'new duality' [711], according to which the ratio Γ_{ee}/e_q^2 has the same value for all $q\bar{q}$ ground states:

$$\frac{1}{e_q^2}\Gamma_{ee}(T) = \frac{9}{4}\Gamma_{ee}(J/\psi) = 9\Gamma_{ee}(\phi) = 18\Gamma_{ee}(\omega) = \frac{8}{4}\Gamma_{ee}(\rho) \qquad (7.7)$$

$$\simeq 12.2 \text{ KeV} \quad \text{(average [722])}$$

The electronic width was determined from the T excitation cross section as plotted in Fig. 7.3b versus the nominal machine energy. The cross section points are corrected for losses due to trigger conditions and off-line cuts which remove beam gas and QED background. These cuts are described in detail elsewhere [712,713]. The most important cuts are that at least 60% of the CMS-energy is observed, and that events with more than 2 (observed) charged particles have at least 2 negative particles. The efficiencies ε have been determined using $q\bar{q}$ simulated events for the continuum and electromagnetic decays of the T ($\varepsilon = 72\%$),

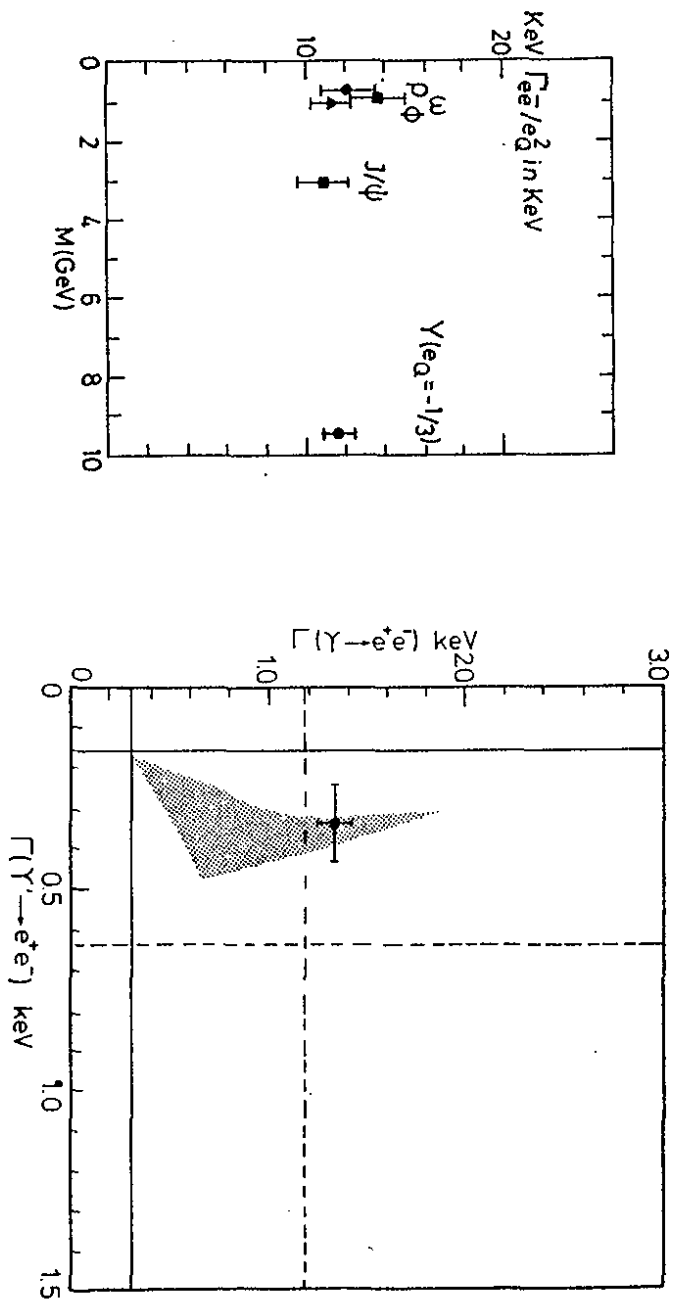

Fig.7.4

(a) Reduced leptonic width Γ_{ee}/e_q^2 for vector meson ground states as a function of mass.

(b) Lower bounds on Γ_{ee} for Υ and Υ' for different quark charges. The shaded area indicates the charge 1/3 predictions of 20 different potential models. A comparison with the DORIS data shows good agreement with charge 1/3 and excludes 2/3.

and 3-gluon simulated events for the Υ direct decays ($\varepsilon = 89\%$). The difference in efficiencies, together with the uncertainties in the ratio of the electromagnetic to direct decays of the Υ (determined from $\sigma^{on}(e^+e^-\to\mu^+\mu^-)$, see section 7.4.1), add 7.5% to the systematic error of Γ_{ee}, which otherwise is dominated by the 5% uncertainty in the luminosity.

The excitation curve shown in Fig. 7.3b is calculated from a superposition of the Υ production cross section

$$\sigma_{RES}(e^+e^-\to\Upsilon\to\text{hadrons}) = \frac{12\pi M^2}{s}\cdot\frac{\Gamma_{ee}\cdot\Gamma_{had}}{(M^2-s)^2+\Gamma_{tot}^2 M^2} \qquad (7.8a)$$

and the continuum cross section

$$\sigma_{cont}(e^+e^-\to\text{hadrons}) = R\cdot\sigma_{\mu\mu} \qquad (7.8b)$$

by allowing for a beam energy spread according to eq. (7.2) and for radiation in the initial state [714]. In the fit of the resonance parameters of eqs. (7.8) to the cross section we eliminated the ratio $\Gamma_{had}/\Gamma_{tot} = 1-3\cdot B_{ee}$ by using $B_{ee} = 2.2\%$ (see section 7.4). This leads to

$$\Gamma_{ee} = 1.33 \pm 0.14 \text{ keV} \qquad (7.9)$$

together with $R = 3.7 \pm 0.4$.

Combining (7.9) and (7.7) we find

$$e_q^2 = 1/9.2 \qquad (7.10)$$

with an uncertainty of $\approx 25\%$, in perfect agreement with the bottom charge $e_b = -1/3$ (see also Fig. 7.4a), and in clear disagreement with the top charge $e_t = 2/3$. The inequality (7.6) leaves both charge values acceptable, even though $e_q = 2/3$ is marginal. Applying (7.6) to the electronic widths of ψ' [722] and Υ' [715] clearly rules out $e_q = 2/3$ (see Fig. 7.4b). In a completely model independent way the toponium hypothesis is finally ruled out by the total cross section of the continuum which excludes a threshold associated with $\Delta R = 4/3$ above the Υ resonance region (see chapter 6.1).

7.4 Decay modes of the T , and the total width

From the previous discussion it is clear that the T is produced in electromagnetic and in strong interactions. Correspondingly there will be strong ('direct') decays into hadrons (Γ_{dir}, Fig. 7.2f) and electromagnetic decays into lepton pairs ($\Gamma_\gamma(e, \mu, \tau)$, Fig. 7.2d) and into hadrons as well (Γ_γ (hadrons), Fig. 7.2e). The events from electromagnetic T decays have the same properties as those produced by e^+e^- annihilation outside the T resonance (see Fig. 7.2), and we have the relation $\Gamma_\gamma^T(\text{hadrons})/\Gamma_\gamma^T(\mu\bar{\mu}) = \sigma(e^+e^- \to \text{hadrons})/\sigma(e^+e^- \to \mu\bar{\mu}) \equiv R$. The total width is then composed as follows

$$\Gamma_{tot} = \Gamma_\gamma(e,\mu,\tau,) + \Gamma_\gamma(\text{hadrons}) + \Gamma_{dir}(\text{hadrons}) \qquad (7.11)$$

$$= 3 \cdot \Gamma_{\ell\ell} + R \cdot \Gamma_{\ell\ell} + \Gamma_{dir}$$

Supporting evidence for direct T decays comes also from the fact that multihadron final states at T energies show topological properties different from the nearby continuum (see section 7.5). A quantitative determination of Γ_{dir} (or Γ_{tot}) is possible by a measurement of the electronic (B_{ee}) or generally the leptonic branching ratio $B_{\ell\ell}$ (we assume $B_{ee} = B_{\mu\mu}$) which yields

$$\Gamma_{tot} = \Gamma_{\ell\ell}/B_{\ell\ell} \qquad (7.12a)$$

$$\Gamma_{dir} = \Gamma_{\ell\ell}(B_{\ell\ell}^{-1} - (3 + R)) \qquad (7.12b)$$

A measurement of the leptonic branching ratio $B_{\ell\ell}$ is the key to Γ_{dir} and Γ_{tot}.

7.4.1 The leptonic branching ratio

In the PLUTO experiment the branching ratio $B_{\ell\ell}$ has been determined from the decays $T \to \mu^+\mu^-$ [716] and $T \to e^+e^-$ [717]. Details of the event analysis are given in chapter 4 and in [716, 717, 718]. In both reactions, the difference between the lepton pair cross section on the T, and the QED expectation was used to determine the T contribution for $e^+e^- \to \ell^+\ell^-$. The corresponding measurements in the nearby continuum with the same detector, under the same running conditions and with the same analysis chain were used to check and ensure agreement with the QED prediction. This is important since the difference between "on" T and QED cross sections is marginal.

The μ pair sample contains a total of 155 events, from which 9.5 events as due to cosmic background are statistically subtracted. The production angle distribution is shown in Fig. 7.5. It agrees with a $1 + \cos^2\theta$ shape. The number of e^+e^- pairs from $e^+e^- \to T \to e^+e^-$ is very small as compared to the number of Bhabha events (2953 events in total, on the T). However in the backward direction an excess over the QED cross section is observed in the "on" T range (Fig.7.6). The full curve is the first order QED cross section, modified by radiative corrections [719] and angular resolution. No such excess is observed in Bhabha scattering outside the T (Figs. 4.7a). The excess has been determined by fitting a $1 + \cos^2\theta$ term and the Bhabha shape to the data of Fig. 7.6.

In an energy intervall from 9.450 to 9.465 GeV, which corresponds to $2 \cdot \Delta$ according to eq. 7.2, the average excess cross sections are

$$\sigma(ee \to T \to \mu^+\mu^-) = (0.25 \pm 0.22)\ \text{nb} \qquad (7.13a)$$

$$\sigma(ee \to T \to e^+e^-) = (0.59 \pm 0.34)\ \text{nb} \qquad (7.13b)$$

Division by the average excess total cross section $\bar{\sigma}_{tot}^T = \bar{\sigma}_{had}^T + 3 \cdot \bar{\sigma}_{ee}^T$, where σ_{had} is shown in Fig. 7.3b, we find the branching ratios

$$B_{\mu\mu} = (2.2 \pm 2.0)\% \qquad (7.14a)$$

$$B_{ee} = (5.1 \pm 3.0)\% \qquad (7.14b)$$

or the average leptonic branching ratio

$$B_{\ell\ell} = (3.1 \pm 1.7)\%. \qquad (7.14)$$

7.4.2 The fraction of direct hadronic decays

Even though the result for $B_{\ell\ell}$ is only marginally different from zero, it allows safe conclusions on the existence of direct T decays. The relative share of direct decays in the observed hadronic decay modes is

$$\frac{\Gamma_{dir}}{\Gamma_{had}} = \frac{1 - (3+R)B_{\ell\ell}}{1 - 3B_{\ell\ell}} = 0.87 \pm 0.05 \qquad (7.15)$$

when using R = 3.7.

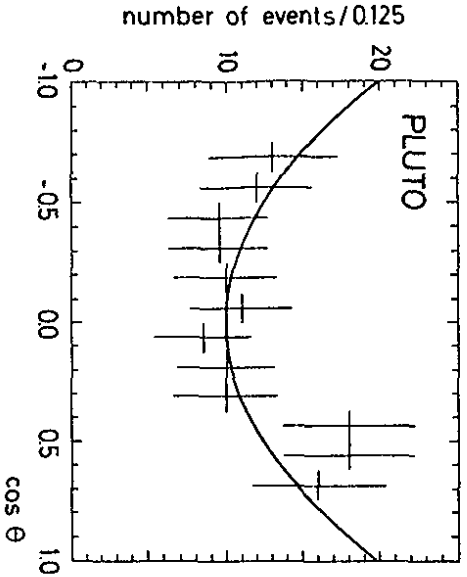

Fig.7.5

Angular distribution for muon pairs produced in the Ypsilon region. Data on and off resonance are combined. The curve is proportional to $1+\cos^2\theta$.

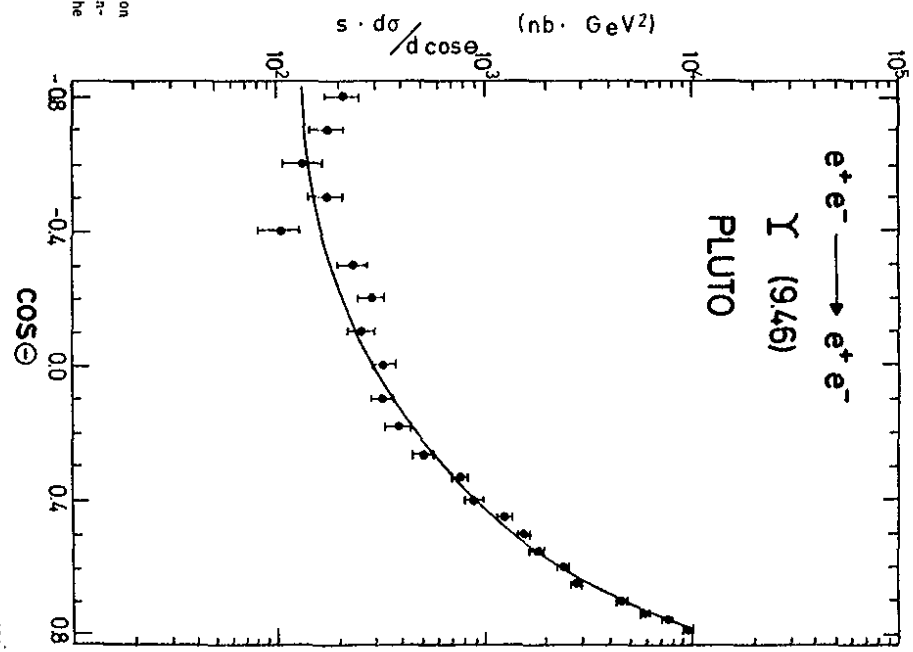

Fig.7.6

The differential cross section $s\,d\sigma/(d\cos\theta)$ for reaction $e^+e^- \to e^+e^-$ on the resonance ($9.45 \leq E_{cm} \leq 9.465$). The full curve is the QED part including the effects of radiation and of finite angular resolution. The dashed curve also includes the direct decay $\Upsilon \to e^+e^-$.

The multihadron final states, the details of which we will describe in section 7.5, are thus dominated by direct decays.

7.4.3 The total width of the Υ

The total width Γ_{tot} depends critically on the leptonic branching ratio (7.12a), and only if $B_{\ell\ell}$ is significantly different from zero, an upper limit on Γ_{tot} can be inferred. If we combine the PLUTO result (7.14) with the two other measurements [720, 721] which are also close to a 2 s d. significance, to $B_{\ell\ell} = 3.2 \pm 1.0$, we find - with our value of $\Gamma_{ee} = 1.33$ keV -

$$1/\Gamma_{tot} = 0.024 \pm .008 \text{ keV}^{-1} \qquad (7.16a)$$

$$\Gamma_{tot} = 42^{+20}_{-11} \text{ keV} \qquad (7.16b)$$

$$\Gamma_{dir} = 32^{+20}_{-11} \text{ keV} \qquad (7.16c)$$

and $$25 < \Gamma_{tot} < 122 \text{ keV at 90\% c.l.} \qquad (7.16d)$$

This shows that the Υ is indeed a narrow state with a total width comparable to the 63 ± 9 keV [722] of the J/ψ.

7.4.4 Γ_{dir} and the running strong coupling constant

With several assumptions, the direct width (7.16c) allows a determination of the strong running coupling constant from Υ decays. QCD provides 2 relations [703, 704]:

$$\frac{\Gamma_{3g}}{\Gamma_{ee}} = \frac{10}{81} \cdot \frac{\pi^2 - 9}{\pi} \cdot \frac{\alpha_s^3(Q^2)}{\alpha^2 \cdot e_b^2} \qquad (7.17)$$

$$\frac{\Gamma_{3g}}{\Gamma_{\gamma gg}} = \frac{5}{36} \cdot \frac{\alpha_s(Q^2)}{\alpha \cdot e_b^2} \qquad (7.18)$$

The second relation cannot be used here since we have not found any evidence for the γgg transition [712]. This null result is consistent with an expected value of 0.03 for $\Gamma_{\gamma gg}/\Gamma_{3g}$ [704a,f,g].

In the first relation, Γ_{ee} has been reliably measured (7.9), and (7.16c) gives the upper limit $\Gamma_{3g} \leq \Gamma_{dir}$, or

$$\frac{\Gamma_{3g}}{\Gamma_{ee}} \leq \frac{\Gamma_{dir}}{\Gamma_{ee}} = 25 \,^{+15}_{-\ 8} \qquad (7.19)$$

Unfortunately the way Γ_{dir} has been measured does not render any evidence that Γ_{dir} can be identified with Γ_{3g}. As we will see in section 7.4, the topological properties of the observed events are consistent with a 3 gluon decay mode, but experimentally we cannot exclude substantial contributions from other decays, e.g. through more than 3 gluons.

Such contributions to Γ_{dir} would increase the value of α_s obtained from (7.17) when using $\Gamma_{3g} = \Gamma_{dir}$. There is, however, a further problem from the fact that (7.17) is a result for massless gluon kinematics. T decays are close to threshold for jet formation, and kinematic limitations may lead to a smaller width Γ_{3g} and to a reduced value for α_s from (7.17). Ignoring all these problems we find

$$\alpha_s = 0.16 \,^{+0.03}_{-0.02} \qquad (7.20)$$

This value of the running coupling constant in the T decay is consistent with $\alpha_s = 0.16 \pm .02$ found at $Q^2 \approx 900$ GeV^2 from the $e^+e^- \to qqG$ cross section (see section 6.3.3). Using the QCD prescription (eq. 6.4) to extrapolate the latter value to T decay energies we find $\alpha_s(Q) = .19^{+.03}_{-.03}$ and $.24^{+.06}_{-.05}$ for $Q = M(T)$ and $Q = M(T)/3$ [723], respectively. There is no contradiction to either of the two extrapolations.

7.4.5 The C-parity forbidden decay $T \to \gamma\gamma$

From the analysis described in section 4, and the data shown in Fig. 4.6c we can infer an upper limit on the branching ratio of this forbidden decay of

$$B^{T}_{\gamma\gamma} < 1.4\% \qquad (95\%\ \text{c.l.}) \qquad (7.21)$$

7.5 Topological properties of direct T decays - Search for 3 gluon decay

A visual inspection of T events makes clear that 3-jet events are not the dominant topological pattern. This is not really surprising since already more than 3 GeV per jet are necessary to make "visible" 2-jet events in e^+e^- annihilation. At T energies therefore the lowest energetic jet in general will not be energetic enough to form a visible jet.

The distribution of the gluon energies, and of the angles between them can be calculated from the matrix element for $T \to 3g$ [704]. The notation for the massless gluon kinematics is explained in Fig. 7.7a, b, and also the 3 gluon Dalitz plot. The expected distributions of the 3 ordered relative gluon energies ($x_1 \geq x_2 \geq x_3$) are shown in Fig. 7.7d. On the average we expect $\langle x_3 \rangle = 0.39$, corresponding to $k_3 = 1.84$ GeV, which is clearly below the threshold for jet formation. Also, the opening angle θ_1 between the 2 lower energetic gluons is not always large enough to allow for a spatial separation of the two respective jets. The average value $\langle \cos\theta_1 \rangle = 0.26$ corresponds to 75^0. The fragments of 2 gluons may overlap in space such that they do not produce 2 separated jets. For both of these reasons, a potential 3-jet pattern can degrade to a 'soft' 2-jet pattern. The kinematic situation which is most favourable for the formation of 3 jets, namely that all 3 gluons emerge with about the same energy ($x_1 \sim x_2 \sim x_3 \sim 2/3$, $\theta_1 \sim \theta_2 \sim \theta_3 \sim 120^0$ at the Dalitz plot center) is expected for only a very small fraction of the events (see Fig. 7.7c, d).

Therefore, in searching for evidence for a 3-gluon decay of the T, we look for 3 and 2 jet structures, and for coplanar and collinear event shape properties, respectively. To this end we compare the measured T direct decays with simulated 3-gluon ("3G") decays, with phase space ("PS") events as to give the reference points for events without any topological structure, and with $q\bar{q}$ 2-jet events measured in the nearby continuum ("9.4 GeV") or simulated ("FF").

We use the eigenvalues Q_i of the momentum tensor (see sect. 6.3.1) to measure collinear (2-jet) and coplanar (3-jet) correlations (sect. 7.5.2) and also the linear jet measures thrust and triplicity to search for 2-jet and 3-jet pattern in the direct T decays (sect. 7.5.3). The results reported here come from an analysis which included charged particles, and neutral particles with an electromagnetic shower [712, 724]. Results from a previous analysis of charged particles only can be found in Ref. [725].

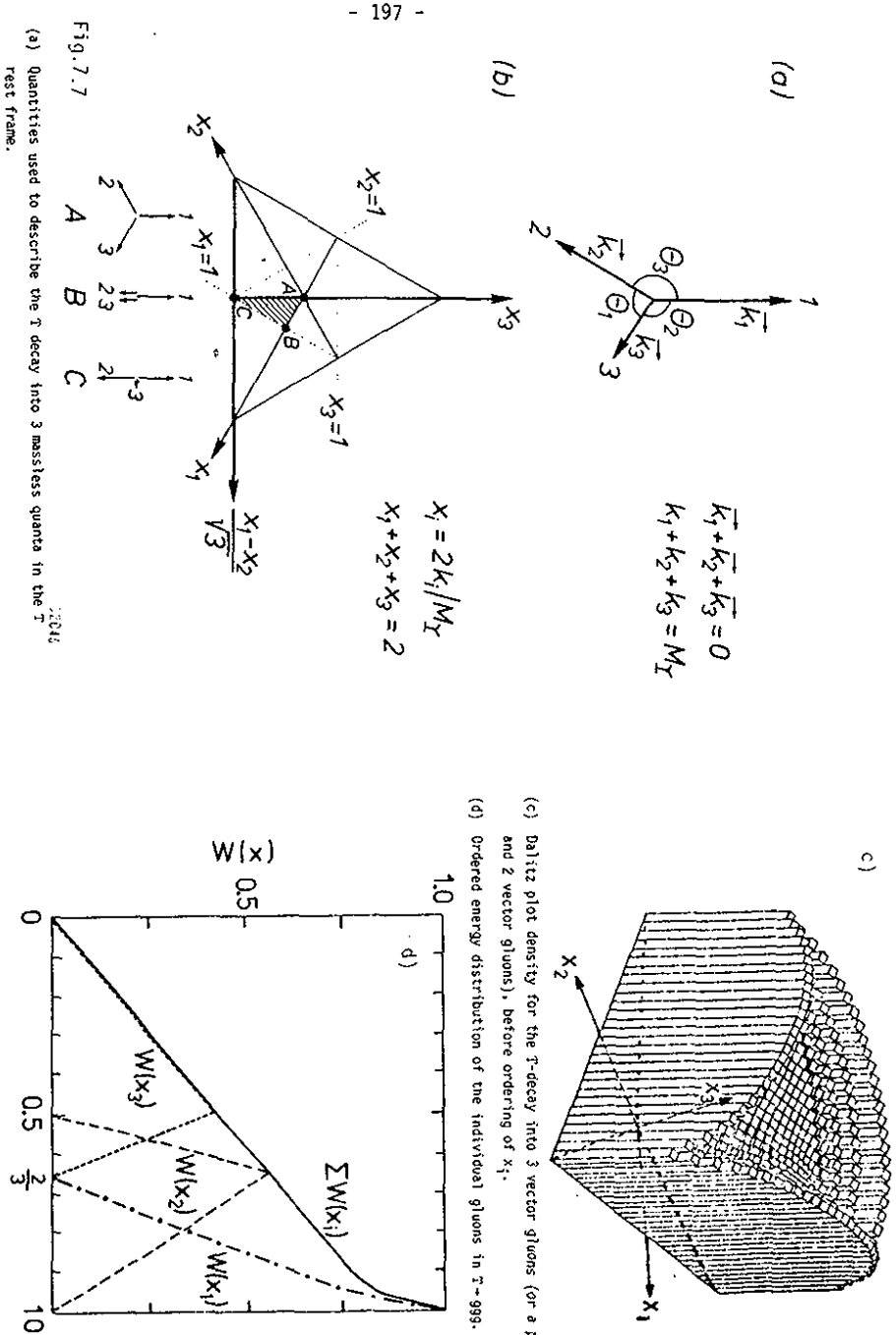

Fig.7.7
(a) Quantities used to describe the T decay into 3 massless quanta in the T rest frame.
(b) Dalitz plot of the gluon energies. Momentum conservation limits the populations to the dotted triangles. By ordering $x_1 \geq x_2 \geq x_3$ they are further restricted to the shaded area.
(c) Dalitz plot density for the T-decay into 3 vector gluons (or a photon and 2 vector gluons), before ordering of x_i.
(d) Ordered energy distribution of the individual gluons in T→ggg.

7.5.1 The direct decay sample

To follow up this program, we have prepared a sample of events representing the T direct decays. The sample of hadron events "on" the T has contributions from the continuum (Fig. 7.2b) and from the T (Fig. 7.2c), via its electromagnetic (Fig. 7.2e) and direct (Fig. 7.2f) decays. The two former contributions are monitored by the μ pair production rate, "on" (Fig. 7.2a and 7.2d) and "off" (Fig. 7.2a) the T energy, through the relation $N^{had}_{\Upsilon} = b\, N^{\mu\mu}$ with the same factor b on and off the resonance (b = R if acceptance is corrected for). The number of direct decays N^{had}_{dir} can then be obtained from the number 'on' the T (N^{had}_{on}) and from events measured "off" the T (N^{had}_{off}) by the relation

$$N^{had}_{dir} = N^{had}_{on} - \frac{N^{\mu\mu}_{on}}{N^{\mu\mu}_{off}} \cdot N^{had}_{off} \qquad (7.22)$$

In the PLUTO data $N^{\mu\mu}_{on} / N^{\mu\mu}_{of} = 1.32 \pm 0.24$ was measured. Since hadronic final states from the continuum and from the electromagnetic T decays have identical properties eq. [7.22] can also be used to produce subtracted distributions representing the direct decays.

In the following analysis, only events with at least 4 charged tracks were used. This additional cut (see section 7.3.2) leaves $N_{on} = 1781$ events ($9.450 < W < 9.466$ GeV), and $N_{off} = 442$ events ($9.25 < W < 9.422$ GeV), yielding

$$N^{\Upsilon}_{dir} = 1198 \text{ events} \qquad (7.23)$$

In other words, 2 out of 3 hadron events of our data sample on the T are due to direct T decays.

7.5.2 Event shape in momentum space

Using the eigenvalues Q_i derived from the momentum tensor (sect. 6.3.1), we can describe the deviation from extreme collinear jet shapes ($Q_1 = Q_2 = 0$) by sphericity S, and the deviation from extreme planarity ($Q_1 = 0$) by flatness F [726] which is the excentricity of the momentum components perpendicular to the sphericity axis:

$$F = \frac{Q_2 - Q_1}{Q_2} = 1 - \frac{\Sigma p^2_{\perp out}}{\Sigma p^2_{\perp in}} \qquad (7.24)$$

Here the sum runs over all tracks of an event. The index 'out' labels the direction out of the (2,3)-plane, and the index 'in' labels the direction in that plane and perpendicular to the sphericity (i = 3) axis. We also consider the ratio of the linear sums $\Sigma|P_{\perp out}| / \Sigma|P_{\perp in}$ ($= P_{out}/P_{in}$, in short), in this case with respect to the triplicity plane, and the most energetic triplicity vector. Table 7.1 summarizes the results for the respective average values, from T direct decays and continuum data, and from the 3 models. Note that the PS and 3G

Table 7.1 Event shape and jet measures, average observed values, with errors.

event typ	sphericity S	flatness F	P_{out}/P_{in}	thrust T	triplicity T_3	x_1	θ_3 (degree)
PS (MC)	0.50 1	0.60 1	0.56 1	0.69 1	0.84 1	0.83 1	146 1
3G (MC)	0.39 1	0.63 1	0.55 1	0.72 1	0.86 1	0.86 1	151 1
T (data)	0.415 8	0.632 9	0.548 7	0.732 4	0.870 1	0.862 2	151.0 0.5
9.4 (data)	0.277 8	0.673 9	0.498 8	0.808 4	0.910 2	0.909 3	158.5 0.6
FF (MC)	0.28 1	0.65 1	0.52 1	0.80 1	0.91 1	0.90 1	159 1

events are generated with the same (charged) multiplicity as the direct T decays, and FF events and 9.4 GeV data have a lower multiplicity (see section 7.6.1).

The sphericity of the T decays shows a significant collinear correlation effect, i.e. a difference to the phase space value. The associated 2-jet character is softer, however, than in $q\bar{q}$ events. There is good agreement between the sphericity values from the 3G model events and the T decays.

The flatness of the T decay is only slightly larger than the PS value, indicating at most a very small planar correlation. The linear ratio of P_{out}/P_{in} is even closer to the PS value. Whether this indication is real can be checked further by looking at events with large sphericity since 3-jet events, if they exist, should concentrate at larger sphericity values than 2-jet events. In table 7.2 we show the flatness in three sphericity intervals, for T decays, 3G and PS events. The flatness of T events, however, does not grow significantly, relative to the PS values, when going from small to large sphericities.

Table 7.2 Average observed flatness in several sphericity intervals

Sphericity	Flatness		
	PS	T	3G
0.9...0.6	.58 ± .01	.60 ± .02	.62 ± .01
0.6...0.3	.61 ± .01	.62 ± .01	.64 ± .01
0.3...0.0	.63 ± .01	.67 ± .02	.63 ± .01

A larger flatnes than in phase space events, is a necessity for a 3 jet pattern. The obvious lack of such a correlation in T decays, however, cannot be considered as evidence against the 3 gluon decay mode. This can be seen from the flatness values of the simulated 3G events. They agree perfectly with the T decay data.

The event shape analysis of the T direct decays in terms of the Q_i eigenvalues thus renders clear evidence for a 2-jet character which is weaker than for off resonance events. No planar correlations are observed in T decays. The topological features can however be well understood as the result of a 3 gluon decay mode with subsequent fragmentation.

7.5.3 Jet formation: Thrust and Triplicity analysis

A possible 3-jet character of the T decays can also be investigated by attempting to reconstruct jets directly. We use thrust (T) and triplicity (T_3) maximization for 2-jet and 3-jet construction, respectively. The values of T and T_3 (with $T \leq T_3$ by definition) then allow, in principle, to separate 2-jet and 3-jet and other (e.g. spherical) events as sketched in Fig. 7.8a. The separation is efficient at energies high enough for 2-jet and 3-jet formation, as can be seen in Fig. 7.8c which shows the T_3 vs T scatter plot for $q\bar{q}$, 3G and PS events generated at W = 30 GeV. At T energies, unfortunately, 3G events do not populate areas different from PS or $q\bar{q}$ events (Fig.7.8b). The loss of separability is not due to imperfections of the detector since in these plots we used MC events before submission to the detector. It is rather due to the strength of the fragmentation effects. In Fig. 7.9 we compare the T_3-T correlation from T decays to PS and 3G simulated events after detector. To ease a quantitative evaluation we

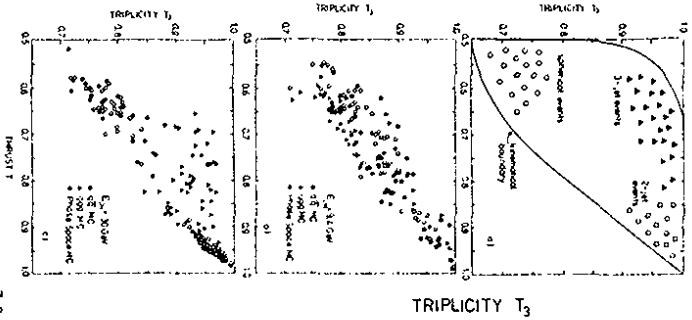

Fig.7.8 Scatter diagrams of triplicity (T_3) versus thrust (T), (a) schematic, and from MC simulations at W = 30 GeV (b) and at W = 9.4 GeV (c).

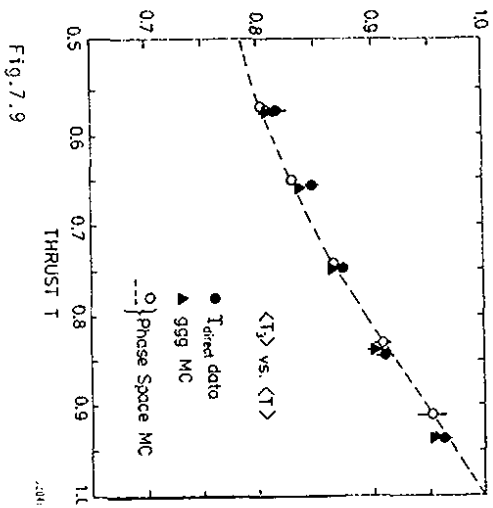

Fig.7.9 Scatter diagram of average tripicity versus average thrust for the T direct decay data and various models.

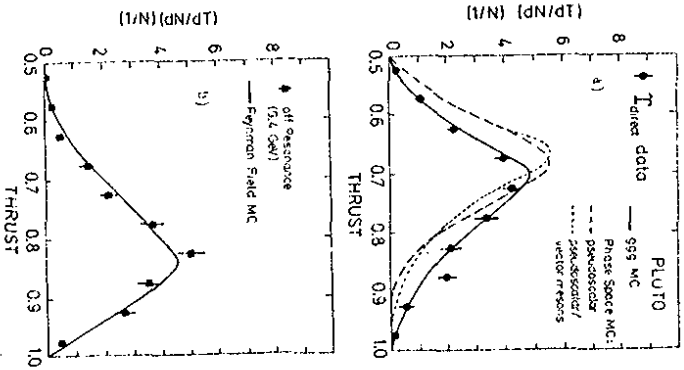

Fig.7.10 Distributions of observed thrust for T-direct (a) and off-resonance events (b) compared to various Monte Carlo models.

show $\langle T_3 \rangle$ vs $\langle T \rangle$, in several thrust intervals. The T, PS and 3G points fall on a common curve. This means that no 3-jet structure is revealed by the triplicity method in our data from the T decay.

The only jet structure that is observed in this analysis is a collinear 2-jet structure. In Fig. 7.10 we show the (observed) thrust distributions (a) for T decays, 3G and PS, and (b) for 9.4 data and $q\bar{q}$ MC. The T thrust distributionlies "between" the respective continuum and phase space distributions, and is significantly different from either one as is evident from the thrust average values in table 7.1. This clearly demonstrates that the T direct decay mechanism does not proceed through a $q\bar{q}$ intermediate state, but still imposes a non trivial kinematic correlation on the final state topology. In Fig. 7.10a we observe a perfect agreement with the three gluon decay mechanism.

Because of the good agreement between T decay data and 3G model we can use the model events to study the effects of hadronization and detector resolution and acceptance on the correlation between original gluon kinematics and reconstructed jet quantities. These studies show [712, 724], that the measured thrust distribution (Fig. 7.10) can be corrected for detector effects, but not for hadronization, and that the thrust direction is close enough to the original most energetic gluon such that the thrust angular distribution can be corrected for both, detector and hadronization effects. Fig. 7.11 shows the corrected experimental thrust distribution. The dotted line indicates the thrust prediction at the parton (3 gluon) level, where $T = x_1$ (see Fig. 7.7d). If the T decays are entirely via the 3 gluon decay mode the difference between the data points and the curve comes from gluon hadronization. Hadronization at T energies obviously deforms the original parton structure considerably. The average thrust corrected for detector effects is

$$\langle T \rangle = 0.73 \pm 0.01 \qquad (7.25)$$

Fig. 7.12 shows the angular distribution of the thrust axis corrected for detector and hadronization effects. It is consistent with the prediction for vector gluons (solid line), and is inconsistent with the prediction of scalar gluons [727] (dashed line). This result provides clear evidence against scalar gluons.

Also, the parton quantities x_1 and θ_3 (see Fig. 7.7a) on the average are clearly correlated with the corresponding values determined from the triplicity vectors.

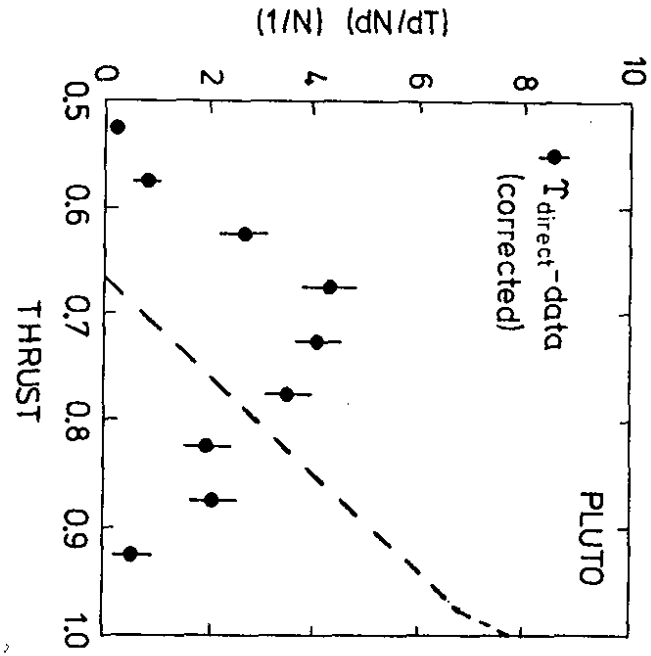

Fig.7.11 Corrected thrust distribution for the T direct decay. The dotted curve indicates the thrust predicted at the 3 gluon level.

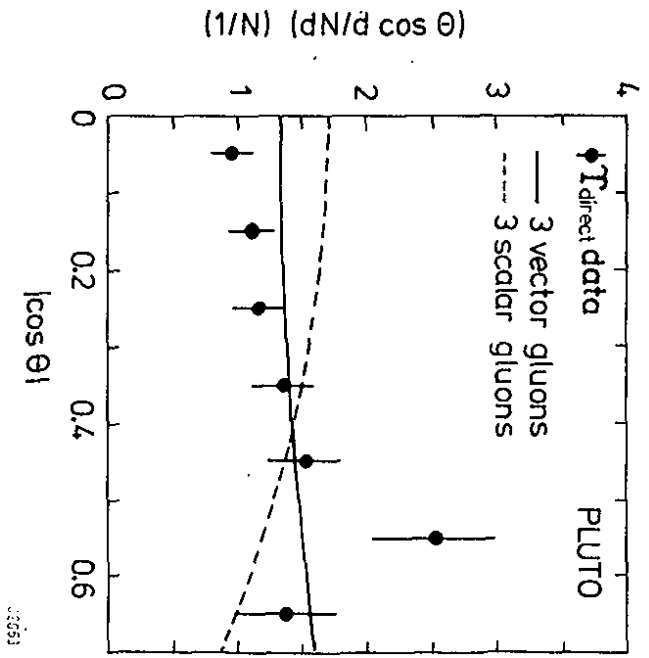

Fig.7.12 Distribution of |cosθ|, corrected for detector and hadronization effects. θ is the angle between the thrust axis and the beam axis. The curves are predicted for T-decay into 3 vector or 3 scalar gluons, resp..

Table 7.1 gives the average values from data and model expectations. In Fig.7.13 we show the θ_3 distribution. Again, the data and the three gluon decay model agree very well. Further distributions of triplicity related variables are given in refs. [724, 728].

The 3-gluon Monte Carlo studies also show that hadronization destroys the orientation of the 3-gluon plane such that in general it cannot be recovered from the triplicity vectors. Therefore the orientation of the triplicity plane cannot be used to check the gluon spin assignment [729].

7.6. Inclusive single particle properties

Here we describe some differences of T and continuum events in terms of properties of single charged tracks [+] [730] and neutral short lived kaons.

7.6.1 Multiplicity of charged tracks

According to predictions [704a,e,h,j] one expects from 3 gluon hadronization a higher charged track multiplicity than from $q\bar{q}$ hadronization, because 3 jets should give more hadrons than 2 jets (at same total energy), and also since gluons have larger color charge than quarks (by factor 9/4) gluons should produce jets with more hadrons than quarks (at same jet energy). For the T a rise of 1.5 - 3 units is predicted [704h], i.e.

$$\langle n_{ch} \rangle^{T}_{ggg} \sim 9 \qquad (7.26a)$$

The average charged multiplicity for T direct decays measured by PLUTO [712] is

$$\langle n_{ch} \rangle^{T}_{dir} = 8.2 \pm 0.1 \qquad (7.26b)$$

while in the continuum we obtained (see section 6)

$$\langle n_{ch} \rangle^{off\ T} = 6.9 \pm 0.1 \qquad (7.26c)$$

The observed rise of 1.3 ± 0.2 units is slightly smaller but not inconsistent with the expected values.

[+] Neutral pions are not included since resolving of single neutral pions is difficult to achieve.

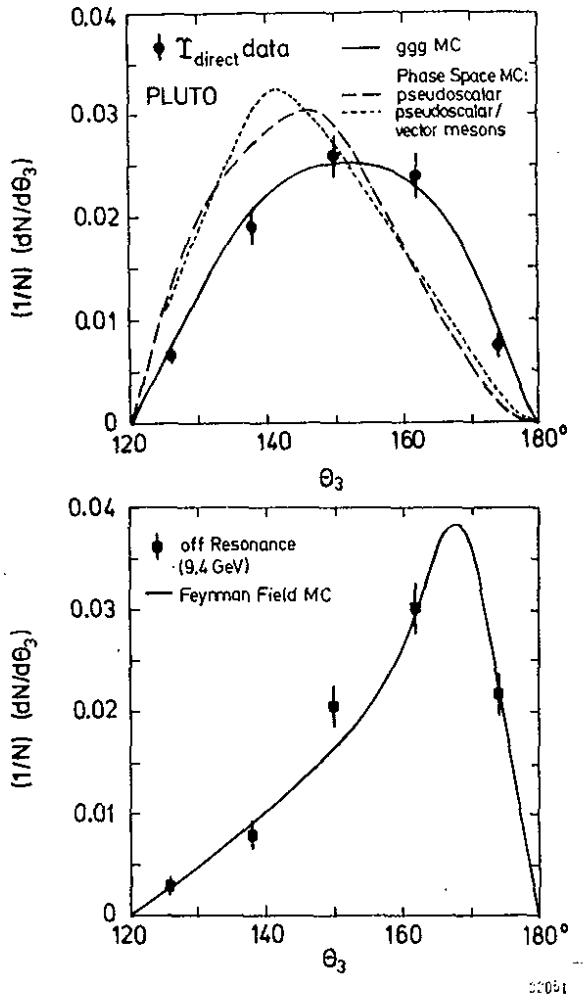

Fig.7.13

Distribution of the reconstructed angle θ_3 between the two most energetic triplicity jets for T-direct and off-resonance data compared to various Monte Carlo models (uncorrected).

7.6.2 Momentum distributions

A change in multiplicity implies a change in the average particle momenta. In table 7.3 we compare the average values of continuum and T events [725, 726] for $p_\perp$, $p_{\parallel}$ (w.r.t. thrust), and P_{out} (w.r.t. the acoplanarity plane), and the slope parameter B of a fit [713] to the inclusive charged particle momentum spectrum by

$$d\sigma/dx = A \cdot \exp\{-B \cdot x_p\} \qquad (7.27)$$

Table 7.3 Properties of charged particle momenta (observed)

data type	B	$\langle p_{\parallel} \rangle$ MeV/c	$\langle p_\perp \rangle$ MeV/c	$\langle p_{out} \rangle$ MeV/c
PS (MC)	10.7 ± 1	.58 1	.47 1	.177 6
3G (MC)	8.9 2	.55 1	.38 1	.140 6
T data	10.9 3	.49 1	.34 1	.129 3
9.4 GeV data	7.8 2	.62 2	.33 1	.118 3
FF (MC)	7.8 1	.72 1	.32 1	.115 2

The average values in table 7.3 are not corrected for detector and event selection effects. In particular, the values for B come from an event sample selected differently than the one used for $\langle p_{\parallel} \rangle$, $\langle p_\perp \rangle$ and $\langle p_{out} \rangle$. Nevertheless these quantities provide interesting information on the difference between $q\bar{q}$ continuum events and direct T decays:

(i) $\langle p_\perp \rangle$ with respect to the thrust axis in T direct decays is not larger than in continuum events. Since $\langle p_{out} \rangle$ from T is not smaller than in the continuum this reflects the result from the topological investigations (see sect. 7.5) that no planar T decays are observed.

(ii) $\langle p_{\parallel} \rangle$ in T decays is significantly smaller than in continuum, and similarly the momentum distribution slope parameter B in (7.27) is significantly larger. The smaller single particle momenta, together with an unchanged $p_\perp$, are the reason for the softer 2-jet T topology observed in section 7.5.

For completeness we also include the corresponding values from the three models in table 7.3. It is obvious that the single charged particle properties of the T are less well reproduced than the topological event quantities in table 7.1, by the 3G model used here.

7.6.3 Inclusive K^0_S production

Since the T direct decays proceed through a mechanism for hadronization different from $q\bar{q}$ fragmentation it is interesting to compare the flavour content of T decays with continuum events and with T hadronization models. The PLUTO experiment has measured the K^0_S production [731]. Fig. 7.14 shows the K^0_S momentum distribution, *corrected for K^0 detection efficiency, off the T (a) and for T* direct decays (b). The T direct distribution falls off faster than the continuum. Either K^0 distribution has a shape similar to the respective inclusive distributions of charged particles. Also for charged particles the inclusive momentum distribution is steeper for T direct decays than in the continuum, as indicated by the slope parameters B in table 7.3. For the K^0 yield we find the *ratios*

		T direct	continuum	
K^0_S	per event	.97 ± .22	.73 ± .16	(7.28)
K^0_S	per charged track	.12 ± .03	.11 ± .02	

The share of K's among final state particles obviously is very similar in direct T decays and in $q\bar{q}$ jets at T energy, even though the parton processes are very different. The expectation for the inclusive K^0 distribution from the Lund model [732] for a 3-gluon hadronization is shown as solid curve in Fig. 7.14b. It agrees in shape and rate with the experimental result.

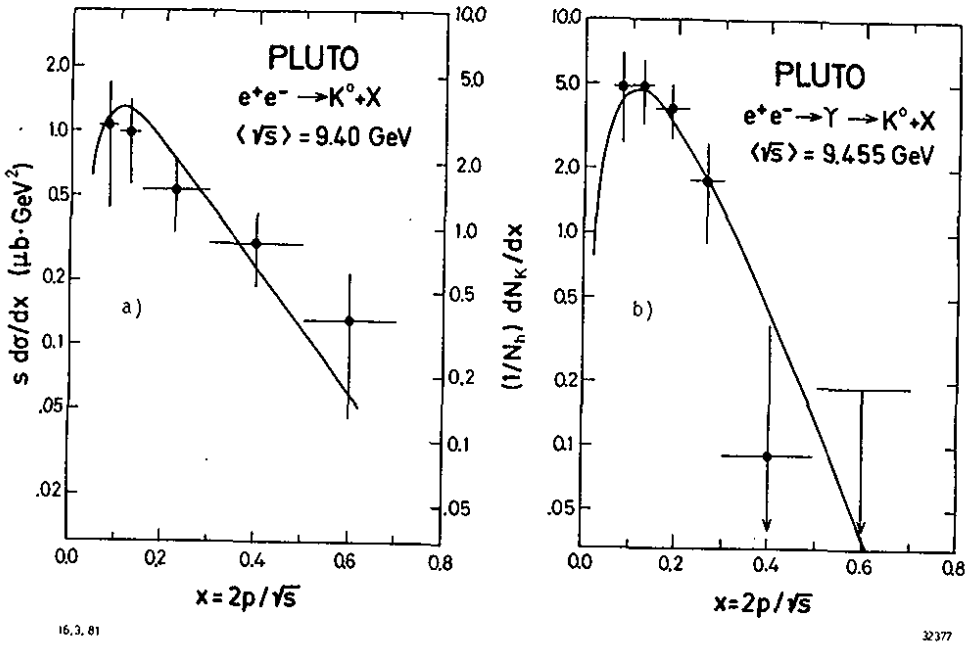

Fig.7.14

(a) $s d\sigma/dx$ for the continuum at $\sqrt{s} = 9.4$ GeV. Also given is the yield per hadronic event $1/N_h\ (dN_K/dx)$ with $N_K = 2\ N_{K^0_S}$. The curve indicates the model prediction.

(b) Yield per T-event, $1/N_T(dN_K/dx)$ for the T-direct decays after background subtraction. The curve represents the prediction of a $T \to 3$ gluon decay *model (see text)*.

7.7 Summary and conclusions for T (9.46)

(1) The charge of the T constituent quarks is $|e_b| = {}^1/_3$.

(2) The T is a narrow state, with $25 < \Gamma_{tot} < 122$ KeV at 90% c.l.

(3) 87 ± 5% of the hadronic T decays are due to non electromagnetic ('direct') decays.

(4) The topology of the direct decays is significantly different from $q\bar{q}$ final states. A decay through colourless gluons $b\bar{b} \to g \to qq$ is ruled out.

(5) The T topology is also significantly different from a structureless topology as simulated by phase space.

(6) The direct decays show a soft 2-jet character, but neither a distinct 3-jet pattern nor a planar topology. This is expected from a study of simulated T decays as the consequence of a 3 gluon decay mechanism with a subsequent quark like hadronization of the gluons. At the T, energies are too low for the formation of three separated jets.

(7) The angular distribution of the thrust axis agrees with the expectation for a decay into 3 vector gluons, and clearly rules out the possibility of a decay into 3 scalar gluons.

(8) The observed increase in charged track multiplicity of $\Delta n = 1.3 \pm 0.2$ for the T is consistent with the expectations of QCD.

(9) K^0s are produced with the same fraction relative to charged particles in T direct decays and in continuum events. Inclusive K^0 and charged particle momentum distributions are similar in shape for T direct decays.

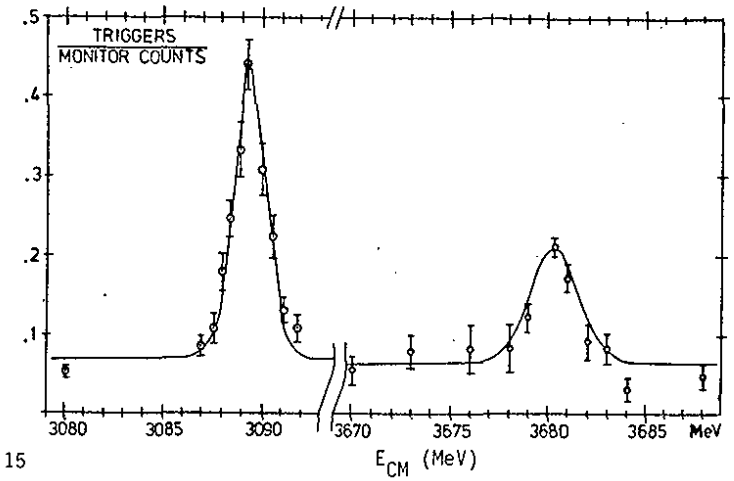

Fig.7.15

Excitation of J/ψ and ψ' resonances as of December 1974. Curves indicate the resolution of beam energies.

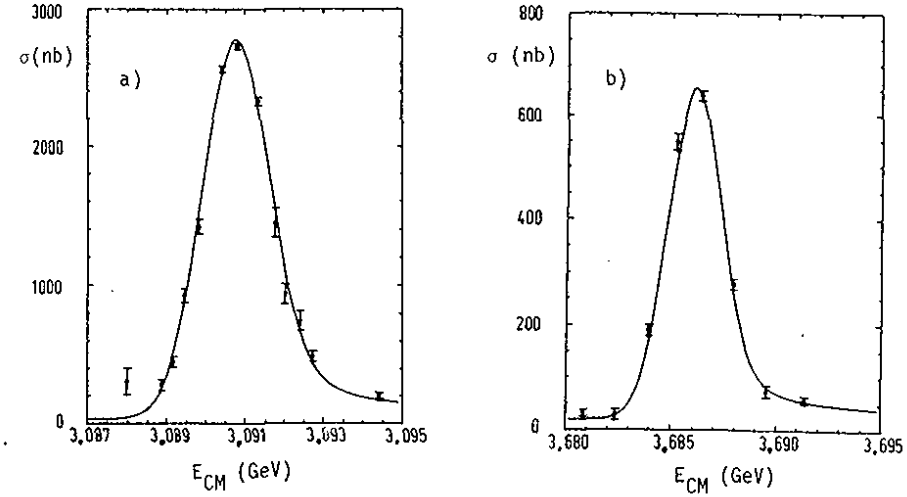

Fig.7.16

Cross section for J/ψ (a) and ψ' (b) excitation, corrected for acceptance. For resonance parameters see eq. (7.30).

7.8 J/ψ and ψ' resonances

Briefly after the discovery of the J/ψ [733] and the ψ' [734] resonances in 1974, their excitation was also measured by experiments [735, 736] at the DORIS storage ring which was just brought into operation. Fig. 7.15 shows the increase of multiprong counts in the PLUTO hardware trigger, from the first measurements made at all with the PLUTO detector, in late fall 1974. From later measurements of the cross section for $e^+e^- \to$ hadrons (see Fig. 7.16), the masses M and the electronic widths Γ_{ee} have been determined [737], using eq. (7.7) and the ratios $\Gamma_{had}/\Gamma_{tot}$ [722]:

	M(MeV)	Γ_{ee} (keV)	
J/ψ	3091 ± 3	5.3 ± 0.6	(7.30)
ψ'	3686 ± 4	1.9 ± 0.2	

The error in the masses comes from the uncertainty in the DORIS absolute energy calibration of 0.1% at J/ψ and ψ' energies. Mass and width values are consistent with results from SPEAR [738], and the masses agree with the DASP measurement [739]. The electronic width Γ_{ee} (J/ψ) corresponds to an electric charge of $e_q = 2/3$ for the constituent quarks (see Fig. 7.4a) in agreement with the charm flavour assignment.

There is an impressive amount of results on J/ψ and ψ' multiprong decay modes [722], mainly from the SLAC-LBL MARK I and the Crystal Ball collaboration. The PLUTO experiment has contributed one new decay mode, the radiative decay $J/\psi \to \gamma f$ [740]. In the following subsections we briefly review the topological properties of J/ψ and ψ' multiprong decays, and describe the analysis of the decay $J/\psi \to \gamma f$. Other PLUTO results on J/ψ decays can be found in [740,741].

7.8.1 Topological decay properties

The J/ψ decays into hadrons proceed mainly (83%) in a non electromagnetic (direct) mode as can be inferred from the leptonic branching ratio $B_{\ell\ell}$ [722]. The J/ψ hadronic multiprong decays however show no jet structure at all. The average thrust and sphericity values agree with the phase space expectation (see Fig. 6.13), and also with the continuum data at these energies.

Also the average charged track multiplicity shows no difference on and off J/ψ, whereas for ψ' it is slightly larger [737]:

$\langle n_{ch} \rangle$	J/ψ	ψ'	
on	3.6 ± .1	4.3 ± .1	(7.31)
off	3.6 ± .1	3.7 ± .1	

The increase on the ψ' can be understood quantitatively as an effect of the large branching ratio for the decay mode $\psi' \to \pi^+\pi^-$ J/ψ (BR = 33%) Therefore it is clear that global topological quantities do not provide a handle for tests on J/ψ decay mechanisms, e.g. like the 3-gluon or the radiative 2-gluon decay as expected by QCD (see Fig. 7.2). Exclusive channels, however, can allow for some checks of QCD expectations, as described in the next subsection.

7.8.2 The decay rate $J/\psi \to \gamma f$

This radiative decay was found in the PLUTO experiment [740], and also measured by DASP [742]. It has a surprisingly large branching ratio of 0.20 ± 0.07%, similar in size to the 0.3% for the branching ratio of the hadronic decay $J/\psi \to \omega f$ [722, 741b]. Events of the type $\pi^+\pi^-\gamma$ were searched for in a total of 84000 hadronic J/ψ decays by selecting charge balanced 2-prong events with a photon conversion visible in the track chambers, and passing a 3 constraints fit to the hypothesis $e^+e^- \to \pi^+\pi^-\gamma$. According to MC studies a fraction (21%) of the decays $J/\psi \to \pi^+\pi^-\pi^0$ is accepted by these criteria, and the majority of the accepted events is on that account. The effective $\pi^+\pi^-$ mass distribution (Fig. 7.17) shows a prominent ρ^0 peak, and a clear f(1270) peak. Since C parity conservation does not allow for $\rho^0\gamma$ and $f\pi^0$ final states we observe $J/\psi \to \rho^0\pi^0$ and fγ decays in these events, with the following branching ratios:

	Events	BR (%) (corrected for other decay modes)	
$J/\psi \to \gamma f$	35 ± 10	0.20 ± 0.07	(7.32)
$\gamma f'$		<0.023 (90% c.l.)	
$\rho^0\pi^0$	183 ± 16	1.6 ± 0.4	

The large branching ratio for $J/\psi \to \gamma f$ fits nicely into the QCD picture for radiative decays as indicated in the diagrams in Fig. 7.18. Lacking a

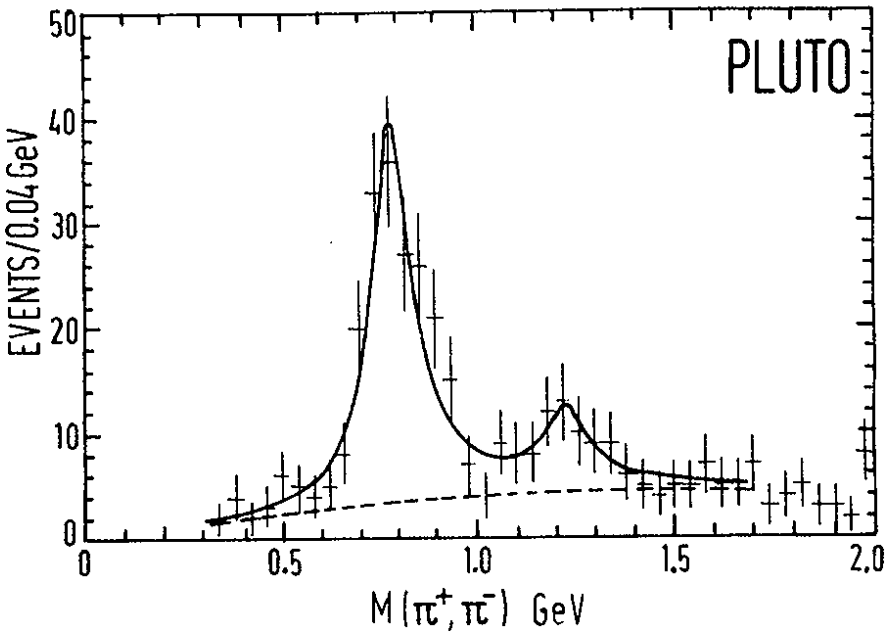

Fig.7.17

$J/\psi \to f\gamma$ decay. The $M(\pi^+\pi^-)$ distribution, excluding events lying in the $\rho^\pm$ mass bands. The solid line represents the best fit to the data and the dashed curve is the estimated background.

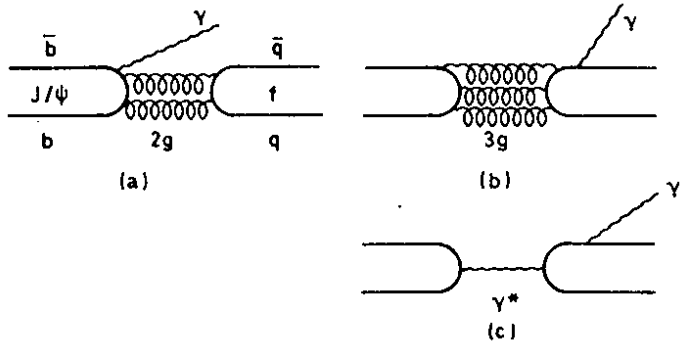

Fig.7.18

Diagrams for the $J/\psi \to \gamma f$ decay, with photon emission before (a) and after the $c\bar{c} \to q\bar{q}$ transition (b,c).

quantitative prediction for the width due to diagram (a) when 2 gluons mediate the transition $c\bar{c} \to q\bar{q}$, one expects here a larger contribution than from diagram where (b) either 3 gluons (strong decay) or (c) one photon (electromagnetic decay) are required. In fact the branching ratios for the latter two mechanisms, where the photon is radiated from the $q\bar{q}$ quarks can be estimated by vector meson dominance relations. For the isospin conserving 3 gluon mode (Fig.7.18b) we use $B(J/\psi \to \omega f) = 0.29 \pm 0.07\%$ [722] to get

$$B(J/\psi \to \gamma f, \text{"3g"}) = 4 \cdot 10^{-6} \qquad (7.33a)$$

and for the isospin not conserving electromagnetic (Fig. 7.18c) mode we use $B(J/\psi \to \rho f) < B(J/\psi \to 4\pi) = 0.4 \pm 0.1\%$ [743] to get

$$B(J/\psi \to \gamma f, \text{"}\gamma\text{"}) \leq 2 \cdot 10^{-5} \qquad (7.33b)$$

The observed rate is more than 100 times larger than the estimates for these mechanisms, confirming qualitatively the expectation based on gluon counting. The observed branching ratio is similar to those found for the radiative decays $J/\psi \to \gamma\eta, \gamma\eta'$ [722] which may proceed in an analogous way.

Applying kaon masses to the 2 prong events we have also searched for the decay $J/\psi \to \gamma f'$ (K^+K^-). No resonance signal was found. The upper limit on the branching ratio is included in (7.32). The ratio $B(J/\psi \to \gamma f')/B(J/\psi \to \gamma f) < 0.12 \pm 0.05$ seems to deviate from a value of 0.5 expected for a SU_3 pure singlet mixing of $q\bar{q}$ with $c\bar{c}$ states (diagram (a) of Fig. 7.18) in an unbroken SU_3 model [744]. This observation was confirmed by DASP [745] and has been discussed further in [746].

7.8.3 f polarization

The process $e^+e^- \to J/\psi \to \gamma f$ has 3 independent f helicity amplitudes A_0, A_1 and A_2. Their relative sizes, say $x = A_1/A_0$ and $y = A_2/A_0$, fix the f polarization. They have been calculated for the 2 gluon transition (Fig. 7.18a) [747], allowing for a further check of this mechanism. Very similar predictions follow, however, also from other assumptions, e.g. from a tensor meson dominance model (TMD) [748], which gives however no prediction for the rate, or from an electromagnetic transition [749] which conflicts with the observed rate. The predictions are shown in Fig. 7.19.

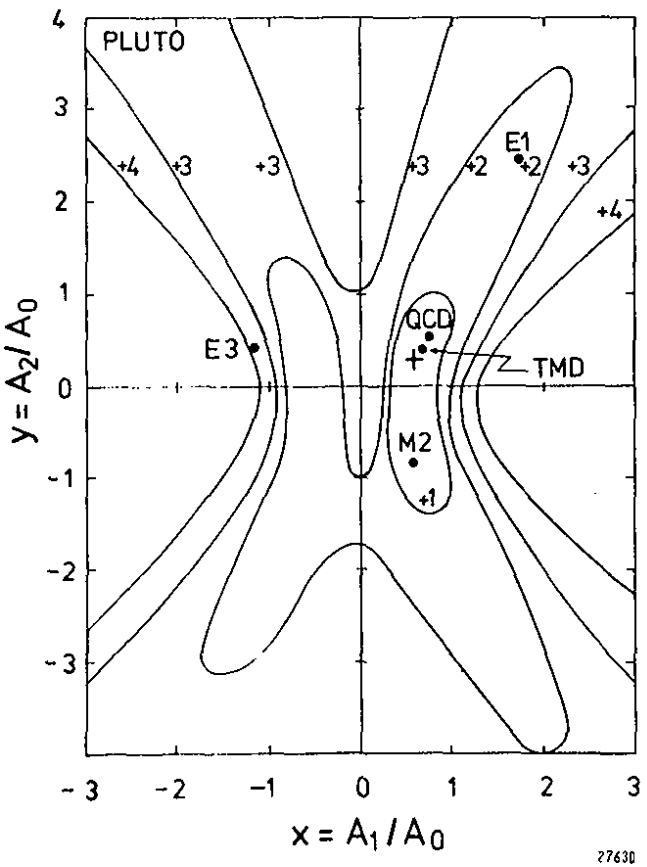

Fig.7.19

Equal χ^2 countours drawn in the $x = A_1/A_0$, $y = A_2/A_0$ plane obtained from the fit to the $e^+e^- \to J/\psi \to f\gamma \to \pi^+\pi^-\gamma$ process. The crossed point is the minimum value. The predicted QCD and TMD points are taken from refs. 747 and 748. The expected values for pure E1, M2 and E3 multipole radiation transitions are also shown.

The two quantities x, y can be measured from the f production and decay angular distribution [750]

$$W(\delta_p,\delta_M,\phi_M) \propto 3x^2 \sin^2\delta_p \sin^2 2\delta_M + (1+\cos^2\delta_p)\left[(3\cos^2\delta_M - 1)^2 + \frac{3}{2}y^2\sin^4\delta_M\right] - \sqrt{3}x\sin 2\delta_p \sin 2\delta_M(3\cos^2\delta_M - 1 - \sqrt{\frac{3}{2}}y\sin^2\delta_M)\cos\phi_M + \sqrt{6}y\sin^2\delta_p\sin^2\delta_M(3\cos^2\delta_M - 1)\cos 2\phi_M, \quad (7.34)$$

$\delta_p = \sphericalangle(f,e^+)$ in e^+e^- CMS

δ_M, ϕ_M = polar and azimuthal π^+ angles in the helicity frame of the $\pi^+\pi^-$ system.

The analysis is described in more detail in ref. [740b,c]. Fig. 7.19 shows a plot of constant χ^2 contours as determined from the one-dimensional projections $W(\cos\delta_p)$, $W(\cos\delta_M)$ and $W(\phi_M)$, in the x - y plane. The minimum ($\chi^2 = 26$ for 25 constraints) at

$$A_1/A_0 = 0.6 \pm 0.3, \qquad A_2/A_0 = 0.3\ ^{+0.6}_{-1.6} \quad (7.35)$$

is in good agreement with the prediction for the 2-gluon transition.

In summary, the $J/\psi \to \gamma gg$ decay mode provides a plausible explanation for the large $J/\psi \to \gamma f(1270)$ branching ratio, and is in agreement with the f polarization. [+] However, the branching ratio for $J/\psi \to \gamma f'(1515)$ seems to be smaller than expected from simple SU_3 arguments in this picture.

[+] Evidence for the $J/\psi \to \gamma gg$ transition has also been observed in the inclusive photon energy distribution by the SLAC-LBL MARK II collaboration [751].

References

701 a) S.W.Herb et al., Phys.Rev.Letters 39 (1977) 252
b) W.R.Innes et al., Phys.Rev.Letters 39 (1977) 1240
c) W.R.Innes, private communication

702 V.A. Matveev, B.V.Struminskii and A.N.Tavkhelidze, DUBNA Report P-2524 (1965), submitted to "High Energy Physics"; H.Pietschmann and W.Thirring, Phys.Lett. 21 (1966) 713; R. Van Royen and V.F.Weisskopf, Nuovo Cim. 50 (1967) 617; 51 (1967) 583

703 T.Appelquist, H.D.Politzer, Phys.Rev.Lett. 34 (1975) 43, and Phys.Rev. D12 (1975) 1404

704 a) K.Koller, T.F.Walsh, Phys.Lett. 72B (1977) 227 (E: 73B (1978) 504)
b) K.Koller, T.F.Walsh, Nucl.Phys. B140 (1978) 449
c) K.Koller, H.Krasemann, T.F.Walsh, Z.Physik C, Particles and Fields 1 (1979) 71
d) T.A.DeGrand, Y.G.Ng, S.H.H.Tye, Phys.Rev. D16 (1977) 3251
e) S.J.Brodsky, T.A.DeGrand, R.R.Horgan, D.G.Coyne Physics Letters 73B (1978) 203
f) H.Fritzsch, K.H.Streng, Physics Letters 74B (1978) 90
g) A.de Rujula, J.Ellis, E.G.Floratos, M.K.Gaillard, Nucl. Phys. B138 (1978) 387
h) I.I.Y.Bigi, S.Nussinov, MPI-PAE/PTh 44/78 (1978)
j) S.Brodsky, J.Gunion, Phys.Rev.Lett. 37 (1976) 402

705 a) We are deeply indepted to the work of D.Degêle, H.Gerke, K.Holm, R.D.Kohaupt, G.Mühlhaupt, H.Nesemann, S.Pätzold, A.Piwinski, R.Rossmanith, K.Wille and A.Wrulich.
b) D.Degêle et al., report DESY 79/08

706 a) PLUTO Coll., Ch.Berger et al., Phys.Lett. 76B (1978) 243
b) DASP II Coll., C.W.Darden et al., Phys.Lett. 76B (1978) 246

707 J.L.Richardson, Phys.Lett. 82B (1979) 272

708 W.Celmaster, Phys.Rev. D19 (1979) 1517

709 R.Barbieri et al., Nucl. Phys. B105 (1976) 125

710 J.L.Rosner, C.Quigg, and H.B.Thacker, Phys.Lett. 74B (1978) 350
H.B.Thacker, C.Quigg, and J.L.Rosner, Phys.Rev. D18 (1978) 274, 287

711 M.Böhm, H.Joos and M.Krammer, Acta Phys.Austr. 38 (1973) 123, J.J.Sakurai, Phys.Lett. 46B (1973) 207, D.R.Yennie, Phys.Rev.Lett. 34 (1975) 239, F.E.Close, D.M.Scott, D.Sivers, Phys.Lett. 62B (1976) 213, T.Walsh, DESY Report 76/13 (1976), G.J.Gounaris, Phys.Lett. 72B (1977) 91 M.Greco, Phys.Lett. 77B (1978) 84

712 PLUTO Coll., Ch.Berger et al., Z.Physik C8 (1981) 101

713 Ch.Gerke, Dissertation, Hamburg (1980), Int.Rep. DESY-PLUTO 80/03 (1980)

714 M.Greco, G.Pancheri-Srivastava, Y.Srivastava, Nucl.Phys. B101 (1975) 234

715 a) LENA Coll., J.K.Bienlein et al., Phys.Lett. 78B (1978) 360
b) DASP II Coll., G.W.Darden et al., Phys.Lett. 78B (1978) 364

716 PLUTO Coll., Ch.Berger et al., Z. Physik C1 (1979) 343

717 PLUTO Coll., Ch.Berger et al., Phys.Lett. 93B (1980) 497

718 PLUTO Coll., Ch.Berger et al., Z.Physik C4 (1980) 269

719 F.A.Berends et al., Nucl.Phys. B63 (1973) 381, Nucl.Phys. B68 (1974) 541, Phys.Letters 63B (1976) 432

720 DASP II Coll., H.Albrecht et al., Phys.Lett. 93B (1980) 500

721 LENA Coll., B.Niczyporuk et al., DESY 80/53 (1980)

722 Particle Data Group, Rev.Mod.Phys. 52 (1980)

723 For a recent discussion on the choice of $Q^2 = M^2$ or $Q^2 = (M/3)^2$ we refer to: R.G.Roberts, CERN report TH 3024 (1981)

724 H.J.Meyer, Dissertation, Siegen (1981)

725 PLUTO Coll., Ch.Berger et al., Phys.Lett 82B (1979) 449

726 G.Knies, Proceedings of the XIVth Rencontre de Moriond, p.99 (1979)

727 K.Koller, H.Krasemann, Phys.Lett. 88B (1979) 119

728 a) PLUTO Coll., Ch.Berger et al. (talk by S.Brandt), Proceedings of the International Conference on High Energy Physics, Geneva 1979, p.338 (and DESY 79/53)
b) PLUTO Coll., C.Grupen, Proceedings of the XX Int.Conf. on High Energy Physics, Madison 1980 (and Siegen, Preprint SI-80-11)

729 T.F.Walsh, P.M.Zerwas, Phys.Lett. 93B (1980) 53

730 See also H.Meyer, Proceedings of the 1979 International Symposium on Lepton and Photon Interactions at High Energies, FNAL (1979) (and DESY 79/81)

731 PLUTO Coll., Ch.Berger et al., submitted to Phys.Lett.B, and DESY report 81-018 (1981)

732 T.Sjöstrand, Lund preprints, LU TP 79-8 (1979) and LU TP 80-3 (1980)

733 J.J.Aubert et al., Phys.Rev.Letters 33, 1404 (1974)
J.E.Augustin et al., Phys.Rev.Letters 33, 1406 (1974)

734 C.Bacci et al., Phys.Rev.Letters 33, 1408 (1974)

735 DASP Coll., W.Braunschweig et al., Phys.Lett. 53B (1974) 393

736 PLUTO Coll., L.Criegee et al., Phys.Lett. 53B (1975) 489

737 A.Bäcker, Thesis (1977), internal report DESY F33-77/03

738 P.A.Rapidis et al., Phys.Rev.Lett. 39 (1977) 526, 974 (E)

739 DASP Coll., W.Braunschweig et al., Phys.Lett. 63B (1976) 115

740 a) PLUTO Coll., G.Alexander et al., Phys.Lett. 72B (1978) 493
b) PLUTO Coll., G.Alexander et al., Phys.Lett. 76B (1978) 652
c) K.Derikum, Thesis (1978), internal report DESY F33-78/03

741 a) PLUTO Coll., L.Criegee et al., DESY 75/32 (unpublished)
b) PLUTO Coll., J.Burmester et al., Phys.Lett. 72B (1977) 135

742 DASP Coll., R.Brandelik et al., Phys.Lett. 74B (1978) 292

743 Mark I Coll., B.Jean-Marie et al., Phys.Rev.Lett. 36 (1976) 291

744 T.Walsh, in Storage Ring Physics (Rencontre de Moriond, 1976) ed. J.Tran Thanh Van, Paris (1976), and DESY report 76/13

745 DASP Coll., R.Brandelik et al., Z.f.Phys. C1 (1979) 233

746 H.J.Lipkin and H.R.Rubinstein, Weizman Institute Preprint WIS-78/13 Ph (unpublished)

747 M.Krammer, Phys.Lett. 74B (1978) 361

748 W.Gampp and H.Genz, Phys.Lett 76B (1978) 319

749 H.Krasemann, private communication

750 P.K.Kabir and A.J.G.Hey, Phys.Rev.D13 (1976) 3161

751 D.L.Scharre et al., Phys.Rev. D23 (1981) 43

Figure Captions

7.1 Columbia-Fermilab-Stony Brook: invariant mass distribution of $\mu^+\mu^-$ from $p + Be \to \mu^+\mu^- + X$: evidence for T and T' [701].

7.2 Diagrams for lepton pair (a) and hadron (b) and T (c) production in e^+e^- annihilation. Diagrams for electromagnetic (d,e) and direct (f) T decays. QCD diagrams for T decays (g,h).

7.3 Total cross section for $e^+e^- \to$ hadrons at T energies, (a) as from the fast analysis chain used during the T search and (b) after final evaluation. The curves are a fit of the continuum and the T cross section, to the data. They include the radiative corrections and the machine energy width.

7.4(a) Reduced leptonic width Γ_{ee}/Q_q^2 for vector meson ground states as a function of mass.

(b) Lower bounds on Γ_{ee} for T and T' for different quark charges. The shaded area indicates the charge 1/3 predictions of 20 different potential models. A comparison with the DORIS data shows good agreement with charge 1/3 and excludes 2/3.

7.5 Angular distribution for muon pairs produced in the Ypsilon region. Data on and off resonance are combined. The curve is proportional to $1+\cos^2\theta$.

7.6 The differential cross section s $d\sigma/(d\cos\theta)$ for reaction $e^+e^- \to e^+e^-$ on the resonance ($9.45 \leq E_{cm} \leq 9.465$). The full curve is the QED part including the effects of radiation and of finite angular resolution. The dashed curve also includes the direct decay $T \to e^+e^-$.

7.7(a) Quantities used to describe the T decay into 3 massless quanta in the T rest frame.

(b) Dalitz plot of the gluon energies. Momentum conservation limits the populations to the dotted triangles. By ordering $x_1 \geq x_2 \geq x_3$ they are further restricted to the shaded area.

(c) Dalitz plot density for the T-decay into 3 vector gluons (or a photon and 2 vector gluons), before ordering of x_i.

(d) Ordered energy distribution of the individual gluons in $T \to ggg$.

7.8 Scatter diagrams of triplicity (T_3) versus thrust (T), (a) schematic, and from MC simulations at W = 30 GeV (b) and at W = 9.4 GeV (c).

7.9 Scatter diagram of average triplicity versus average thrust for the T direct decay data and various models.

7.10 Distributions of observed thrust for T-direct (a) and off-resonance events (b) compared to various Monte Carlo models.

7.11 Corrected thrust distribution for the T direct decay. The dotted curve indicates the thrust predicted at the 3 gluon level.

7.12 Distribution of $|\cos\theta|$, corrected for detector and hadronization effects. θ is the angle between the thrust axis and the beam axis. The curves are predicted for T-decay into 3 vector or 3 scalar gluons, resp..

7.13 Distribution of the reconstructed angle θ_3 between the two most energetic triplicity jets for T-direct and off-resonance data compared to various Monte Carlo models (uncorrected).

7.14(a) $s d\sigma/dx$ for the continuum at $\sqrt{s} = 9.4$ GeV. Also given is the yield per hadronic event $1/N_h\ (dN_K/dx)$ with $N_K = 2\ N_{K^0_s}$. The curve indicates the model prediction.

(b) Yield per T-event, $1/N_T(dN_K/dx)$ for the T-direct decays after background subtraction. The curve represents the prediction of a $T \to 3$ gluon decay model (see text).

7.15 Excitation of J/ψ and ψ' resonances as of December 1974. Curves indicate the resolution of beam energies.

7.16 Cross section for J/ψ (a) and ψ' (b) excitation, corrected for acceptance. For resonance parameters see eq. (7.30).

7.17 $J/\psi \to f\gamma$ decay. The $M(\pi^+\pi^-)$ distribution, excluding events lying in the $\rho^\pm$ mass bands. The solid line represents the best fit to the data and the dashed curve is the estimated background.

7.18 Diagrams for the $J/\psi \to \gamma f$ decay, with photon emission before (a) and after the $c\bar{c} \to q\bar{q}$ transition (b,c).

7.19 Equal χ^2 countours drawn in the $x = A_1/A_0$, $y = A_2/A_0$ plane obtained from the fit to the $e^+e^- \to J/\psi \to f\gamma \to \pi^+\pi^-\gamma$ process. The crossed point is the minimum value. The predicted QCD and TMD points are taken from refs. 747 and 748. The expected values for pure E1, M2 and E3 multipole radiation transitions are also shown.

8. Photon-photon interactions

High energy $e^+ - e^-$ storage rings provide an effective tool for studying photon-photon interactions [801-810]. The fast moving electrons are surrounded by a Lorentz-contracted Coulomb field, equivalent to a photon flux which rises with the energy E_B like [800]

$$N(\omega)\, d\omega = \frac{2\alpha}{\pi} \frac{d\omega}{\omega} \cdot \ln \frac{E_B}{m_{el}} \qquad (8.1)$$

At PETRA energies the photon fluxes are sufficiently large to produce a sizeable rate of hadronic events, which in fact is comparable to the one originating from the one-photon annihilations.

Compared to hadron-hadron interactions the photon-photon collisions show several interesting features:

1. The C-parity of two photon system is positive, so that the production of C-even mesons (like the f^0) can be studied free of background from C-odd states (ρ^0, etc.)
2. The linear polarization of both interacting photons can be varied by fixing the e^+ and e^- scattering planes.
3. Most important, the 'virtuality' Q^2 of both photons can be varied with the electrons' kinematics, thus allowing a more complete investigation of the $\gamma\gamma$ dynamics than for other elementary particles.
4. Particle production in $\gamma\gamma$ collisions can be viewed as the dissociation of one photon into a pair of charged particles like leptons, pions and, most interesting, quarks, and the simultaneous structure analysis with the 2nd photon. In the case of hadron production, the variation of the kinematics allows a continuous survey from the low-Q^2 regime, which is determined by the scattering cross section between extended vector mesons (VDM) to the higher momentum transfers which first probe the structure of the vector mesons and eventually of quasi-free quark-antiquark states. The latter ones are completely predictable from perturbative QCD [811, 813], and should therefore allow fundamental checks of the theory.

It should also be noted that the short-distance domain of partons and QCD is not only reachable with highly virtual photons, but also with quasi-real ones, provided high transverse momenta are selected in the final state [814, 815]. In contrast to high-$p_\perp$ hadron-hadron interactions such $\gamma\gamma$ processes proceed in a 'pure' mode without any spectator particles present, again providing clean tests of QCD.

8.1 Kinematics

This section briefly describes the relation between the observed reaction,

$$e^+e^- \rightarrow e^+e^- X, \qquad (8.2a)$$

and the processes of interest, namely inelastic electron-photon scattering

$$e\,\gamma \rightarrow e\,X, \qquad (8.2b)$$

and in particular photon-photon interactions

$$\gamma\gamma \rightarrow X. \qquad (8.2c)$$

The kinematical variables and the matrix element used are shown in Fig. 8.1a. The incident e^+ and e^- (all called 'electrons') are colliding head-on with equal (highly relativistic) energies. 'X' is taken to be a hadronic state. +

The squared mass q_i^2 (virtuality) of the photons is given by

$$q_i^2 = (p_i - p_i')^2 = -4EE_i' \sin^2 \Theta_i/2 - m^2 \omega_i^2/EE_i' \quad (i=1,2) \qquad (8.3a)$$

with

$$\omega_i = E - E_i' \qquad (i=1,2) \qquad (8.3b)$$

are the laboratory photon energies, and m is the electron mass. The notation

$$Q^2 = -q_1^2 \qquad (8.3c)$$

will be often used.

+ Hadron production through one virtual photon (Fig. 8.1b) is assumed to be suppressed by the kinematics, and neglected here.

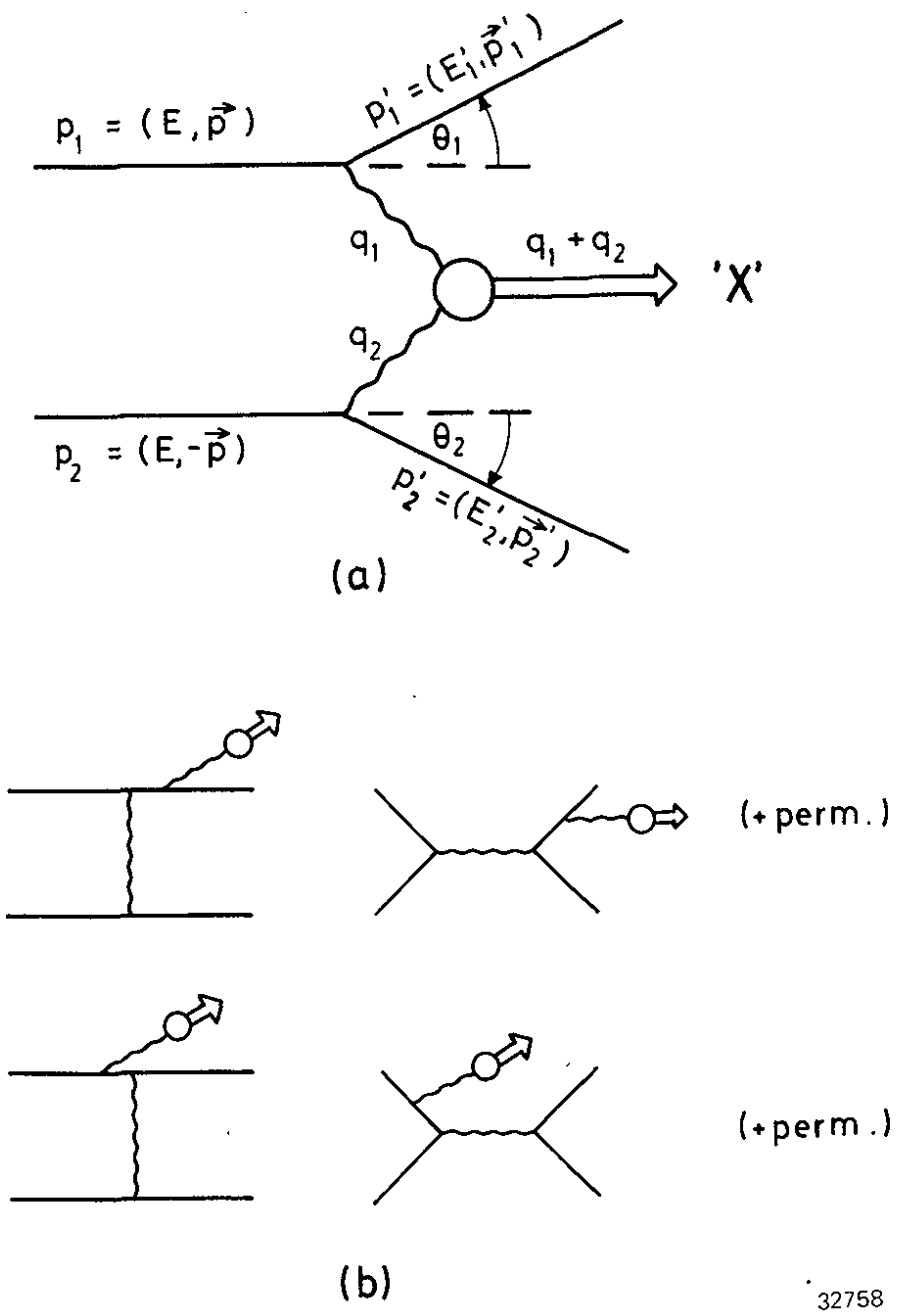

Fig. 8. 1 (a) Photon photon diagram with notations for four vectors and laboratory variables. (b) 'Compton' or 'bremsstrahlung' diagrams.

The invariant mass W of the hadron system X is given by

$$W^2 = (q_1 + q_2)^2 = 4\,\omega_1\,\omega_2 - 4\,E_1' E_2' \sin^2 \frac{\Theta_{12}}{2} \qquad (8.4)$$

with Θ_{12} being the angle between $\vec{p}_1'$ and $-\vec{p}_2'$.

The inclusive cross section for reaction (8.2) can either be expressed in terms of eight structure functions of the photon (Equ. 8.2b) [808-810], or more conventionally through eight total cross sections for hadron production by polarized virtual photons (Equ. 8.2c), each multiplied with complicated kinematical factors (see [807] and App. A1). The extraction of the $\gamma\gamma$ cross sections with the help of approximated kinematical factors has been extensively discussed in the literature [805-807, 809, 810, 812, 816-823]$^{+}$.

It was first pointed out and exploited by the PLUTO group [820-822] that the analysis is particularly simple for experiments in which one of the scattered electrons is measured ('single tag'), and the other one confined to very small scattering angles^{++} ('anti-tag'):

$$\Theta_2 \leq \Theta_2^{max} << 1 \qquad (8.5)$$

$^{+}$ With unpolarized electrons only six cross sections can be separated.

$^{++}$By covering all angles $> \Theta_2^{max}$ with electron detectors.

If Θ_2^{max} is small enough, the anti-tag condition forces the second photon to be very close to real (Equ. 8.3), transverse, and on average unpolarized. Reaction (8.2a) can then be considered inelastic electron scattering off a beam of quasi-real photons (8.2b), with only <u>two</u> structure functions contributing.

Similar to Hand's electroproduction formula [824] the e-e cross section $d\sigma_{ee}$ can be expressed in terms of the cross sections σ_t for transverse and σ_ℓ for longitudinal virtual photons colliding with real ones:

$$d\sigma_{ee} = \Gamma_t dE_1' d\Omega_1 (\sigma_t + \varepsilon\sigma_\ell) \cdot N(\omega_2, \Theta_2^{max}) d\omega_2 \quad . \tag{8.6}$$

Here Γ_t and ε are the flux and polarisation of the firt photon, and $N(\omega_2, \Theta_2^{max})$ is the flux of the second one [812, 822]:

$$\Gamma_t dE_1' d\Omega_1 = \frac{\alpha}{2\pi^2} \frac{1}{|q_1^2|} \frac{E_1'}{E} \left(\frac{E^2 + E_1'^2 \cos^4\Theta_1/2}{E - E_1' \cos^2\Theta_1/2} - \frac{2m^2\omega_1^2}{|q_1^2|} \right) dE_1' d\Omega_1 \tag{8.7}$$

$$\varepsilon = 2E\, E_1' \cos^2(\Theta_1/2) / (E^2 + E_1'^2 \cos^4(\Theta_1/2)) \tag{8.8}$$

$$N(\omega_i, \Theta_i^{max}) d\omega_i = \frac{\alpha}{\pi} \frac{d\omega_i}{\omega_i} \left(\frac{E^2 + E_i'^2}{E^2} \ln \frac{2E\, E_i' \sin(\Theta_i^{max}/2)}{m\, \omega_i} - \frac{E_i'}{E} \right). \tag{8.9}$$

Equations 8.6-8.9 are valid not only for small angles Θ_1 of the first electron [819], but for <u>all</u> Θ_1, provided the condition

$$|q_2^2| \ll W^2 \tag{8.10}$$

is fulfilled. Appendix A1 will give a short derivation[+)] and an estimate showing that, within plausible dynamical assumptions, the neglected longitudinal contributions are indeed very small.

[+)] The more complicated two-term formula for differential cross sections has been derived in Ref.[823].

A straightforward angular integration of (8.7) leads to the important case of 'double antitagging' [+]

$$d\sigma_{ee} = \sigma_t \cdot N(\omega_1, \Theta_1^{max})\, d\omega_1 \cdot N(\omega_2, \Theta_2^{max})\, d\omega_2 \tag{8.11}$$

with the spectra of the two colliding quasi-real photon beams given by (8.9).

If the final state consists of a resonance of mass M, spin J, and the widths Γ_f, $\Gamma_{\gamma\gamma}$ and Γ respectively for the decay into the detected final state, two photons, and all, the cross section has to be replaced by [826]

$$\sigma_t = 8\pi \cdot (2J+1) \cdot \frac{\Gamma_{\gamma\gamma} \cdot \Gamma_f}{(W^2 - M^2)^2 + \Gamma^2 M^2} \tag{8.12}$$

8.2 Selection of $\gamma\gamma$ events

The trigger acceptance for $\gamma\gamma$ events includes the following classes

(1) 'no-tags' (no signal $\geq$ 4 GeV in LAT or SAT) together with $\geq$ 2 'long opposite tracks' in the central detector ($\cos\Theta < 0.63$, $|\Phi_1 - \Phi_2| > 94^o$, $p_\perp > 350$ MeV/c)

(2) 'single tags' ($\geq$ 4 GeV in LAT or SAT) together with $\geq$ 1 long (see above) and $\geq$1 'short' track ($|\cos\Theta| < 0.87$, $p_\perp > 100$ MeV/c), or $\geq$ 2 'long' tracks.

In part of the experiment only one short track was required.

(3) 'double tags' ($\geq$ 4 GeV for one and $\geq$ 1.5 GeV for the other scattered electron) together with $\geq$ 1 short track or a minimum shower signal in the barrel.

All events with $\geq$ 2 reconstructed tracks originating from the vicinity of the beam line ($\pm$ 15 mm) are considered $\gamma\gamma$ candidates. The separation of $\gamma\gamma$, annihilation, and background events is based on the measurement of the vertex coordinate z along the beam (z = o marks the interaction point as determined from Bhabha scattering), and the total (charged + neutral) energy E_{VIS} measured in the calorimeter-like central detector. The z distribution of the candidates

[+] For simplicity the notations 'untagged' and 'no-tag' will also be used for the doubly antitagged events.

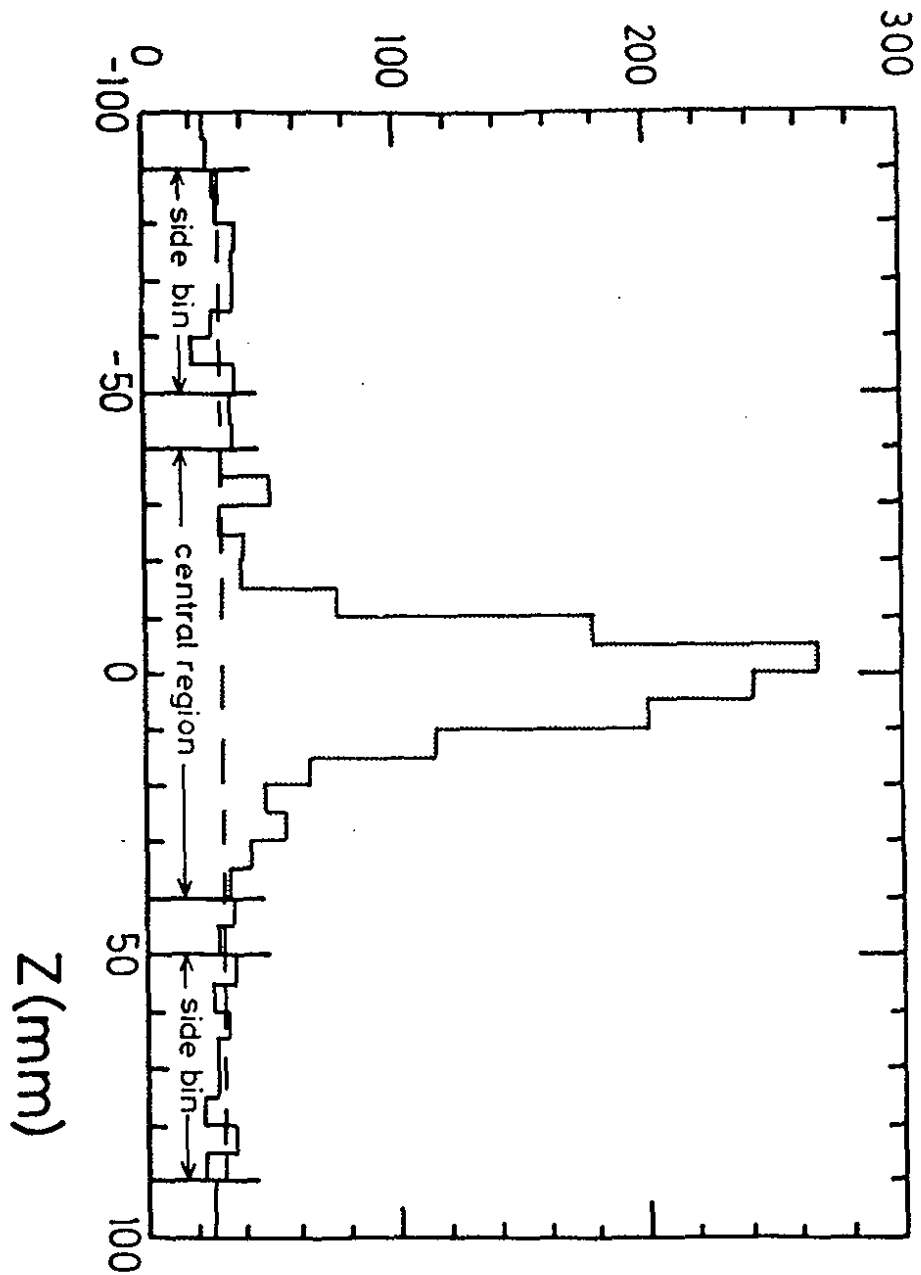

Fig. 8. 2 Vertex distribution along the beam axis, showing the regions used for background subtraction. Shaded area is the net beam-beam signal.

(Fig. 8.2; 12 GeV data after cosmic rejection) shows a pronounced beam-beam signal on top of a flat background. The net beam-beam signal is obtained by subtracting from the central region the background as inferred from equivalent side bins. Fig. 8.3 gives the energy distribution of all events from the central z region, of the net beam-beam signal, and of the subsample of tagged events. At high energies the one-photon annihilation events produce a broad peak with negligible background. The low-energy peak consists partly of beam-gas background, but to a larger fraction of $\gamma\gamma$ events (shaded area). The subsample of the tagged events (hatched) also peaks at low energies, in agreement with the interpretation.

Fig. 8.3 demonstrates that it is possible to analyse $\gamma\gamma$ events even in the untagged mode. The main results for the two-prong class (Sect. 8.3) have indeed been obtained from untagged (more precisely: from doubly antitagged) events. Hadron production, as described in Sect. 8.4, has been measured in the single-tag (= 'single tag * antitag') mode.

8.3 Production of lepton and hadron pairs

Two-particle production by two photons is interesting for several reasons:

1. The production of $\mu^+\mu^-$ and e^+e^- pairs can be calculated in QED. The measurement checks QED calculations of order α^4.

2. The reaction $\gamma\gamma \to \mu^+\mu^-$ sets the scale for 'pointlike' particle production in the investigation of $\gamma\gamma \to q\bar{q} \to 2$ jets. For high transverse momenta the quarks are expected to appear pointlike, and the ratio of both cross sections to approach a constant [814].

3. The production of low-energy $\pi^+\pi^-$ pairs is sensitive to π-π phase shifts in even angular momentum states [803], and in particular measures the $\gamma\gamma$ coupling of C-even mesons like the f^0.

The dominant two-body channels are e^+e^- and $\mu^+\mu^-$ pairs. Pion pairs in general cannot be separated from the $\mu^+\mu^-$ channel because particle momenta are too low. Non-resonant pion pair production is expected to contribute less than 10% of the total muon yield [809]. The production of $\pi^+\pi^-$ resonances however should show up as peaks above the smooth, QED predicted distribution of invariant two-body masses.

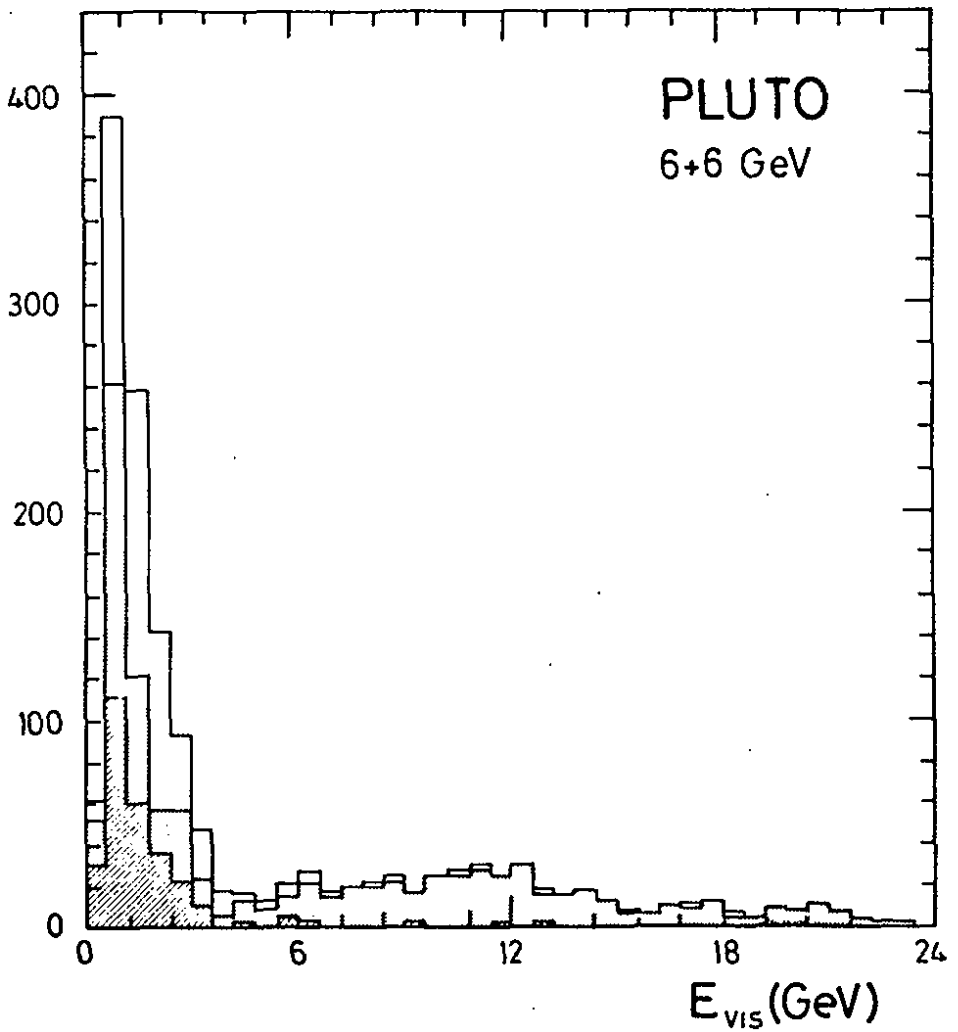

Fig. 8. 3 Distribution of the observed energy for all events of the 'central region' (Fig. 8.2), and the subclasses of all beam-beam events (shaded) and the tagged beam-beam events .

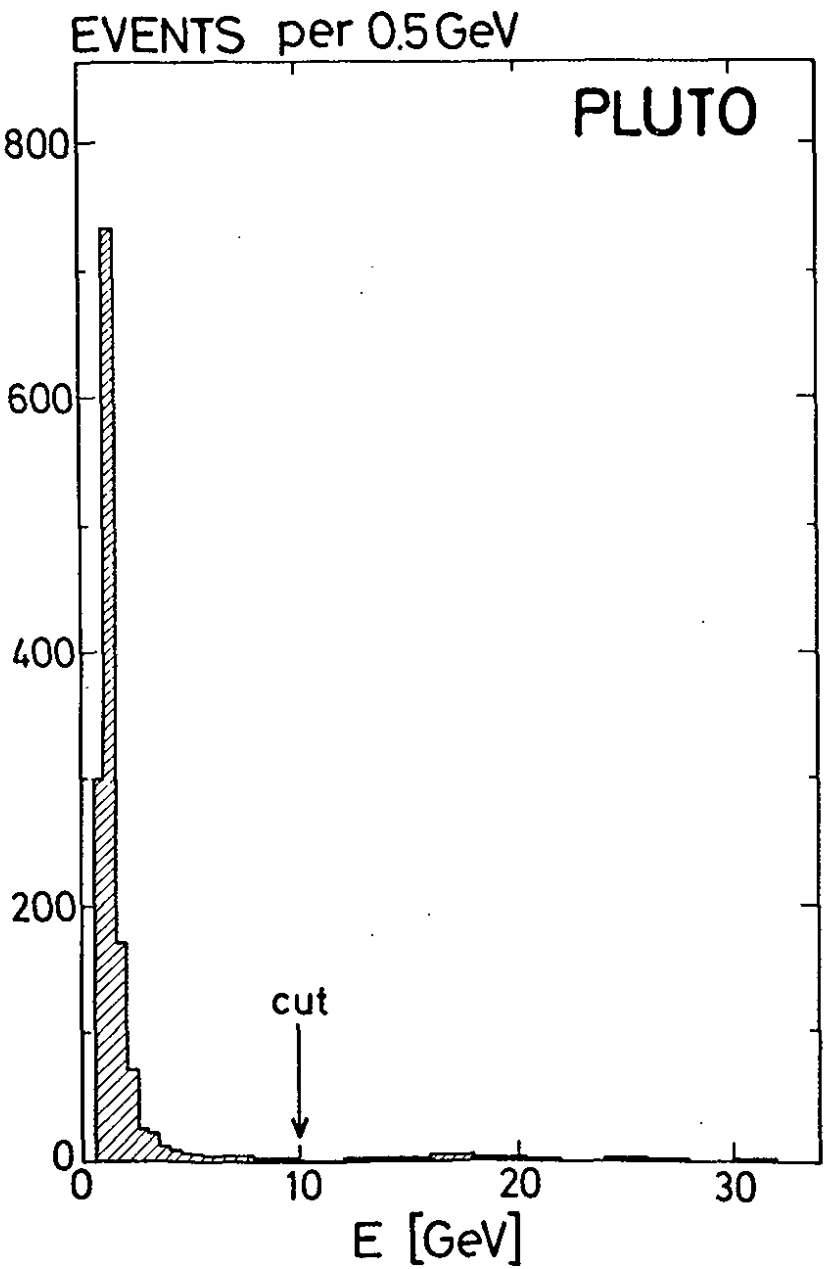

Fig. 8. 4 Total energy of acollinear twoprong events as observed in the central detector. Background has been subtracted in all of Figs. 8.4 - 8.10.

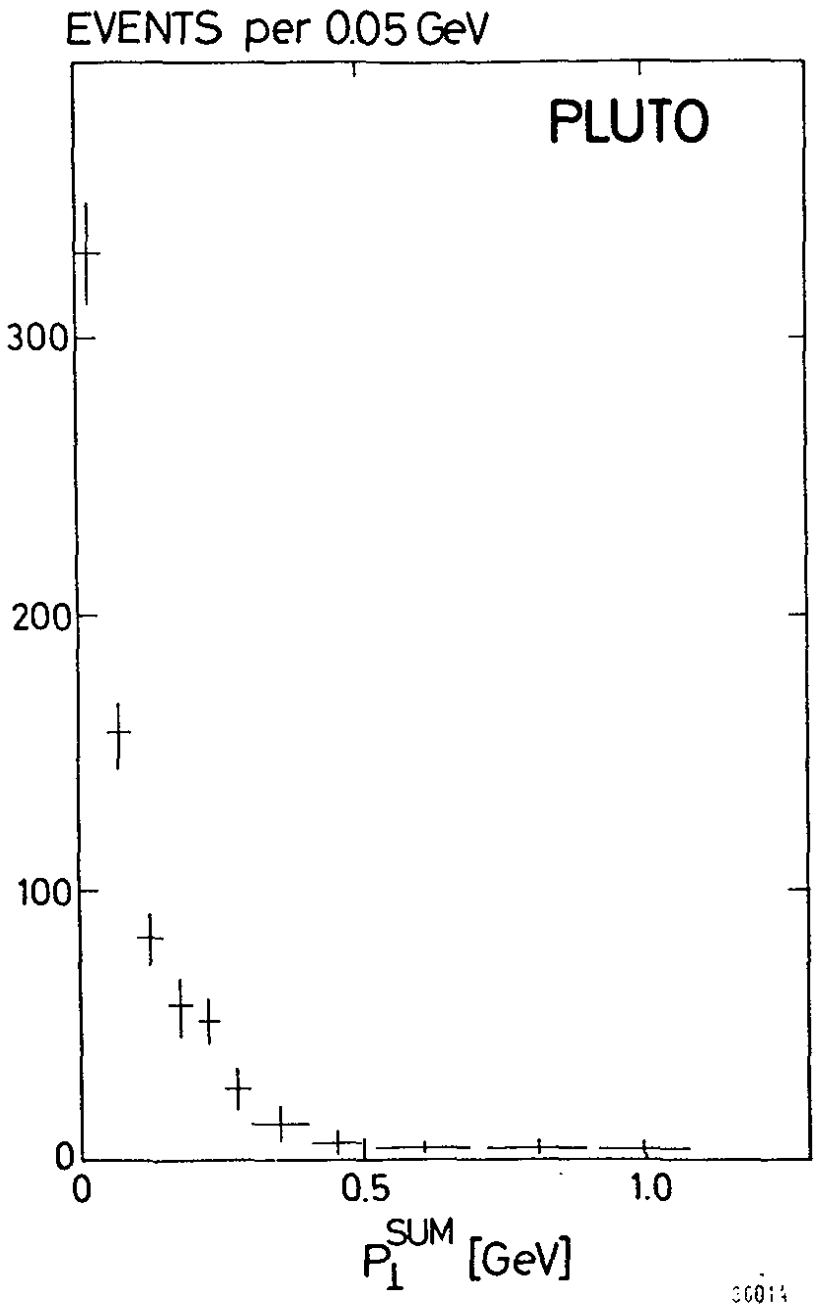

Fig. 8. 5 Missing transverse momentum of twoprong events.

A clean sample of anti-tagged events was obtained from the data taken at E_B = 15 GeV by selecting events with exactly two tracks and no neutral energy [828]. The two tracks were required to have $p_\perp > 400$ MeV, $\cos\Theta < 0.56$, and an acoplanarity angle > 15^o. These cuts strongly suppress events from e^+e^- annihilation, and cosmics. The beam-gas contamination was less than 10% on average, and subtracted separately for every data point. The distribution of the observed energy (Fig. 8.4) and of the missing transverse momentum (Fig. 8.5) show as the characteristic feature large missing energy combined with small missing transverse momentum, in complete agreement with the kinematics of the two-photon process. Events with $E_{vis} > 10$ GeV were excluded as possible radiative annihilation events.

Fig. 8.6 gives the spectrum of the invariant masses, taking pion masses for both particles. The full curve is an absolute QED prediction for ee, and $\mu^+\mu^-$ pairs [829, 830], with pion masses substituted for all. Radiative corrections [827], and non-resonant $\pi\pi$ production, all believed to be effects of order 10%, are not included. Within these uncertainties the agreement is good, except for the interval between 1.0 and 1.5 GeV. Here one observes an excess which can be very well described by a resonance with position and width of the f^o meson. The signal as obtained from fitting both the nonresonant and the resonant part corresponds to (128±27) f^o mesons. The observed angular range and the statistics are too small to distinguish between the two possible helicities, $\lambda = 2$ and $\lambda = 0$. Assuming $\lambda = 2$ to dominate one obtains with the help of Equ. 8.11 and 8.12:

$$\Gamma(f^o \to \gamma\gamma) = (2.3 \pm 0.5(stat.) \pm 0.35(syst.)) \text{ keV} \qquad (8.13)$$

The virtuality of both photons is so low, $\langle |q_i^2| \rangle \simeq 0.007$ GeV^2, that the result can be considered as the f^o width for the decay into two real photons. It can be compared to numerous theoretical predictions as listed in table 8.I

Table 8.1 Predictions for the width $\Gamma(f \to \gamma\gamma)$

Reference	$\Gamma_{\gamma\gamma}$ (keV)
831	0.8
832	> 1
833	1.2 - 2.3
826	2.6
834	5.07
835	7
836	5.7
837	8

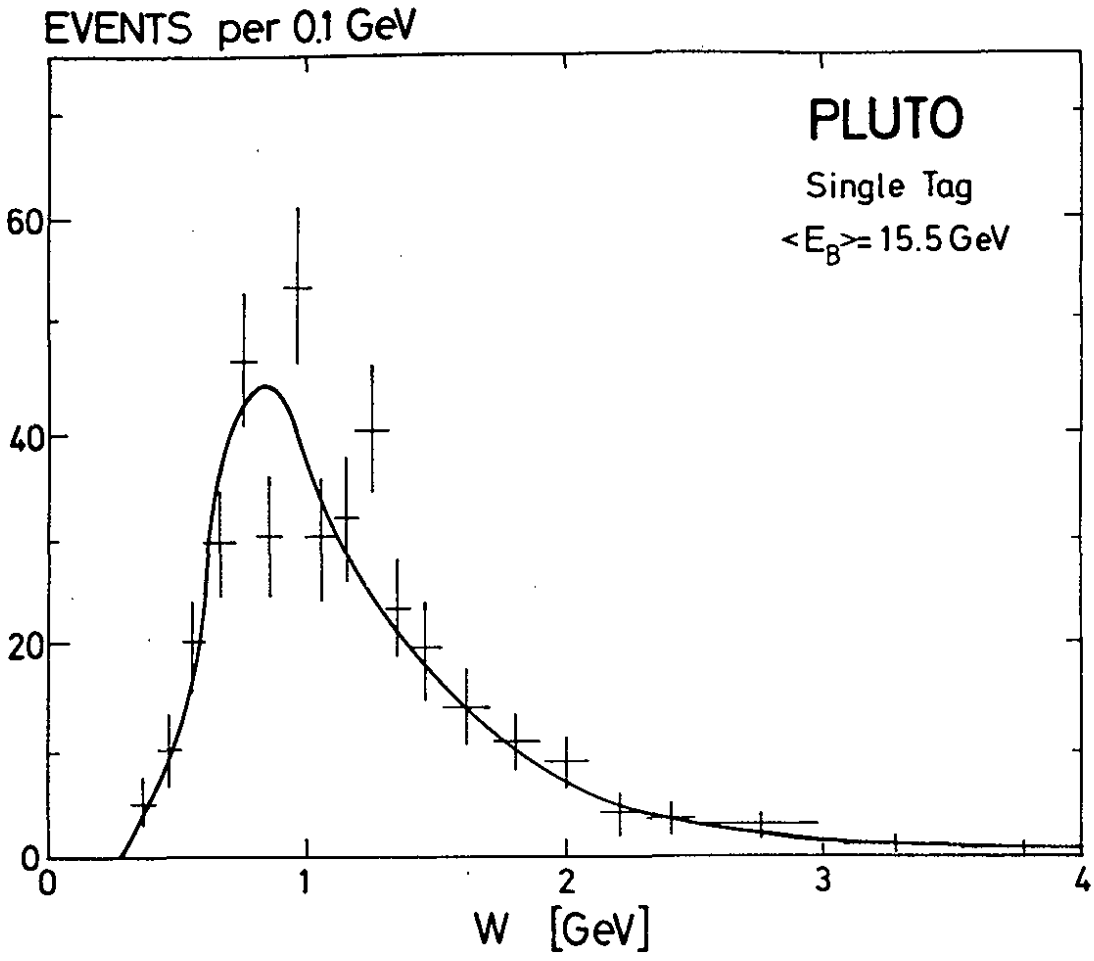

Fig. 8. 7 Invariant mass distribution of the two-prong events with a single tag in the SAT, together with QED prediction.

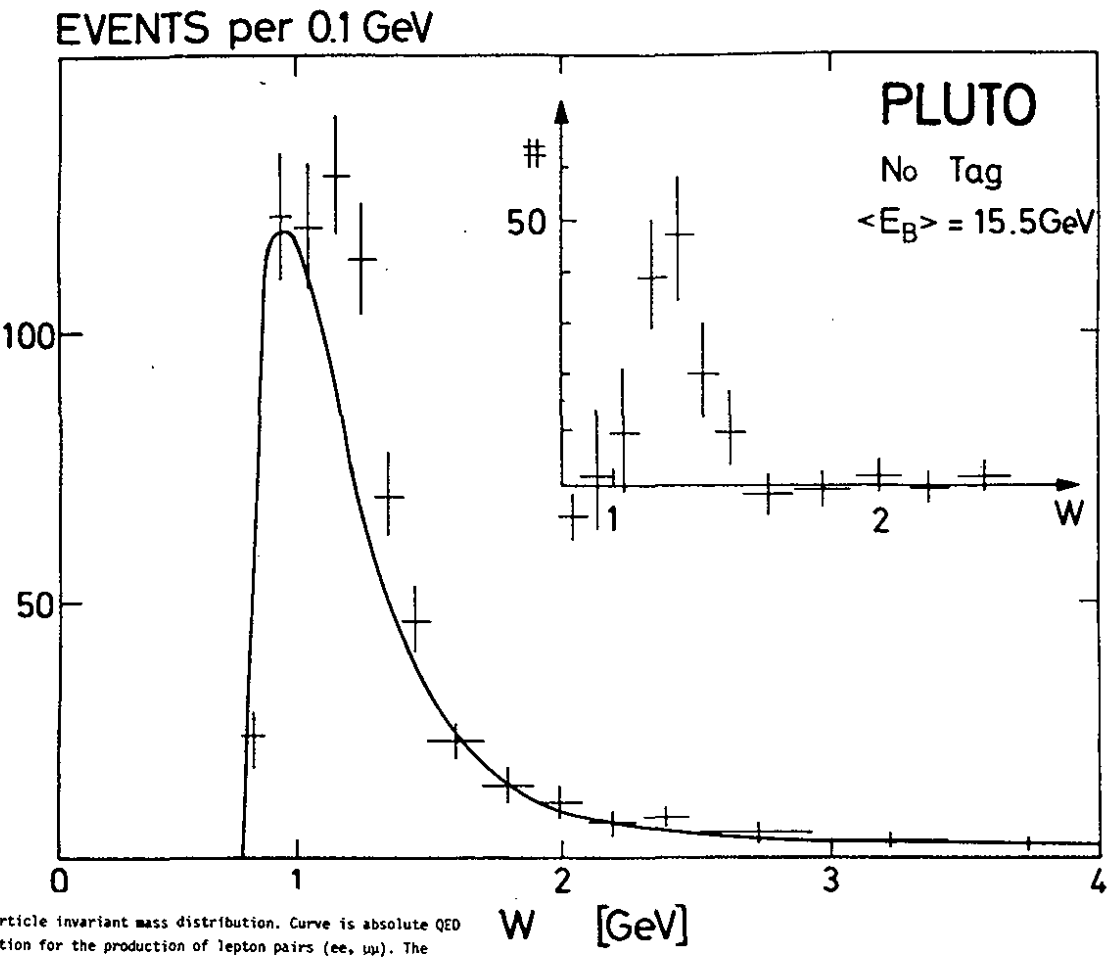

Fig. 8. 6 Two-particle invariant mass distribution. Curve is absolute QED prediction for the production of lepton pairs (ee, μμ). The insert shows the difference between the data and the QED prediction. Pion masses have been inserted for the display of the observed as well as the predicted invariant masses.

Reference	$\Gamma_{\gamma\gamma}$ (keV)
838	8
839	9.2
840	11.3
841	21 ±6
842	28
experiment	2.3 ±0.5

The experimental width is close to the values obtained from a non-relativistic quark model with an oscillator potential. In judging other predictions one should note, however, that some of them were derived using old experimental input which should be updated. As an example, the prediction of Ref. [836] should now read 3 keV [843]. It should also be noted that the experimental result would change to 4.4 keV, if, quite contrary to theoretical expectations, the helicity zero state would dominate in the production.

In the same experiment [828] the considerably smaller sample of single-tag events was also analysed. The invariant mass distribution (Fig. 8.7) shows, on top of the QED prediction [830] only a small enhancement at the f^0 mass. It can be attributed to the f^0 production via one quasi-real photon, as above, and one virtual one with $\langle|q_2^2|\rangle = 0.28\ \text{GeV}^2$. Assuming again $\lambda=2$ production, the analysis acc. to Eqs. 8.6 and 8.12 leads to an upper limit

$$\Gamma(f^0 \to \gamma^*\gamma) < 2.6\ \text{keV at 95\% C.L.} . \qquad (8.14)$$

The analysis of the two-prong production has thus demonstrated, within systematic uncertainties of typically 15%, a quantitative agreement with the lowest order QED prediction. A clear resonant enhancement has been observed at the f^0 mass, and has been used to extract its $\gamma\gamma$ width. This constitutes, via the inverse reaction, the first measurement of the very small branching ratio

$$B(f^0 \to \gamma\gamma) = (1.3 \pm 0.4) \times 10^{-5} \qquad (8.15)$$

8.4 The total hadronic $\gamma\gamma$ cross sections

Hadron production in photon-photon interactions appears to be a new and promising testing ground for a large range of hadron and quark dynamics. The different regions can be reached by just varying the virtuality $Q^2 = -q_1^2$ of one of the photons, while keeping the other one (the 'target') close to real. For large Q^2, the reaction tests the structure of the target photon, as described by the structure functions $F(x,Q^2)$ ($x = Q^2/(Q^2 + W^2)$, see [825]). The photon is expected to change with increasing x from a $q\bar{q}$ bound state in a *long-distance potential, the ρ meson,* to a free $q\bar{q}$ system which is completely determined by short-distance dynamics, and calculable in perturbative QCD [813]. Preliminary results from this region have already been reported [850].

In contrast, the low Q^2 cross section is expected to be dominated by hadronic diffraction and particle-exchange mechanisms, in accordance with the vector dominance model (VDM). The asymptotic diffraction cross section at $Q^2 \approx 0$ is given by factorization:

$$\sigma_{\gamma\gamma}(\infty) = \sigma_{\gamma p}{}^2/\sigma_{pp} \approx 240\ \text{nb} \qquad (8.16)$$

An extrapolation to the low-energy region by resonance-Regge duality, and to $Q^2 \neq 0$ by a simple ansatz for the ρ form factor leads to [844,845]

$$\sigma_t\,(W,Q^2) = (240\ \text{nb} + 270\ \text{nb}\cdot\text{GeV}/W + B/W^2)\ /\ (1 + Q^2/m_\rho^2)^2 \qquad (8.17)$$

The term B/W^2 is neglected in the VDM predictions [844,845] but has been added here to *describe deviations at small W (which may result from the 'quark box diagram', see* below).
The low- and medium Q^2 cross section has been measured by the PLUTO group at beam energies around 7 GeV [821] and 15 GeV [822,851]. Single tag events were defined by one photon tagged with the SAT, the other one anti-tagged, and an energy W_{vis} observed in the central PLUTO detector in form of either ≥ 3 tracks, or 2 tracks and ≥ 1 non associated photon or π^0. This fixes the kinematics and allows a measurement of $\sigma_t + \varepsilon\sigma_\ell$ according to Equ. (8.6).

The detection efficiency was calculated with the Monte Carlo simulation described in sect. 3.8.5.3. The simulation reproduces the observed charged and neutral multiplicities, as well as the p_T distribution (Fig. 3.13).

Fig. 8.8 gives the total cross section $\sigma_t + \varepsilon\sigma_\ell$ as it appears at the observed hadronic energy W_{vis}. According to the simulation, W_{vis} is typically 15-20% lower than the true photon-photon c.m. energy W. The photon polarization parameter is close to one, $\langle\varepsilon\rangle = 0.95$. The energy dependence of the cross section is weak above 3 GeV, in agreement with the VDM prediction (Equ. 8.17 with B = 0). At lower energies, however, one observes a strong dependence on W_{vis}.

The Q^2-dependence of the cross section is given in Figs. 8.9a and b separately for low and high W_{vis}. Both show a similar falloff consistent with the ρ form factor. Therefore, within the accuracy of the data the W- and Q^2-dependence of the cross section can be separated as formulated in (8.17). A fit gives $B = (2250 \pm 500)$ nb · GeV^2, and leaves the other 'VDM' terms practically unchanged.

The cross section at $Q^2 = 0$ as obtained from the fit is shown in Fig. 8.10 as a function of the true W. The full lines represent the 1σ error limits. The estimated systematic error, resulting mainly from the acceptance calculation, is ±20%. The VDM expectation according to (8.17) with B = 0 is shown as a dashed line.

The origin of the significant and sizeable $1/W^2$ term in the cross section is not clear. It has been suggested [846] that a 'quark box diagram' should contribute:

$$\sigma_{Box} = \frac{4\pi\alpha^2}{W^2} \cdot 3\sum_{\text{flavours}} e_q^4 \ln\frac{W^2}{m_q^2} \qquad (8.18)$$

While the W-dependence agrees, the magnitude as calculated with 3 flavours and an effective quark mass $m_q = 100$ MeV is a factor of 2 too small. Also, the Q^2-dependence is expected weaker than observed in Fig. 8.9a. On the other hand, it seems not to be possible to explain the full observed $1/W^2$ contribution in terms of Regge poles or cuts [847].

Multihadron production definitely deviates from the (asymptotic) VDM extrapolation (eq. 8.17 with B = 0) at $W \lesssim 3$ GeV, and requires a substantial contribution consistent with a $1/W^2$ dependence. In the range of $5 < W < 10$ GeV the measured cross section and the VDM prediction agree. The Q^2 dependence is consistent with the ρ form factor at all values of W.

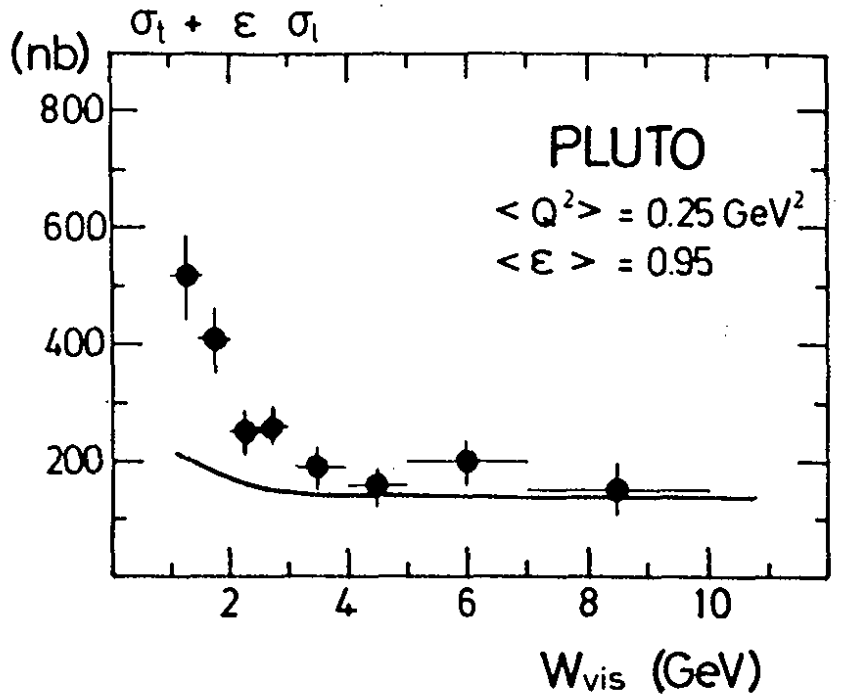

Fig. 8. 8 Total cross section $\sigma_t + \varepsilon\sigma_l$ as a function of the observed invariant mass W_{vis} of the hadron system. The solid line gives the prediction of the VMD model, folded with the energy response of the detector.

31941

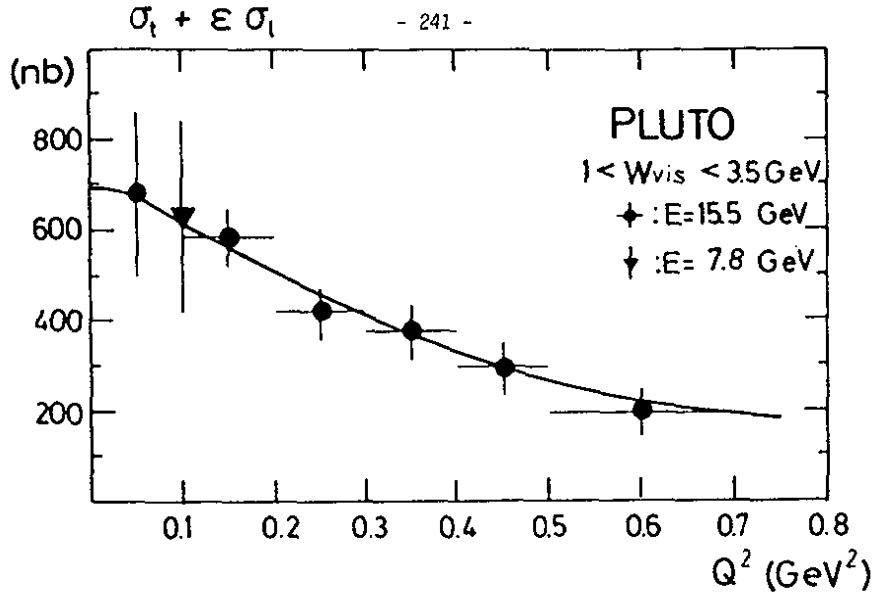

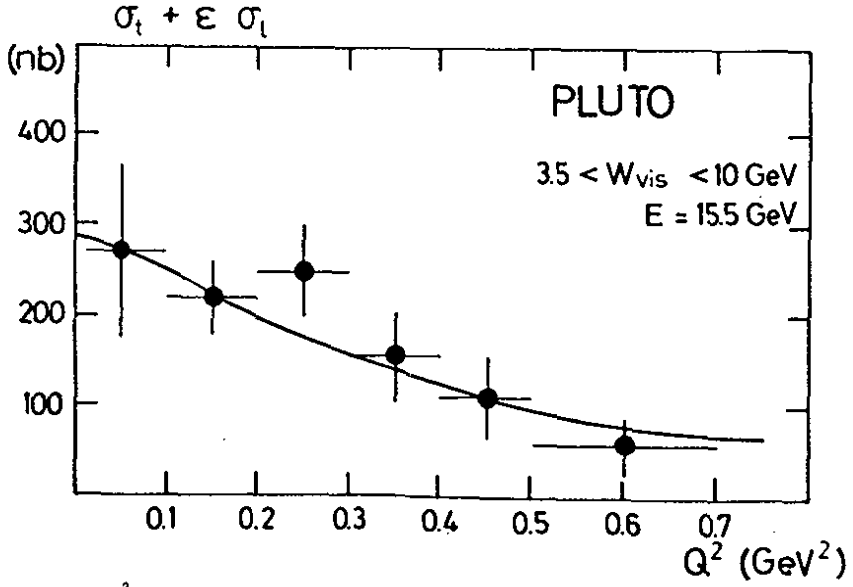

Fig. 8. 9 Q^2 dependence of the total hadronic cross section $\sigma_t + \varepsilon\sigma_l$ for (a) small and (b) large visible energies. The solid lines are the predictions from ρ meson dominance.

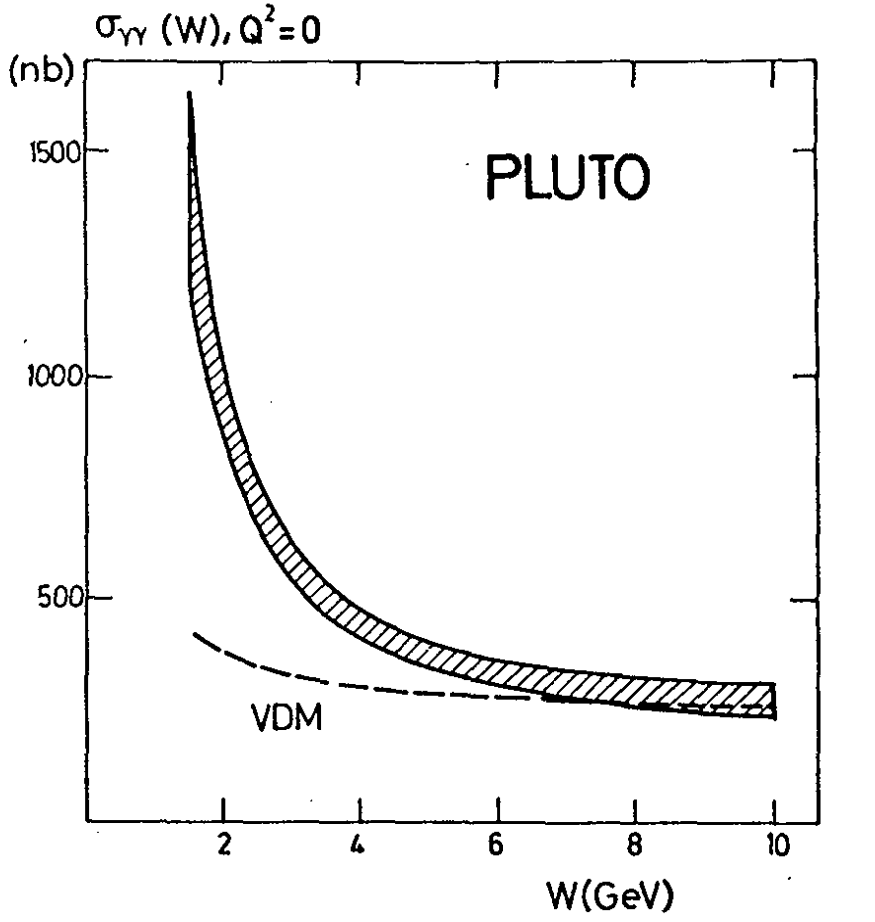

Fig. 8.10 Total hadronic cross section σ_t extrapolated to $Q^2 = 0$, versus the true photon-photon invariant mass. The hatched band shows the 1 std. limits as obtained from the fit. The VDM prediction is given by the dashed line.

8.5 High $p_\perp$ jets

A direct way to observe point-like interactions of real photons with quarks is the reaction:

$$\gamma\gamma \rightarrow q\bar{q} \rightarrow 2 \text{ jets} \tag{8.19}$$

where the jets have large transverse momenta with respect to the beam. Refs. [814,815] suggest that the 2-jet and inclusive 1-jet cross sections from this mechanism are much larger than those for high $p_\perp$ jets produced via the VDM in ρ^0-ρ^0 scattering. The ratio $R_{\gamma\gamma}$ of the quark to the muon cross section is given by the fourth power of the quark charges e_q:

$$R_{\gamma\gamma} = \frac{\sigma(\gamma\gamma \rightarrow 1 \text{ jet} + X)}{\sigma(\gamma\gamma \rightarrow \mu^+\mu^-)} = 3 \sum_{q=u,d,s,c} e_q^4 = \frac{34}{27} \tag{8.20}$$

First order QCD corrections are small for high $p_\perp$ (of the jets) [814, 848, 849].

Fig. 8.11 shows one example of a two-jet event which is coplanar with the beam, but not collinear, and labelled as a $\gamma\gamma$ reaction by a tag in the SAT. A small sample of such two-jet events has been collected and is being analysed. Preliminary results [825] are consistent with the hard scattering mechanism (8.19).

In conclusion, the first data obtained by the PLUTO group have demonstrated that hadron production by high energy photon-photon reactions can be detected and analysed, and that the results mostly agree with naive expectations from the VDM. In addition, they indicate the exciting possibility that hard scattering contributions may already be visible in the total cross section at low Q^2, and also in the production of high - $p_\perp$ jets.

New data with higher statistics, covering a wider range of Q^2, are presently being analysed, and will help to test these first interpretations with greater precision.

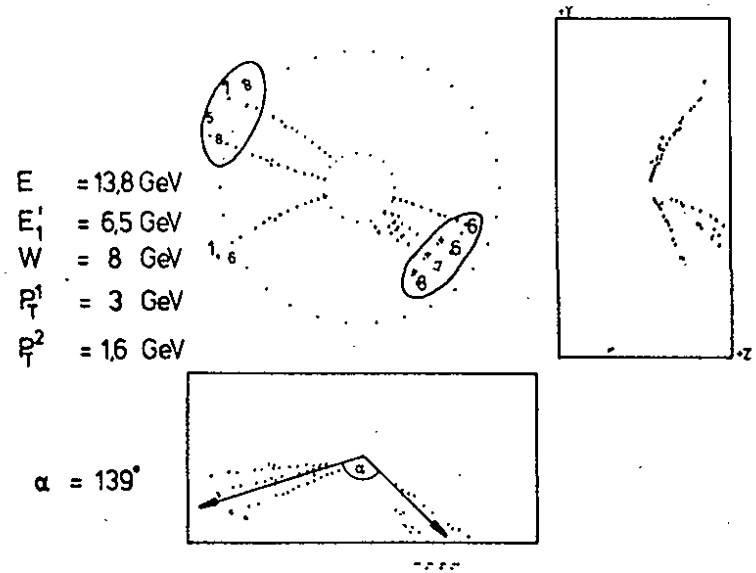

Fig. 8.11 Three projections of photon-photon produced two-jet event with kinematics as obtained from the tagging counter and the central detector. The figures in the x-y projection show the neutral energy signal as observed in the barrel and endcap shower counters.

APPENDIX A1: Electron-electron and photon-photon cross sections

A general relation between the inelastic electron-electron and total photon-photon cross sections has first been given in Ref. [807], and can also be found in Refs. [810, 812]. Using variables as defined in Fig. 8.1 it can be formulated as

$$d\sigma_{ee} = (\Gamma_T^1\sigma_{TT}\Gamma_T^2 + \Gamma_S^1\sigma_{ST}\Gamma_T^2 + \Gamma_T^1\sigma_{TS}\Gamma_S^2 + \Gamma_S^1\sigma_{SS}\Gamma_S^2 + A\cos 2\phi + B\cos\phi)\, dE_1' d\Omega_1 dE_2' d\Omega_2 \qquad (A1.1)$$

The Γ^i can be considered flux factors for transverse (T) and longitudinal (S) photons. They are given by

$$\Gamma_T^i\, dE_i' d\Omega_i = 2\,\rho_i^{++}\, C_i\, dE_i'\, d\Omega_i$$
$$\Gamma_S^i\, dE_i' d\Omega_i = \rho_i^{00}\, C_i\, dE_i\, d\Omega_i \qquad (A1.2)$$

where the $\rho_i^{\lambda\lambda'}$ are photon density matrices in the helicity basis ($\lambda = -, 0, +,$):

$$\rho_i^{00} = (2p_i q_{3-i} - q_1 q_2) / X \quad - 1$$
$$2\rho_i^{++} = \rho_i^{00} + 2 - 4\,m^2/\,|q_i^2| \qquad (A1.3)$$

with

$$X = (q_1 q_2)^2 - q_1^2\, q_2^2 \qquad (A1.4)$$

The phase space and propagator factor $C_1 C_2$ has been artificially split into:

$$C_1 = \frac{\alpha}{4\pi^2}\,\frac{1}{|q_1^2|}\,\frac{\sqrt{X}}{(p_1+p_2)\cdot q_2}$$
$$C_2 = \frac{\alpha}{4\pi^2}\,\frac{1}{|q_2^2|}\,\frac{(p_1+p_2)\cdot q_2}{p_1 p_2} \qquad (A1.5)$$

ϕ is the azimuthal angle between the scattering planes, as seen in the photons' c.m. system. A and B have a similar structure as the other terms, but will disappear due to the azimuthal symmetry of the detection as discussed below.

Factorization of the relation (A1,1) means that the factors Γ_T^i and Γ_S^i depend only on the variables of the electron 'i' and can therefore be interpreted as the independently radiated photon flux. This has been shown to hold if both electron angles are small [805, 807, 819]. Factorization also occurs, as shown below, if only <u>one</u> of the electrons is emitted at small angle Θ_2, and the virtuality of the emitted photon is small

$$\Theta_2 \ll 1 \qquad (A1.6a)$$

$$|q_2^2| \ll W^2 \qquad (A1.6b)$$

Equ. A1.6b 'usually' follows from A1.6a, except for very small photon energies.

With the help of (8.3), (8.4), and the general relation

$$2\,p_{3-i}q_i = 4\,\omega_i E - q_i^2 \qquad (i = 1,2) \qquad (A1.7)$$

one obtains in the approximation (A1.6)

$$\sqrt{X} \approx q_1 q_2 \simeq 2\omega_2 (E - E_1' \cos^2\Theta_1/2) \qquad (A1.8)$$

and the final expressions (whose symmetry has partly been enforced by substituting $\omega_2 \leftrightarrow E - E_2' \cos^2\Theta_2/2$) :

$$C_i = \frac{\alpha}{4\pi^2}\,\frac{1}{|q_i^2|}\,\frac{E - E_i' \cos^2\Theta_i/2}{E} \qquad (i = 1,2) \qquad (A1.9)$$

$$\Gamma_T^i = \frac{\alpha}{4\pi^2}\frac{1}{|q_i^2|}\frac{E_i'}{E}\frac{E^2+E_i'^2\cos^4\Theta_i/2 - 2m^2\omega_i^2/|q_i^2|}{E - E_i'\cos^2\Theta_i/2} \qquad (i = 1,2) \qquad (A1.10)$$

$$\Gamma_S^i = \frac{\alpha}{4\pi^2}\frac{1}{|q_i^2|}\frac{E_i'}{E}\frac{2\,E\,E_i'\cos^2\Theta_i/2}{E - E_i'\cos^2\Theta_i/2} \qquad (i = 1,2) \qquad (A1.11)$$

These equations show the desired factorization for arbitrary scattering angles Θ_i. Integration over $d\Omega_2 = d\phi_2\, d\cos\Theta_2$ cancels the ϕ-dependent terms in (A1.1)[+], and leads to Equ. 8.6 with $\sigma_t = \sigma_{TT}$, $\sigma_l = \sigma_{ST}$, and $\Gamma_t = \Gamma_T^1$.

For small Θ_2^{max} the contributions of σ_{TS} and σ_{SS} are small, because due to gauge invariance they vanish proportional to q_2^2 [812]. A quantitative estimate can be made if one assumes that the q_2^2-dependence is governed by the hadron (ρ) form factor

$$F_\rho = 1 / (1 + |q_2^2|/m_\rho^2) \qquad (A1.12)$$

like

$$\sigma_{TS} \simeq (1 - F_\rho) \cdot \sigma_{TT} \qquad (A1.13)$$

$$\sigma_{TT} \simeq F_\rho^2 \cdot \sigma|_{q_2=0} \qquad (A1.14)$$

For the case of PLUTO at PETRA, integration of $\sigma_{TS}\Gamma_S^2$ up to $\Theta_2^{max} \simeq 0.02$ leads to a contribution of only 1% relative to $\sigma_{TT}\Gamma^2{}_T$. Even for larger Θ_2^{max} the relative contribution will stay small. The same applies to the contribution of $\sigma_{SS}\Gamma_S^2$ relative to $\sigma_{ST}\Gamma_T^2$.

Therefore, as long as the ratio of longitudinal to transverse cross sections does not rise faster than $1 - F_\rho$, the omission of σ_{TS} and σ_{SS} in (8.6) and of σ_{ST} in (8.11) is fully justified.

[+] Averaging over the azimuth of the first electron, ϕ_1, has tacitly been assumed. Otherwise a ϕ-dependence of A and B could remain from the W-dependence on ϕ_2.

[800] C.F. Weizsäcker, Z. Physik 88 (1934) 612
L.D. Landau and E. M. Lifshitz, Sov. Phys. 6 (1934) 244
E. I. Williams, Math. Fys. Medd. 13 (1935) N4

[801] F. Low, Phys. Rev. 120 (1960) 582

[802] F. Calogero and C. Zemach, Phys. Rev. 120 (1960) 1860

[803] P.C. DeCelles and J.F. Goehl, Jr., Phys. Rev. 184 (1969) 1617

[804] N. Arteago-Romero, A. Jaccarini and P. Kessler, Acad. Sci. B 129 (1969) 153; B 269 (1969) 1129

[805] V.E. Balakin, V.M. Budnev and I.F. Ginzburg, Zh. Exp. Teor. Fiz. Pisma 11 (1970) 559 (JETP Letters 11 (1970) 388)

[806] J.S. Brodsky, T. Kinoshita and H. Terezawa, Phys. Rev. Lett. 25 (1970) 972

[807] V.M. Budnev and I.F. Ginzburg, Yad. Fiz 13 (1971) 353 (Sov. J. Nucl. Phys. 13 (1971) 198)

[808] T.F. Walsh, Phys. Lett 36B (1971) 121

[809] J.S. Brodsky, T. Kinoshita and H. Terezawa, Phys. Rev. Lett 25 (1970) 972 and 27 (1971) 280; Phys. Rev. D4 (1971) 1532

[810] G. Bonneau, M. Gourdin and F. Martin, Nucl. Phys. B 54 (1973) 573

[811] T.F. Walsh and P. Zerwas, Phys. Lett. 44B (1973) 195

[812] V.M. Budnev, I.F. Ginzburg, G.V. Meledin and V.G. Serbo, Phys. Rep. 15C (1975) 182

[813] E. Witten, Nucl. Phys. B 120 (1977) 189

[814] J.S. Brodsky, T.A. DeGrand, J.F. Gunion and J.H. Weis, Phys. Rev. Lett. 41 (1978) 672

[815] C.H. Llewellin Smith, Phys. Lett. 79B (1978) 83

[816] C.G. Brown and D.H. Lyth, Nucl. Phys. B 53 (1973) 323

[817] G. Bonneau and F. Martin, Nucl. Phys. B 68 (1974) 367

[818] C. Carimalo, P. Kessler and J. Parisi, Phys. Rev. D 20 (1057) 1979

[819] J.H. Field, Nucl. Phys. B 168 (1980) 477

[820] Ch. Berger in Proc. 1979 Int. Symp. on Lepton and Photon Interactions at High Energies, Fermilab 1979, ed. by and Proc. 1979 Int. Conf. on Two-Photon Interactions, Lake Tahoe, ed. by J.F. Gunion

[821] PLUTO Collab., Ch. Berger et al., Phys. Lett. 89B (1979) 120

[822] PLUTO Collab., Ch. Berger et al., Phys. Lett. 99B (1981) 287

[823] C. Carimalo, P. Kessler and J. Parisi, Phys. Rev. D 20 (1979) 2170, Phys. Rev. D 21 (1980) 669

[824] L.N. Hand, Phys. Rev. 129 (1963) 1834

[825] Ch. Berger, Proceedings of the International Workshop on $\gamma\gamma$ Interactions, Amiens, April 1980, Springer Lecture Notes in Physics 134 (1980)

[826] V.M. Budnev and A.E. Kaloshin, Phys. Lett. 86B (1979) 351
[827] C. Cochard and S. Ong, Phys. Rev. D 19 (1979) 810
[828] PLUTO Collab., Ch. Berger et al., Phys. Lett. 94B (1980) 254
[829] R.Bhattacharya, J. Smith and G. Grammer, Phys. Rev. D 15 (1977) 3267
[830] J.A.M. Vermaeseren, private communication
[831] A. Bramon and M. Greco, Nuovo Cimento Lett. 2 (1971) 522
[832] D. Faiman, H.J. Lipkin and H.R. Rubinstein, Phys. Lett 59B (1979) 269
[833] S.B. Berger and B.T. Feld, Phys. Rev. D8 (1973) 3875
[834] N. Levy, P. Singer and S. Toaff, Phys. Rev. D13 (1976) 2662
[835] H. Kleinert, L.P. Staunton and P.H. Weisz, Nucl. Phys. B38 (1972) 87
[836] B. Schrempp-Otto, F. Schrempp and T.F. Walsh, Phys. Lett. B36 (1971) 463
[837] B. Renner, Nucl. Phys. B30 (1971) 634
[838] J. Babcock and J.L. Rosner, Phys. Rev. D 14 (1976) 1286
[839] M. Greco and Y.Srivastava, Nuovo Cimento 43A (1978) 88
[840] G. Schierholz and K. Sundermeyer, Nucl. Phys. B 40 (1972) 125
[841] V.N. Novikov and S.I. Eidelman, Sov. J. Nucl. Phys. 21 (1975) 529
[842] G.M. Radutzkij, Sov. J. Nucl. Phys. 8 (1969) 65
[843] F. Schrempp, private communication
[844] J.L. Rosner, BNL report 17522 (1972) 316
[845] T.F. Walsh, J. Physique C2 Suppl. 3 (1974) 77
S.J. Brodsky, ibid., p. 69
[846] M. Greco and Y. Srivastava, Nuovo Cimento 43A (1978) 88
[847] V.M. Budnev, I.F. Ginzburg and V.G. Serbo, Phys.Lett. 96B (1980) 387
[848] J.H. Field, E. Pietarinen, and K. Kajantie, Nucl. Phys. B 171 (1980) 377
[849] F.A. Berends, Z. Kunszt and R. Gastmans, Phys. Lett. 92B (1980) 186
and DESY 80/89 (1980)
[850] PLUTO Collaboration, W. Wagner, Proc. of the XX Int. Conf. on High Energy Physics, Madison 1980.
[851] F.Raupach, thesis, Univ. of Aachen preprint PITHA 81/05

Figure Captions

Fig. 8. 1 (a) Photon photon diagram with notations for four vectors and laboratory variables. (b) 'Compton' or 'bremsstrahlung' diagrams.

Fig. 8. 2 Vertex distribution along the beam axis, showing the regions used for background subtraction. Shaded area is the net beam-beam signal.

Fig. 8. 3 Distribution of the observed energy for all events of the 'central region' (Fig. 8.2), and the subclasses of all beam-beam events (shaded) and the tagged beam-beam events (hatched).

Fig. 8. 4 Total energy of acollinear twoprong events as observed in the central detector. Background has been subtracted in all of Figs. 8.4 - 8.10.

Fig. 8. 5 Missing transverse momentum of twoprong events.

Fig. 8. 6 Two-particle invariant mass distribution. Curve is absolute QED prediction for the production of lepton pairs (ee, μμ). The insert shows the difference between the data and the QED prediction. Pion masses have been inserted for the display of the observed as well as the predicted invariant masses.

Fig. 8. 7 Invariant mass distribution of the two-prong events with a single tag in the SAT, together with QED prediction.

Fig. 8. 8 Total cross section $\sigma_t + \varepsilon\sigma_l$ as a function of the observed invariant mass W_{vis} of the hadron system. The solid line gives the prediction of the VMD model, folded with the energy response of the detector.

Fig. 8. 9 Q^2 dependence of the total hadronic cross section $\sigma_t + \varepsilon\sigma_l$ for (a) small and (b) large visible energies. The solid lines are the predictions from ρ meson dominance.

Fig. 8.10 Total hadronic cross section σ_t extrapolated to $Q^2 = 0$, versus the true photon-photon invariant mass. The hatched band shows the 1 std. limits as obtained from the fit. The VDM prediction is given by the dashed line.

Fig. 8.11 Three projections of photon-photon produced two-jet event with kinematics as obtained from the tagging counter and the central detector. The figures in the x-y projection show the neutral energy signals as observed in the barrel and endcap shower counters.

Acknowledgements

We are indebted to all members of the PLUTO collaboration who did the work reportet here, who helped in many discussions to clarify the issues, and who took over much of our work while we were writing this report. We also thank the technical services of DESY for their invaluable help, and in particular Mrs. E.Kuklinski for carefully typing (and patiently retyping) the manuscript.